Interfacing Long-Lived Mechanical Oscillators and Superconducting Quantum Circuits

Thesis by
Alkım Berke Bozkurt

In Partial Fulfillment of the Requirements for the
Degree of
Doctor of Philosophy



CALIFORNIA INSTITUTE OF TECHNOLOGY
Pasadena, California

2026
Defended December 1, 2025

© 2026

Alkım Berke Bozkurt
ORCID: 0000-0003-0633-8902

All rights reserved

"Take but degree away, untune that string,
And, hark, what discord follows!"

— William Shakespeare, Troilus and Cressida

ACKNOWLEDGEMENTS

I would like to first thank my advisor Mohammad Mirhosseini. Joining the lab as a first-generation graduate student was a unique opportunity, and I feel very fortunate to have learned a vast array of practical skills directly from him. These lessons ranged from wirebonding a chip (which I am alleged to have performed quite destructively, per his evaluation) to the nuances of delivering an effective scientific talk. Beyond his technical mentorship, Mohammad possesses an endless enthusiasm and a deep investment in research, always making time for in-depth discussions. During these conversations, he regularly provided me with crucial perspective when I was struggling with the mundane but profound challenges of experimental research, helping me keep my eyes on the bigger picture. For all of this, I am deeply thankful.

My first introduction to scientific research was during my undergraduate years with Serdar Kocaman. I would like to thank him for teaching me how to imagine science, for his endless generosity with his time, and for his continued support. His care and mentorship are truly appreciated.

In our lab, we dabble in cryogenics, which unfortunately is accompanied by the endless thumping of the pulse tube. Despite my affinity for the avant-garde in music, I never learned how to enjoy this piece of musique concrete. I could only retain my sanity by hearing the warm voices of my fellow labmates, to whom I am grateful.

Omid and I spent countless days attaching, detaching and re-attaching cables. Through the fortune of repeated error, we managed to converge on a correct configuration, where we could finally convince ourselves that things worked (though it would take greater effort to convince Mohammad). His persistence, hard work and deep faith in what we do made everything we did possible. Thank you for your patience when I would go on my lengthy rants, for all the fun conversations in the fridge room, and for always being willing to employ your height for the great cause of science.

Justin joined our efforts towards the end of my time in the lab. His enthusiasm in the face of challenges and his joy of learning was inspiring to me at a time when the luster of new things had started to wane. I have a lot of respect for his hard work and the tremendous wrist agility that allowed him to perform lift-off on endless

chips. Thank you for refreshing my view of our work just when I needed it. And remember: one day a more junior student will arrive, and your days of lift-off will come to an end.

Han and I worked together during the early years of my PhD. Before then, I hadn't engaged in true experimental science, that is, the persistent battle against entropy. His stoic nature in the face of challenges and his patience when I stumbled were crucial to us overcoming the many hurdles we encountered. Thank you for teaching me all about nanofabrication and for always being the one willing to handle the dangerous acid treatments for our chips.

Chaitali was the only postdoc in our then small lab when I first joined. She was a great mentor, who I could always approach with any question, no matter how small. She patiently taught me how to operate the dilution refrigerator and fabricate a superconducting qubit, among many other essential skills. Thank you for your gentleness and kindness. I was truly fortunate to have you around when I was a clueless graduate student.

I shared much of my initial cluelessness with Frank, who joined the lab shortly after I did. I could always count on him and his PowerPoint slides. He was always ready to chat, whether about intriguing scientific ideas, how research should ideally be conducted, or the beauty of his latest bicycle. Thank you for being such a joy to be around, and for allowing me to survive without a car through the endless rides you offered me.

Our lab then proceeded to grow rapidly. Abhishek was the only one who truly knew what our lab was like before officially joining, having previously done his undergraduate summer research with us. I would like to thank you for choosing our group, for your kindness and for being a great companion for extremely weird concerts. Alongside Abhishek, Parth has introduced me to the excellent Indian cuisine, and been my primary paneer supplier. Thank you for the shiny kurta, for teaching me about QuTIP, and for being a great tennis partner, even while wearing jeans. Stanley has been a great office mate, whose growth as a researcher has been a privilege to witness. Thank you for all your Taiwanese snacks and respecting me a little too much. Hao has been the other occupant of our office, whose economy of speech provided a great contrast to Stanley. Thank you for your kindness and your endless dedication which has always inspired me. Billy, deeply tuned into the quantum community, could always be relied on to provide opinions about a recent development I had no clue about. Thank you for the insights, and for reigniting my

tennis ambition by giving me a proper beatdown. Arnav always brought a relaxed energy to the lab. Thank you for demonstrating an impressive groundedness and for reminding me what a real work-life balance looks like.

Beyond the graduate students and postdocs, I had the privilege of working with excellent undergraduate students. I am grateful for Kaushal's deep curiosity for details, which cautioned me against the engineering tendency to become too pragmatic. Yue's rigorous and diligent work provided design improvements we have been harnessing for years, and Mark has been diligently exploring some of the interesting avenues that would have otherwise gone untouched.

I would like to thank our laboratory manager Anne, who has been extremely helpful and kind throughout my PhD. I never needed to worry about logistics; she made everything so easy and smooth. I also would like to thank our options manager Tanya who was essential to my navigation of the unique structure of Caltech. I am also thankful to the KNI staff, who maintained and trained me on the scientific equipment that was crucial for my work.

I also gratefully acknowledge the support of the Eddleman Quantum Institute through a Graduate Fellowship.

Outside of the lab, I had the opportunity to meet a lot of great people, who I could call my friends. They helped alleviate the alienation that one inevitably experiences upon moving to a new and foreign place. With them, I could explore the local music scene, play tennis, have an elaborate dinner, find someone to reciprocate my complaints or watch a game. In order to prevent my acknowledgments from acquiring a monstrous size, I will confine myself to listing their names. I trust that they know their importance. These people, a significant portion of whom, through some odd coincidence, happen to be my compatriots, are: Mert, Utku, Su, Eyyüp, Sahil, Arda, Damla, Bilgehan, Pranav, Atakan, Cenk, Volkan, Kemal, Scott, Elie, Taylan, Efe and many more... For your presence, I am thankful.

Finally, I would like to thank my family, in particular my parents and my little brother. I had to start my PhD remotely due to COVID, which meant having to attend classes and have meetings at very odd times. However, this also gave me a chance to be with my family for some small portion of my PhD, which we all cherished. Afterwards, despite being separated by an ocean and many time zones, I never stopped feeling their support and love. I always carried a small piece of home with me. I am grateful for everything, *sağ olun*. I also want to thank my partner

Mücella. I am very fortunate to have you by my side. Thank you for your patience and understanding. I am excited to put the Atlantic behind us.

ABSTRACT

The investigation of mechanical oscillators in the quantum regime is of great interest for quantum science and technology. Particularly, mechanical oscillators can be utilized in quantum sensing, frequency conversion, quantum information processing, and fundamental tests of quantum gravity. For these applications, preparation and control of non-classical states of motion is crucial. However, since mechanical motion is extremely linear, coupling to an external nonlinear system or engineering nonlinear interactions is necessary for this purpose.

Superconducting qubits are an attractive platform for quantum control of motion, due to their strong single-photon nonlinearity and high coherence. Coupling them to mechanical oscillators through piezoelectricity has enabled the deterministic preparation and characterization of non-classical motional states. However, piezoelectric materials require complex heterogeneous integration, which often limits mechanical coherence. Piezoelectric oscillators coupled to superconducting qubits exhibit relatively low quality factors ($Q \sim 10^4 - 10^6$), restricting the ultimate utility of these systems. These limitations motivate the development of alternative methods that can combine high mechanical coherence with quantum control.

In this thesis, we employ the nonlinearity of electrostatic forces to engineer interactions between mechanical oscillators and superconducting microwave circuits. This material agnostic approach allows us to form our mechanical oscillators out of single-crystal silicon, a non-piezoelectric material with extremely low acoustic loss. First, we demonstrate the feasibility of this approach by achieving strong coupling to a microwave resonator while remaining in the ground state. Next, we couple our mechanical oscillator to a transmon superconducting qubit, enabling deterministic quantum control of motion and the investigation of mechanical coherence at the single quanta level. We observe an extraordinarily large mechanical quality factor ($Q \sim 10^9$), highlighting the effectiveness of our method in achieving long mechanical lifetimes.

We then systematically investigate the origins of acoustic decoherence in our devices, observing that microscopic two-level-system defects play a major role. We obtain clear signatures of their presence and interaction with our mechanical oscillator, extending the understanding of acoustic decoherence at millikelvin temperatures. Leveraging this knowledge, we demonstrate that frequency noise from these defects

can be mitigated using dynamical decoupling sequences implemented with our qubit.

Our mechanical lifetimes, which exceed those of the best superconducting qubits by an order of magnitude, open new possibilities for storing microwave quantum information in motional states. In addition, our material-agnostic approach is broadly applicable and can enable electromechanical interfaces across a wide range of non-piezoelectric materials relevant to quantum science.

PUBLISHED CONTENT AND CONTRIBUTIONS

[1] A. B. Bozkurt, O. Golami, Y. Yu, H. Tian, and M. Mirhosseini, "A mechanical quantum memory for microwave photons", Nature Physics **21**, 1469–1474 (2025) 10.1038/s41567-025-02975-w,

A.B participated in the conception of the project, worked on the fabrication of devices, conducted measurements, analyzed the data, and participated in the writing of the manuscript.
A.B. and O.G. contributed equally to this work.

[2] A. Bozkurt, H. Zhao, C. Joshi, H. G. LeDuc, P. K. Day, and M. Mirhosseini, "A quantum electromechanical interface for long-lived phonons", Nature Physics **19**, 1326–1332 (2023) 10.1038/s41567-023-02080-w,

A.B participated in the conception of the project, worked on the fabrication of devices, conducted measurements, analyzed the data, and participated in the writing of the manuscript.

[3] H. Zhao, A. Bozkurt, and M. Mirhosseini, "Electro-optic transduction in silicon via gigahertz-frequency nanomechanics", Optica **10**, 790–796 (2023) 10.1364/OPTICA.479162,

A.B participated in the conception of the project, worked on the fabrication of devices and participated in the writing of the manuscript.

[4] A. Bozkurt, C. Joshi, and M. Mirhosseini, "Deep sub-wavelength localization of light and sound in dielectric resonators", Optics Express **30**, 12378–12386 (2022) 10.1364/OE.455248,

A.B participated in the conception of the project, simulated the devices, and participated in the writing of the manuscript.

TABLE OF CONTENTS

Acknowledgements . . . iv
Abstract . . . viii
Published Content and Contributions . . . x
Table of Contents . . . x
List of Illustrations . . . xiii
List of Tables . . . xv
Chapter I: Introduction . . . 1
Chapter II: Electrostatic Coupling . . . 5
2.1 Classical Description . . . 5
2.2 System Quantization . . . 9
2.3 Equivalent Electrical Circuit Model . . . 17
2.4 Electromechanical Interaction Rate . . . 18
Chapter III: Phononic Crystal Electrostatic Transducers . . . 22
3.1 Phononic Crystals . . . 22
3.2 Design Principles . . . 23
3.3 Designing Extended Acoustic Modes . . . 28
3.4 Vacuum Gap . . . 33
Chapter IV: Electrostatic Coupling to a Microwave Resonator . . . 35
4.1 Introduction . . . 35
4.2 A phononic crystal electrostatic transducer . . . 37
4.3 Characterization and measurements . . . 39
4.4 Coherence Properties . . . 40
4.5 Probing the limits of parametric-enhancement . . . 42
4.6 The Strong-Coupling Regime . . . 44
4.7 Interaction with Two-level Systems . . . 46
4.8 Conclusions and Outlook . . . 47
4.9 Methods . . . 48
Chapter V: Quantum Control of Motion by a Superconducting Qubit . . . 58
5.1 System Description . . . 60
5.2 Qubit-Oscillator Interactions . . . 61
5.3 Mechanical Decoherence . . . 64
5.4 Discussion and outlook . . . 67
5.5 Methods . . . 68
Chapter VI: Decoherence due to Two-Level-System Defects . . . 79
6.1 Mechanics-TLS interactions . . . 79
6.2 TLS-induced Acoustic Loss . . . 83
6.3 TLS-induced Frequency Noise . . . 89
Chapter VII: Role of Metals in Acoustic Decoherence . . . 101
7.1 Experiment . . . 101

7.2 Discussion . . . 105
Chapter VIII: Outlook . . . 109
8.1 Quantum Information Processing with Mechanical Oscillators . . . 109
8.2 Experiments with Microscopic Quantum Defects . . . 118
Bibliography . . . 121
Appendix A: Supplementary Information for Chapter 4 . . . 146
A.1 Electrostatic Interaction . . . 146
A.2 Measurement Setup . . . 148
A.3 Mechanics Design . . . 150
A.4 Thermometry . . . 152
Appendix B: Supplementary Information for Chapter 5 . . . 157
B.1 Measurement setup . . . 157
B.2 Electrical Circuit . . . 158
B.3 Voltage biasing . . . 159
B.4 Thermometry . . . 162
B.5 Mechanical lifetime measurements . . . 164
Appendix C: Supplementary Information for Chapter 7 . . . 166
C.1 Acoustic Loss due to Electron-Phonon Scattering . . . 166

LIST OF ILLUSTRATIONS

Number *Page*

2.1 Electrostatic transduction . . . 6
2.2 Moving capacitor and quantum electrical circuit . . . 10
2.3 Equivalent electrical circuit model . . . 17
3.1 Moving capacitor diagram. . . . 24
3.2 Transducer diagram isometric perspective . . . 25
3.3 Phononic crystal unit cell . . . 26
3.4 Phononic shields . . . 27
3.5 Phononic crystal oscillator optimization. . . . 30
3.6 Fabrication disorder simulations. . . . 32
3.7 Electromechanical interaction rate vs vacuum gap. . . . 33
4.1 Electrostatic transduction. . . . 36
4.2 Microwave spectrum. . . . 40
4.3 Mechanical lifetime measurements. . . . 41
4.4 Probing the limits of parametric-enhancement. . . . 43
4.5 Demonstration of strong-coupling regime. . . . 45
4.6 Interaction of the mechanical resonator with the TLS bath . . . 46
4.7 Microwave frequency tuning. . . . 50
4.8 Purcell filter. . . . 51
4.9 Pull-in instability. . . . 52
4.10 Mechanical lifetime. . . . 54
4.11 Temperature saturation. . . . 55
4.12 Power saturation. . . . 56
5.1 Experimental setup. . . . 60
5.2 Coherent qubit-oscillator interaction. . . . 62
5.3 Quantum state preparation and tomography. . . . 64
5.4 Mechanical lifetime. . . . 65
5.5 Mitigating mechanical dephasing. . . . 66
5.6 Microwave design. . . . 71
5.7 Phonon distribution measurement. . . . 74
5.8 Inverse Purcell decay. . . . 76
5.9 TLS spectroscopy. . . . 77

6.1 Acoustic loss. . . . 85
6.2 Oscillator decay rate vs temperature. . . . 88
6.3 Anomalous oscillator frequency shift. . . . 90
6.4 Dephasing vs temperature. . . . 92
6.5 Mechanical frequency fluctuations. . . . 95
6.6 Ramsey and echo fits. . . . 98
6.7 Ramsey and Hahn echo coherence times. . . . 100
7.1 Chip Image. . . . 102
7.2 Mechanical frequency shift with temperature. . . . 103
7.3 Mechanical linewidth. . . . 104
7.4 Driven response of mechanical oscillator. . . . 106
8.1 Memory infidelity. . . . 112
8.2 Virtual gate infidelity. . . . 115
A.1 Equivalent electrical circuit. . . . 147
A.2 Moving capacitor design. . . . 149
A.3 Mechanical quality factor. . . . 151
A.4 Resonator bath thermalization. . . . 154
B.1 Measurement setup. . . . 158
B.2 Electrical circuit diagram. . . . 158
B.3 DC voltage effects on qubit. . . . 160
B.4 Leakage current measurements. . . . 162
B.5 Qubit vs mechanics population. . . . 163
B.6 Intermediate-phonon-number measurement. . . . 164

LIST OF TABLES

Number *Page*

4.1 Summary of device parameters 49
5.1 Summary of device parameters 69
A.1 Equivalent circuit parameters for device B. 148
A.2 Parameters of the moving capacitor. 151
B.1 Lifetime of waveguide coupled oscillators. 165

Chapter 1

INTRODUCTION

The elastic deformation of solids near equilibrium is fundamentally described within the framework of harmonic oscillators. In the last 50 years, advances in our ability to tailor the geometry of solids at the microscale have opened new frontiers in science and technology utilizing these mechanical oscillators [1]. Within the realm of classical technologies, these micro-electro-mechanical systems (MEMS) have become ubiquitous and serve crucial functionalities [2]. For instance, the high sensitivity of these mechanical oscillators to external forces has been harnessed to make mass, inertial, and pressure sensors [3–5]. Alongside their functionality as sensors, the small velocity of acoustic waves in solids has motivated the development of compact mechanical components for processing microwave signals [6]. The applications are vast and their impact has been transformative.

The exploration of mechanical oscillators in the quantum regime promises to have a similarly transformative impact on quantum science and technology. For example, the limits for the sensitivity of a mechanical oscillator are inherently set by quantum mechanics [7]. By preparing non-classical states of motion, it becomes possible to harness uniquely quantum resources that yield metrological performance unattainable with classical means [8–10]. Beyond their enhanced sensing capabilities, these quantum mechanical oscillators can provide unique functionalities in hybrid quantum architectures, where they interface with diverse physical systems. For instance, analogous to the use of mechanical filters in classical signal processing, mechanical oscillators could be utilized in processing quantum signals in computing architectures [11, 12]. They can also be used in the conversion of quantum signals between microwave and optical frequency bands, a crucial task for establishing quantum network with superconducting qubits [13, 14].

However, operating mechanical oscillators in the quantum regimes presents challenges:

1. **Ground state operation**: Mechanical oscillators are inevitably coupled to their environment, which leads to them being driven by random forces as a consequence of the dissipation-fluctuation theorem [15]. At ambient temper-

atures, the thermal fluctuations greatly exceeds the energy scale associated with quantum fluctuations ($k_b T \gg \hbar\omega_{\mathrm{m}}$, where T is the temperature of the mechanical oscillator and ω_{m} is its frequency). As a result, thermal noise dominates the oscillator's dynamics, making the observation of quantum phenomena extremely challenging under these conditions.

This challenge has motivated significant efforts towards cooling mechanical oscillators to their ground state of motion, where the thermal motion is reduced below the level of quantum fluctuations [15]. Such cooling can be achieved through two general strategies: passive and active cooling. In the passive approach, mechanical oscillators are engineered to oscillate at high frequencies ($\omega_m/2\pi \sim 5$ GHz) such that they reside at their ground state when cooled down to the base temperature of a dilution refrigerator [16] ($k_b \times 50$ mK $\ll h \times 5$ GHz). Alternatively, in the active approach, cooling is achieved by engineering coupling between a mechanical oscillator and another entity that functions as a cold bath [17, 18] or by employing feedback control [19].

2. **Non-classical state preparation**: The dynamics of a harmonic oscillator subject to a classical drive is confined to Gaussian states (i.e, coherent, thermal). Consequently, the more general class of non-Gaussian quantum states (such as Fock states or bosonic code states) that are of interest for various applications are not accessible to such systems [20]. The presence of a nonlinearity, in principle, allows this challenge to be overcome [21]. However, intrinsic mechanical nonlinearities are extremely weak compared to their dissipation rates, which hinders the preparation of non-classical states in purely mechanical systems [22].

   Therefore, one needs to form a hybrid quantum system, where the mechanical oscillator is coupled to an ancillary nonlinear system or where a nonlinear interaction is engineered [23]. In cavity optomechanics, the radiation pressure interaction between mechanical oscillators and electromagnetic cavities has been been extensively investigated for this purpose [15]. However, the standard linearization of the optomechanical interaction restricts the system to Gaussian states, and non-Gaussian states can only be generated probabilistically through single-photon detection [24].

   Alternatively, the strong single-photon nonlinearity, fast control, and the high coherence of superconducting qubits can be exploited to control mechanical

oscillators [23]. One approach to generate coupling between qubits and mechanical oscillators has been the enhancement of radiation pressure forces by an electrostatic biasing field [25, 26], an approach known as *electrostatic coupling*. However, challenges associated with engineering coupling strengths that exceed the decoherence rates and excess thermal population of the mechanical oscillator have been prohibitive for the preparation of non-Gaussian mechanical states via this approach [27–32].

On the other hand, the use of piezoelectric materials has enabled access to the strong coupling regime, where the interaction strength between oscillator and qubit exceeds the decoherence rates [16, 33]. The combination of strong coupling with passive ground state cooling has enabled the deterministic preparation and characterization of non-classical states of motion via this approach [34–36].

As noted above, piezoelectric coupling of passively cooled mechanical oscillators to superconducting qubits has been very successful in exploring the fundamental quantum behavior of mechanical objects [37, 38]. However, for practical applications, the fidelity with which a state can be prepared, manipulated, and stored is essential. This in turn relates to the interplay between the coupling strength and the decoherence rates of the individual components of the system [39, 40].

A factor that restricts the ultimate potential of previously demonstrated systems is their limited mechanical lifetimes. The best observed quality factors ($Q \approx 3 \times 10^6$) [41] remain well below those attainable with alternative materials that are not constrained to be strongly piezoelectric ($Q \gtrsim 10^9$) [42–44]. Importantly, the excess acoustic dissipation has not been attributed to any fundamental limitation of piezoelectricity itself, but rather to the material quality and surface properties of piezoelectric devices [45, 46]. Qubits can lose energy to the substrate via acoustic channels if fabricated on a piezoelectric substrate [47]. This necessitates heterogeneous integration of piezoelectric materials, a process that presents substantial challenges in achieving high material quality and thus contributes to higher losses.

In this thesis, we explore electrostatic coupling as an alternative pathway to couple mechanical oscillators to superconducting qubits. By harnessing the material agnostic nature of this mechanism, we aim to utilize materials that have been shown to exhibit extremely low acoustic dissipation, such as single-crystal silicon [48]. By solving the technical challenges that has previously hindered the performance of

electrostatically coupled qubit-oscillator systems [27–31], the lifetime of mechanical oscillators that has been brought under quantum control can be significantly extended. Such an achievement would have strong implications for the applications of mechanical oscillators in quantum information processing, frequency conversion, and sensing.

The next two chapters introduce the core principles underlying our approach. Chapter 2 presents the basic physics of electrostatic coupling between photons and phonons, including a quantum mechanical description of the interaction. In Chapter 3, we introduce the specific geometry we employ to engineer electrostatic coupling and outline the associated design principles.

Our main experimental results are presented in Chapters 4-5. In Chapter 4, we realize electrostatic coupling between a mechanical oscillator and a microwave resonator. Our measurements demonstrate the fundamental principles of electrostatic coupling and show that this interaction can be sufficiently enhanced to reach strong-coupling while while maintaining ground-state operation. We also observe the first indications that our approach can provide improvements in mechanical lifetimes. In Chapter 5, the mechanical oscillators are directly coupled to a superconducting qubit. This system facilitates the quantum control of mechanical motion, allowing for the generation and characterization of non-classical motional states. We further investigate the mechanical coherence in the single phonon regime and demonstrate mechanical quality factors approaching one billion.

Chapters 6 and 7 focus on the mechanisms underlying acoustic decoherence. Specifically, Chapter 6 focuses on how two-level-system defects (TLS) contribute to acoustic decoherence. Here, we provide the theory of this process, starting from the basics of TLS-mechanics interactions. Furthermore, we present additional measurements supporting the major role played by TLS in limiting mechanical coherence. Chapter 7 investigates the contribution of metallic moving parts to acoustic decoherence, through an experiment aimed at isolating the acoustic decoherence from metals. Our results show that metals can indeed introduce excess acoustic loss and frequency noise.

Finally, Chapter 8 provides an outlook of for our research, focusing on potential future research directions with our system and specific pathways for further improvements.

Chapter 2

ELECTROSTATIC COUPLING

This chapter discusses the physics of electrostatic coupling. Starting with the classical dynamics, we describe the interaction between electromagnetic and acoustic fields in the presence of an electrostatic voltage bias. Then we proceed with the quantization of this system, providing a quantum mechanical description of the system. We then provide the equivalent electrical circuit model for the moving capacitor. Finally, we present a perturbative approach for calculating the electromechanical interaction rate.

2.1 Classical Description

Electrostatic transducers, which utilize Coulomb forces between charged capacitors to drive and readout mechanical motion are ubiquitous in MEMS technology. They are employed in various applications due to their relative ease of fabrication, excellent miniaturization, and low power consumption [49].

The basic physics of electrostatic actuation can be described by considering the canonical example of a charged capacitor with mechanically compliant plates, which is driven by an external voltage source (see Fig. 2.1).

In this picture, the moving capacitor is assumed to oscillate around its equilibrium position with displacement x. Therefore, total capacitance of the moving capacitor ($C_{\mathrm{m}}(x)$) is a function of the mechanical displacement. For simplicity, in the following analysis we omit the explicit dependence on x when denoting the capacitance value of the moving capacitor.

An external voltage supply with a voltage of V_{dc} generates static charge on the mechanical oscillator, which can be expressed as

$$Q_{\mathrm{dc}} = C_{\mathrm{m}} V_{\mathrm{dc}}. \tag{2.1}$$

This static lies at the origin of the the resonant interaction between the mechanical and electromagnetic fields as will be shown later.

Similarly, we have a radio-frequency (RF) voltage source with voltage V_{rf}, whose purpose in this setting is to drive and readout mechanical motion. Associated with

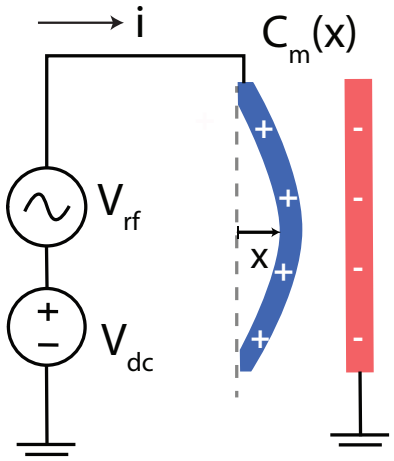


Figure 2.1: **Electrostatic transduction.** Diagram of an electrostatic transducer connected to external voltage sources. The DC source generates the static charge and the RF source drives mechanical motion. The static charge is visualized on the moving capacitor by the + and - signs. In this diagram only one of the planes of the moving capacitor is mechanically compliant while the other one remains fixed.

this voltage source, there exists RF charge of magnitude

$$Q_{\mathrm{rf}} = C_{\mathrm{m}} V_{\mathrm{rf}}. \tag{2.2}$$

Since we have a conservative system here, we can calculate the electrical force on the mechanical oscillator based on the total electrical energy stored on the capacitor, which is given as [1]

$$U = \frac{Q^2}{2C_{\mathrm{m}}} = \frac{(Q_{\mathrm{rf}} + Q_{\mathrm{dc}})^2}{2C_{\mathrm{m}}}. \tag{2.3}$$

The electrical Coulomb force can then be expressed as

$$F_{\mathrm{e}} = \frac{\partial U}{\partial x} = \frac{1}{2}\frac{C_{\mathrm{m}}}{\partial x}\left(V_{\mathrm{dc}}^2 + 2V_{\mathrm{dc}}V_{\mathrm{rf}} + V_{\mathrm{rf}}^2\right), \tag{2.4}$$

where we have substituted the expression for the DC and RF charges into Eq. (2.3).

For the common scenario of a RF drive near resonance with mechanical motion, only the term proportional to $V_{\mathrm{dc}}V_{\mathrm{rf}}$ will be resonantly driving the mechanical oscillator. Therefore, we can neglect the other terms and express the resonant electrical force on the mechanical oscillator as

$$F_{\mathrm{e}} \approx \frac{C_{\mathrm{m}}}{\partial x} V_{\mathrm{dc}} V_{\mathrm{rf}}. \tag{2.5}$$

Beyond using the electrical force to drive mechanical motion, as discussed above, we also seek to electrically measure mechanical displacements. This can be achieved

by monitoring the current passing through the moving voltage source, which can be expressed as [50]

$$i = \frac{\partial(Q_{\mathrm{rf}} + Q_{\mathrm{dc}})}{\partial t} = \underbrace{C_{\mathrm{m}} \frac{\partial V_{\mathrm{rf}}}{\partial t}}_{\text{drive}} + \underbrace{(V_{\mathrm{dc}} + V_{\mathrm{rf}}) \frac{\partial C_{\mathrm{m}}}{\partial x} \frac{\partial x}{\partial t}}_{\text{motional}} = i_{\mathrm{drive}} + i_{\mathrm{motional}}. \tag{2.6}$$

Here there are two components: (i) the current associated with the RF drive on the capacitor (i_{drive}), where the charges oscillate with the external voltage supply, and (ii) the motional current (i_{motional}) which is proportional to the velocity of the mechanical oscillator. This motional component provides information about mechanical motion, allowing its electrical readout. For resonant detection, only the component that oscillates with the mechanical frequency is relevant. Therefore, we can express the motional current as

$$i_{\mathrm{motional}} \approx V_{\mathrm{dc}} \frac{\partial C_{\mathrm{m}}}{\partial x} \frac{\partial x}{\partial t}. \tag{2.7}$$

Thus, the nonlinearity of the Coulomb interaction in the presence of a static charge can give rise to electrical forces that drive mechanical motion (see Eq. (2.5) and allow its readout (see Eq. (2.7)). Both of these equations have terms proportional to $V_{\mathrm{dc}} \partial C_{\mathrm{m}}/\partial x$, which one generally wishes to maximize in practical applications.

The sensitivity of the capacitor to mechanical displacements ($\partial C_{\mathrm{m}}/\partial x$) is dependent of the geometry of the capacitor and the mechanical displacement profile. For complex geometries, numerical methods are required for the analysis. However, for the special case of a parallel plate vacuum capacitor of area A and gap d, where one plate undergoes translational motion along the axis separating the two plates, the mechanical capacitance can be expressed as

$$C_{\mathrm{m}} = \frac{\epsilon_0 A}{d - x}. \tag{2.8}$$

For small displacements ($x \ll d$), the sensitivity is

$$\left.\frac{\partial C_{\mathrm{m}}}{\partial x}\right|_{x=0} = \frac{\epsilon_0 A}{d^2}. \tag{2.9}$$

Hence the sensitivity can be significantly increased by scaling down the gaps of the actuator.

The other relevant parameter is the maximum bias voltage (V_{dc}), which is limited due to Coulomb attraction between the plates. Specifically, the moving plate gets

subjected to an electrostatic force, which is the static component in Eq. (2.4),

$$F_{\mathrm{c}} = \frac{1}{2}\frac{\partial C_{\mathrm{m}}}{\partial x}V_{\mathrm{dc}}^2. \tag{2.10}$$

This Coulomb force in turn competes with the spring force of the moving capacitor, which is given by Hooke's law as

$$F_{\mathrm{s}} = -kx, \tag{2.11}$$

where k is the spring constant of the mechanically compliant plate. Therefore the net force is

$$F_{\mathrm{net}} = \frac{1}{2}\frac{\partial C_{\mathrm{m}}}{\partial x}V_{\mathrm{dc}}^2 - kx. \tag{2.12}$$

This net force can be utilized to solve the equilibrium position (x_{eq}) of the moving capacitor, by finding the displacement value that satisfies $F_{\mathrm{net}} = 0$.

The stability of the equilibrium position is set by how the net force varies in the presence of perturbations. Based on the conventions we have used, where positive force indicates attraction towards the other plate, if a positive perturbation δx leads to an increase in the force this is an unstable equilibrium point and it is stable otherwise. Therefore, stable operation requires that

$$\left.\frac{\partial F_{\mathrm{net}}}{\partial x}\right|_{x=x_{\mathrm{eq}}} < 0. \tag{2.13}$$

The maximum bias voltage value that satisfies the above equation is called the pull-in voltage (V_{pi}), which sets the limits for the maximum voltage that can be applied to an electrostatic actuator. Above this voltage, the dynamics of the system is unstable and the mechanically compliant plate snaps to other plate due to Coulomb attraction.

In general, Eq. (2.13) is a complex nonlinear equation that is challenging to solve, as one must first determine the equilibrium point and then evaluate its stability for each applied V_{dc} value. This procedure can, however, be readily carried out using numerical methods. For the special case of a parallel plate capacitor, there exists an analytical solution where the pull-in voltage is [1]

$$V_{\mathrm{pi}} = \sqrt{\frac{8kd^3}{27\epsilon_0 A}}. \tag{2.14}$$

Similarly, the capacitor gap value at the equilibrium position, when this voltage is applied can be found to be

$$d - x_{\mathrm{eq}}\Big|_{V_{\mathrm{dc}}=V_{\mathrm{pi}}} = \frac{2}{3}d. \tag{2.15}$$

2.2 System Quantization

The classical description of the dynamics of electrostatic actuators provided in the previous section, while useful for understanding the system's physics, is insufficient to fully capture its behavior in the quantum regime. To describe the system at this level, it is necessary to quantize both the acoustic and electromagnetic fields.

The full Hamiltonian of our system ($\hat{H}_{\mathrm{sys}}$) will have terms that relate to the dynamics of the mechanical oscillator, the dynamics of electromagnetic fields, and the interaction between the two.

The acoustic field can be simply quantized by noting that the motion of a mechanical oscillator near equilibrium can be described as a quantum harmonic oscillator, whose Hamiltonian is

$$\hat{H}_{\mathrm{m}} = \frac{1}{2} m_{\mathrm{eff}} \omega_{\mathrm{m}}^2 \hat{x}^2 + \frac{\hat{p}^2}{2m_{\mathrm{eff}}}. \tag{2.16}$$

In this Hamiltonian, m_{eff} is the effective mass of the mechanical oscillator (for a discussion of effective mass, see [15]), ω_{m} its resonance frequency, and $\hat{x}$ ($\hat{p}$) is the position (momentum) operator which satisfy the commutation relation $[\hat{x}, \hat{p}] = i\hbar$. The Hamiltonian can be recast by utilizing the creation and annihilation operators, where the annihilation operator $\hat{b}$ is defined as

$$\hat{b} = \sqrt{\frac{m_{\mathrm{eff}}\omega_{\mathrm{m}}}{2\hbar}}\hat{x} + i\frac{1}{\sqrt{2\hbar m_{\mathrm{eff}}\omega_{\mathrm{m}}}}\hat{p}, \tag{2.17}$$

satisfying the commutation relation $[\hat{b}, \hat{b}^\dagger] = 1$. With these operators, the mechanical Hamiltonian can be written as

$$\hat{H}_{\mathrm{m}} = \hbar\omega_{\mathrm{m}}\hat{b}^\dagger\hat{b}. \tag{2.18}$$

With the acoustic field quantized, we can move on to the electromagnetic fields. In our experiments, which will be later on described in the thesis, the moving capacitors will be connected to quantum microwave circuitry. In particular, it will be attached to microwave resonators and superconducting qubits. These circuits can be analyzed by following the framework of circuit quantization [51].

In this framework, we will choose the node flux $\hat{\Phi}$ to be analogous to the position variable, such that the capacitive terms will contribute to the kinetic energy of the system and the inductive terms will contribute to the potential energy of the system.

We consider the case of a moving capacitor with a quantized position ($C_{\mathrm{m}}(\hat{x})$) connected to microwave circuitry. Here the circuitry consists of a capacitor (C_{r}) in parallel with arbitrary inductive elements, whose potential energy is $\mathcal{U}_L(\hat{\Phi})$. This setup is visualized in Fig. 2.2a.

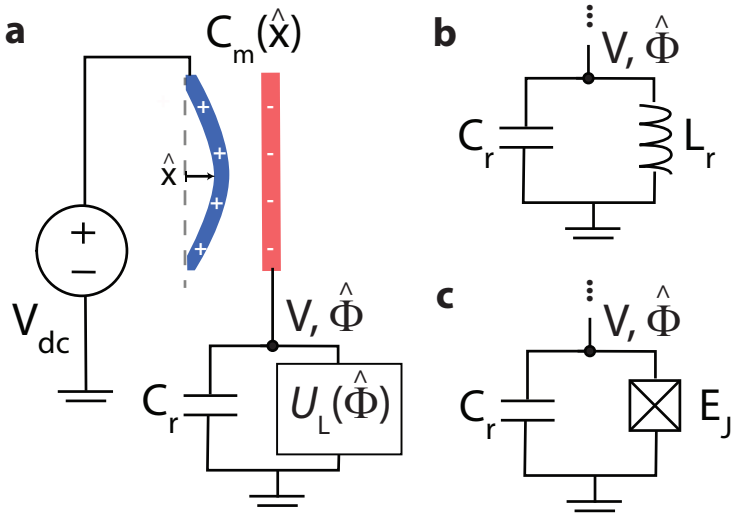


Figure 2.2: **Moving capacitor and quantum electrical circuit. a,** Diagram of a moving capacitor connected to a quantum microwave circuit consisting of a capacitor C_{r} shunted by arbitrary inductive elements with inductive energy of $\mathcal{U}_L(\hat{\Phi})$. The dc voltage at the node above the capacitor represented by the variable V. The quantum fluctuations at the same node are represented by the node flux $\hat{\Phi}$. **b-c,** Electrical circuit diagrams of a linear microwave resonator (**b**) and a transmon qubit (**c**).

The Lagrangian of the quantum electrical circuit is written as

$$\mathcal{L}_e = \mathcal{T}_C - \mathcal{U}_L. \tag{2.19}$$

The total capacitive energy can be expressed as

$$\mathcal{T}_C = \frac{1}{2}C_{\mathrm{m}}(\hat{x})(V_{\mathrm{dc}} - V - \dot{\hat{\Phi}})^2 + \frac{1}{2}C_{\mathrm{r}}(V + \dot{\hat{\Phi}})^2, \tag{2.20}$$

where V is the dc voltage at our chosen node and the dot above operators indicate the time derivative.

For the common case where the displacement amplitude of the moving capacitor is much smaller than the gap, we can Taylor expand the moving capacitor value around the equilibrium position to the first order as

$$C_{\mathrm{m}}(\hat{x}) \approx C_{\mathrm{m}}(x_{\mathrm{eq}}) + \left.\frac{\partial C_m}{\partial x}\right|_{x=x_{\mathrm{eq}}} \hat{x}. \tag{2.21}$$

In the following analysis, we will not explicitly denote that the derivative is always evaluated at the equilibrium position for brevity.

Note that the equilibrium position can be calculated by solving the classical equations for the system as discussed in the previous section. For brevity, we will denote the moving capacitor value at the equilibrium position as

$$\bar{C}_\mathrm{m} = C_\mathrm{m}(x_\mathrm{eq}). \tag{2.22}$$

Next, we expand the capacitive energy, ignoring the static terms (i.e. terms that do not include any of the operators $\hat{x}$ or $\hat{\Phi}$), since they do not contribute to the dynamics of the Hamiltonian and provide only energy offsets. We obtain

$$\mathcal{T}_C = \frac{1}{2}\left(\bar{C}_\mathrm{m} + \partial_x C_\mathrm{m}\hat{x}\right)\left(2(V_\mathrm{dc} - V)\dot{\hat{\Phi}} + \dot{\hat{\Phi}}^2\right) + \frac{1}{2}C_\mathrm{r}(2V\dot{\hat{\Phi}} + \dot{\hat{\Phi}}^2). \tag{2.23}$$

Based on the capacitive energy, the conjugate charge operator is defined as

$$\hat{Q} = \frac{\partial \mathcal{T}_C}{\partial \dot{\hat{\Phi}}}, \tag{2.24}$$

and satisfies the commutation relation $[\hat{\Phi}, \hat{Q}] = i\hbar$. For our specific system, it can be found to be

$$\hat{Q} = \underbrace{(-\bar{C}_\mathrm{m}\bar{V}_\mathrm{dc} + C_\mathrm{r}V)}_{Q_\mathrm{off}} - \partial_x C_\mathrm{m}\hat{x}\bar{V}_\mathrm{dc} + (C_\Sigma + \partial_x C_\mathrm{m}\hat{x})\dot{\hat{\Phi}}, \tag{2.25}$$

where Q_off is the static offset charge and $C_\Sigma = C_\mathrm{r} + \bar{C}_\mathrm{m}$. To simplify our notation, we define $\bar{V}_\mathrm{dc} = V_\mathrm{dc} - V$, which corresponds to the voltage drop on the moving capacitor.

The circuit Hamiltonian can then be obtained via the Legendre transformation

$$\hat{H}_\mathrm{circ} = Q\dot{\hat{\Phi}} - \mathcal{L}. \tag{2.26}$$

Since expressions for the capacitive energy (Eq. (2.23)) and the canonical charge operator (Eq. (2.25)) have already been derived, we can substitute them into this expression to obtain the Hamiltonian. This procedure yields

$$\hat{H}_\mathrm{circ} = \underbrace{\frac{(\hat{Q} - Q_\mathrm{off})^2}{2C_\Sigma} + \mathcal{U}_L(\hat{\Phi})}_{\hat{H}_\mathrm{e}} \underbrace{- \frac{\partial_x C_\mathrm{m}\bar{V}_\mathrm{dc}\hat{Q}\hat{x}}{C_\Sigma} - \frac{\partial_x C_\mathrm{m}\hat{Q}^2\hat{x}}{2C_\Sigma^2}}_{\hat{H}_\mathrm{int}}, \tag{2.27}$$

where $\hat{H}_\mathrm{e}$ is the Hamiltonian of the electrical subsystem (defined by the capacitors and inductive elements) and $\hat{H}_\mathrm{int}$ is the interaction Hamiltonian. From the above derivation, we see that the charge oscillating with mechanical motion interacts with the charge fluctuations of the quantum electrical circuit, leading to the electromechanical interaction.

For the electromechanical interaction, we only keep the term of the form $\hat{Q}\hat{x}$, which is relevant for resonant interactions that will be explored in the rest of the thesis. We have thus ignored the term proportional to $\hat{Q}^2\hat{x}$, which is weaker and becomes relevant when the oscillator interacts with electrical signals at half the mechanical frequency. Therefore, we can write

$$\hat{H}_\mathrm{int} = -\frac{\partial_x C_\mathrm{m} \bar{V}_\mathrm{dc} \hat{Q}\hat{x}}{C_\Sigma}. \tag{2.28}$$

We note that $V_\mathrm{dc} - V$ is simply the voltage drop on the mechanical oscillator.

The full system Hamiltonian can be then obtained as the combination of the mechanical, electrical, and interaction Hamiltonians

$$\hat{H}_\mathrm{sys} = \hat{H}_\mathrm{m} + \hat{H}_\mathrm{e} + \hat{H}_\mathrm{int}. \tag{2.29}$$

For simplicity, we have truncated the Taylor expansion of the moving capacitance at first order in Eq. (2.21), since this approximation already captures the essential physics of the electromechanical interaction, which is the main focus here. Including higher order terms would give rise to weaker effects, such as electrostatic frequency renormalization of the mechanical oscillator, an electrostatically induced mechanical Kerr-type nonlinearity [52, 53] and higher order couplings between mechanical motion and electrical charge.

To analyze the full system, we must specify the functional form of the inductive energy, which defines the electrical circuit to which the mechanical oscillator is coupled. From this, we can derive the electrical and interaction Hamiltonians, providing a complete description of the system's quantum dynamics under the closed-system assumption. Here, we focus on two specific cases that will appear in later chapters: (i) a linear microwave resonator and (ii) a transmon qubit.

Linear Microwave Resonator

A linear microwave resonator corresponds to a simple LC circuit. In our system, this is realized an inductor L_r shunting the capacitor C_r, as shown in Fig. 2.2b. The

inductive energy for this configuration is given by

$$\mathcal{U}_L = \frac{\hat{\Phi}^2}{2L_\mathrm{r}}, \tag{2.30}$$

leading to the electrical Hamiltonian

$$\hat{H}_\mathrm{e} = \frac{\hat{Q}^2}{2C_\Sigma} + \frac{\hat{\Phi}^2}{2L_\mathrm{r}}, \tag{2.31}$$

where the charge offset has been removed by a gauge transformation. This Hamiltonian is that of a linear harmonic oscillator, which can be rewritten as

$$\hat{H}_\mathrm{e} = \hbar\omega_\mathrm{r}\hat{a}^\dagger\hat{a}, \tag{2.32}$$

where $\omega_\mathrm{r} = (C_\Sigma L_\mathrm{r})^{-1/2}$ is the resonance frequency of the microwave resonator and the annihilation operator is defined as

$$\hat{a} = \sqrt{\frac{C_\Sigma\omega_r}{2\hbar}}\hat{\Phi} + \frac{i}{\sqrt{2\hbar C_\Sigma\omega_\mathrm{r}}}\hat{Q}. \tag{2.33}$$

The charge operator can be expressed based on the creation and annihilation operators to be

$$\hat{Q} = -iQ_\mathrm{zpf}(\hat{a} - \hat{a}^\dagger), \tag{2.34}$$

where $Q_\mathrm{zpf} = \sqrt{\hbar\omega C_\Sigma/2}$ is the zero-point fluctuations of charge. The displacement operator can be similarly expressed as

$$\hat{x} = x_\mathrm{zpf}(\hat{b} + \hat{b}^\dagger), \tag{2.35}$$

where $x_\mathrm{zpf} = \sqrt{\hbar/2m_\mathrm{eff}\omega_\mathrm{m}}$ is the zero-point fluctuations of displacement.

Substituting these expression into the interaction Hamiltonian, we obtain

$$\hat{H}_\mathrm{int} = iV_\mathrm{dc}\partial_x C_\mathrm{m} x_\mathrm{zpf} Q_\mathrm{zpf}(\hat{a} - \hat{a}^\dagger)(\hat{b} + \hat{b}^\dagger)/C_\Sigma, \tag{2.36}$$

where we due to the inductive shunt, the node will be grounded at dc, leading to $V = 0$. This equation can be cast into the form

$$\hat{H}_\mathrm{int} = i\hbar g_\mathrm{em}(\hat{a} - \hat{a}^\dagger)(\hat{b} + \hat{b}^\dagger), \tag{2.37}$$

where g_em is the electromechanical interaction rate, which can be obtained to be

$$g_\mathrm{em} = V_\mathrm{dc}\partial_x C_\mathrm{m} x_\mathrm{zpf} V_\mathrm{zpf}/\hbar. \tag{2.38}$$

Here, $V_\mathrm{zpf} = Q_\mathrm{zpf}/C_\Sigma = \sqrt{\hbar\omega_\mathrm{r}/2C_\Sigma}$ is the zero-point fluctuations of voltage.

As will be discussed in the later sections of this chapter, Equation (2.38) will form the basis of our electromechanical interaction rate analysis and simulations. Moreover, its dependence on the system parameters will motivate our design, with the goal of maximizing the interaction rate.

In the common scenario where the mechanical and electrical resonators are near resonance, the interaction Hamiltonian can be further simplified by applying the rotating-wave approximation

$$\hat{H}_{\text{int}} = i\hbar g_{\text{em}}(\hat{a}\hat{b}^\dagger - \hat{a}^\dagger\hat{b}), \tag{2.39}$$

leading to the familiar beamsplitter type interaction. This interaction enables electrical driving and readout of mechanical motion [18, 54].

However, since we have linear coupling between two harmonic oscillators, the dynamics of the system remains constrained to Gaussian states as discussed in the previous chapter. Therefore, an external source of nonlinearity is needed for quantum control of mechanical motion, which can be readily provided by Josephson junctions. In the following, we will visit the special case of a nonlinear superconducting circuit in the form of a transmon qubit interacting with the mechanical oscillator.

Transmon Qubit

A transmon qubit can be obtained by shunting a Josephson junction, which has a Josephson energy of E_J, with a capacitor, as illustrated in Fig. 2.2c. The inductive energy of this circuit is

$$\mathcal{U}_L = -E_J \cos\left(2\pi\frac{\hat{\Phi}}{\Phi_0}\right), \tag{2.40}$$

where $\Phi_0 = h/2e$ is the magnetic flux quantum and e is the electron charge. By defining the superconducting phase ($\hat{\varphi} = 2\pi\hat{\Phi}/\Phi_0$) and reduced charge ($\hat{n} = \hat{Q}/2e$), the Hamiltonian of the transmon can be written as

$$\hat{H}_{\text{e}} = 4E_C(\hat{n} - n_g)^2 - E_J\cos\hat{\varphi}, \tag{2.41}$$

where $n_g = Q_{\text{off}}/2e$ is the reduced offset charge and the charging energy is given as $E_C = e^2/2C_\Sigma$.

We note that this Hamiltonian is identical to that of a Cooper pair box. The transmon simply corresponds to a specific regime of this Hamiltonian ($E_J/E_C \gtrsim 30$) where the impact of the offset charge on the energy levels, called charge dispersion, is greatly suppressed [55]. Specifically, this charge dispersion reduces exponentially

with E_J/E_C ratio ($\propto \exp(-\sqrt{8E_J/E_C})$ and can be made negligibly small. As a result, the effect of the offset charge can be ignored in the transmon Hamiltonian. In addition, the transmon regime leads to small quantum phase fluctuations, allowing the Taylor expansion of the Josephson potential to be truncated at fourth order [56] as

$$\hat{H}_\mathrm{e} \approx 4E_C\hat{n}^2 + \frac{1}{2}E_J\hat{\varphi}^2 - \frac{1}{24}E_J\hat{\varphi}^4. \tag{2.42}$$

The fourth-order term introduces a nonlinearity in the transmon, such that the Hamiltonian can be cast as

$$\hat{H}_\mathrm{e} = \sum_{k=0}\left(k\sqrt{8E_JE_C} - \frac{k(k-1)}{2}E_C\right)|k\rangle\langle k|. \tag{2.43}$$

This corresponds to the energy structure of a Kerr nonlinear oscillator with resonance frequency $\sqrt{8E_JE_C}$ and Kerr nonlinearity of $-E_C$. Due to the Kerr nonlinearity, the frequencies of neighboring transitions are different (i.e., $\omega^{i\to i+1} - \omega^{i-1\to i} = -E_C$), which allows for independent addressing of individual levels.

We then move on to the analysis of the interaction Hamiltonian. The dc voltage V can be obtained based on capacitive voltage division to be

$$V = V_\mathrm{dc}\frac{C_\mathrm{m}}{C_\Sigma}. \tag{2.44}$$

The interaction Hamiltonian can then be written as

$$\hat{H}_\mathrm{int} = -\partial_x C_\mathrm{m} x_\mathrm{zpf} V_\mathrm{dc}\beta\frac{2e\hat{n}}{C_\Sigma}(\hat{b} + \hat{b}^\dagger), \tag{2.45}$$

where we have defined $\beta = C_\mathrm{r}/C_\Sigma$.

With this, we have access to the full system Hamiltonian of a moving capacitor connected to a transmon. The system can be further simplified in common operating regimes. We will encounter the case when the mechanical oscillator is near resonant to the transition between the ground and first excited state of the qubit ($\omega_\mathrm{m} \approx \omega_\mathrm{ge} = \sqrt{8E_JE_C} - E_C$) and detuned significantly from other transitions. In this case, the Hilbert space of the transmon can be restricted to ground and first excited state, where it is treated as a two-level-system (i.e. a qubit) with the Hamiltonian

$$H_\mathrm{e} = \hbar\frac{\omega_\mathrm{ge}}{2}\hat{\sigma}_z, \tag{2.46}$$

where σ_z is the Pauli-z operator. Following the truncation, the interaction Hamiltonian with the qubit can be written as

$$\hat{H}_\mathrm{int} = -\partial_x C_\mathrm{m} x_\mathrm{zpf} V_\mathrm{dc}\beta\frac{2en_\mathrm{eg}}{C_\Sigma}(\hat{\sigma}^+ + \hat{\sigma}^-)(\hat{b} + \hat{b}^\dagger), \tag{2.47}$$

where $n_{\mathrm{eg}} = \langle e|\,\hat{n}\,|g\rangle$ is the qubit charge transition matrix element and $\hat{\sigma}^{+} = |e\rangle\langle g|$ ($\hat{\sigma}^{-} = |g\rangle\langle e|$) is the qubit raising (lowering) operator.

With the rotating-wave-approximation, the interaction Hamiltonian takes the form

$$\hat{H}_{\mathrm{int}} = -\partial_x C_{\mathrm{m}} x_{\mathrm{zpf}} V_{\mathrm{dc}} \beta \frac{2en_{\mathrm{ge}}}{C_\Sigma}(\hat{\sigma}^{+}\hat{b} + \hat{\sigma}^{-}\hat{b}^{\dagger}) = \hbar g_{\mathrm{em}}(\hat{\sigma}^{+}\hat{b} + \hat{\sigma}^{-}\hat{b}^{\dagger}), \tag{2.48}$$

where the electromechanical interaction rate is given as

$$g_{\mathrm{em}} = -\partial_x C_{\mathrm{m}} x_{\mathrm{zpf}} V_{\mathrm{dc}} \beta \frac{2en_{\mathrm{ge}}}{\hbar C_\Sigma}. \tag{2.49}$$

The interaction rate can also be written in terms of the phase transition matrix element $\varphi_{\mathrm{ge}} = \langle e|\,\hat{\varphi}\,|g\rangle$,

$$g_{\mathrm{em}} = -\partial_x C_{\mathrm{m}} x_{\mathrm{zpf}} V_{\mathrm{dc}} \beta \frac{\omega_{\mathrm{ge}}\varphi_{\mathrm{ge}}}{2e}, \tag{2.50}$$

where we have used the identity $n_{\mathrm{ge}} = \varphi_{\mathrm{ge}}\hbar\omega_{\mathrm{ge}}/8E_C$.

Generally numerical tools are required to evaluate the transition matrix elements for superconducting qubits. For the special case of a transmon, the matrix elements of linear circuits constitute a very good approximation for nearest neighbor transitions [55]

$$\frac{2en_{\mathrm{ge}}}{C_\Sigma} \approx \sqrt{\frac{\hbar\omega_{\mathrm{ge}}}{2C_\Sigma}}. \tag{2.51}$$

Similarly, one can express the phase transition matrix element as

$$\varphi_{\mathrm{ge}} \approx \left(\frac{2E_C}{E_J}\right)^{1/4}. \tag{2.52}$$

Having derived the Hamiltonians for the individual subsystems and their interaction, the full system Hamiltonian is given by

$$H_{\mathrm{sys}}/\hbar = \omega_{\mathrm{m}}\hat{b}^{\dagger}\hat{b} + \frac{\omega_q}{2}\sigma_z + g_{\mathrm{em}}(\hat{\sigma}^{+}\hat{b} + \hat{\sigma}^{-}\hat{b}^{\dagger}), \tag{2.53}$$

which is the famous Jaynes-Cummings Hamiltonian [57]. By controlling the time evolution of the system, it is possible to construct arbitrary quantum states of the oscillator [58]. Hence, we clearly see how the qubit nonlinearity enables the quantum control of the mechanical oscillator in this setup.

We note that the above analysis is generally applicable to any nonlinear quantum electrical circuit that can be effectively treated as a two-level system and follows the form in Fig. 2.2a. For each circuit the voltage V can be found by analyzing the circuit at dc and the matrix element can be evaluated via numerical means. These quantities would then allow the calculation of the electromechanical interaction rate.

2.3 Equivalent Electrical Circuit Model

In the previous section, we showed that the full system Hamiltonian can be obtained through the circuit quantization formalism when a moving capacitor is connected to a node of a quantum electrical circuit. Nevertheless, this method, which relies on analyzing the dynamics of a displacement dependent capacitor, quickly becomes unwieldy for more complex circuits.

The electrical response of a mechanical oscillator can be modeled to be identical to that of a microwave resonator through Foster synthesis [59]. Such an equivalent circuit representation for the mechanical oscillator would enable us to use powerful tools developed for the analysis of complex electrical quantum circuits, such as black box quantization [60] and specialized software packages [61, 62].

In principle, one can obtain multiple equivalent models for a mechanical oscillator [45]. Here, we will utilize the formalism of a capacitively coupled LC resonator (see Fig. 2.3). We prefer this model since the analysis of capacitively coupled circuits is ubiquitous within the field of circuit quantum electrodynamics.

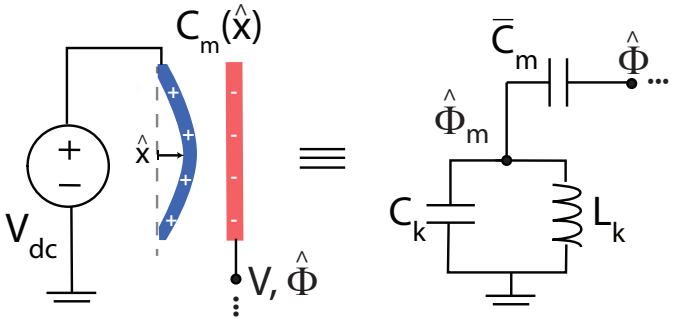


Figure 2.3: **Equivalent electrical circuit model.** Electrical circuit model of the voltage biased moving capacitor, connected to an arbitrary node of a quantum circuit with dc voltage V and node flux $\hat{\Phi}$. $\bar{C}_\mathrm{m}$ denotes the value of the motional capacitor at equilibrium ($x = x_\mathrm{eq}$). $\hat{\Phi}_\mathrm{m}$ is the node flux associated with the equivalent electrical LC circuit.

This circuit consists of an equivalent capacitor (C_k) and inductor (L_k) capacitively coupled to the remaining circuitry through the motional capacitor ($\bar{C}_\mathrm{m}$). In order to obtain the equivalent circuit model, one must first analyze the circuit at dc and find the voltage drop on the moving capacitor ($\bar{V}_\mathrm{dc}$).

The value of the equivalent capacitor C_k can then be obtained based on our analysis in the previous section. Specifically we have found the interaction Hamiltonian for a general scenario (see Eq. (2.28)). The magnitude of this interaction would have

to be identical for the equivalent circuit as well. The interaction Hamiltonian due to the capacitive coupling of the equivalent circuit can be written as [51]

$$\hat{H}_{\text{int}} = -i\bar{C}_{\text{m}}\sqrt{\frac{\hbar\omega_{\text{m}}(C_{\text{k}}+\bar{C}_{\text{m}})}{2}}\frac{\hat{Q}}{C_{\Sigma}}(\hat{b}-\hat{b}^{\dagger}). \tag{2.54}$$

Therefore, by setting the magnitude of the interaction term to be identical to Eq. (2.28), we can obtain the value of the capacitor C_{k} to be

$$C_{\text{k}} = \frac{\hbar\bar{C}_{\text{m}}^2\omega_m}{2(\partial_x C_{\text{m}}\bar{V}_{\text{dc}}x_{\text{zpf}})^2} - \bar{C}_{\text{m}}. \tag{2.55}$$

The value of the equivalent inductor can be obtained based on the condition that the resonance frequency of the equivalent electrical resonator matches that of the mechanical oscillator

$$L_{\text{k}} = \omega_{\text{m}}^{-2}(C_{\text{k}}+\bar{C}_{\text{m}})^{-1}. \tag{2.56}$$

With this we have obtained the expression for the components of the equivalent electrical circuit for the mechanical oscillator.

The utility of this model can be demonstrated through the ease it provides for the analysis of a voltage biased mechanical oscillator connected to a transmission line of impedance Z_0. Based on black box quantization, the decay rate of the electrical circuit to the transmission line can be calculated to be

$$\Gamma_{\text{m}} = \frac{\omega_{\text{m}}^2\bar{C}_{\text{m}}^2 Z_0}{C_{\text{k}}+\bar{C}_{\text{m}}}. \tag{2.57}$$

By substituting the value of C_{k} into this equation, we obtain

$$\Gamma_{\text{m}} = \frac{2Z_0\omega_{\text{m}}(\partial_x C_{\text{m}}V_{\text{dc}}x_{\text{zpf}})^2}{\hbar} = \frac{Z_0(\partial_x C_{\text{m}}V_{\text{dc}})^2}{m_{\text{eff}}}, \tag{2.58}$$

where we note that in this scenario $\bar{V}_{\text{dc}} = V_{\text{dc}}$. This is a simple circuit theory derivation for a result that can only be obtained from first principles through a more involved analysis [50].

2.4 Electromechanical Interaction Rate

We have obtained the expression for the interaction rate between a mechanical oscillator and superconducting circuits (see Section 2.2). In general, analytically evaluating this expression for an arbitrary structure is not possible, instead one must utilize numerical methods. In this section we will describe how we specifically

perform this evaluation based on simulations of the electromagnetic and acoustic fields in a device.

For simplicity, we will treat the special case where a mechanical oscillator is coupled to a microwave resonator. This analysis can be easily modified for different microwave circuits. For completeness, we reproduce the expression we have derived for the interaction rate (Eq. (2.38))

$$g_{\mathrm{em}} = V_{\mathrm{dc}} \partial_x C_{\mathrm{m}} x_{\mathrm{zpf}} V_{\mathrm{zpf}} / \hbar. \tag{2.59}$$

As the voltage bias is an external parameter that can be adjusted by changing the applied voltage, we are specifically interested in calculating interaction rate per Volt which is defined as

$$g_0 = g_{\mathrm{em}} / V_{\mathrm{dc}} = \partial_x C_{\mathrm{m}} x_{\mathrm{zpf}} V_{\mathrm{zpf}} / \hbar. \tag{2.60}$$

Since the interaction is relatively weak (we are far from the ultrastrong coupling regime), one can follow a perturbative approach for analyzing the system [63].

First, the microwave resonator can be simulated to obtain zero-point fluctuations of voltage (V_{zpf}). Specifically, for the microwave simulations, the moving capacitor can be modeled to be fixed at its equilibrium position with a capacitance of $\bar{C}_{\mathrm{m}}$. The microwave resonance frequency (ω_{r}) and the total capacitance (C_Σ) can be obtained via electromagnetic simulations. The zero-point fluctuations of voltage can then be calculated to be

$$V_{\mathrm{zpf}} = \sqrt{\frac{\hbar \omega_{\mathrm{r}}}{2 C_\Sigma}}. \tag{2.61}$$

Second, the mechanical motion of the moving capacitor can be simulated. We specifically use finite-element model solvers to find the eigenmodes of the moving capacitor. The eigenmode of interest has frequency ω_{m} and a displacement profile $\mathbf{Q}(\mathbf{r})$ (where $\mathbf{r}$ is the space coordinate). Generally, the displacement profile one obtains from numerical simulations is not normalized since the mode profile scaled with a c-number still is an eigenmode for the system.

With the displacement profile at hand, the effective mass can be defined to be

$$m_{\mathrm{eff}} = \frac{\int d\mathbf{r}\, |\mathbf{Q}(\mathbf{r})|^2 \rho(r)}{\max[|\mathbf{Q}(\mathbf{r})|^2]}, \tag{2.62}$$

where the integral is calculated over the volume of the solid and $\rho(r)$ is the density of the solid material at position $\mathbf{r}$. We note that there exists a freedom in defining the

effective mass [15]. The specific convention we use is chosen to be consistent with some of the previous literature on optomechanical and electromechanical crystals following [64].

The zero-point fluctuations of displacement can then be calculated to be

$$x_{\mathrm{zpf}} = \sqrt{\frac{\hbar}{2m_{\mathrm{eff}}\omega_{\mathrm{m}}}}. \tag{2.63}$$

We can then define a normalized displacement profile as

$$\tilde{\mathbf{Q}}(\mathbf{r}) = x_{\mathrm{zpf}}\frac{\mathbf{Q}(\mathbf{r})}{\max[|\mathbf{Q}(\mathbf{r})|]}, \tag{2.64}$$

such that its maximum displacement magnitude is set by x_{zpf}.

The electromechanical interaction rate corresponds to the change in the stored electrical energy induced by mechanical motion. The dominant mechanism by which this occurs is the moving boundary effect [65]. In this picture, mechanical deformation modifies the geometry of the electromagnetic domain boundaries, leading to a perturbation of the electrical energy. The magnitude of this perturbation can be expressed through surface integrals [66]. For our specific case, this surface integral is

$$\hbar g_{\mathrm{em}} = \oint dA\, \left((\tilde{\mathbf{Q}}(\mathbf{r})\cdot\hat{n})(\Delta\varepsilon\mathbf{E}^{\parallel}(\mathbf{r})_{\mathrm{dc}}\mathbf{E}^{\parallel}(\mathbf{r})_{\mathrm{rf}} - \Delta\varepsilon^{-1}\mathbf{D}^{\perp}(\mathbf{r})_{\mathrm{dc}}\mathbf{D}^{\perp}(\mathbf{r})_{\mathrm{rf}}\right), \tag{2.65}$$

where $\hat{n}$ is the surface normal and $\Delta\varepsilon = \varepsilon_1 - \varepsilon_2$ and $\Delta\varepsilon^{-1} = 1/\varepsilon_1 - 1/\varepsilon_2$ are the electrical permittivity contrast between the two materials that are on the boundary covered by the surface integral. In the special case of metallic electrodes, one can take $\varepsilon \to \infty$ and eliminate the contribution from the tangential field components, leaving only the normal-field term.

$\mathbf{E}^{\parallel}(\mathbf{r})$ ($\mathbf{D}^{\perp}(\mathbf{r})$) is the electric (displacement) field component parallel (normal) to the surface. These components are evaluated for the dc and rf field configurations, as indicated by the subscripts. The required field distributions can be obtained from electrostatic simulations, where V_{dc} (V_{zpf}) is applied to the capacitor electrodes for the dc (rf) simulation. Treating the rf field electrostatically is valid when the capacitor behaves as a lumped element, which is generally satisfied in practical circuits where the moving capacitor is placed at a voltage antinode and its parasitic inductance is much smaller than the total inductance of the resonator. We also note that setting $V_{\mathrm{dc}} = 1$ V here provides the interaction rate per volt (g_0).

We explicitly treat the dc and rf fields separately, since materials can respond to them in fundamentally different ways. As an illustrative example, consider lightly doped silicon, which we employ in our experiments (as discussed in later chapters). At microwave frequencies, silicon simply behaves as a dielectric with a permittivity of $\varepsilon_{\mathrm{Si}} \approx 11.7\varepsilon_0$, where ε_0 is the vacuum permittivity. In contrast, for sufficiently large voltages ($qV_{\mathrm{dc}} \gtrsim E_c$, where $E_c/q \sim 1.1\mathrm{V}$ is the bandgap of silicon) a space charge region is formed on the material surface through bending of the Fermi level to the dopant level, even at cryogenic temperatures [67]. Under these conditions, silicon screens static electric fields and exhibits a metal-like response [68].

Consequently, for our moving capacitors made exclusively out of silicon and metals, the electromechanical interaction rate can be approximated as

$$\hbar g_{\mathrm{em}} \approx -\oint dA \left(\tilde{\mathbf{Q}}(\mathbf{r}) \cdot \hat{n}\right)\left(\Delta\varepsilon^{-1}\mathbf{D}^{\perp}(\mathbf{r})_{\mathrm{dc}}\mathbf{D}^{\perp}(\mathbf{r})_{\mathrm{rf}}\right), \tag{2.66}$$

since $\mathbf{E}^{\parallel}(\mathbf{r})_{\mathrm{dc}} = 0$ for all boundaries, when silicon exhibits a metallic response at dc. This modeling approach has been successful in estimating the electromechanical interaction rates for our structures [50, 69].

Chapter 3

PHONONIC CRYSTAL ELECTROSTATIC TRANSDUCERS

In the previous chapter we have provided a theoretical description of electrostatic coupling between acoustic and electromagnetic waves. Owing to the perturbative nature of the electromechanical interaction, the moving capacitor can be designed independently of the microwave resonator, as previously discussed. This chapter we focus exclusively on the design of our moving capacitors, which we refer to as *phononic crystal electrostatic transducers* [69].

3.1 Phononic Crystals

Our moving capacitor design, which will be detailed in the later sections, incorporates phononic crystal structures. Prior to expanding on our design, we provide a brief introduction to phononic crystals here.

Phononic crystals are structures where acoustic wave propagation is modified through periodicity [70, 71]. The periodicity of a structure is characterized through the set of lattice vectors $\mathbf{R}$, for which the system exhibits translational symmetry (i.e. $\rho(\mathbf{r}) = \rho(\mathbf{r}+\mathbf{R})$ for all lattice vectors). Within such periodic media, the eigenmodes of the system are Bloch waves with a displacement profile of the form [64]

$$\mathbf{Q}_\mathbf{k}(\mathbf{r}) = \mathbf{u}(\mathbf{r}) \exp(i\mathbf{k}\cdot\mathbf{r}), \tag{3.1}$$

where $\mathbf{k}$ is the crystal momentum and the envelope function $\mathbf{u}(\mathbf{r})$ inherits the periodicity of the lattice, $\mathbf{u}(\mathbf{r}) = \mathbf{u}(\mathbf{r}+\mathbf{R})$.

The physical lattice has an associated reciprocal lattice, defined as the Fourier transform of the real-space lattice. A direct consequence of discrete translational symmetry in the system is the conservation of crystal momentum, modulo reciprocal lattice vectors. As a result, crystal momentum is uniquely defined only within a single unit cell of reciprocal space, conventionally chosen to be the one containing the origin, known as the first Brillouin zone [72].

Within the first Brillouin zone, the acoustic modes form a set of discrete bands in which the mode frequency varies continuously with the crystal momentum. The dispersion of these bands govern the behavior of phononic crystals and can be

engineered to produce a variety of phenomena, including bandgaps, flat bands with vanishing group velocity, and bound states in the continuum, among others [71, 73].

We are specifically interested in phononic crystals for two main reasons:

1. Phononic crystals can be engineered to exhibit phononic bandgaps, frequency ranges within which acoustic waves cannot propagate through the structure [74–77]. Such structures, often referred to as phononic or radiation shields, can therefore function as mirrors for acoustic cavities whose resonance frequency resides within the bandgap. They are extremely effective in suppressing acoustic radiation to the environment, allowing the demonstration of mechanical oscillators that exhibit extremely high quality factors ($Q \gtrsim 10^9$) [42, 44, 78]. In our work, we employ phononic shields to anchor mechanical oscillators and minimize radiation losses to the environment.

2. Phononic crystals can be engineered to support extended modes, where the acoustic mode profile corresponds to the collective oscillation of multiple unit cells. Designing structures with such spatially extended modes enables larger electromechanical interaction rates than those achievable with a single unit cell (i.e., a non-periodic structure). This enhancement arises primarily because extended structures can exhibit larger motional capacitance values, which improves the electromechanical interaction rate.

3.2 Design Principles

Basic Geometry

The fundamental components of our moving capacitors are illustrated in Fig. 3.1. In designing this structure, we draw upon techniques developed for electromechanical and optomechanical crystals [75, 79]. Our moving capacitor is a planar structure, where a nanobeam patterned as a 1D phononic crystal oscillator is suspended between two outer electrodes, with a vacuum gap separating them. The phononic crystal is composed of multiple unit cells, where elliptical holes are patterned to generate a periodic structure. The collective motion of the phononic crystal oscillator modulates the vacuum gap and leads to a dependence of the motional capacitance on the displacement ($C_{\mathrm{m}}(x)$), giving rise to the electromechanical interaction. The phononic crystal oscillator is clamped with periodic cross shaped phononic shields, which minimize acoustic radiation.

For the specific geometry we are illustrating, the two outer electrodes serve as the

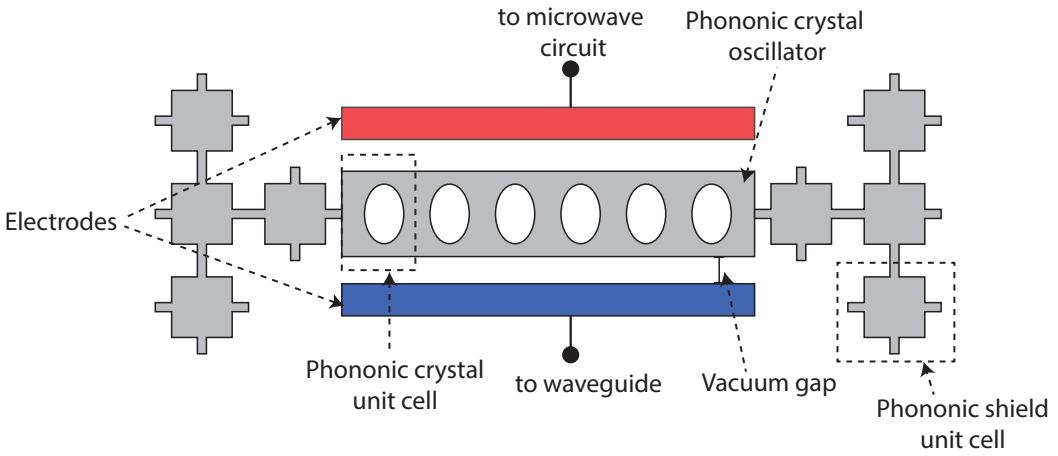


Figure 3.1: **Moving capacitor diagram.** Top view of a phononic crystal electrostatic transducer. The components of the device are indicated and labeled with dashed lines. In this diagram only the outer electrodes are metalized. In the full device, the red (blue) electrode is galvanically connected to the microwave circuit (waveguide).

two electrodes of the capacitor. One of them is attached to the waveguide for voltage biasing the capacitor and the other one is connected to the microwave circuitry. We note that there exists another variant of this geometry where the nanobeam is metalized and serves as the first electrode of the moving capacitor, while the two outer electrodes are connected and function as the second electrode (such a design will be illustrated in Chapter 4). These two variants share a lot of the same design principles and differ mainly in terms of the interaction rate and the mechanical coherence. In this chapter, for simplicity, we will only focus on the geometry with a metal free central beam (shown from a different perspective in Fig. 3.2), which we have utilized in our recent experiments (see Chapter 5).

Materials

The specific dielectric we use to form our devices is single-crystal silicon. We choose silicon as it possesses extremely low acoustic loss at cryogenic temperatures [48] and a low density of defects [80]. High quality silicon-on-insulator (SOI) films are commercially available and can be patterned into phononic crystals, which are subsequently suspended by etching the underlying oxide layer [81]. These properties have enabled the demonstration of phononic crystal oscillators with extremely high quality factors [42, 78]. Additionally, established fabrication techniques allow integration of superconducting qubits with mechanical oscillators on SOI substrates [82]. Together, these advantages make silicon a highly attractive platform for

combining mechanical oscillators with low dissipation and superconducting circuits.

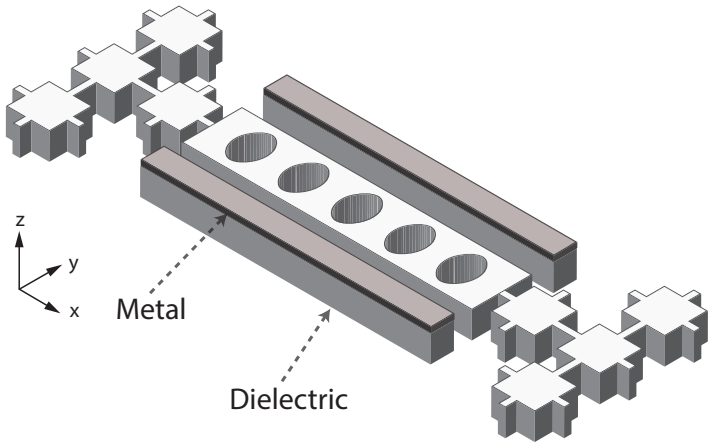


Figure 3.2: **Transducer diagram isometric perspective.** In this device, the outer electrodes are covered with a thin layer of metal, shown with a brown color. Rest of the device is not metalized and is made exclusively out of a dielectric material.

Phononic Crystal Design

Next we move on to the design of our phononic crystal oscillator, which begins at the unit cell level. A representative unit cell, consisting of a rectangular prism with an elliptical hole, is shown in Fig. 3.3a. These unit cells are periodically arranged along the x-axis, forming a 1D phononic crystal. Because of this periodicity, the acoustic modes of the unit cell take the form of Bloch waves, which can be represented through a band diagram. The crystal momentum (k_x) values are uniquely defined within the irreducible Brillouin zone, spanning from the Γ-point ($k_x = 0$) to the X-point ($k_x = \pi/a$), where a is the lattice constant.

Because the moving capacitor possesses a symmetry plane parallel to the x–z plane, the acoustic modes can be classified according to their parity under reflections across this plane [64]. Only modes that possess even reflection symmetry couple to the electrical fields, as can be seen from the expression for the electromechanical interaction rate (Eq. (2.65)). Therefore, in the band diagram shown in Fig. 3.3b, we restrict our attention to the even modes.

Our focus is on modes at the Γ-point, since these modes carry no net momentum. For modes with finite momentum ($k_x \neq 0$), the electromechanical interaction rate is suppressed. This suppression arises because the mode envelope oscillates across the device, leading to cancellation when the surface integral for the interaction rate is evaluated. The specific mode we choose (indicated by the red dot in Fig. 3.3b) has a

mode profile of a breathing mode. This breathing motion leads to the modulation of the capacitor gap as the beam breaths inwards and outwards with time, as illustrated in Fig. 3.3c. The parameters of the unit cell is chosen such that the unit cell has a resonance frequency of $\omega_m/2\pi \approx 5$ GHz, which is convenient for coupling to superconducting circuitry.

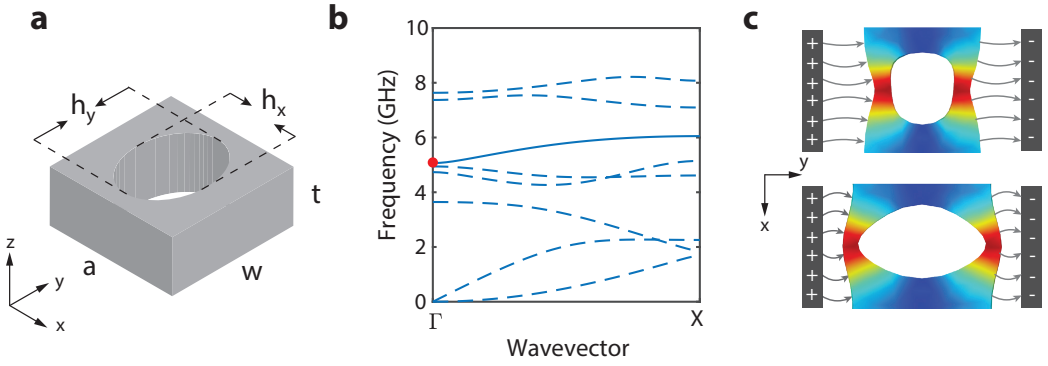


Figure 3.3: **Phononic crystal unit cell. a,** Diagram of a unit cell with length a, width w, thickness t, and an elliptical hole with axes dimensions of h_x and h_y. **b,** Band diagram showing modes with even symmetry with respect to reflections along the x-z plane. The chosen mode, which resides at the Γ point, is indicated with the red dot. The specific band that hosts our mode of interest is indicated with a solid line. Rest of the bands are shown as dashed lines. **c,** Exaggerated displacement profile of the chosen mechanical mode. The colormap indicates the displacement magnitude. The two images are separated by half an oscillation period in time, illustrating the breathing motion which modulates the vacuum gap.

A phononic crystal oscillator can be formed by stacking multiple unit cells and clamping them with phononic shields. For our design we utilize cross type phononic shields [42, 75]. These shields are periodic in two dimensions and are arranged in a square lattice (see Fig. 3.4a). The first Brillouin zone for such a square lattice is another square in the momentum space as shown in Fig. 3.4b. The phononic shields can be designed to possess a wide 2D bandgap centered around the frequency of interest (see Fig. 3.4c).

Now that we have our unit cell and the phononic shields, we can design a phononic crystal oscillator. An important design parameter is the number of unit cells that compose the nanobeam. To decide on this parameter, we first look at how the electromechanical interaction rate scales with the number of unit cells for a uniform displacement profile (i.e. all unit cells oscillating together with identical displacement amplitudes).

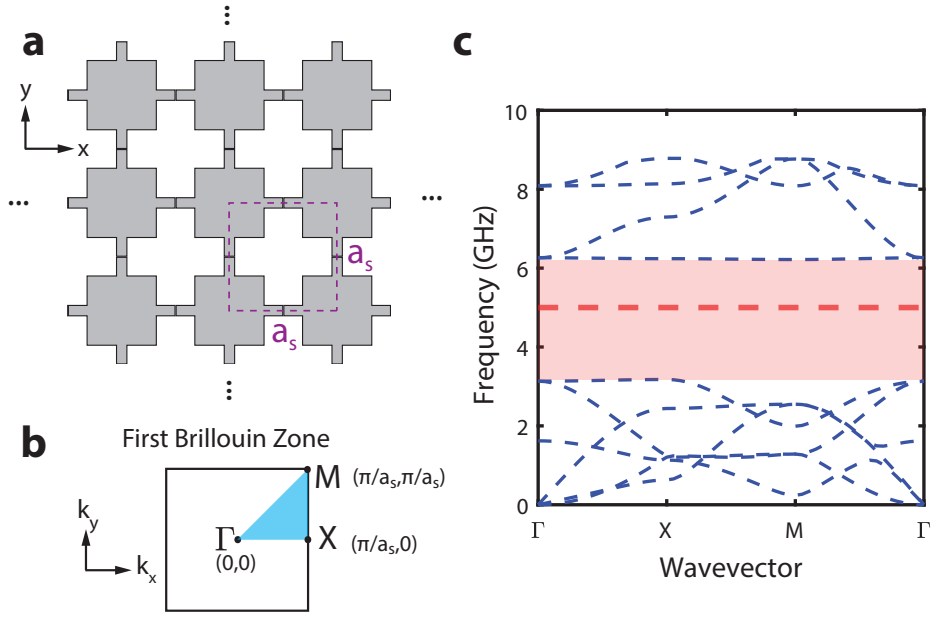


Figure 3.4: **Phononic shields. a,** Diagram of a two-dimensional array of phononic shields, with each shield having a unit cell constant of a_s. The unit cell is indicated with the dashed purple rectangle. **b,** First Brillouin zone in momentum space for a square lattice. The blue shaded region indicates the irreducible Brillouin zone **c,** Band diagram of our phononic shield, traversing the boundary of the irreducible Brillouin zone. The modes of the shields are indicated by the dashed blue lines. The red shaded region is the bandgap of the structure. The frequency of the mechanical oscillator to be clamped with the shields is indicated by the red dashed line.

For our planar structures, the motional capacitance scales with a linear proportion to the number of cells ($\partial_x C_\mathrm{m} \propto N_\mathrm{cell}$). However, the effective mass scales linearly with the number of cells as well ($m_\mathrm{eff} \propto N_\mathrm{cell}$), leading to a reduction in the zero-point fluctuations of displacement ($x_\mathrm{zpf} \propto N_\mathrm{cell}^{-1/2}$). Assuming that the change in the motional capacitance is not large enough to significantly change the total capacitance of the microwave circuit (i.e. $\bar{C}_\mathrm{m} \ll C_\Sigma$), the electromechanical interaction rate scales with the number of unit cells as $g_\mathrm{em} \propto N_\mathrm{cell}^{1/2}$. Therefore, with a view to maximizing the interaction rate, we would like to have as many unit cells as possible.

However, there exist challenges associated with realizing a uniform displacement profile for a large number of unit cells:

1. In contrast to the idealized infinite phononic crystal, a finite chain supports modes whose spatial profiles and frequencies are modified by boundary effects. The broken translational symmetry at the clamping points leads to

modification of the acoustic field near the boundaries, resulting in deviations from the uniform amplitude distribution of infinite Bloch modes.

2. Fabrication disorder, which is always present for a realistic device, leads to distortion of the acoustic mode profile. From a tight-binding picture, this can be understood as the competition between inter-cell coupling and disorder induced detuning, which alters the mode structure. In extreme cases, disorder can even break up an extended mode, leading to Anderson localization.

These two limitations and how we combat them is the focus of the next section.

3.3 Designing Extended Acoustic Modes

Numerical Optimization

The impact of boundary effects on the acoustic profile, which leads to deviations from uniform amplitude across the cells, is shown in Fig. 3.5a. Such effects are inherent to any finite structure composed of identical unit cells. A potential way to overcome this challenge is to utilize unit cells that are not identical. For a certain choice of parameters, the variation of the cavity parameters can compensate boundary effects, resulting in more extended and uniform modes.

However, designing such a structure is challenging due to the large parameter space that must be explored. A practical solution is to numerically optimize the phononic crystal oscillator. For this purpose, we follow methods previously developed for optimizing optomechanical crystals [75, 83].

In this optimization, we must define a cost function that would lead us to our design targets. Achieving a more uniform mode profile across the structure directly contributes to enhancing the interaction rate, making it a natural target for maximization by the optimization procedure. Therefore, the cost function that will be minimized during the optimization is defined as

$$F(\mathbf{p}) \triangleq -g_0,$$

where g_0 is the electromechanical interaction rate per Volt and $\mathbf{p}$ is a vector that corresponds to the parameters of the system, which will be defined below.

The unit cells of our phononic crystal are parametrized as shown in Fig. 3.3a. For a

cavity with 2N+1 cells, the parameters of the j-th cell from the center are

$$a_j = a_N - (a_N - a_0) f(x_j), \tag{3.2}$$

$$h_{xj} = \left(a_j - 2\delta\right) \eta_j + \delta, \tag{3.3}$$

$$h_{yj} = (w - 3\delta)\gamma_j + \delta \tag{3.4}$$

$$\eta_j = \eta_N - (\eta_N - \eta_0)\, f\left(x_j\right), \tag{3.5}$$

$$\gamma_j = \gamma_N - (\gamma_N - \gamma_0)\, f\left(x_j\right), \tag{3.6}$$

where $f(x_j)$ is the quadratic tapering function, which is defined as

$$f(x_j) = 1 - x_j^2,\ x_j = j/N. \tag{3.7}$$

The parameters η and γ (constrained to be between 0 and 1) enable us to parametrize the elliptical hole dimensions (h_x, h_y), while ensuring that we have features larger than the minimal feature size that can be fabricated of δ, which we set to be 60 nm. Due to the quadratic tapering, the dimensions of the central (0-th) and final (N-th) unit cell is sufficient to describe the entire structure. The thickness of the beam (t) is set to be 220 nm based on the device layer thickness of our films. The vacuum gap is fixed at 70 nm. We also assume that the moving capacitor is connected to a microwave oscillator with impedance of $Z = 350\,\Omega$, which roughly matches that of transmon superconducting qubits.

Another important requirement is that the target frequency of the mechanical oscillator be $\sim$ 5 GHz. This can be satisfied by ensuring that the center unit cell gives us a 5 GHz resonance. Specifically, before each iteration in the optimization process, we determine the parameter a_0 that yields a 5 GHz resonance for the current combination of η_0, γ_0 and w. This value of a_0 is then used for the simulation of the moving capacitor and the subsequent calculation of g_{em} for a given structure, making it a dependent parameter for the optimization procedure. If there is no value of a_0 that satisfies our resonance frequency requirement, then we set $F = \infty$ and move on to the next sampled set of parameters.

As can be inferred from the discussion above, the parameters to be optimized are as follows: $\mathbf{p} = (a_N, \eta_0, \eta_N, \gamma_0, \gamma_N, w)$. To minimize our cost function we use the Nelder-Mead algorithm, which is a global optimization method [84]. In our case, we see that the algorithm can converge in relatively few iterations. The result of an example optimization run is visualized in Fig. 3.5b, showing a roughly 50% improvement in the interaction rate compared to the initial uniform structure that was provided to the algorithm. One can further see in Fig. 3.5c, how the parameters

of the structure vary until convergence occurs. The resultant optimized phononic crystal oscillator is shown in Fig. 3.5d. The optimized structure has a significantly more uniform displacement profile, where each unit cell has comparable displacement amplitude, in line with our understanding of how the interaction rate scales. Therefore, the optimization algorithm successfully increases the electromechanical interaction rate by enabling the design of structures in which boundary effects are minimized.

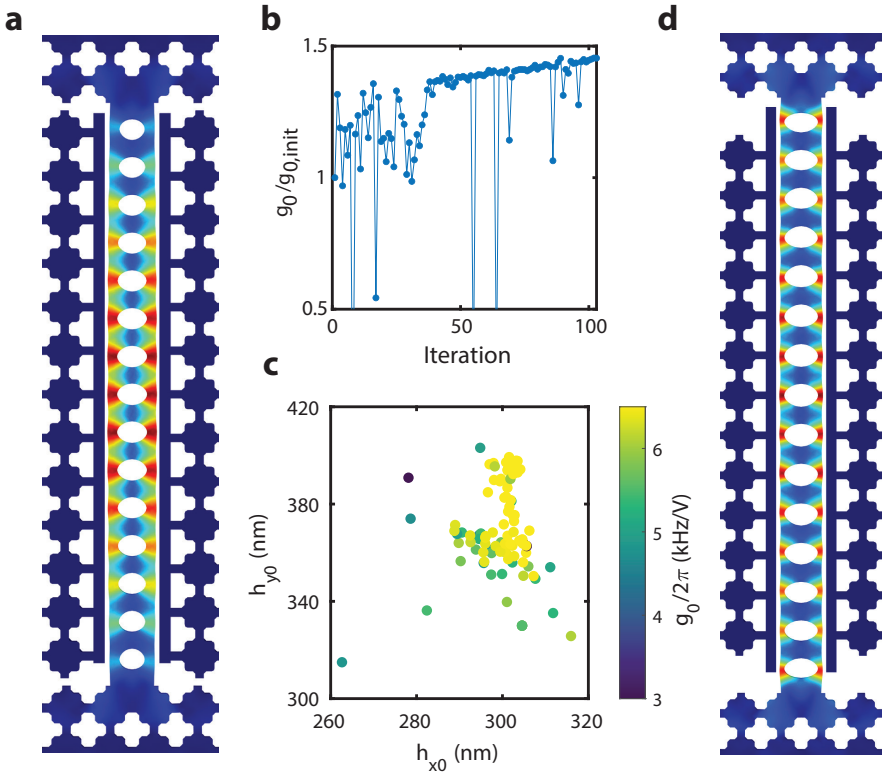


Figure 3.5: **Phononic crystal optimization.** **a,** Exaggerated displacement profile of a phononic crystal oscillator made out of 15 identical unit cells. The colormap indicates the displacement amplitude. **b,** An example optimization run, which demonstrates the improvement in the interaction rate over the initial point ($g_{0,\mathrm{init}}$) and convergence of the algorithm. **c,** Variation in the hole parameters of the central unit cell throughout the optimization routine. **d,** Displacement profile of the optimized structure.

Fabrication Disorder

The optimization procedure above is conducted under the assumption that the fabricated devices can exactly match the designs. However, even with state-of-the-art electron beam lithography techniques, there exist nanometer scale fluctuations in

patterned structures, commonly termed fabrication disorder. For structures that have patterned holes like our phononic crystal oscillators, the disorder manifests itself as random fluctuations in the position and the size of the holes [85]. This disorder in turn leads to a change in the frequency of each unit cell, altering the profile of the extended mode. In the limit of very large disorder, this effect can even lead to mode breakup and Anderson localization [86]. As disorder effects become more pronounced for extended structures, it can limit the number of unit cells of our phononic crystal oscillator.

Fabrication disorder is known to play a significant role in limiting the quality factor of photonic crystals [87], and its modeling has been extensively studied. In particular, the impact of disorder has been explored numerically using Monte-Carlo simulations, in which the positions and dimensions of holes are varied randomly [88, 89]. This approach has also proven effective for investigating disorder effects in phononic crystals [42].

We adopt this approach to investigate how disorder modifies our acoustic mode profile. In each realization, the center position of every unit cell is randomly perturbed $(x_j, y_j) \rightarrow (x_j + \delta x_j, y_j + \delta y_j)$ along with the hole dimensions $(h_{xj}, h_{yj}) \rightarrow (h_{xj} + \delta h_{xj}, h_{yj} + \delta h_{yj})$ (see Fig. 3.6a). Here $\delta x_j, \delta y_j$ $(\delta h_{xj}, \delta h_{yj})$ are independent Gaussian random variables with zero-mean and standard deviation of σ (2σ), where σ quantifies the magnitude of the fabrication disorder in the system. For each realization, the system is simulated to extract the electromechanical interaction rate, providing a measure of how disorder effects the mechanical mode. Multiple realizations are simulated to extract statistics of the system.

First, we investigate how the electromechanical interaction rate scales in the absence of disorder ($\sigma = 0$) as shown in Fig. 3.6b. For the optimized structures, the scaling matches our theory ($g_{\mathrm{em}} \propto N_{\mathrm{cell}}$) very well, indicating the benefit of increasing the number of unit cells in an ideal situation.

However, we are mainly interested in what happens in the presence of disorder. It is very challenging to characterize the precise degree of fabrication disorder in a system [85]. We instead rely on results from literature that suggest that disorder can span a range from 1 nm [85, 87] to around 4 nm [90] for devices similar to ours. Based on these, we choose to investigate $\sigma = 2, 4$ nm. We perform Monte-Carlo simulations, where we look at the statistics of 50 random realizations for each N_{cell} and disorder magnitude. As can be seen in Fig. 3.6c, the disorder leads to a reduction in the electromechanical interaction rate, which becomes more pronounced for higher

magnitudes of disorder. Based on the simulations, we choose the number of unit cells for our devices to be $N_{\text{cell}} = 15$, as the benefits of larger number of cells appear to start diminishing at this point, especially for larger disorder.

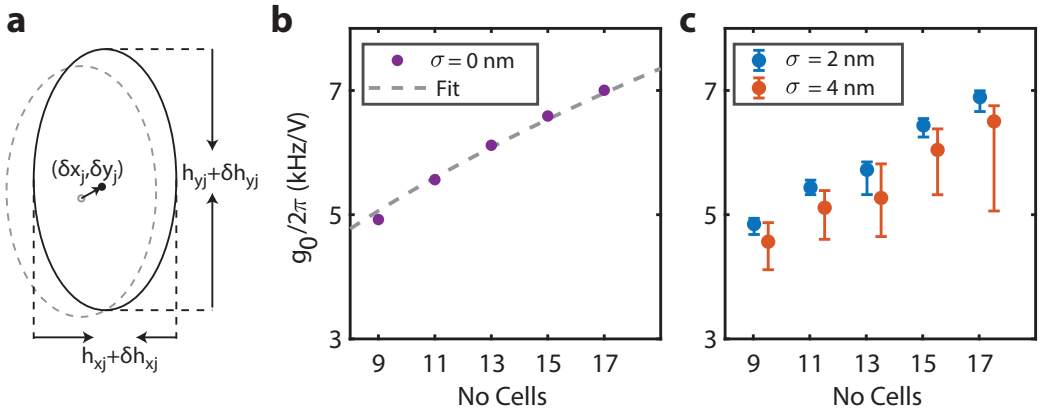


Figure 3.6: **Fabrication disorder simulations.** **a,** Random displacements and dimension variations for an elliptical hole. The dashed gray ellipse stands for the original hole with ideal dimensions and solid lines indicate the modified hole. **b,** Electromechanical interaction rate as a function of number of cells for optimized structures without fabrication disorder. The gray line shows a fit of the form $g_0/2\pi = 1.7$ kHz/V $\times \sqrt{N_{\text{cell}}}$. **c,** Electromechanical interaction rate in the presence of disorder with $\sigma = 2, 4$ nm. The data points indicate the median of 50 realizations and the error bars show the interquartile range between 10-90% for the realizations. The data for $\sigma = 4$ nm is offset horizontally for greater visibility.

Following the fabrication of these devices, we have measured $g_0 = 4.2$ kHz/V (see Fig. 5.2), which is slightly smaller than the 4 nm disorder result of $6.0^{+0.3}_{-0.8}$ kHz/V. This is potentially indicative of a relatively high level of disorder in our structures. Methods to mitigate disorder in order to further boost interaction rates will be the subject of future studies.

Beyond altering the mode profile, fabrication disorder sets the effectiveness of the acoustic shields in suppressing acoustic radiation as well [42]. The impact of the fabrication disorder on acoustic radiation can be estimated through Monte Carlo simulations, similar to the ones described above. Based on these simulations, we select a shielding structure comprising 8 unit cells, which is expected to exhibit an extremely large radiation limited quality factor ($Q > 10^{12}$), for a disorder magnitude of 4 nm.

3.4 Vacuum Gap

In the optimization routine described in the previous section, we assumed a 70 nm vacuum gap separating the phononic crystal oscillator from the outer electrodes. This specific value because it is the smallest gap size we have been able to fabricate with the fabrication techniques we employ (for fabrication details see Section 4.9 and Section 5.5). Since, for the small gaps of interest, the electric field lines remain nearly unchanged while only the field magnitude varies, the optimized phononic crystal parameters are effectively independent of the exact gap value selected.

Nevertheless, the gap dimension strongly affects the electric field magnitude and therefore plays a critical role in determining the electromechanical interaction rate. For example, for an ideal parallel plate capacitor, the electromechanical interaction rate scales with the gap size (d) as $g_{\mathrm{em}} \propto d^{-2}$. For our more complex geometry, we can numerically investigate how the electromechanical interaction rate scales with gap size. As shown in Fig. 3.7, the electromechanical interaction rate scales as $g_{\mathrm{em}} \propto d^{-1.3}$ for our structure. We see clearly that reducing the vacuum gap can provide a pathway to significantly boost the interaction rate.

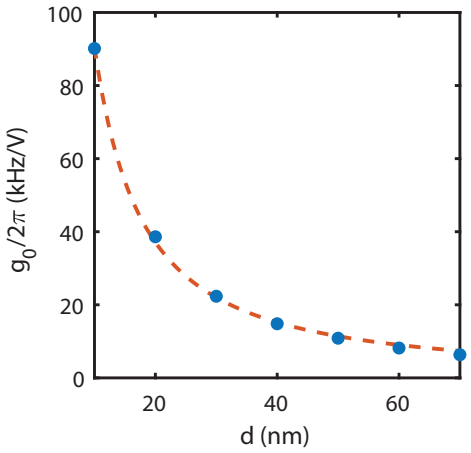


Figure 3.7: **Electromechanical interaction rate vs vacuum gap.** Blue data points indicate simulation results of the electromechanical interaction rate for varying vacuum gap dimensions. We utilize the optimized phononic crystal oscillator with 15 unit cells for these simulations. The red dashed line is a fit of the form $g_{\mathrm{em}} \propto d^{-b}$, where $b = 1.3$.

In the previous analysis, we considered only the electromechanical interaction rate per Volt (g_0). However, in practical scenarios, the relevant quantity is the maximum achievable electromechanical interaction rate, which depends on the maximum applied bias voltage. This maximum voltage is determined by the lesser of two limiting

factors: (i) the pull-in instability, discussed in Section 2.1, which depends on the device geometry, and (ii) the maximum voltage rating of the electrical components used to wire the device, which in our experiments has been limited to around 50 V.

For the optimized design with 15 unit cells and a 70 nm gap, we measured a pull-in voltage of $V_{\text{pi}} = 64\text{V}$, which is sufficiently high that the limitation arises from the wiring rather than the device itself. However, since the pull-in voltage decreases with decreasing gap size, this effect must be considered when investigating smaller gaps or less stiff structures.

Chapter 4

ELECTROSTATIC COUPLING TO A MICROWAVE RESONATOR

Reproduced with permission from Springer Nature.

A. Bozkurt, H. Zhao, C. Joshi, H. G. LeDuc, P. K. Day, and M. Mirhosseini, "A quantum electromechanical interface for long-lived phonons", Nature Physics **19**, 1326–1332 (2023) 10.1038/s41567-023-02080-w,

4.1 Introduction

Phonons, the quanta of energy stored in vibrations in solids, promise unique opportunities for storing and communicating quantum information. The intrinsic mechanisms for phonon dissipation get suppressed at low temperatures [48], leading to extremely low acoustic loss in single crystal materials [91, 92]. Additionally, the inability of sound waves to propagate in vacuum makes it possible to trap phonons in wavelength-scale dimensions via geometric structuring, leading to near-complete suppression of environment-induced decay [42]. Finally, phonons interact with solid-state qubits and electromagnetic waves across a broad spectrum, making them near-universal intermediaries for cross-platform information transfer [93]. Motivated by these properties, pioneering work in the past two decades has enabled sensitive measurement and control of mechanical oscillators in the quantum regime via optical and electrical interfaces, making them viable candidates for quantum sensors, memories, and transducers [94, 95].

While optomechanical experiments have been successful in measuring phonons with millisecond-to-second lifetimes [42, 96], accessing long-lived mechanical resonances with electrical circuits has been more challenging. In the gigahertz frequency range, where the spectral proximity to superconducting qubits holds the most promise for quantum technologies, piezoelectricity is the predominant mechanism for converting microwave photons to phonons. Piezoelectric devices have been used with remarkable success in coupling mechanical modes to superconducting qubits [34–36]. However, their need for hybrid material integration, sophisticated fabrication process and reliance on lossy poly-crystalline materials [45] has limited the state-of-the-art experiments to mechanical lifetimes of around one microsecond in devices with compact geometries [36, 97]. This evidently large gap between

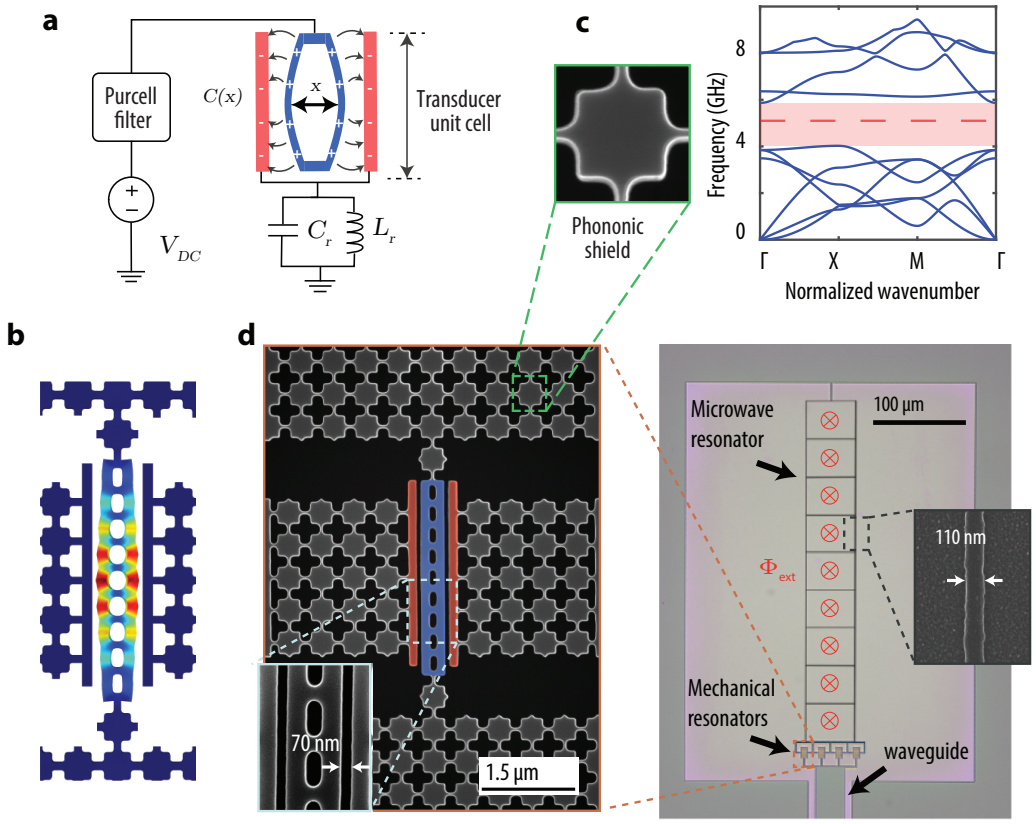


Figure 4.1: **Electrostatic transduction.** (a) The circuit diagram of an electrostatic transducer coupled to a microwave cavity (shown as an LC resonator). The Purcell filter delivers the static biasing voltage to the transducer without incurring radiative loss to the microwave cavity. (b) Simulated displacement profile of the confined mechanical resonance with the largest electromechanical coupling. (c) Schematics of the unit cell and the band diagram of a phononic shield. (d) Left: The scanning electron microscope (SEM) image of the fabricated transducer clamped by the phononic shields. The inner and outer electrodes are shown in false color. Right: The optical microscope image of the fabricated microwave resonator. Inset shows the TiN nanowires.

the mechanical lifetimes accessible to optical and electrical interfaces motivates the pursuit of less invasive forms of electromechanical interaction. Creating better electrical interfaces for long-lived phonons can revolutionize our current quantum toolbox by pairing the superior coherence of acoustics with the massive nonlinearity of Josephson junction circuits [23].

Here, we realize electromechanical coupling between microwave photons in a superconducting circuit and long-lived phonons in a 5-GHz crystalline silicon oscillator. To achieve this, we rely on *electrostatic transduction*, where we use a

static electric field, as opposed to conventionally used radio-frequency drives, to realize a parametrically-enhanced interaction in a microwave cavity with a motion-dependent capacitor. The absence of alternating currents from the driving field in this scheme eliminates conductive loss, allowing us to achieve large parametrically-enhanced coupling rates without causing heating in the system. To further enhance electromechanical interactions, we rely on frequency-tunable high-impedance microwave resonators made from TiN superinductors. Relying on these innovations, we are able to demonstrate electromechanical interaction in the strong coupling regime, enabling the coherent exchange of microwave photons and phonons at a cooperativity of $C \approx 1200$. We measure mechanical lifetimes in the few-phonon regime, demonstrating quality factors in excess of 8 million (at 5 GHz) in our best devices. To the best of our knowledge, this is the highest value measured via electrical interfaces in this frequency band for compact device geometries. Crucially, we observe no parasitic heating for a large range of electrostatic biasing fields in our system, allowing us to operate in the quantum ground state as verified by calibrated thermometry measurements in a dilution refrigerator. The combination of long lifetimes, strong interaction, and the compact geometry of our platform promises future experiments in employing mechanical modes as microwave-frequency quantum memories, improved microwave-optical transducers, and new measurement capabilities for exploring the origins of acoustic loss in crystalline materials.

4.2 A phononic crystal electrostatic transducer

The operating principles of our experiment can be understood by considering a capacitor with mechanically moving electrodes connected to an external DC voltage source. In this setting, the mechanical vibrations of the capacitor electrodes create a time-dependent dipole oscillating at the mechanical resonance frequency. Connecting this charged moving capacitor (i.e. the *transducer*) to an electromagnetic cavity (see Fig. 4.1a) leads to an interaction between the voltage operator of the photons in the cavity ($\hat{V}/V_{\mathrm{zpf}} = i(\hat{a} - \hat{a}^\dagger)$) and the quantized mechanical displacement operator ($\hat{x}/x_{\mathrm{zpf}} = (\hat{b} + \hat{b}^\dagger)$). This interaction can be described by the Hamiltonian (see Section 2.2)

$$\hat{H}_{\mathrm{int}} = i\left(x_{\mathrm{zpf}}\partial_x C\right) V_{\mathrm{zpf}} V_{\mathrm{DC}} (\hat{a}\hat{b}^\dagger - \hat{a}^\dagger \hat{b}) = i\hbar g_{\mathrm{em}} (\hat{a}\hat{b}^\dagger - \hat{a}^\dagger \hat{b}). \tag{4.1}$$

Here, x_{zpf} and V_{zpf} represent the zero-point motion and voltage of the phonon and photon fields, respectively. The coupling rate is a function of the geometry (through $\partial_x C$) and the applied bias voltage V_{DC}, and arises as a result of the change in the

stored electrical energy as a function of mechanical motion. The DC voltage in this process thus functions similarly to a pump in a parametric process [18]. Unlike conventional parametric electromechanics, however, electric fields at zero frequency are not accompanied by alternating currents. As we will see, this distinction is crucial in our experiment, since it increases the net coupling rate at large voltages without being limited by the dissipation in the superconducting cavity [79, 98].

Despite its conceptual simplicity, electrostatic transduction is challenging to realize at GHz frequencies [29, 68]. Getting substantial coupling requires increasing the motion-dependent capacitance and the zero-point displacement. This combination has been previously achieved in low-mass, narrow-gap suspended capacitors, which support MHz-frequency mechanical resonances [99]. However, the frequency scaling of acoustic loss in metals (speculated to be caused at grain boundaries [45, 100, 101]) makes these structures unsuitable for GHz frequencies. Additionally, the short wavelength of GHz-frequency phonons leads to increased acoustic radiative loss to the surrounding environment, making it challenging to localize high-Q resonances.

Our solution is to utilize planar nano-structured devices made from crystalline silicon membranes. In our platform, we deposit a thin metallic layer (of titanium nitride, TiN) on top of a patterned silicon membrane to form a transducer (see Fig. 4.1b). The transducer consists of a one-dimensional phononic crystal formed on the inner electrode of a vacuum-gap capacitor. The in-plane movement of the 'breathing' mechanical mode in this structure leads to the modulation of the capacitance. We have maximized the rate of change of this motion-dependent capacitance by fabricating capacitors with narrow gaps in the range of 65-70 nm. Additionally, we have maximized the capacitance by increasing the number of phononic crystal unit cells to the limit set by the onset of disorder effects, which leads to mode distortion as observed in finite-element simulations (see Appendix A.3). A key benefit of this planar geometry is the possibility of creating phononic crystals with a wide band gap for all phonon polarizations [42]. We use these 'phononic shields' for clamping the transducer to its surrounding membrane (see Fig. 4.1c, d).

Size mismatch is a central challenge in coupling the presented phononic crystal transducer to a microwave circuit. Set by the wavelength of phonons ($\sim$ 1 μm at the target frequency of 5 GHz), the transducer's small size results in a poor overlap between mechanical motion and the electric field from the microwave cavity, and consequently in weak electromechanical interaction. To overcome this challenge, we maximize the electric energy density in the transducer by minimizing

the microwave cavity's total capacitance. Formally, this leads to an enhancement of the zero-point voltage of the microwave photons in the cavity, which scales with the resonator's characteristic impedance as $V_{\mathrm{zpf}} \propto \sqrt{Z}$ [102]. Recent work on error-protected superconducting qubits has established techniques for creating high-impedance microwave cavities made from disordered superconductors [103, 104]. The *kinetic inductance* of charge carriers in these materials leads to a high impedance in wires with small cross sections [105]. In our experiment, we form a microwave resonator (Fig. 4.1d) by patterning a nanowire from thin-film titanium nitride (thickness $\sim$ 15 nm). The microwave resonator is directly attached to two electrodes in the transducer. Beyond magnifying the electromechanical interactions by providing a large V_{zpf}, kinetic inductance is tunable via external magnetic fields [95], which allows for in-situ control of the resonance frequency of the microwave cavity in our experiment.

4.3 Characterization and measurements

We have characterized fabricated electromechanical resonators in a dilution refrigerator with a base temperature of 20 mK (see details at Methods). A coplanar waveguide is connected to the device for simultaneously applying DC voltages to our mechanical capacitor and probing our microwave resonator in reflection via its coupling to the waveguide. In the absence of electromechanical coupling, we can measure the bare microwave cavity response using a vector network analyzer (see Fig. 4.2a). To locate the mechanical resonance, we apply a DC voltage and continuously tune the frequency of the microwave resonator via an external magnetic field (see Section 4.9). The electromechanical interaction leads to a large reflection at the point where the microwave and mechanical frequencies cross, giving rise to a feature similar to electromechanically-induced transparency (Fig. 4.2b) [99]. We extract the electromechanical coupling rate using a fit to the theory expressions for the microwave response (see Fig. 4.2c), and plot it as a function of the applied voltage in Fig. 4.2d. As evident, the coupling rate is found to be a linear function of the voltage bias with a slope ($g_{0,\mathrm{B}}/2\pi$ = 45.4 $\pm$ 1.1 kHz/V) closely matching the results from numerical modeling (see Appendix A.3). In addition, we present measurement results from a second device with identical geometry but with a small coupling $g_{0,\mathrm{A}}/2\pi$ = 22.0 $\pm$ 1.4 kHz/V, which is likely impacted by mode-breakup due to fabrication disorder. An interesting feature in the data is the small non-zero coupling at the zero-voltage bias, where zero coupling is achieved at a negative offset voltage. This feature is persistent in a shorted capacitor geometry and in

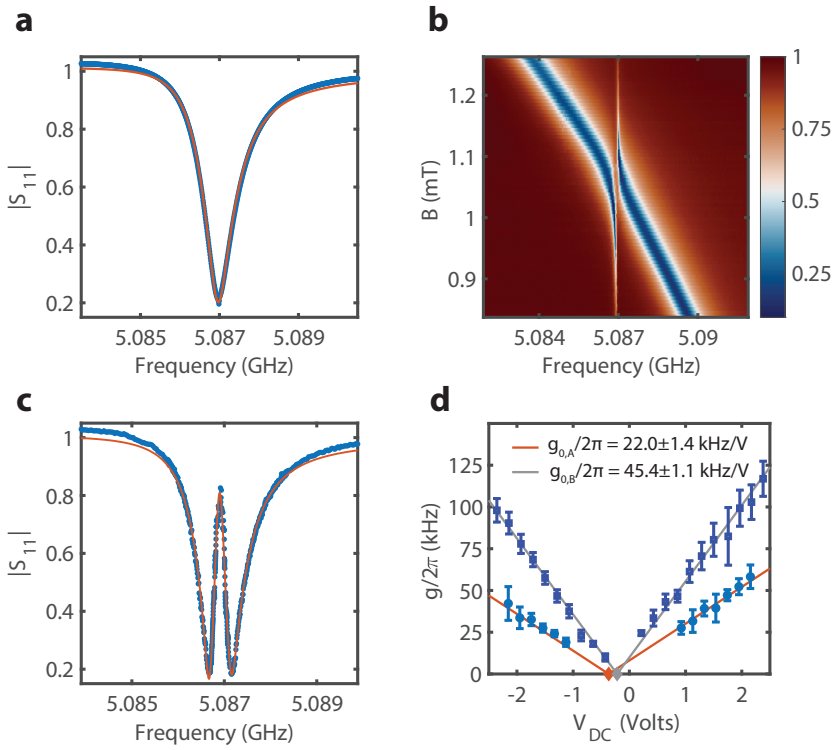


Figure 4.2: **Microwave spectrum.** (a) The reflection spectrum of a TiN microwave cavity with the DC voltage set to zero and with the cavity detuned from the mechanical resonance. From the theoretical fit (red line) we find internal decay rate $\kappa_i/2\pi = 520$ kHz and external decay rate $\kappa_e/2\pi = 800$ kHz. (b) The reflection spectrum of the cavity, biased at $V_{\mathrm{DC}} = 10$ V, as a function of the external magnetic field showing a signature of the mechanical mode at 5.087 GHz. (c) A cross-section of the data at (b), showing the reflection spectrum of the resonant microwave-mechanics system. The red lines depict theory fits to the microwave response. (d) The extracted coupling rates from microwave spectrum traces at different voltages, plotted for two devices. The zero-coupling voltage offset voltages for device A (B) is -0.36 V (-0.22 V). The 2σ error bars around the mean are extracted from the fit uncertainty. The data in parts (a-c) are taken with device A.

the absence of a voltage source, which may point to the work function difference between TiN/Si and trapped charges at the interface as its origin [106, 107].

4.4 Coherence Properties

We next investigate the coherence properties of our devices by exciting the mechanical resonator with a pulse and registering its free decay via electromechanical readout. In this measurement, the electromechanical readout rate is a function of the detuning between the mechanical and microwave resonances, $\Gamma_{\mathrm{em}} = g^2\kappa/(\Delta^2+(\kappa/2)^2)$. At any given detuning, the total decay rate of the mechanics is given by $\Gamma = \Gamma_i+\Gamma_{\mathrm{em}}$,

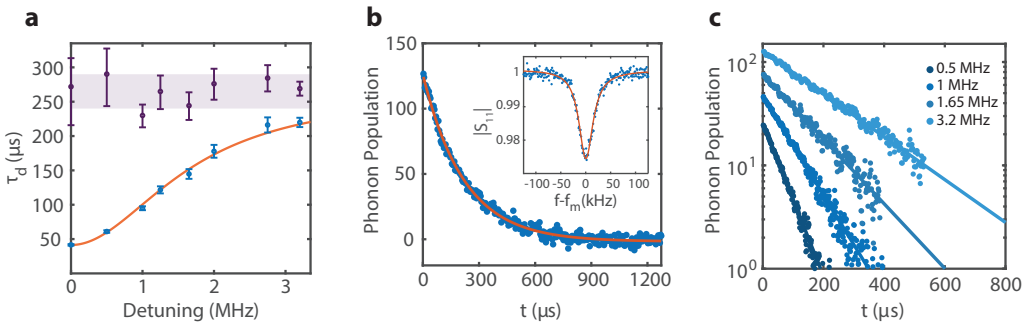


Figure 4.3: **Mechanical lifetime measurements**. (a) The total lifetime (τ_d) extracted from ringdown measurements for different mechanics-microwave detunings $\Delta/2\pi$ (blue points). The red line shows a theory fit, finding $\tau_{d,i} = 265 \pm 25\ \mu s$. The purple-shaded region indicates this range. The purple data points show $\tau_{d,i}$ found at each detuning by subtracting the contribution from the electromechanical readout. The presented data is extracted from fits of exponential decay, with 2σ errorbars representing the confidence interval. (b) Free energy decay (ringdown) data for the maximum detuning of 3.2 MHz. The fit finds a total lifetime of $220 \pm 6\ \mu s$. Inset: Mechanical spectrum measured at a probe power corresponding to a maximum of 4 phonons in the mechanical resonator. The theory fit gives a linewidth of 33 kHz, corresponding to $\tau_c \approx 10\ \mu s$. (c) Log-scale plots of phonon population vs. time for different initial phonon populations. All data is from device A with a DC voltage of 1.2 V.

where Γ_i is the intrinsic decay rate. In order to precisely measure Γ_i, we perform multiple measurements where we gradually increase Δ, leading to a gradual reduction in Γ_{em} until the total decay becomes dominated by the intrinsic part. Fitting the total decay rate expressed as a function of Δ, we extract an intrinsic lifetime of $\tau_{d,i} = 265 \pm 25\ \mu s$ (Fig. 4.3a), corresponding to a Q factor of 8×10^6. At the largest detuning we achieve, we can reach the regime where the intrinsic decay dominates the dynamics and obtain a total energy decay lifetime τ_d of $220 \pm 6\ \mu s$ (Fig. 4.3b), which strongly supports the large intrinsic lifetime inferred from the fits. We note that the measured mechanical lifetime is remarkably large for a device with compact geometry, corresponding to a quality factor that is more than two orders of magnitude larger than the state-of-the-art piezoelectric devices [36].

Apart from the energy relaxation lifetime, the coherence time of our mechanics bears significance for future quantum applications. We find the coherence time as the reciprocal of half the linewidth extracted from fitting the microwave spectrum in the large detuning regime ($\Delta >> \Gamma, \kappa$). Using this method, we find $\tau_c \approx 10\ \mu s$ (Fig. 4.3b), a value that is substantially shorter than the lifetime. This discrepancy

between the decay and coherence times hints at the presence of frequency jitter and has been previously observed in optomechanical experiments with silicon phononic crystal resonators. While the exact nature of this dephasing remains unknown, it has been hypothesized to be caused by interaction with the two-level system (TLS) defects [42, 96]. To better understand possible dephasing and decay sources, we carry out ringdown measurements for different numbers of phonons in the mechanical resonator. We change the mean intra-cavity phonon number by varying the drive pulse power, in accordance with the readout efficiency Γ_{em}/Γ, keeping the output detection powers nearly constant at the lowest levels detectable by our amplifiers to ensure we can reach the low-phonon regime while maintaining feasible measurement times. Interestingly, we observe exponential decay with no sign of power dependence down to the single-phonon level (see Fig. 4.3c). Although we do not find signatures of saturable loss (a common signature of a TLS bath) in this measurement setting, we find that the coherence and decay times change as a function of the applied DC voltage, providing potential evidence for the presence of TLS defects. This behavior is explored in further detail in the section "Interaction with Two-level Systems".

4.5 Probing the limits of parametric-enhancement

A naturally emerging question is about the maximum achievable rate of electromechanical interaction in our platform. This rate is set by the magnitude of the DC voltage that can be applied before the onset of any spurious heating or instabilities in the system.

We do not expect to see any significant leakage current passing through the devices because of the freezing of the charge carriers at low measurement temperatures. However, applying large voltages to the narrow-gap capacitors in our devices leads to strong electric fields, which may lead to ionization and dielectric breakdown [108]. We measure the leakage current through the transducer structures as a function of applied voltage. As evident in Fig. 4.4a, we see a leakage current (with a characteristic resistance of $\sim$ 500 GΩ) that is found to be dominantly caused by the cables in our measurement, bounding the actual leakage through the device to below the measurement sensitivity of our measurement. When increasing the voltage beyond 30 V, we observe an abrupt spike in the leakage current that was initially attributed to dielectric breakdown. However, imaging of our devices post-warm-up at the room temperature indicates that the sudden leakage is most likely due to the onset of pull-in instability, resulting in the shut-down of the capacitor gap

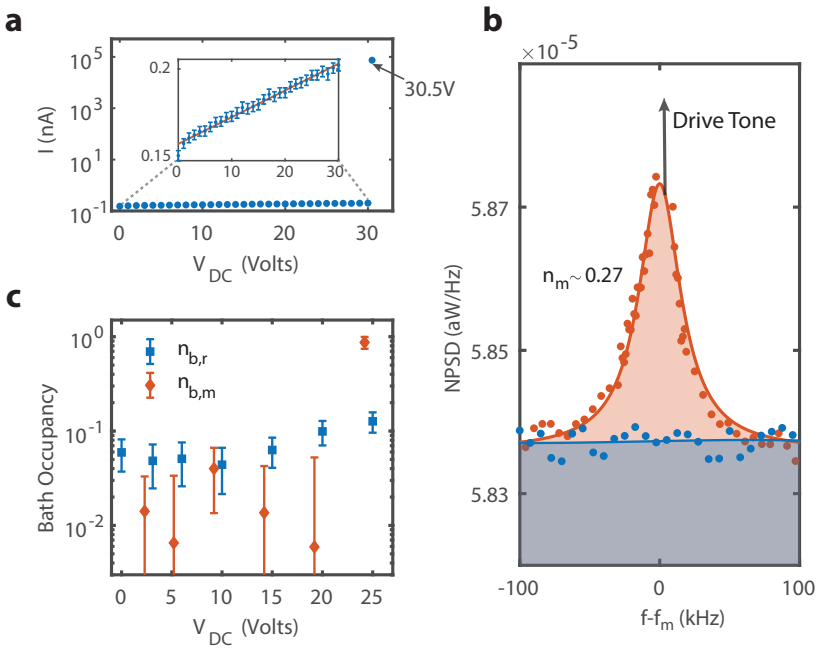


Figure 4.4: **Probing the limits of parametric-enhancement.** (a) The leakage current through the transducer as a function of the applied voltage, measured with a picoammeter. Errorbars are too small to be visible. Inset: A zoomed-in view of the data for the range 0-30 V, with a line fit to a 500 GΩ resistance. The data presented as the mean of 400 measurements for each voltage point, with 2σ errorbars. (b) The driven response of the mechanics at 3.1 V (red points) detected by a spectrum analyzer. The solid line shows a fit to a Lorentzian response. The mechanical resonator is populated due to the inelastic scattering of the drive tone. The mean phonon number is $n_{\mathrm{m}} = 0.27$. The detected emission from the mechanical resonator at 15 V in the absence of the drive (blue points). The background level is set by the added noise from our amplifier chain. (c) The extracted mechanics ($n_{\mathrm{b,m}}$, red points) and microwave bath ($n_{\mathrm{b,r}}$, blue points) occupancy as a function of the applied voltage. We have added a small horizontal offset between the two data sets for greater visibility. The presented data is extracted from theory fits of the power spectral density, with the 3σ error bars extracted based on power fluctuations. All data is from device A.

(see Section 4.9). Repeating this experiment on four identical test devices, we find the onset of this instability in a consistent range (29-31 V).

To probe the signatures of any potential heating under strong electrostatic fields (such as those observed in similar devices with radio-frequency drives [79]), we perform thermometry [18]. The thermometry measurement process for the mechanical resonator is visualized in Fig. 4.4b. We drive the system with a weak tone and measure the incoherent emission from the inelastic scattering of the drive to locate

the mechanical resonance (see Appendix A.4) [109]. A subsequent measurement with no drives shows a negligibly small emission, which is calibrated in experiments with long averages to extract the resonator's occupation. We have found the system of mechanics-microwave to be in the quantum ground state for the entire range of applied voltages in our device (0-25 V). Despite observing no heating, we note that the presence of strong electromechanical cooling (for the mechanical mode) and radiative cooling through the on-chip waveguide (for the microwave cavity) may mask a weak heating process. To find a more sensitive trace of any potential heating, we perform thermometry in a regime where the microwave cavity is detuned far away from the mechanical resonator to reduce the effect of electromechanical cooling and deduce the temperature of the phenomenological intrinsic baths that the mechanical and microwave resonators interact with (see Appendix A.4 for details). Figure 4.4c shows the measured microwave ($n_{\mathrm{b,r}}$) and mechanical bath occupancy ($n_{\mathrm{b,m}}$) as a function of the applied DC bias. As evident, the baths remain in the ground state for a large voltage range, without any sign of heating except for the mechanical bath at 25 V, where the occupancy rises to 0.86 ± 0.08 phonons (attempts to do measurements at higher voltages were unsuccessful due to the onset of the pull-in instability). The slightly higher occupation of the microwave bath across all voltages (including 0 V) is likely caused by the absence of IR shielding in our measurement setup, which leads to the generation of quasiparticles, and can raise the microwave bath temperature in devices with a large kinetic inductance [110, 111]. Regardless, despite the observation of these subtle features testifying to the accuracy of our measurement technique, we do not observe any indication of significant heating in the mechanical resonator or the microwave cavity for a wide range of voltages, which is a promising feature of our electrostatic driving scheme.

4.6 The Strong-Coupling Regime

Having discovered the safe range of voltages we can apply to our devices, we investigate the maximum electromechanical coupling rate within reach. For this purpose, we use device B, which has a larger g_0. Setting the external voltage to 25 V, we sweep our microwave frequency by changing the external magnetic field, which gives rise to an avoided crossing feature between the microwave and mechanics as seen in Fig. 4.5a. Fitting the frequencies of the two hybridized modes, we extract a parametrically-enhanced electromechanical coupling rate of $g_{\mathrm{em}}/2\pi = 1.08$ MHz. This value corresponds to $g_0 = 42.7$ kHz/V which matches the values we have calculated at low voltages, indicating that the parametric enhancement scales linearly

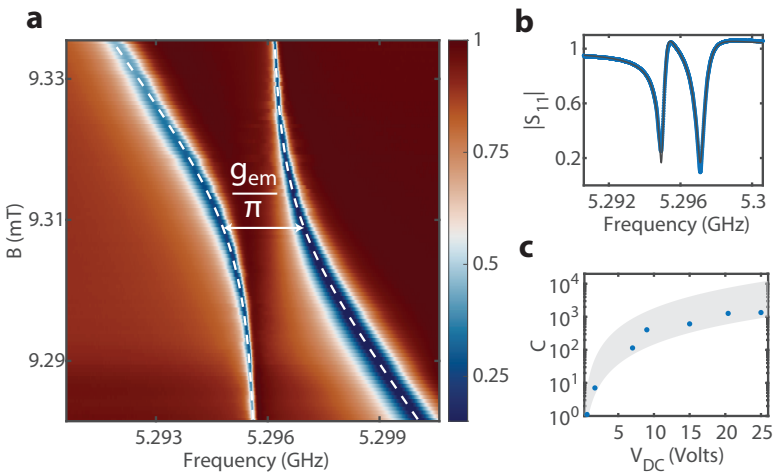


Figure 4.5: **Demonstration of strong-coupling regime.** (a) Measured reflection spectrum showing avoided crossing between the mechanical mode biased at $V_{\mathrm{DC}} = 25$ V and the microwave cavity tuned with a magnetic field. The theory fit (dashed lines) gives a parametrically-enhanced coupling rate of $g_{\mathrm{em}}/2\pi = 1.08$ MHz. (b) A cross-section of the data in (a) shows the splitting between the two hybridized modes on resonance. The black solid line is a theory fit that includes the Fano effect accounting for the observed asymmetry. (c) The electromechanical cooperativity was measured at different voltage values. The intrinsic decay rates are obtained by ringdown measurements. The grey-shaded region shows the range of cooperativity values calculated using the maximum values of couplings and lifetimes measured in different devices. The data points in all parts are taken with device B.

with voltage in the entire measurement range. Reaching the strong-coupling regime is manifested clearly in the measurements of the reflection spectrum at resonance, where we see a pair of hybridized modes with linewidths of $(\kappa + \gamma)/2 = 692$ kHz, satisfying $2g_{\mathrm{em}} > \kappa + \gamma$ (Fig. 4.5b). Achieving the strong-coupling regime in our system is significant as it allows the coherent exchange of phonons and microwave photons, a prerequisite for utilizing electromechanical systems in a range of quantum applications. Another key figure of merit in coupling mechanical modes to qubits and microwave resonators is cooperativity, defined as the ratio of the electromechanical readout rate to the intrinsic mechanical decay rate $C = 4g_{\mathrm{em}}^2/(\kappa_i\Gamma_i)$. We use the measured electromechanical coupling rates and the mechanical intrinsic decay rates (from the ringdown measurements) to find the cooperativity as a function of bias voltage (see Fig. 4.5b). For the maximum voltage value of 25 volts, we find $\Gamma_i/2\pi = 4.8$ kHz ($\tau_{\mathrm{d}} = 33\ \mu s$), corresponding to a cooperativity of 1270 (see Appendix A.4). As a guide, we also mark the values of cooperativity assuming the maximum coupling rates and lifetimes measured across different devices on the

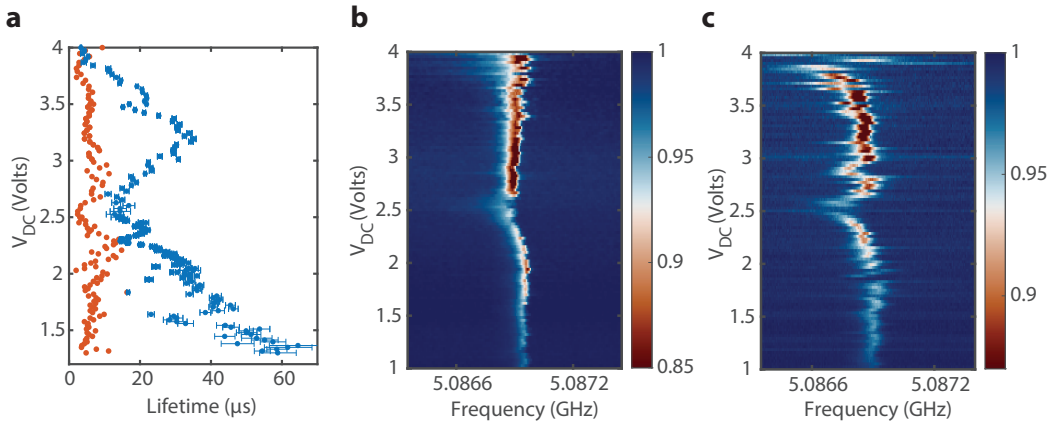


Figure 4.6: **Interaction of the mechanical resonator with the TLS bath**. (a) The measured decay time (τ_d, blue data points) and reciprocal of linewidth ($\tau_c/2$, red data points) were measured as a function of bias voltage. The probe power level is set to -39 dBm. The data is obtained from theory fits with the 2σ errorbars representing parameter confidence interval. (b) The mechanical reflection spectrum at a probe power of -40 dBm. (c) The measurement in part (b) repeated with a probe at -52 dBm power. Probe powers at 2.5 V are reported as a reference. For each voltage point, the power level is adjusted to retain the intra-cavity phonon number in the range 500-3000. All data is from device A.

same plot, finding estimates that exceed 10^4 at 25 V.

4.7 Interaction with Two-level Systems

As noted earlier, we suspect that the mechanical dephasing in our measurements can be attributed to coupling to TLS, which is previously shown to be the dominant loss mechanism for acoustic resonators with substantial surface participation at millikelvin temperatures [42, 45]. Modeled phenomenologically as two nearly-degenerate energy configurations of electrons in amorphous materials, a TLS manifests as a resonant defect with both electrical and acoustic susceptibilities [112, 113]. Using previous theory work as a guide [114] and extracting the spatial distribution of the strain field from FEM numerical modeling, we estimate the spectral density (3/ GHz) and the coupling rate (13 MHz) of individual TLS defects to the nanomechanical resonators in our system. The large coupling rate and the small density suggest a departure from the continuum TLS-bath picture observed in the past work [115, 116], and offers the possibility of observing mechanics-TLS interactions at the individual defect level.

To make this observation, we take advantage of the TLS frequency tuning via the Stark shift [117] from the electrostatic bias in our system (estimated to create TLS

frequency shifts at a rate of 20 GHz/V). Figure 4.6a shows the measured decay and coherence times as a function of voltage, manifesting strong modifications indicative of interaction with TLS defects. Further, we make a measurement of the mechanical spectrum as a function of voltage, observing abrupt frequency shifts (in form of avoided crossings) commensurate with the changes in the coherence and decay times. Finally, by comparing measurement results at two probe powers, we see a saturation behavior in the vicinity of the voltage values where the mechanical mode is heavily affected by TLS (see Fig. 4.6b,c). A more detailed measurement of mechanical linewidth as a function of phonon number at these points provides a good fit to the widely used TLS model. We present additional data demonstrating TLS saturation with power and cryostat temperature in Section 4.9.

4.8 Conclusions and Outlook

In conclusion, we present an integrated cavity electromechanical system capable of achieving MHz-level coupling rates at a mechanical frequency of several GHz. Using this system, we demonstrate electromechanical interaction in the strong coupling regime, with cooperativity exceeding 1200. Relying on an electrostatic driving field, we are able to obtain a large parametric enhancement of the interaction with negligible parasitic heating, leading to operation in the quantum ground state. Device fabrication is performed using a TiN-on-SOI material system, which is compatible with superconducting qubits and optomechanical crystals. Additionally, by relying on thin films and single-crystalline silicon, we are able to show mechanical quality factors above 8 million, corresponding to two orders of magnitude improvement over piezoelectric devices in similar geometries [36, 97]. Finally, we note the material-agnostic nature of the underlying process in our experiment, which holds the potential for adoption in platforms hosting spin qubits [118].

Looking ahead, we envision several avenues for further improvement of the presented devices. The electromechanical coupling rates can be readily increased by multiple folds upon integration of electrostatic transducers with microwave cavities with ultra-high impedance [104, 119], reaching full parity with piezo-electric platforms. Additionally, while we observe record-long lifetimes in devices with electrical connectivity, our measurements remain much shorter than the second-long results from optomechanical experiments in silicon structures with no metallic components [42, 96]. This observation motivates a systematic study of the sources of residual acoustic loss, including the role of metallic components, fabrication disorder in the acoustic shields, and two-level-system defects. A better understanding of the loss mecha-

nisms along with the implementation of proper mitigation techniques is expected to lead to longer mechanical lifetimes. With moderate improvements, achieving the millisecond regime is expected to be within reach in near future, with the potential to deliver transformative impacts on mechanics-based microwave-optical interconnects [50, 95], error-protected bosonic qubits [11], and quantum memories [12, 120].

4.9 Methods

Fabrication

A 4-inch silicon on insulator (SOI) wafer is utilized at the beginning of the fabrication process, and is covered with $\sim$ 15 nm TiN films via sputtering [121]. Following sputtering, the wafer is diced into 1×1 cm^2 dies. For the following steps the patterning of the structures is achieved by electron beam lithography. (i) Deposition of niobium markers followed by lift-off. (ii) Inductively coupled plasma - reactive ion etching (ICP-RIE) of TiN and Si with SF_6/Ar and SF_6/C_4F_8 chemistry. These etching steps are used to define the capacitor vacuum gap, phononic crystal nanobeam, phononic shields, and the release holes throughout the metalized and bare sections of the Si membrane. The devices are released with Hydrogen Fluoride (HF) post-fabrication.

Device Parameters

As part of our experiment we have fabricated and extensively characterized two devices. The parameters obtained from the measurements are described in Table 4.1. Based on these parameters, we select different devices to exhibit specific features of our platform. Due to its larger electromechanical coupling strength, device B can enter the strong coupling regime and attain large cooperativities above 1000. On the other hand, device A has the longest energy decay lifetime we have observed in our platform and is well suited to demonstrate the substantial lifetimes that can be achieved with our devices. Furthermore, as it requires less frequency tuning (due to a smaller mechanics-cavity detuning at zero magnetic field), we are able to measure it at a lower temperature (20 mK), where the heating due to the current on the coil is minimized, which makes it more suitable to perform sensitive thermometry measurements and investigate TLS physics without thermal saturation of TLS.

Table 4.1: **Summary of device parameters.** The referenced maximum decay lifetime and the coherence time are at the few-phonon level.

Parameter	Device A	Device B
$\omega_m/2\pi$ (GHz)	5.087	5.296
$\omega_r^{\max}/2\pi$ (GHz)	5.096	5.483
$\kappa_i/2\pi$ (kHz)	520	775
$\kappa_e/2\pi$ (kHz)	800	490
$g_0/2\pi$ (kHz/V)	22.0	45.4
$\tau_{\mathrm{d}}^{\max}$ (μs)	265	77
$\tau_{\mathrm{c}}^{\max}$ (μs)	16	4
$\mathrm{T_{MXC}}$ (mK)	20	90

Microwave Resonator

The $\lambda/4$ tunable microwave resonators in our work are formed by ICP-RIE etching of TiN films ($t \sim 15$ nm) with a sheet kinetic inductance of 40 pH/□ [1], which are sputtered on high resistivity (> 3 kΩ.cm) SOI substrates (device layer thickness 220 nm, manufactured by SEH). The high kinetic inductance TiN films are chosen for two main reasons: (i) obtaining a large impedance ($Z = \sqrt{L/C}$) resonator in order to enhance the electromechanical interaction ($g_{\mathrm{em}} \propto \sqrt{Z}$) and (ii) attaining a high degree of tunability via an external magnetic field to bring the microwave into resonance with mechanics. These goals are satisfied by forming a $\lambda/4$ resonator, with the inductive component realized by a nanowire. The total kinetic inductance in this structure is a function of film properties and geometry

$$L_{\mathrm{k}} = L_{\square}\frac{8}{\pi^2}\frac{l}{w}, \tag{4.2}$$

where $L_{\square}$ is the sheet inductance, l is the nanowire length and w is the nanowire width. In order to maximize the impedance, we etch our nanowires to be as narrow as possible, which in our case corresponds to a width of approximately 110 nm. Attempts to reduce wire width below this number led to reduced repeatability in fabrication and a large disorder in resonator frequency.

[1] The unit H/□ (Henry per square) captures the dependence of inductance to the number of squares in a wire. For a wire of length l and width w, the number of squares equals l/w.

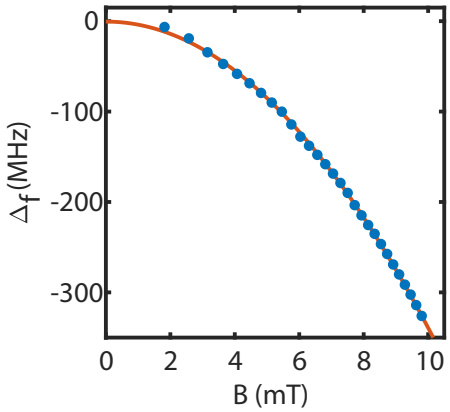


Figure 4.7: **Microwave frequency tuning.** Change in the microwave resonance frequency based on the applied external perpendicular magnetic field. The solid line is a parabolic theory fit.

A current passing through a TiN nanowire modifies the kinetic inductance in a nonlinear fashion

$$L_{\mathrm{k}}(I) = L_{\mathrm{k}}(0)\left[1 + \left(\frac{I}{I_*}\right)^2\right], \tag{4.3}$$

where I_* is the critical current of the nanowire. Patterning of the nanowires to form closed loops and application of an external perpendicular magnetic field, provides a 'wireless' means of modifying the kinetic inductance via the screening current induced through the loops [95]. This is the mechanism we us to tune the resonator's frequency.

With these principles in mind, we utilize a ladder-like topology for our microwave resonator. Finite-element method (FEM) simulations indicate that our kinetic inductance excellently matches Eq. (4.2) and we have negligible geometric inductance, leading to a kinetic inductance participation ratio of approximately unity ($> 98\%$). Furthermore, we calculate the impedance of our resonator to be 2.5 kΩ. The calculated lumped element equivalent circuit parameters for the microwave resonator of device B can be seen in Table A.1. Despite having a substantial impedance, due to our mechanical capacitance being very small, we have a low electrical energy participation ratio for the mechanical capacitor ($\eta = C_{\mathrm{m}}/(C_{\mathrm{m}} + C_{\mathrm{r}})$) of 1.5%. This small participation ratio permits us to connect multiple electromechanical capacitors to our microwave resonator.

Following fabrication, we find the resonance frequencies in good agreement with the device modeling, with a random offset with an approximate mean value of 300

MHz, which we attribute to fabrication disorder in the narrow nanowires. We test the tunability of our devices by applying external magnetic fields via currents passing through a superconducting coil mounted on top of the sample box. For small fractional shifts (normalized to the original frequency), we expect the frequency shift to be given by

$$\Delta_f = -kB^2, \tag{4.4}$$

where k is a device dependent proportionality constant and B is the external perpendicular magnetic field amplitude [95]. This parabolic dependence is verified for device B on Fig. 4.7. We can tune our device by about 6% of their resonance frequency without causing any substantial degradation of the microwave intrinsic quality factor beyond $\kappa_i/2\pi \sim 500$ kHz.

Purcell Filter

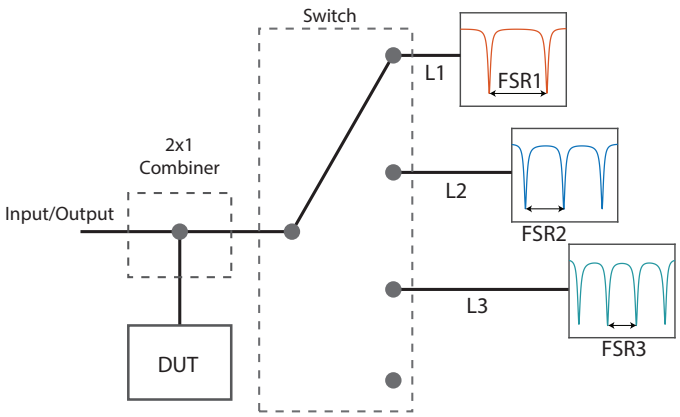


Figure 4.8: **Purcell filter.** Circuit diagram of the Purcell filter configuration. The input/output line is attached to a circulator (not shown in the figure) used for investigation of the devices in reflection mode. The final port of the switch is not connected to a transmission line. The transmission lines have different lengths (L1,L2,L3). Their response is depicted as Lorentzian resonances separated by a given FSR that differs for each cable. DUT: Device under test.

In our design, we prioritize redundancy in terms of the number of mechanical resonators by attaching four electromechanical capacitors to a single microwave resonator. This is done to mitigate the impact of frequency shifts caused by fabrication disorder of the microwave resonators, where the different mechanical resonators span roughly 500 MHz (the disorder in the mechanical frequencies is much smaller than the microwave disorder). However, this approach leads to an increased capacitance between our microwave resonator and the CPW, which gives rise to undesirably

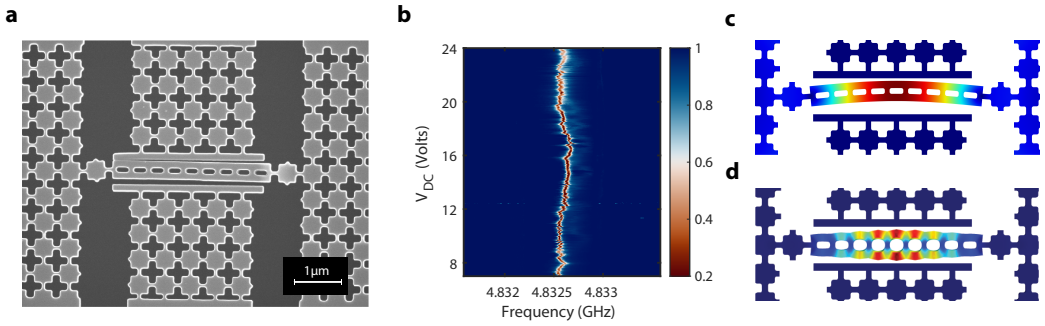


Figure 4.9: **Pull-in instability.** (a) Post-measurement SEM image of a transducer device that had permanently broken down. The pull-in phenomenon can be observed at the top-left corner of the electromechanical capacitor, where the vacuum gap has become shut. (b) Mechanical power spectrum with the cavity populated to 10^5 phonons with a strong drive (10^5). The pull-in voltage for the measured device is measured to be around 30 V. (c) Displacement profile of the 120 MHz first order beam mode. (d) Displacement profile of the 5 GHz breathing mode that takes part in the electromechanical interaction.

large external microwave decay. In order to increase the cooperativity of our system and reach the strong-coupling regime, this decay channel has to be suppressed.

We utilize an off-chip Purcell filter for this purpose as depicted schematically in Fig. 4.8. We place the filter in parallel to our device, where the notch filter reduces the external coupling strength of the microwave resonator. For this purpose, we make use of home-built microwave filters, realized as open transmission lines with a multi-pole spectrum. To get approximate frequency matching between our devices and the filter, we use a mechanical switch that enables us to choose among multiple filters with different free spectral ranges (FSR) between 200-500 MHz. In cases where we get perfect frequency matching between a device and a filter resonance, we can reduce the external decay rate $\kappa_e/2\pi$ to sub-200 kHz levels. Furthermore, we have a port in our switch which is not connected to a transmission line, permitting us to effectively turn our filter off.

Pull-in Instability

Post-measurement imaging of the devices which were subject to breakdown indicates that the breakdown behavior is caused by the pull-in of the inner electrode to an outer electrode, as seen in Fig. 4.9. Once the capacitor gap becomes shut, a short resistive leakage path appears, leading to substantial current flow as observed in our leakage current measurements. This 'pull-in' phenomenon is commonly observed in electrostatic actuators. As the bias voltage is increased, the strong electrostatic

forces can no longer be offset by the mechanical spring force following a certain gap shrinkage, leading to unstable mechanical dynamics [122]. Furthermore, stiction can render this phenomenon irreversible as we have observed, where removal of the external voltage does not lead to recovery of the device.

In the canonical model of an electrostatic transducer, increasing the bias voltage is accompanied by a continuous shrinkage of the gap, and, consequently, a frequency reduction due to the change in the spring constant [123]. We have measured the frequency of the mechanical mode as a function of the bias voltage (see Fig. 4.9) and fit the frequency dependence on voltage to a quadratic function, obtaining a shift coefficient of 0.5 ± 4.7 Hz/V^2, indicating the absence of significant voltage-dependent frequency shift. This absence of significant frequency shifts can be potentially attributed to the multimode nature of our device. In a canonical parallel plate transducer model, the device supports a single mechanical resonance, which experiences a frequency shift as a result of the electrostatic force from the bias. However, in our device, the displacement caused by the electrostatic force most likely follows the mode profile of the fundamental bending mode (see Fig. 4.9c) of the nanobeam whose frequency is approximately at 120 MHz ($k_{\text{eff}} \sim 2 \times 10^5$ N/m). In comparison, the 5 GHz breathing mode utilized in our experiment (see Fig. 4.9d) is much stiffer ($k_{\text{eff}} \sim 8 \times 10^7$ N/m). Therefore, the change in the breathing mode frequency needs to be modeled by considering a displacement profile dictated by another mode at a vastly different frequency.

Ringdown Measurements

In performing the ringdown measurements, we use a constant DC bias at a selected voltage level and control the electromechanical readout rate via setting the detuning between the microwave resonator and the mechanics. We populate the mechanical cavity via sending microwave pulses resonant with the mechanical mode. The pulses are synthesized with an arbitrary waveform generator (AWG), and their length is chosen to be sufficiently long to ensure the mechanical population can reach the steady state. Following the drive pulse, we detect the emitted power in a given interval by processing the downconverted signal from a digitizer. A power measurement (as opposed to field-quadrature) is obtained by summing the square of the demodulated I and Q quadrature values in a detection window in an FPGA. This detection window length is set to be much shorter than the reciprocal of mechanical linewidth to ensure we detect all the phonons emitted from the resonator. The multiple consecutive detection windows during a single measurement gives us a

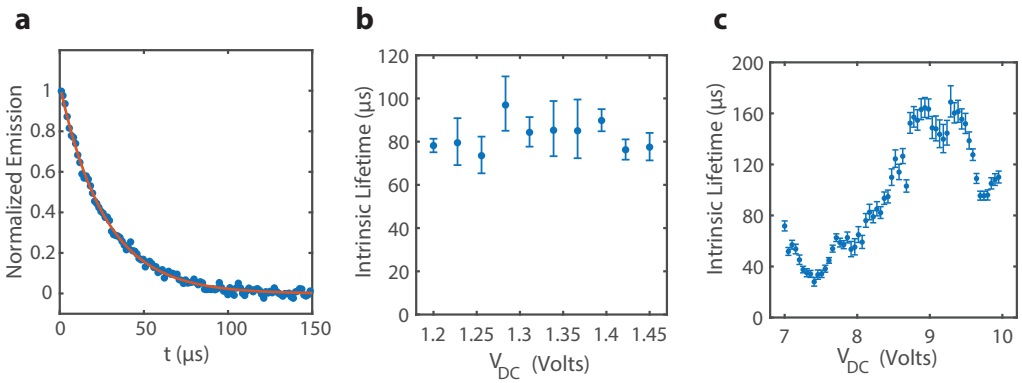


Figure 4.10: **Mechanical Lifetime.** (a) Typical ringdown with an intrinsic lifetime of $\sim 30\ \mu$s. (b) Intrinsic lifetime vs voltage for device A with around 1000 phonons inside the cavity. (c) Intrinsic lifetime vs voltage for device B with around 3000 phonons inside the cavity.

ringdown curve. We then proceed to average many instances of the experiment to improve our signal-to-noise (SNR) ratio and obtain our final data. The AWG, digitizer, and FPGA functionalities are realized using a Quantum Machines OPX+ module. We calibrate the digitizer output using the calibrated gain of our output lines and refer the detected voltage levels to the number of phonons in the cavity.

We carry out multiple ringdowns while sweeping the voltage to find the optimal lifetime in a voltage range. These ringdowns are performed at a large number of phonons in order to improve the SNR and make the measurements more tractable. Apart from showing signatures of spectral collisions with TLS that are manifested as deteriorating lifetimes, these measurements enable us to extract statistics about our lifetimes. We can see that for the two devices we have measured, we can reliably obtain lifetimes around 30 μs by slightly optimizing our voltage level. Such a typical ringdown is visualized in Fig. 4.10a. We can further see that the points where we have improved coherence properties do not exhibit extreme sensitivity to the applied voltage. For example, for the voltage value where we have obtained our best lifetime on device A, we can obtain similar lifetimes in a 250 mV range as shown in Fig. 4.10b.

We can see similar broad regions where the lifetime is enhanced for device B too, as depicted in Fig. 4.10c.

Mechanical Linewidth Characterization

The frequency jitter in our mechanical devices manifests itself as broadening in

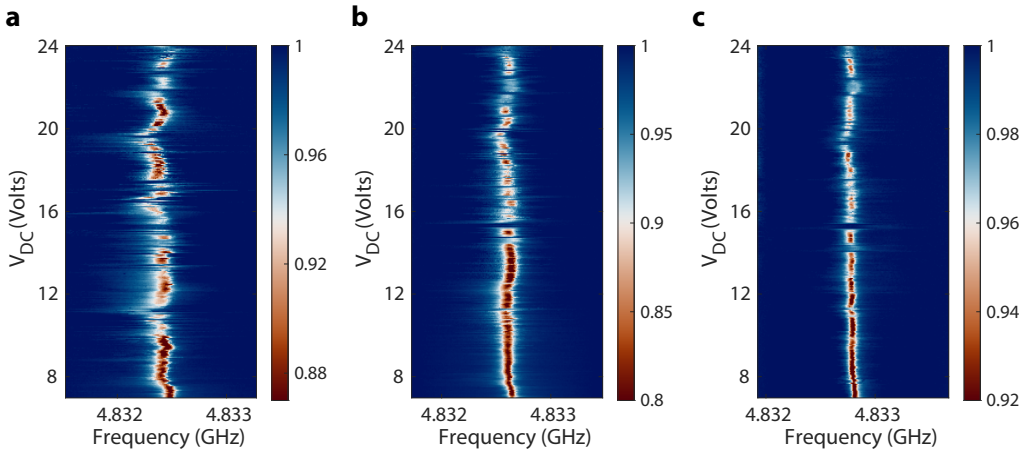


Figure 4.11: **Temperature saturation.** Mechanical reflection spectrum at (a) 30mK, (b) 425mK and (c) 850mK. The drive power level is kept constant.

reflection spectrum measurements. By investigating the dependence of the mechanical linewidth on power level, temperature, and external voltage bias, we can better understand the origin of the observed broadening. Similar measurements have been crucial in probing the loss mechanisms of linear microwave [124–127] and mechanical resonators [115, 116, 128].

To this end, we investigate the temperature dependence of our mechanical linewidth. As seen in Fig. 4.11, increasing the cryostat temperature leads to narrowing of the mechanical linewidth and the suppression of the frequency shifts. This temperature dependence can be attributed to frequency noise due to TLS defects (see Chapter 6).

We also explore the power dependence of our linewidth. We can populate our mechanical resonator with phonons by using a strong detuned pump. This pump probe scheme is chosen to investigate the mechanical linewidth at photon numbers beyond the onset of acoustic nonlinearity. Using a weak probe we can investigate the mechanical linewidth.

As seen in Fig. 4.12, the strong drive permits us to substantially saturate the frequency noise, reaching a mechanical linewidth on the order of 10 kHz at the highest phonon numbers. The combination of the power and temperature dependence of the linewidth is a strong indicator that TLS induced broadening dominates our total linewidth (see the detailed discussion in Chapter 6).

We observe a monotonic saturation behavior of the linewidth as seen in Fig. 4.12c.

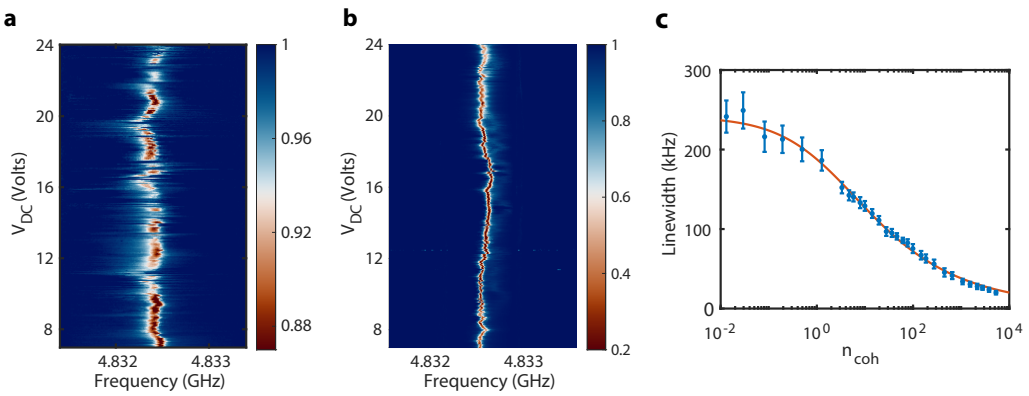


Figure 4.12: **Power saturation.** (a) Mechanical reflection spectrum at a probe power corresponding to 100s of phonons. (b) Mechanical reflection spectrum with a strong pump red detuned from the mechanics by $\sim$ 200 kHz. The pump populates the cavity to around 10^5 phonons. The probe power is identical to (a). (c) Dependence of linewidth on the number of coherent phonons for device B at 3 V. The solid line is a fit to the TLS model. Due to ambiguity in the phonon number inside the cavity for VNA measurements, we use the coherent phonon number n_{coh} in our fit (see thermometry section for this distinction). The data is obtained by Lorentzian theory fits, with the 2σ error bars indicating the confidence interval.

We can fit this data to a TLS model, with the total linewidth γ be expressed as [125]

$$\gamma = \frac{\gamma_{\mathrm{TLS}}}{\sqrt{1 + \left(\frac{n}{n_c}\right)^{\beta}}} + \gamma_0, \tag{4.5}$$

where n is the number of phonons inside the cavity, γ_{TLS} is the TLS limited linewidth, n_c is the critical phonon number, β is a fit parameter and γ_0 is the linewidth from power independent broadening mechanisms. Though the original expression is derived for decay rate of the oscillator, the dephasing can be described to have similar power dependence as well [129]. The fit gives us $\gamma_{\mathrm{TLS}} \sim 240$ kHz and $\gamma_0/2\pi \sim 10$ kHz, indicating that the saturable broadening dominates the total linewidth. The critical phonon number n_c is found to be 2. The parameter β is 0.6, on the order of unity as expected.

In summary our measurements demonstrate: (i) saturation of linewidth with temperature, (ii) saturation of linewidth with power, (iii) observation of random frequency shifts with external voltage bias. We believe that features (i-ii) can be most plausibly explained by saturation of two-level systems [113]. Furthermore, the randomness in the frequency shifts and broadening with voltage are reminiscent of observations of Stark shifts of two-level systems with external electric fields [117]. Therefore, we

believe these features are all consistent with two-level systems being the dominant broadening mechanism.

Beyond TLS, it is important to investigate other broadening mechanisms that may appear due to the large electrostatic fields involved in our experiment. The voltage source in our experiment has a noise magnitude of 200 μV. This noise can potentially lead to fluctuations in the mechanical frequency via the pull-in effect. Using the measured rate of frequency change from thermometry section, we obtain frequency fluctuations on the order of 40 mHz at the highest voltages, which is clearly much smaller than the observed mechanical linewidths. The voltage noise may also introduce fluctuations in the electromechanical readout rate due to the dependence of the coupling strength on the external voltage bias. However, the fractional variation of the fluctuation compared to the mean readout rate is estimated to be around 2×10^{-5}, also too small to play a significant role.

Finally, our experiment's large electrostatic field may lead to the displacement of atoms or trapped charges at the surfaces. However, any possible signatures of such an effect would scale directly with the external voltage (due to the increased electrostatic force). We do not see any global trend where the frequency jitter becomes worse with increased voltage in our data (see Fig. 4.12a). Additionally, we find the voltage-dependent changes in frequency and linewidth repeatable over measurements separated by large time scales (multiple days), which is not consistent with permanent dislocation of atoms or trapped charges [130].

Chapter 5

QUANTUM CONTROL OF MOTION BY A SUPERCONDUCTING QUBIT

Reproduced with permission from Springer Nature

A. B. Bozkurt, O. Golami, Y. Yu, H. Tian, and M. Mirhosseini, "A mechanical quantum memory for microwave photons", Nature Physics **21**, 1469–1474 (2025) 10.1038/s41567-025-02975-w,

Quantum mechanical phenomena are manifested in a wide variety of physical systems, encompassing electromagnetic waves, atoms, and excitations in solid-state matter. The distinct physical properties of these systems, naturally, translate into unique capabilities in sensing, processing, and communicating quantum signals. This insight has motivated the development of hybrid quantum systems, in which different degrees of freedom are combined to harness complementary functionalities [13, 131].

In particular, interconnecting microwave photons and phonons promises multiple opportunities [93]. Microwave photons strongly interact in superconducting quantum circuits, enabling gate operations critical for quantum computing [132]. These interactions, however, also lead to undesired environmental coupling, limiting the coherence times of microwave quantum systems [133]. In contrast, phonons can be well isolated from their environments due to their low propagation speed and the inability to propagate in vacuum [42–44]. However, the bosonic nature of phonons and the weakness of acoustic nonlinearities [22] pose significant challenges to achieving quantum control in purely mechanical systems. Interfacing phonons with microwave photons thus can exploit the inherent complementarity of these domains, combining the processing capabilities of superconducting qubits—a leading platform for quantum computing—with the exceptional storage ability of mechanical oscillators [11, 12, 120].

Interactions between microwave photons and phonons can be engineered by exploiting radiation-pressure forces or piezoelectric materials [23]. Though the radiation-pressure interaction is inherently weak, an electrostatic bias field can substantially enhance these forces, thereby opening a pathway for integrating mechanical oscil-

lators with superconducting qubits [27, 28, 31]. However, reaching strong coupling to a qubit at GHz frequencies—where mechanical oscillators can be passively prepared in their ground state—has remained elusive for this method [29]. On the other hand, deterministic exchange of microwave photons and phonons has been achieved in circuit quantum acoustodynamics (cQAD) systems [16, 33, 36], where superconducting qubits are coupled to piezoelectric mechanical oscillators. Despite the promise of this approach in exploring the fundamental physics of mechanical systems [37, 38], achieving long mechanical lifetimes has proved challenging, primarily due to the complexity of integrating pizeoelectric materials. Consequently, state-of-the-art cQAD systems can only obtain storage times that remain shorter than the best electrical systems [134–136].

Here, we present a device that extends mechanical energy storage times to an order of magnitude beyond those in superconducting qubits and planar microwave resonators. Our approach relies on the electrostatic enhancement of radiation-pressure force in nanoscale structures. By leveraging the material-agnostic nature of our approach, we fabricated mechanical oscillators entirely from single-crystal silicon, a non-piezoelectric material with exceptionally low mechanical loss [48]. We further suppress extrinsic dissipation through phononic band gap engineering to achieve an intrinsic mechanical quality factor of 0.8 billion ($T_1 = 25 \pm 2$ ms). Crucially, our system enters the strong coupling regime with a superconducting qubit, enabling deterministic operations on an ultralong-lived mechanical oscillator. This unprecedented access to qubit control and low mechanical dissipation allows us to probe the microscopic origins of mechanical decoherence and observe signatures of individual two-level-system defects. Moreover, we implement dynamical decoupling to mitigate dephasing, extending the mechanical coherence time ($T_2^* = 64 \pm 4\ \mu s$) via Hahn ($T_2^{\mathrm{E}} = 562 \pm 42\ \mu$s) and Carr-Purcell ($T_2^{\mathrm{CP2}} = 1.02 \pm 0.15$ ms) sequences.

These results mark a critical step towards employing mechanical oscillators as memory elements with a functional advantage for quantum information processing [11, 12, 120]. More broadly, our approach offers a route for extending quantum control to material platforms that harbor long-lived mechanical oscillators but lack a strong piezoelectric response (such as silicon nitride [44], strained silicon [92], diamond [137], and silicon carbide [138]). Investigating a wider range of materials, potentially via these techniques, will ultimately advance our fundamental understanding of mechanical decoherence [139] and may enable applications in quantum-enhanced sensing and transduction [8, 10, 140].

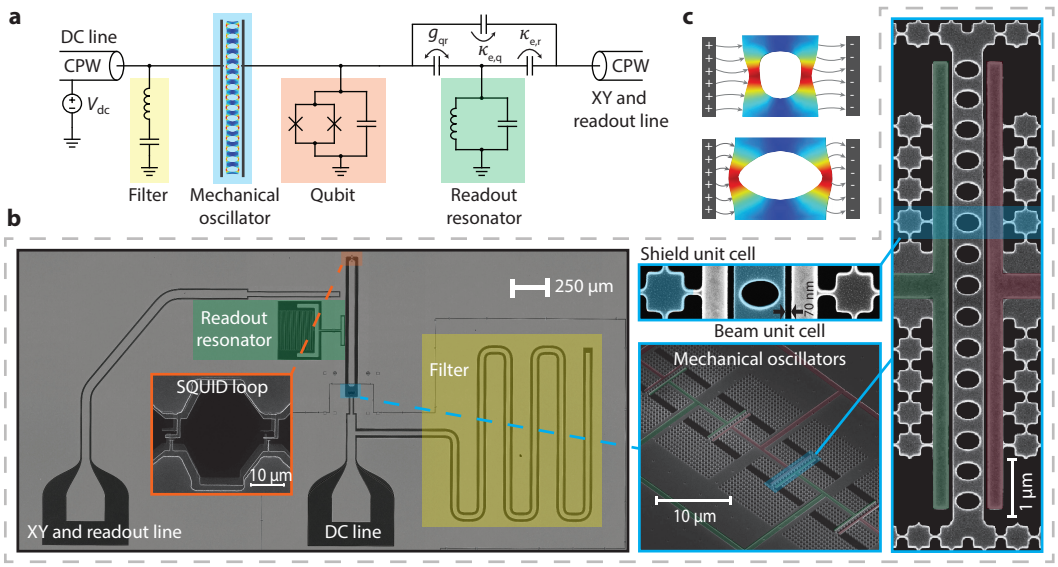


Figure 5.1: **Experimental setup. a,** Circuit diagram of the coupled qubit-oscillator system. **b,** False colored optical microscope image of the device, showing the SQUID loop of the transmon qubit (orange), readout resonator (green), filter (yellow), and mechanical oscillators (blue) alongside the coplanar waveguides (CPW) that deliver DC and RF signals. Insets: False-colored tilted scanning electron microscope (SEM) image of multiple mechanical oscillators, with the red (green) shaded electrodes attached to the qubit (DC line). SEM image of a single mechanical oscillator, with the blue shaded section showing a single phononic crystal unit cell, phononic shields, and the vacuum gap between the oscillator and the electrodes. **c,** Simulated displacement profile of a unit cell of the phononic crystal resonator, alongside an illustration of electric field lines between the electrodes and the nanobeam. The two images demonstrate the 'breathing' motion separated in time by half an oscillation period.

5.1 System Description

Our system consists of a transmon superconducting qubit that is galvanically connected to a mechanically compliant vacuum gap capacitor (see Fig. 5.1a). In this setup, a mechanical resonance can be formed within the capacitor by engineering the motional boundary conditions [69]. Applying an electrostatic field to the moving capacitor with an external source gives rise to an electrical dipole that oscillates with mechanical motion. This oscillating dipole interacts with the electric field from the qubit, giving rise to a coupled system described by the Hamiltonian

$$\hat{H}/\hbar = \frac{\omega_q}{2}\hat{\sigma}_z + \omega_m \hat{b}^\dagger \hat{b} + g_{em}\left(\hat{\sigma}_+ \hat{b} + \hat{\sigma}_- \hat{b}^\dagger\right). \tag{5.1}$$

Here, ω_q (ω_m) is the transition (resonance) frequency of the qubit (oscillator), σ_- ($\hat{b}$) is the qubit (oscillator) annihilation operator, and g_{em} is the electromechanical coupling rate, which depends on the external voltage bias ($g_{em} = g_0 V_{dc}$, see Section 2.2). When the resonance condition is satisfied (i.e, $\omega_q = \omega_m$), the electromechanical interaction enables the exchange of phonons and qubit excitations (i.e., microwave photons).

We implement this system on a silicon-on-insulator platform, where a planar transmon qubit is fabricated on a suspended membrane accommodating moving parts, as shown in Fig. 5.1b (for details, see Section 5.5). The moving capacitor is created by a pair of electrodes surrounding a phononic crystal resonator. We use finite-element modeling to optimize the geometry of the phononic crystal for maximum electromechanical interaction (see Section 3.3). Figure 5.1c shows the mechanical mode profile, where in-plane 'breathing' motion leads to the variations of the vacuum gap along the beam. Crucially, our capacitor design enables the detection of mechanical motion through near-field components of the electric field while avoiding mechanical energy within the metal electrodes (which have previously been identified as sources of considerable mechanical loss [45, 100]). The mechanical oscillator is also surrounded by phononic shields with a full band gap in the vicinity of the mechanical resonance to avoid clamping loss ([42], see Section 3.2). The compact design of the nanomechanical oscillators allows us to connect an array of them to a single transmon qubit. We utilize flux tuning by an off-chip magnet to precisely adjust the qubit frequency to resonance with only one mechanical oscillator while providing sufficiently large detunings to avoid interactions with the other oscillators in the array. We apply the electrostatic field to the moving capacitor via a coplanar waveguide. However, in this geometry, the qubit experiences radiative decay to the coplanar waveguide via the motional capacitance. To mitigate this parasitic effect, we integrate a notch-type microwave filter on the same chip engineered to reflect signals at the qubit frequency while remaining transparent to zero-frequency biasing fields (see Section 5.5). The qubit is also coupled to a microwave resonator for dispersive readout.

5.2 Qubit-Oscillator Interactions

We characterize the fabricated devices in a dilution fridge with a base temperature of 10 mK. With a voltage applied to the motional capacitance, we conduct spectroscopy as we slowly tune the qubit frequency. As shown in Fig. 5.2a, and b, this measurement reveals two avoided mode crossings, from which we extract

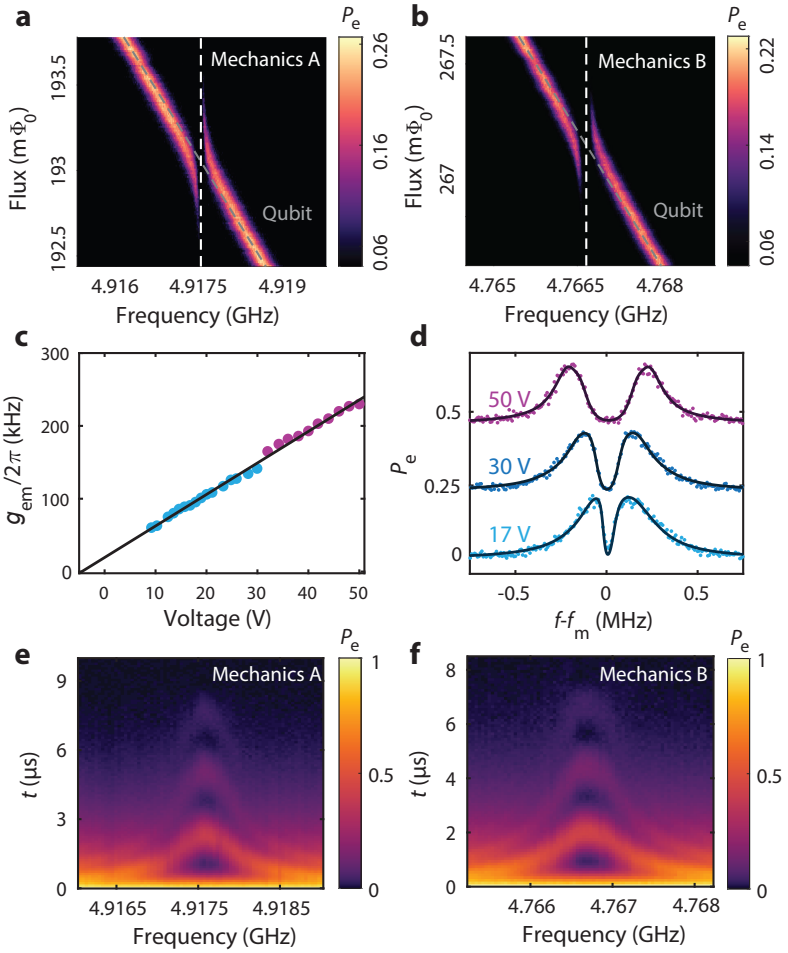


Figure 5.2: **Coherent qubit-oscillator interaction.** **a,** and **b,** Microwave spectroscopy of the qubit under flux tuning, exhibiting avoided crossings with oscillators A and B. Dashed lines indicate bare qubit and oscillator frequencies. **c,** The electromechanical interaction rate of device B as a function of the applied DC voltage (see Appendix B.3 for constraints on applied DC voltage), along with a linear theory fit. The blue (purple) data points are extracted from the spectroscopy (time domain) traces. **d,** Qubit resonant spectroscopy with mechanics B at different voltages, showing the transition from weak to strong coupling regime (with the measurements at 30 V and 50 V offset vertically for visual clarity). A fit to the measurement at 50 V provides the maximum interaction rates, $g_{\mathrm{em,A}}/2\pi = 200$ kHz (data not shown) and $g_{\mathrm{em,B}}/2\pi = 230$ kHz. **e,** and **f,** Qubit time dynamics exhibiting vacuum Rabi oscillations between the qubit and the oscillator. P_{e} is the qubit excited state population and Φ_0 is the flux quantum. The data presented in **a-b** and **e-f** is obtained at a voltage bias of 50 V.

the resonance frequencies of two mechanical oscillators ($\omega_{\mathrm{m,A}}/2\pi = 4.9176$ GHz and $\omega_{\mathrm{m,B}}/2\pi = 4.7667$ GHz) and the electromechanical interaction rates. The interaction rates scale linearly with the voltage bias (see Fig. 5.2c), in line with our

device modeling. Crucially, the interaction can be enhanced sufficiently to yield a pair of resolved hybridized modes at resonance (see Fig. 5.2d), marking the entry to the strong-coupling regime. We confirm operation in this regime by performing time domain measurements, where we observe vacuum Rabi oscillations (see Fig. 5.2e, and f). These oscillations demonstrate the coherent exchange of photons and phonons at the single quantum level, which is the basis for deterministic quantum control of the mechanical oscillator via the qubit.

Beyond strong interactions, quantum operations often require preparing mechanical oscillators in the quantum ground state. Although the cryostat temperature in our experiment is sufficiently low for this purpose ($\hbar\omega_\mathrm{m} \gg k_\mathrm{B}T_\mathrm{fridge}$), the strong electrostatic field at the device can potentially lead to an increased effective temperature via parasitic effects [29, 141]. To investigate these potential effects, we quantify the residual thermal populations of the qubit and mechanical resonator in our system using established thermometry methods [142]. These measurements (see Fig. 5.3a) yield small and comparable mode temperatures for the qubit (60 ± 2 mK) and the mechanical oscillator (72 ± 9 mK). Importantly, we observe no significant change in the qubit temperature in the absence of the bias voltage (62 ± 1 mK), effectively ruling out heating from the electrostatic biasing field.

The combination of strong qubit-oscillator interaction and ground-state operation in our system enables the preparation and measurement of non-classical motional states [34, 143]. For state preparation, we initially prepare the qubit in the desired quantum state and then transfer this state to the mechanical oscillator. Subsequently, we perform Wigner tomography by displacing the mechanical quantum state using a resonant drive and determining its parity through fits of qubit-mechanics Rabi oscillations (see Section 5.5). Figure 5.3b, and c display the phase-averaged tomograms for the mechanical oscillator when prepared in the ground state ($|0\rangle_\mathrm{m}$) and the single-phonon Fock state ($|1\rangle_\mathrm{m}$). We calculate the state preparation fidelity as 0.964 ± 0.007 and 0.711 ± 0.023 for these states, respectively. Notably, the Wigner distribution for the $|1\rangle_\mathrm{m}$ Fock state exhibits negativity, confirming the non-classical nature of this motional state. From master equation simulations, we identify qubit decoherence ($T_{1,\mathrm{q}} = 1.55\ \mu$s and $T^*_{2,\mathrm{q}} = 1.05\ \mu$s) as the primary source of infidelity (see Section 5.5).

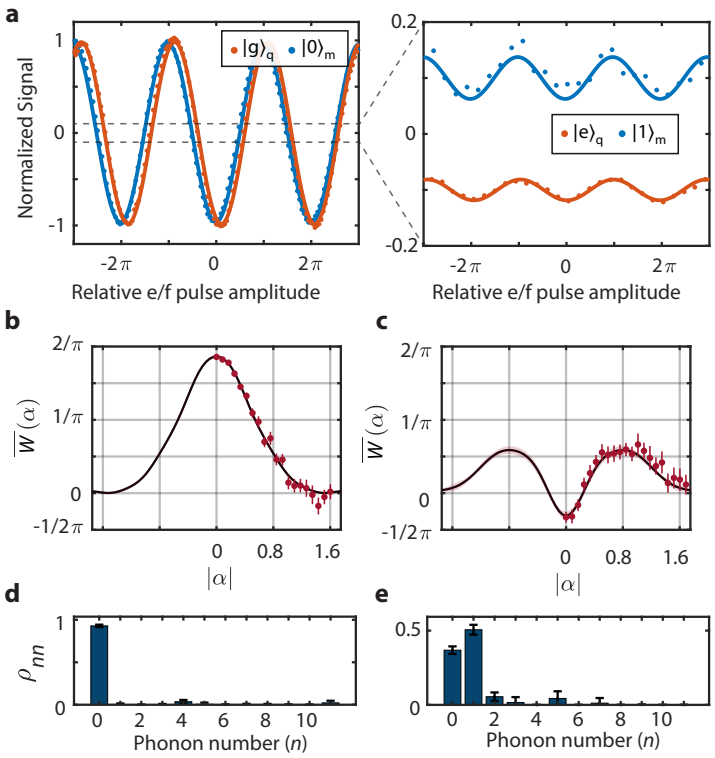


Figure 5.3: **Quantum state preparation and tomography. a,** The thermal population of the qubit's $|g\rangle_q$ ($|e\rangle_q$) level is measured through the amplitude of driven Rabi oscillations in the e-f manifold, as shown in the left (right) panel. For measuring the population in $|g\rangle_q$, we initiate the experiment with a g-e π-pulse (see Appendix B.4). The thermal population of the oscillator's $|0\rangle_m$ ($|1\rangle_m$) energy level is extracted from a similar experiment conducted via the qubit after performing a mechanics-qubit state swap, as shown in the left (right) panel. The data on the left (right) panel is offset horizontally (vertically) for better visibility. **b,** Phase-averaged Wigner tomogram of the mechanical oscillator prepared in the ground state and **c,** the single-phonon excited state, showing $\overline{W}(0) = -0.10 \pm 0.02$. Red data points are calculated by fitting the experimental data (see Section 5.5); the solid dark line denotes the reconstructed Wigner distribution function, with shaded area representing 2σ confidence interval of the numerical reconstruction. **d** and **e,** Diagonal elements of the reconstructed density matrix (ρ_{nn}) for the ground and excited mechanical states, respectively. The error bars in **b-e** represent the 2σ confidence interval obtained from theory fits. All the data is taken at 50 V using mechanics B.

5.3 Mechanical Decoherence

Next, we utilize the qubit as a probe for measuring mechanical lifetime. We begin by preparing the oscillator in a single-phonon Fock state ($|1\rangle_m$, as described previously), allow it to evolve freely for a variable time delay, and measure the remaining population through a swap operation with the qubit. For the oscillator A in our

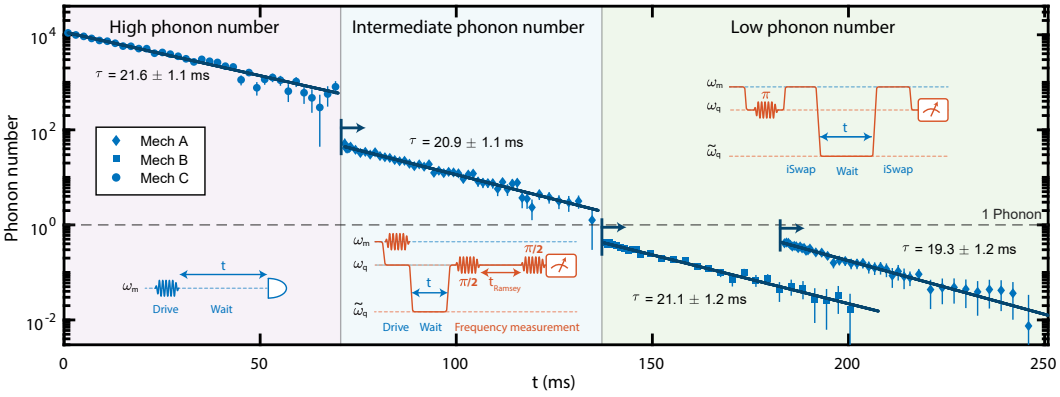


Figure 5.4: **Mechanical lifetime.** We employ three distinct measurement methods, highlighted by shaded areas, to capture decay time measurements across various phonon occupancy levels, with each trace offset in time for visual clarity. The data points represent the mean of ~ 400 measurements for each time instance, with error bars indicating 1σ standard error of the mean. The lifetimes obtained by exponential fits of the form $ae^{-t/\tau}$ are displayed for each measurement, with a 2σ confidence interval. For experiments in the range below 1 phonon, see the main text. For the experiment in the approximate range of 1-100 phonons (mechanics A), we employ the qubit as a phonon-number detector by operation in the dispersive regime [144, 145]. At the highest phonon number range, we measure an array of identical mechanical oscillators on the same chip (represented by mechanics C) with electromechanical readout through a directly connected microwave waveguide (see Appendix B.5). All measurements are conducted at a bias voltage of 40 V. Insets show the pulse sequences used for each measurement. For qubit-based measurements, we use a microwave tone for shifting the qubit's transition frequency away from the oscillator (via the ac Stark effect) to minimize the inverse Purcell decay [146]. For mech A, we characterize and subtract the small contribution from the inverse Purcell decay to find the intrinsic lifetime (25 ± 2 ms, see Appendix B.5).

system, we find an intrinsic lifetime of $T_1 = 25 \pm 2$ ms (see Fig. 5.4). This lifetime is remarkably long, more than two orders of magnitude beyond state-of-the-art circuit quantum acoustodynamics (cQAD) systems [36, 41, 147]. We further investigate the mechanical lifetime in our platform by conducting experiments on different devices and across a wide range of phonon numbers, finding consistent results in the same vicinity (see Fig. 5.4). Remarkably, the energy relaxation dynamics can be well explained by a single exponential decay, with no evidence of commonly observed degradation in the single-phonon regime [45, 148, 149]. We attribute the ultralong lifetimes and the absence of saturable loss to a low density of defects in crystalline silicon [80] and the suppression of phononic density of states in our device geometry [139] (see the analysis in Section 6.2).

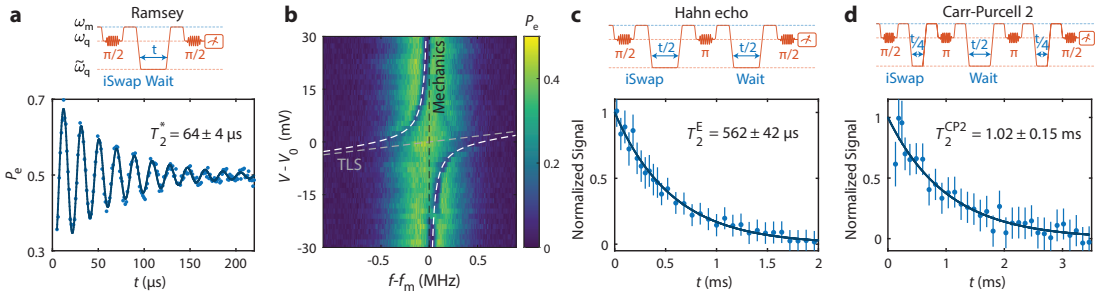


Figure 5.5: **Mitigating mechanical dephasing. a,** Ramsey free induction measurement of mechanical coherence. **b,** Spectroscopy measurements of the mechanics-qubit system as the voltage is varied, demonstrating an avoided crossing between the mechanical oscillator and a defect whose frequency is shifted with voltage. The white dashed lines are theory fits to the two avoided crossing branches with a TLS-mechanics coupling rate of $g_{\mathrm{TLS}}/2\pi \approx 0.5$ MHz. The grey dashed line is the bare TLS frequency with a frequency shift rate of ≈ 0.3 GHz/V. V_0 is the voltage at which the TLS and the mechanics are in resonance. Dynamical decoupling procedures in the form of **c,** Hahn echo measurement with a single refocusing pulse and **d,** Carr-Purcell (CP) measurement with two refocusing pulses. The data points in **c,d** represent the mean of $\sim$ 500 measurements for each time instance, with error bars indicating 1σ standard error of the mean. Dark lines for the coherence measurements (**a,c** and **d**) represent theory fits used to extract the coherence times and the top section demonstrates pulse sequences. The measurements are conducted on mechanics A at an applied DC voltage of 50 V.

Preserving phase coherence, in addition to minimizing energy decay, is a key requirement for storing quantum information. We characterize mechanical coherence within the Hilbert space spanned by the states $|0\rangle_{\mathrm{m}}$ and $|1\rangle_{\mathrm{m}}$ through a Ramsey sequence. In this experiment, the mechanical oscillator is initially prepared in a superposition state $(|0\rangle_{\mathrm{m}} + |1\rangle_{\mathrm{m}})/\sqrt{2}$ and allowed to evolve freely for a variable delay, before applying a $\pi/2$ basis rotation and population readout (preparation, manipulation, and readout performed via the qubit; see Fig. 5.5a). We observe that the Ramsey interferogram from this experiment decays exponentially with a time constant of $T_2^* = 64 \pm 4\,\mu$s. Although this coherence time is comparable to results in other mechanical platforms [35, 41], it is considerably shorter than the oscillator's measured lifetime in our system, pointing to significant dephasing.

Similar disparities between energy decay and coherence times have previously been observed in cavity optomechanics [42, 96], with interactions with TLS defects hypothesized as the underlying cause. We search for signatures of TLS by monitoring the mechanical resonance (via qubit spectroscopy) as we change the voltage bias.

Defects within the mechanical oscillator are expected to undergo Stark shift through interactions with the electrostatic field, enabling in-situ modification of the TLS spectral landscape [117, 150]. Remarkably, these measurements yield a discrete set of avoided mode crossings that collectively paint the picture of a sparse TLS bath (see Fig. 5.5b). From these measurements, we extract the spectral density and the statistical distributions of the deformation potential and dipole orientations, finding them to be in general agreement with the standard tunneling model [112] (see Section 5.5). Notably, we observe pronounced modifications of the mechanical frequency noise in the spectral vicinity of the identified defects, displaying the 'telegrapher' noise from individual defects (see Section 6.3). Collectively, these observations provide experimental evidence for the key components of the TLS-induced decoherence model.

Unlike energy loss, dephasing is, in principle, reversible by reversing a system's time evolution. Such dynamical decoupling operations [151] often require a nonlinear response, which in our setup is provided by coupling to the qubit [152]. Specifically, the oscillator state can be swapped into the qubit, where a refocusing π-pulse is applied on the qubit, and then swapped backed into the oscillator. This three-step sequence effectively implements a refocusing π-pulse on the mechanical oscillator. Figure 5.5c illustrates the control pulse sequence and the measured decay profile from such an experiment, where a refocusing pulse sequence (Hahn echo) is used to mitigate the frequency noise. As evident, the echo coherence time $T_2^{\mathrm{E}} = 562 \pm 42\,\mu$s is substantially longer than T_2^* indicating a "slow" dominant noise source [153]. Interestingly, we observe quantitative agreement between the measured improvement from the echo sequence and the predictions from the TLS noise model, suggesting that TLS defects are the dominant source of dephasing (see Section 6.3). Building on this approach, we implement a longer echo sequence (Carr-Purcell-2), further enhancing the coherence time to the millisecond level, $T_2^{\mathrm{CP2}} = 1.02 \pm 0.15$ ms (see Fig. 5.5d). With improvements in the fidelity of qubit-swap operations, even longer echo sequences can potentially extend the coherence time to the limits set by energy decay [154].

5.4 Discussion and outlook

Looking ahead, a natural next step would be attaining the strong dispersive regime, where universal quantum control can be extended to the large bosonic Hilbert space of the mechanical oscillator [155]. Achieving this goal requires significant improvements in the electromechanical interaction, which we anticipate to be within

reach by miniaturizing the capacitor's vacuum gap [156] and using superconducting qubits with large flux fluctuations [157, 158]. Alternatively, increased qubit coherence—achievable through flip-chip architectures [159, 160]—can relax the need for stronger interactions. Achieving operation in the strong dispersive regime would enable the encoding of bosonic qubits with biased noise on GHz-frequency mechanical oscillators, potentially leading to scalable architectures for fault-tolerant quantum computation [11, 161, 162].

5.5 Methods

Summary of device parameters

The experimentally characterized parameters of our device composed of the qubit, mechanical oscillators, and the readout resonator are listed in Table 5.1.

Fabrication

The devices are fabricated on a 10 mm × 10 mm, high-resistivity (> 3 kΩ.cm) silicon-on-insulator (SOI) chip with a device layer thickness of 220 nm [82]. The fabrication process consists of the following steps:

(i) Etching of the silicon device layer using inductively coupled plasma reactive ion etching (ICP-RIE) with the C_4F_8/SF_6 pseudo-Bosch process, to define mechanical oscillators, phononic shields, and release holes.

(ii) Electron-beam evaporation of aluminum for the DC line, electrodes of moving capacitors, and filter. This layer forms the metal over regions where strong electrostatic fields are present. Since the electrical behavior of the aluminum-silicon interface exhibits extreme sensitivity to surface properties [163], we perform this metallization layer before additional processing that alters the silicon surface (such as HF etch) for reliability purposes.

(iii) Aluminum evaporation to form the readout line, readout resonator, and transmon capacitor, preceded by a brief vapor hydrofluoric acid (VHF) etch.

(iv) Doubled-angle aluminum evaporation and oxidation to form the Josephson junctions, preceded by a short VHF etch.

(v) Ion milling to remove the oxide on aluminum, followed by aluminum bandage evaporation in order to: (a) connect the Josephson junctions to the transmon capacitor and (b) ensure electrical connectivity between layers (ii) and (iii).

(vi) A longer VHF etching to remove the buried oxide layer which partially suspends the device.

Parameter	Value	Description	Component
$\omega_{\mathrm{q}}^{\mathrm{max}}/2\pi$	5.1071 GHz	maximum frequency	transmon
$\alpha_{\mathrm{q}}/2\pi$	226 MHz	anharmonicity	transmon
$\omega_{\mathrm{r}}/2\pi$	7.283 GHz	resonance frequency	readout resonator
$\chi_{\mathrm{qr}}/2\pi$	450 kHz	dispersive shift	transmon-readout resonator
$\kappa_{\mathrm{e,q}}/2\pi$	7 kHz	external decay rate	transmon
$\kappa_{\mathrm{e,r}}/2\pi$	1.9 MHz	external decay rate	readout resonator
$\omega_{\mathrm{m}}/2\pi$	4.9176/4.7667 GHz	resonance frequency	mechanics A/B
$g_{\mathrm{em}}/2\pi$	200/230 kHz	electromechanical interaction rate	mechanics A/B
$T_{1,\mathrm{q}}$	1.70/1.55 μs	lifetime	transmon
$T_{2,\mathrm{q}}^{*}$	1.30/1.05 μs	Ramsey coherence time	transmon
$T_{1,\mathrm{m}}$	$19.3 \pm 1.2/21.1 \pm 1.1$ ms	lifetime	mechanics A/B
$T_{2,\mathrm{m}}^{*}$	$64 \pm 4/67 \pm 5$ μs	Ramsey coherence time	mechanics A/B
$T_{2,\mathrm{m}}^{\mathrm{E}}$	$562 \pm 42/268 \pm 23$ μs	Echo coherence time	mechanics A/B
$T_{2,\mathrm{m}}^{\mathrm{CP2}}$	$1.02 \pm 0.15/0.54 \pm 0.11$ ms	CP2 coherence time	mechanics A/B
C_{T_1}	$1.3 \times 10^5/1.7 \times 10^5$	damping cooperativity	mechanics A/B
C_{T_2}	132/147	dephasing cooperativity	mechanics A/B

Table 5.1: **Summary of device parameters.** Parameters $\kappa_{\mathrm{e,q}}$ and $\kappa_{\mathrm{e,r}}$ denote the decay rates of the qubit and the readout resonator into the shared xy and readout line, respectively. The reported electromechanical coupling rate is characterized at a voltage bias of 50 V. The qubit's lifetime and Ramsey coherence time are characterized and reported at the frequencies of oscillator A/B, respectively. The mechanical lifetime (coherence time) is characterized at a bias voltage of $\approx$ 40 V ($\approx$ 50 V), where the uncertainty in characterization is indicated with 2σ confidence intervals. The damping (dephasing) cooperativity is calculated as $C_{T_1} = 4g_{\mathrm{em}}^2 T_{1,\mathrm{m}} T_{1,\mathrm{q}}$ ($C_{T_2} = g_{\mathrm{em}}^2 T_{2,\mathrm{m}}^{*} T_{2,\mathrm{q}}^{*}$).

All the patterning of steps (i)–(v) is carried out using electron-beam lithography.

Microwave design

Our microwave qubit is a transmon with $E_{\mathrm{J,max}}/h = 15.9\,\mathrm{GHz}$ and $E_{\mathrm{C}}/h = 226$ MHz, having a maximum frequency of 5.107 GHz. The transmon is designed with a relatively large $E_{\mathrm{J,max}}/E_{\mathrm{C}}$ ratio of ≈ 70, in order to minimize potential dephasing due to charge noise. The charge noise induced dephasing of a qubit is set by a combination of (i) charge dispersion, which quantifies the maximum change in the qubit frequency due to variations in offset charge and (ii) the magnitude of charge noise present in the system [55]. In an isolated transmon, the charge noise remains significantly below a single electron ($10^{-4} - 10^{-3}e$) [164]. However, in our hybrid device, a large voltage is applied to the qubit in our experiment, which

can potentially cause excess charge noise. As the charge dispersion provides an upper bound on the dephasing, significantly suppressing it can ensure insensitivity to charge noise regardless of the noise present in the system. Therefore, we have conservatively designed our qubit with a charge dispersion of $\approx$ 1 kHz for the g-e transition. Due to the exponential dependence of the charge dispersion on E_J/E_C [55], the noise insensitivity can be achieved with a small cost to the electromechanical interaction strength which scales as $\sqrt{E_C/E_J}$. In the future, characterizing the charge noise can potentially enable us to operate with a smaller E_J/E_C ratio and slightly improve our electromechanical interaction rate.

The SQUID loop of the transmon is composed of two asymmetric junctions, with an asymmetry ratio of 6. The asymmetric junctions reduce the sensitivity to flux noise as the qubit frequency is tuned at the cost of a reduced tuning range [165], which is $\approx$ 800 MHz in our case. However, even with reduced sensitivity to flux noise, we observe that the coherence time of our qubit degrades substantially away from the sweet spot, suggestive of dephasing dominated by flux noise. Specifically, we see that the pure dephasing increases from $\Gamma_\phi/2\pi \sim 10$ kHz at the sweet spot to $\Gamma_\phi/2\pi \sim 100$ kHz in the spectral vicinity of the mechanical oscillators. It is possible to characterize the flux noise by measuring the qubit coherence time at different frequencies and relating it to the first order sensitivity of the qubit frequency to flux [165]. Through this method, we have determined that almost all of the observed dephasing can be attributed to flux noise with a noise amplitude of $\sqrt{A_\Phi} \approx 10\,\mu\Phi_0$. This noise amplitude is larger than state-of-the-art transmons which can reach $\sqrt{A_\Phi} \approx 1\,\mu\Phi_0$ level [165, 166]. We have previously observed differing levels of flux noise on transmons fabricated on the same chip. This indicates that the source of flux noise resides on chip and relates to our fabrication process, instead of being due to instrumentation or wiring. The precise origin of this excess flux noise will be the focus of future investigations.

The qubit is capacitively coupled to a lumped element $\lambda/4$ resonator at a frequency of $\omega_r/2\pi \approx 7.3$ GHz with an interacton rate $g_{qr}/2\pi = 105$ MHz for dispersive readout (see Fig. 5.6a). The coplanar waveguide that is capacitively coupled to the readout resonator ($\kappa_{e,r}/2\pi = 1.9$ MHz) is also coupled to the qubit ($\kappa_{e,q}/2\pi = 7$ kHz) to function as both a readout and xy line. The xy coupling to the qubit is engineered to be relatively strong in order to reduce power requirements for ac Stark shift tones, which are also applied through the same port.

The mutual capacitance between the DC line and the transmon qubit is $\approx$ 2 fF

according to electromagnetic simulations. This capacitance consists of the mechanical capacitance, the parasitic capacitance of the wires, and the stray capacitance between the feedline and the transmon central electrode. In the absence of any filtering, this undesirable capacitive coupling between the DC line and qubit is expected to cause external decay with a rate of $\approx 2\pi \times 350$ kHz into the waveguide. In order to avoid this, we utilize a notch-type filter. At its resonance frequency, the $\lambda/4$ CPW resonator functions as an impedance transformer, where the $50\,\Omega$ environment is converted into a short, preventing radiation [167]. The precise design of the filter relies on electromagnetic simulations, where the length of the $\lambda/4$ stub is designed such that the transmission from the launchpad of the waveguide to the feedline that is connected to the mechanical resonator is suppressed at the qubit frequency, as seen in Fig. 5.6b. By combining these modular electromagnetic simulations and circuit analysis, we estimate the suppression of qubit radiative decay to be substantial ($\lesssim 2\pi \times 1$ kHz) in the spectral vicinity of the mechanical oscillators. Due to the stub being galvanically attached to the waveguide and being open on the other end, it doesn't interfere with the application of DC voltage. However, the filter also precludes direct electrical addressing of the mechanical resonators via the DC line and instead the driving of mechanical oscillators has to be realized via the xy line, mediated by the qubit.

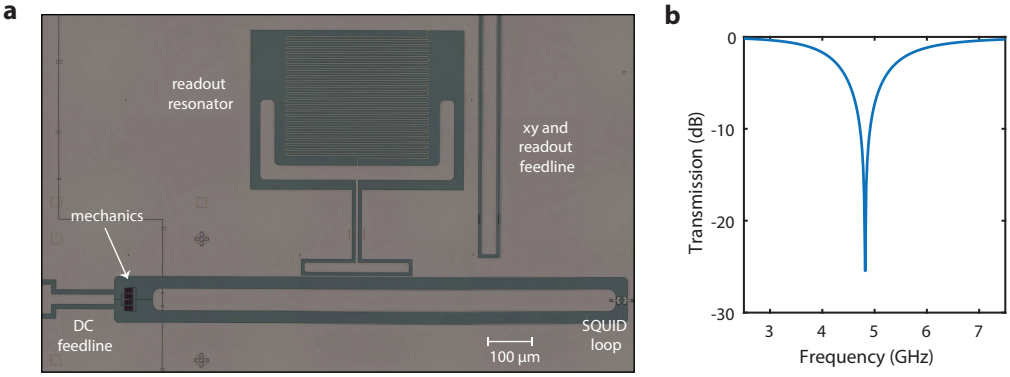


Figure 5.6: **Microwave design. a,** Optical microscope image of the device, focusing on the features around the transmon. **b,** Simulated transmission between the launchpad and the feedline for the DC line, showing a notch type response centered at 4.8 GHz.

We observe qubit lifetimes ($T_1 \sim 1.7\,\mu$s) that exceeds the decay limit into the DC line ($T_1 \sim 0.4\,\mu$s), which was characterized via previous generation devices that lacked a filter. Collectively, these observations suggest that the notch filter

suppresses the radiative decay of the qubit. However, experimentally quantifying the precise suppression level of the notch filter poses a challenge. As the filter is designed to possess a large bandwidth ($\sim$ 1.5 GHz) and is expected to be extremely overcoupled, its resonant response cannot be resolved via reflection measurements due to ripples in our setup. In order to explore the filter behavior, we modified our setup and conducted measurements with the cable that connects the bias-T to the DC line detached (see the original setup in Fig. B.1). This configuration is expected to alter the radiative decay by modifying the effective impedance seen at the waveguide. These experiments demonstrated a twofold improvement in the qubit lifetime ($T_1 \sim 3\,\mu$s), suggesting the presence of significant radiative loss in our experiments.

Importantly, the observed radiative loss is significantly larger than the estimate from modular simulations and circuit model analysis (radiative lifetime limit of $T_1 \sim 150\,\mu$s). To further investigate this, we conducted chip scale electromagnetic simulations, where we found the simulated decay rate of the qubit to the DC line ($\sim 2\pi \times 20$ kHz) to be comparable to the measured radiative decay magnitude. This result suggest that modular simulations of the filter—which formed the basis of our filter design—did not fully capture all the effects in our system. Chip scale simulations that incorporate near field effects between the filter and transmon will be utilized to better understand the origin of the imperfect suppression of the filter and improve its operation in the future.

The discussion above indicates that the intrinsic lifetime of our qubit is $T_1 \sim 3\,\mu$s. We note that this lifetime is comparable to other transmons fabricated on silicon-on-insulator substrates in the literature [82, 168, 169], suggesting that our fabrication is in line with standards. Further improvements can be potentially obtained by better understanding the qubit loss mechanisms via systematic investigations. However, reaching start-of-the-art qubit coherence ($T_1 \sim 100\,\mu$s) is likely to require a flip chip approach that can employ silicon or sapphire substrates for the qubit chip [159, 160].

Wigner tomography

We calculate the Wigner function of the mechanical oscillator initialized to state ρ by measuring the phonon parity. The Wigner function of the prepared state ρ at coordinate α ($W_\rho(\alpha)$) is proportional to the displaced parity of the mechanical oscillator $P_\rho(\alpha)$, through the relation

$$W_\rho(\alpha) = \frac{2}{\pi} P_\rho(\alpha). \tag{5.2}$$

To calculate the parity we leverage the information in the Rabi oscillations between the qubit and the mechanical oscillator [36, 170]. From these Rabi oscillations, we calculate the phonon number distribution, and consequently, phonon parity which are related by

$$P_\rho(\alpha) = \mathrm{Tr}\left(\hat{D}^\dagger(\alpha)\hat{\rho}\hat{D}(\alpha)\hat{\Pi}\right) = \sum_n (-1)^n p_{n,\rho}(\alpha), \tag{5.3}$$

where $\hat{\Pi}$ is the parity operator and $p_{n,\rho}(\alpha)$ is the phonon population corresponding to the Fock state n for an initialized state of ρ following a displacement of α. Importantly, during our measurements, we randomize the phase of the displacement $\alpha = re^{i\theta}$ (where θ is sampled uniformly from the interval $[0, 2\pi]$), which leads to the measurement of the phase averaged Wigner function $\overline{W}(r)$ [171]. Since the states we are interested in preparing ($|0\rangle_\mathrm{m}$ and $|1\rangle_\mathrm{m}$) are phase-symmetric, the phase averaging provides a significantly reduced measurement overhead, while retaining fundamental features of the Wigner function.

To perform Wigner tomography after preparing a mechanical state, we first detune the qubit by approximately 5 MHz and then apply a phase-randomized Gaussian pulse to the qubit at mechanics frequency for 8 μs. This drive, mediated via the qubit through the electromechanical interaction, effectively converts into a displacement of the mechanical oscillator with complex displacement amplitude α, where we choose the phase of α randomly for each instance of the experiment. Subsequently, we bring the qubit into resonance with mechanics for time t and measure the qubit population as a function of t. This results in Rabi oscillation where an example of such measurement is depicted in Fig. 5.7a. We prepare the ground mechanical state by moving the qubit to the mechanics' frequency and waiting approximately 25 μs to make sure that they are both at their ground states. For the excited state preparation, we repeat the same procedure followed by detuning the qubit by around 5 MHz and exciting it using a π-pulse. Then, we bring the qubit back into resonance with the mechanics and wait for T_swap to transfer the excited state to mechanics. The pulse sequences for the ground and excited state preparation and tomography are shown as the inset of Fig. 5.7a.

To derive the phonon number distribution, we fit the measured Rabi oscillation using the QuTiP package to solve the master equation. For this purpose, we first find the resulting Rabi oscillations corresponding to mechanics being in the Fock state n and qubit in the ground state ($|g, n\rangle_{q,m}$) [170]. Then, by decomposing the measured Rabi oscillations into Rabi functions from the simulation, the phonon

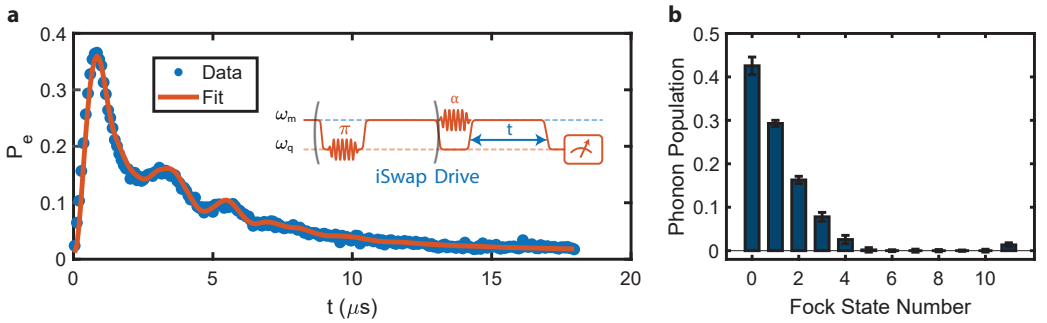


Figure 5.7: **Phonon distribution measurement.** **a,** Measurement of the qubit population as a function of time for the ground state tomography of mechanics B with a displacement amplitude of 0.9. The inset depicts the pulse sequence for the ground (excited) state tomography. **b,** Calculated phonon distribution from the fit of the data presented in **a**. The bar chart represents the population of each Fock state where the error bars show the 2σ confidence interval for the fit obtained via bootstrapping.

number distribution is calculated. As discussed above the Wigner function is calculated for each α, which gives us the phase-averaged measured Wigner function. For the errors, we use bootstrapping done by resampling with replacement from the calculated data. An example of such fitted Rabi oscillation and phonon number distribution is shown in Fig. 5.7a, and b, respectively. Additionally, to characterize the magnitude of the coherent displacement, we fit a Poisson distribution to the phonon number distribution for ground state tomography and calibrate the drive amplitude corresponding to a required displacement amplitude.

After measuring the Wigner function for the prepared density matrix ρ, we reconstruct this density matrix ρ' of the prepared mechanical states by minimizing the difference between the measured Wigner function and the calculated Winger function given by

$$W_{\rho'}(\alpha) = \frac{2}{\pi} \sum_{n} \langle n | \hat{D}^{\dagger}(\alpha) \hat{\rho}' \hat{D}(\alpha) \hat{\Pi} | n \rangle . \tag{5.4}$$

For this minimization, we used CVX, a package for solving convex programs [172], with a Hermitian semi-definite ρ and subjecting it to be diagonal (due to the measurement being phase-randomized and hence the Wigner function being spherically symmetric) and have a trace of one. For the errors, we use the Monte Carlo method where we generate statistics for the elements of the density matrix by choosing a phonon distribution value using Gaussian distribution with the mean and standard deviation of the calculated values and errors in the previous step, respectively.

The expected state preparation fidelities can be estimated through master equation simulations of the qubit-oscillator system. At the measurement voltage of 50 V, the electromechanical interaction rate is given to be $2\pi \times 230$ kHz for oscillator B. The decoherence rates utilized in the simulation is obtained through time domain characterization. Near mechanical oscillator B, the qubit has a lifetime of $T_{1,\mathrm{q}} = 1.55\ \mu$s and a Ramsey coherence time of $T^*_{2,\mathrm{q}} = 1.05\ \mu$s, constituting the main decoherence channel for the qubit-oscillator system ($T^*_{2,\mathrm{B}} \approx 50\ \mu\mathrm{s} \gg T_{2,\mathrm{q}}$). Further utilizing the thermal populations extracted through thermometry measurements, the state preparation fidelities for $|0\rangle$ and $|1\rangle$ are estimated to be 0.989 and 0.759, comparable to the measured fidelities of 0.964 ± 0.007 and 0.711 ± 0.023 (where the fidelity is defined as $F = \sqrt{\langle\psi|\,\rho\,|\psi\rangle}$, with $|\psi\rangle$ being the target state). These observations suggest that qubit decoherence is the main contributor to state preparation infidelity, with the remaining infidelity most likely originating from imperfections in experimental procedures.

The inverse Purcell decay

In our coupled qubit-oscillator system, the mechanical oscillators experience inverse Purcell decay due to their interaction with a much shorter-lived qubit, which limits the mechanical lifetime, particularly at small detunings. The measured decay rate of the mechanical oscillator can therefore be expressed as the sum of intrinsic and inverse Purcell decay rates, $\Gamma = \Gamma_\mathrm{i} + \Gamma_\kappa$. For typical detunings of our experiment, where $|\Delta| \gg \kappa, g$, the total decay rate is given by [173]

$$\Gamma = \Gamma_\mathrm{i} + \left(\frac{g_\mathrm{em}}{\Delta}\right)^2 \kappa. \tag{5.5}$$

Here, $\Delta = \omega_\mathrm{q} - \omega_\mathrm{m}$ is the detuning between the qubit and the oscillator, and κ is the qubit decay rate.

To quantify the contribution of the inverse Purcell decay, we measure the mechanical decay rate while varying the detuning Δ. As shown in Fig. 5.8, the theoretical model aligns closely with the experimental data. From the fit parameters, we can calculate the intrinsic decay rate of the oscillator by subtracting the inverse Purcell decay contribution.

These measurements were performed in the low-phonon-number regime, where we subtract a small background offset—accounting for the residual thermal population—from all data points. To minimize the inverse Purcell decay during the free energy decay measurements, we detune the qubit frequency from the mechanical

resonance by approximately 30–40 MHz during relatively long waiting times. However, since rapid tuning of the qubit frequency via an ac Stark shift [174] requires a microwave tone, larger frequency shifts require higher drive power, which can induce qubit heating. To address this, we maintain a smaller detuning of around 3–6 MHz during fast operations, such as qubit gate operations and readout, as oscillators are less affected by the inverse Purcell decay.

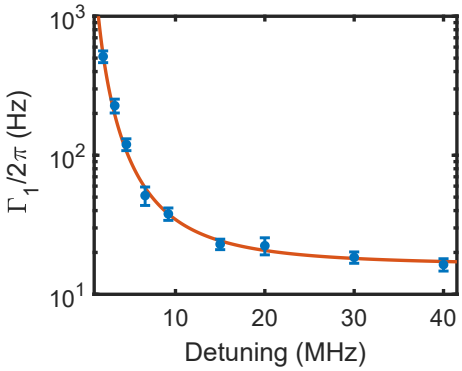


Figure 5.8: **Inverse Purcell decay.** Mechanical decay rate as a function of the detuning between the qubit and mechanics, demonstrating the inverse Purcell decay of the mechanics through the qubit, performed on mechanics A. The data points indicate the decay rates obtained vai exponential fits for each measurement and the error bars represent 2σ confidence interval of the fits. The solid line shows the theory fit to the total decay rate based on Eq. (5.5).

TLS Spectroscopy

During our TLS spectroscopy measurements, we have seen numerous individual TLS interact with our mechanical oscillator, as shown in Fig. 5.9a. We can model the result of spectroscopy measurements through the Hamiltonian

$$\hat{H}/\hbar = \frac{\omega_q}{2}\hat{\sigma}_z + \frac{\omega_{TLS}}{2}\hat{\sigma}_{z,TLS} + \omega_m \hat{b}^\dagger \hat{b} + g_{em}\left(\hat{\sigma}_+ \hat{b} + \hat{\sigma}_- \hat{b}^\dagger\right) + g_{TLS}\left(\hat{\sigma}_{+,TLS}\hat{b} + \hat{\sigma}_{-,TLS}\hat{b}^\dagger\right) + \frac{\Omega_q}{2}\left(e^{-i\omega_d t}\hat{\sigma}_+ + e^{i\omega_d t}\hat{\sigma}_-\right), \quad (5.6)$$

where ω_{TLS} (ω_d) is the TLS (qubit drive) frequency, $\hat{\sigma}_{-,TLS}$ is ($\hat{\sigma}_{+,TLS}$) the TLS lowering (raising) operator, g_{TLS} is the TLS-mechanical oscillator transverse coupling rate and Ω_q is the qubit Rabi drive strength. This Hamiltonian includes both the qubit–mechanics interaction (see Eq. (5.1)) and the TLS–mechanics interaction (see Eq. (6.6)). For the TLS–mechanics interaction, we have neglected the longitudinal coupling term that is not relevant in this context and applied the rotating wave approximation.

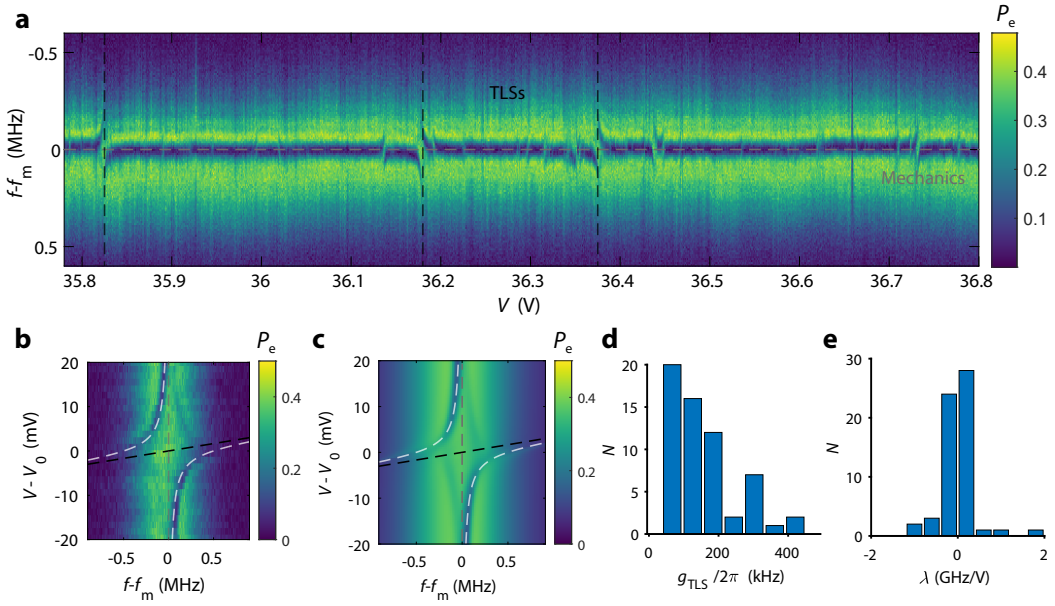


Figure 5.9: **TLS spectroscopy.** **a,** Spectroscopy trace of the qubit-mechanics system as the voltage is varied, illustrating the coupling between the mechanics and individual TLSs through multiple avoided crossings. The black dashed lines highlight a selection of prominent individual TLSs. **b,** A magnified view of a specific mechanics-TLS avoided crossing (identical to the avoided crossing presented in Fig. 5b). The white dashed lines represent a theory fit to the avoided crossing. The black dashed line is the bare TLS frequency. **c,** Avoided mechanics-TLS mode crossing obtained by solving the full master equation (with parameters $\lambda \approx 0.3$ GHz/V and $g_{\mathrm{TLS}}/2\pi \approx 0.5$ MHz), confirms the features seen in experimental data. **d,e** Histograms of the lower bounds for TLS-mechanics interaction rate and TLS tuning rate obtained from avoided crossing fits. N is the number of TLS within a bin.

Notably, the TLS frequency in the near vicinity of the mechanical oscillator frequency can be expressed as

$$\omega_{\mathrm{TLS}} = \omega_{\mathrm{m}} + 2\pi \times \lambda(V - V_0), \tag{5.7}$$

where λ is the TLS tuning rate per volt, V is the applied voltage, and V_0 is the voltage bias value at which the TLS is in resonance with the mechanical oscillator. The tuning rate λ for a TLS can be further expressed as [114]

$$h\lambda = \frac{\epsilon}{E}\mathbf{p} \cdot \mathbf{E}, \tag{5.8}$$

where $\mathbf{p}$ is the TLS dipole moment and $\mathbf{E}$ is the electric field at the position of the TLS with 1 V applied to the electrodes. We see that we can faithfully reproduce the measurement results through master equation simulations in the steady-state (compare the measurement result in Fig. 5.9b to the simulation results in Fig. 5.9c). We

note that in the measurements, the qubit corresponds to the broad green feature and the mechanical oscillator manifests itself as dark lines, which physically corresponds to a dip in the spectroscopy response at the mechanical oscillator frequency.

As demonstrated above, the spectroscopy traces can be utilized to extract TLS parameters such as the interaction rate and the tuning rate by fitting avoided crossings. Ideally, this procedure can be applied to all of the observed TLS to obtain statistics. However, we encounter experimental challenges in fully resolving the avoided crossings. Mainly, the splitting of the hybridized modes ($2g_{\mathrm{TLS}}$) can place them outside of the qubit linewidth (the qubit frequency is kept fixed in the experiment), or the signal associated with hybridized modes can be too weak to observe due to decoherence induced by TLS. Therefore, we cannot reliably observe the entirety of the avoided crossing for all of the individual TLS, instead we only see the tail ends of the avoided crossing for some of them. The change in the mechanical frequency due to the TLS for the tail end ($\Delta_{\mathrm{TLS}} \gg g_{\mathrm{TLS}}$) can be expressed as $-g_{\mathrm{TLS}}^2/\Delta_{\mathrm{TLS}}$, where $\Delta_{\mathrm{TLS}} = \omega_{\mathrm{TLS}} - \omega_{\mathrm{m}} = 2\pi \times \lambda(V - V_0)$. Since both the interaction rate g_{TLS} and the tuning rate λ are unknown, we can extract both of these parameters only under the assumption of finding the lower bounds on both of them. Nonetheless, we will follow this procedure for the TLS where only the tail ends are visible, and obtain statistics concerning the lower bounds, which still include valuable information. For the following discussions concerning the statistics of tuning rates and coupling rates, the quantities analyzed will be these lower bounds.

Exploring a tuning range of 5 V, between 35 V and 40 V, we observe avoided crossings with 60 TLS, 56 of which have a coupling rate above $2\pi \times 50$ kHz, with the distribution of the coupling rates demonstrated in Fig. 5.9d. Based on the observed interaction rates, we can infer that TLS exhibit deformation potential values extending to 0.5 eV (see Section 6.1 for acoustic strain calculations), consistent with results from literature [139, 175]. The tuning rate distribution is shown in Fig. 5.9e, where 31 of them have positive tuning rates and 29 of them have negative tuning rates, in line with the expected equal probability based on random dipole orientations and TLS density. The number of observed TLS combined with the average tuning rate magnitude (0.22 GHz/V) can be used to obtain an upper bound of 13.8 GHz^{-1} on the TLS density ($\rho = P_D V$). This upper bound is compatible with the density value of 14 GHz^{-1} we have obtained from first principles in Section 6.1 and utilized for our calculations of the decay rate.

Chapter 6

DECOHERENCE DUE TO TWO-LEVEL-SYSTEM DEFECTS

In the previous two chapters, we have obtained experimental evidence suggesting that two-level-system defects (TLS) play a significant role in acoustic decoherence. In Chapter 4, we have seen that the acoustic decoherence rate depends on the power, temperature and voltage, in accordance with theory of TLS (see Section 4.7). Later on, in Chapter 5, we have observed direct signatures of interactions between individual TLS and mechanical oscillators, verifying the presence of these defects in our devices (see Section 5.5).

In this chapter, we present further analysis related to TLS-induced acoustic decoherence. We begin by describing interactions between TLS and mechanical oscillators, with an emphasis on how these interactions give rise to decoherence processes. By combining the theory of decoherence with a modeling of mechanical oscillators, we show how decoherence rates can be estimated. These estimates are then applied to the devices introduced in Chapter 5, allowing for direct comparison with experimental data. This analysis furnishes us with methods to model decoherence in mechanical oscillators which can be used to improve device performance in future experiments.

6.1 Mechanics-TLS interactions

Standard Tunneling Model

TLS are microscopic defects in solid-state systems. These defects were initially hypothesized to explain the anomalous thermal properties and universal behavior of amorphous materials at temperatures below 1 K [112, 176]. While early studies focused on fundamental physics, the advent of quantum technologies has sparked renewed interest in TLS, as they are a major source of noise and decoherence in quantum devices [113]. Specifically, these defects are known to limit the coherence of superconducting quantum circuits [177, 178] and mechanical oscillators [42, 45, 115, 116, 130, 148, 179]. At the same time, these quantum devices now serve as powerful platforms for probing TLS dynamics in previously inaccessible regimes, enabling the study of individual defects [175, 180] which provides access to detailed statistics [150, 181].

Even though the exact physical origins of these defects remain disputed, they are understood to be associated with disorder, surface adsorbates and amorphous interfaces [113]. Despite the uncertainty in origin, their behavior can be effectively described phenomenologically by the standard tunneling model (STM) [112], whose key results we will briefly reproduce below.

Within STM, TLS are modeled as a particle confided within a double-well potential. The tunneling energy Δ_0 characterizes the rate of quantum tunneling between the two wells, while the asymmetry energy ϵ denotes the energy difference between them. Together, these parameters define the TLS Hamiltonian

$$\hat{H}_{\text{TLS}} = \frac{1}{2}(\epsilon\tilde{\sigma}_{z,\text{TLS}} + \Delta_0\tilde{\sigma}_{x,\text{TLS}}) = \frac{1}{2}E\hat{\sigma}_{z,\text{TLS}}, \tag{6.1}$$

where $\tilde{\sigma}_{x,\text{TLS}}$ and $\tilde{\sigma}_{z,\text{TLS}}$ are Pauli operators defined in the double-well basis. Diagonalizing this Hamiltonian yields the energy eigenbasis, represented by $\hat{\sigma}_{z,\text{TLS}}$, with an energy splitting $E = \sqrt{\epsilon^2 + \Delta_0^2}$.

The tunneling and asymmetry energies are randomly distributed, with a probability distribution of

$$P(\epsilon, \Delta_0) = \frac{P_D}{\Delta_0}, \tag{6.2}$$

where P_D is the TLS density, which is a material dependent property.

The TLS interact with external fields through modification of the asymmetry energy as

$$\epsilon = 2\tilde{\gamma} \cdot \tilde{\mathbf{S}} + 2\mathbf{p} \cdot \mathbf{E} + \epsilon_0, \tag{6.3}$$

where $\tilde{\gamma}$ is the TLS deformation potential tensor, $\tilde{\mathbf{S}}$ is the external strain field, $\mathbf{p}$ is the TLS dipole moment, $\mathbf{E}$ is the external electrical field, and ϵ_0 is the asymmetry offset due to the environment. As can be seen from Eq. (6.3), static electric and strain fields can alter the TLS frequency by modifying the asymmetry energy, effectively tuning these defects [150, 175].

The Hamiltonian describing the interaction between TLS and a mechanical oscillator which generates a time varying strain field can be obtained by quantizing the strain term in Eq. (6.3) and substituting it into Eq. (6.1)

$$\hat{H}_{\text{TLS-m}}/\hbar = (g_{\text{TLS}}\hat{\sigma}_{x,\text{TLS}} + g_{\text{TLS},\ell}\hat{\sigma}_{z,\text{TLS}})(\hat{b}^\dagger + \hat{b}). \tag{6.4}$$

Here, g_{TLS} ($g_{\mathrm{TLS},\ell}$) is the transverse (longitudinal) interaction rate between the TLS and mechanical oscillator. These interaction rates are given as

$$\begin{aligned} \hbar g_{\mathrm{TLS}} &= \frac{\Delta_0}{E}\tilde{\gamma}\cdot\tilde{\mathbf{S}}, \\ \hbar g_{\mathrm{TLS},\ell} &= \frac{\epsilon}{E}\tilde{\gamma}\cdot\tilde{\mathbf{S}}, \end{aligned} \tag{6.5}$$

where $\tilde{\mathbf{S}}$ is the value of the normalized strain tensor (normalization based on zero-point fluctuations of strain) at the defect position. For simplicity, we omit the explicit position dependence in our equations. As will be detailed in the following sections, both the longitudinal and transverse interactions can give rise to acoustic decoherence.

The description we have provided here corresponds to the interaction of a single TLS with a mechanical oscillator. However, in reality, the mechanical oscillator interacts with a bath of TLS defects, where the full Hamiltonian of the system is given as

$$\hat{H}/\hbar = \omega_{\mathrm{m}}\hat{b}^\dagger\hat{b} + \sum_{\mathrm{TLS}} \omega_{\mathrm{TLS}}\,\hat{\sigma}_{z,\mathrm{TLS}} + (g_{\mathrm{TLS}}\,\hat{\sigma}_{x,\mathrm{TLS}} + g_{\mathrm{TLS},\ell}\,\hat{\sigma}_{z,\mathrm{TLS}})(\hat{b}^\dagger + \hat{b}), \tag{6.6}$$

where $\omega_{\mathrm{TLS}} = E_{\mathrm{TLS}}/\hbar$ is the TLS frequency.

Due to the random nature of the TLS frequencies, positions and orientations, the dynamics of the full system is challenging to describe. One option is to rely on numerical methods, where one can investigate multiple realizations of TLS in a device and investigate the statistical behavior of the full system [42]. An alternative approach, which we follow, is to utilize average properties of the TLS, which makes modeling the system significantly easier [139]. In the following, we describe how this analysis can be performed specifically for the devices presented in Chapter 5.

Device Modeling

The device properties that enter into estimates of TLS-induced acoustic decoherence are primarily (i) TLS density, (ii) mechanics-TLS interaction rates, and (iii) TLS decoherence rates [139]. As the first two properties tie into the composition and geometry of the mechanical oscillator they will be discussed here. The third item, which is the TLS decoherence rate, is set by interactions between TLS and the surrounding environment, which will be discussed in the following sections.

First, we look at the TLS spectral density. The nanobeam hosting the mechanical oscillator is expected to host TLS primarily on the amorphous silicon oxide on the

surface [182], since the bulk single-crystal silicon is known to have a significantly lower TLS density [80]. The surface area of the nanobeam can be calculated to be 12 μm^2. The thickness of the amorphous region on the silicon surface has been shown to be on the order of 3 nm [183], giving us a total volume of $V = 0.04\,\mu$m^3 that would host TLS. For a TLS density per unit energy and unit volume of P_D, the TLS spectral density is given by $\rho = VP_D$ [114]. Assuming $P_D \approx 5{\times}10^{44}$ (J.m^3)$^{-1}$ based on the literature [139], we expect to have a TLS spectral density of $\rho \approx 14\,\mathrm{GHz}^{-1}$ interacting with our mechanical oscillator.

Second, we look at the mechanics-TLS interaction rate (g_{TLS} and $g_{\mathrm{TLS},\ell}$). The strain field associated with the mechanical motion can be obtained from numerical modeling using finite element method simulations. The strain field is normalized to ensure that the total strain energy in the system corresponds to $\hbar\omega_{\mathrm{m}}/4$ (i.e. normalized to the zero-point energy). The strain and the deformation potential are both tensorial in nature. Since the shear strain components are very small in our system, we can only focus on the normal components, where we find that the average strain field magnitude on the nanobeam surface is $\approx 4 \times 10^{-9}$ m/m. For the deformation potential, we can use an angle averaged value on the order of 1 eV for silicon oxide [139]. The strain magnitude combined with the deformation potential value leads to an estimate for the interaction rate on the order of $|\tilde{\gamma} \cdot \tilde{\mathbf{S}}|/h \approx 1$ MHz.

We therefore expect a sparse TLS bath, where the frequency separation between TLS is much less than the mechanics-TLS interaction rate (i.e. $\rho^{-1} \ll g_{\mathrm{TLS}}/2\pi$). We indeed observe such a sparse bath experimentally (see Section 5.5), with the above estimates being generally consistent with our experimental observations. Owing to experimental limitations, we were only able to determine approximate bounds on the relevant parameters. Therefore, in the following analysis, we rely on the above estimates, which remain within the experimentally inferred ranges.

We nonetheless note that the calculation of the volume that hosts TLS is subject to significant uncertainty because of the strong dependence of the surface properties on fabrication procedures [183, 184]. Therefore, the following estimates for the TLS-induced acoustic loss are expected to have similarly large uncertainty and possess roughly an order of magnitude level precision.

6.2 TLS-induced Acoustic Loss

Resonant absorption

We first focus on loss due to the transverse mechanics-TLS interaction, described in Eq. (6.6). The transverse interaction gives rise to energy exchange between the mechanical oscillator and the TLS when they are resonant, which can manifest as acoustic loss. This acoustic loss depends on the interaction rate, the frequency detuning between the parties, and the TLS decay and dephasing rates. For an ensemble of TLS, the total mechanical decay rate can be expressed as [185]

$$\Gamma_{1,\mathrm{m}} = \sum_{\mathrm{TLS}} \frac{g_{\mathrm{TLS}}^2 \Gamma_{1,\mathrm{TLS}} \tanh\left(\hbar\omega_{\mathrm{TLS}}/2k_B T\right)}{(\omega_{\mathrm{m}} - \omega_{\mathrm{TLS}})^2 + \Gamma_{2,\mathrm{TLS}}^2 + \Omega_{\mathrm{TLS}}^2 \Gamma_{2,\mathrm{TLS}} \Gamma_{1,\mathrm{TLS}}^{-1}}, \tag{6.7}$$

where $\Gamma_{1,\mathrm{m}} = 1/T_{1,\mathrm{m}}$ is the decay rate of the mechanics due to transverse interactions with TLS, expressed through a sum that adds up the decay contributions of all the individual TLS. $\Gamma_{1,\mathrm{TLS}}$ ($\Gamma_{2,\mathrm{TLS}}$) is the TLS decay (decoherence) rate and $k_B T$ is the thermal energy at a temperature of T. $\Omega_{\mathrm{TLS}} = 2g_{\mathrm{TLS}}\sqrt{\bar{n}}$ is the Rabi rate between the oscillator that has $\bar{n}$ mean phonons and the TLS. The $\Omega_{\mathrm{TLS}}^2 \Gamma_{2,\mathrm{TLS}} \Gamma_{1,\mathrm{TLS}}^{-1}$ represents power broadening, which leads to the familiar power saturation of TLS loss.

As can be seen in Eq. (6.7), the decay is more pronounced for TLS that satisfy the resonance condition with the mechanical oscillator, due to which this loss mechanism due to transverse coupling is referred to as *resonant absorption* in the literature [42, 45, 139]. This sensitivity to detuning lies at the origin of the voltage dependence of the lifetime we observe in experiments (see Fig. 6.1a), where the TLS frequencies get modified by the static electric field associated with our voltage bias.

As discussed before, in a physical system, TLS defects have random positions, orientations, and energies. As a result, several quantities in Eq. (6.7) such as frequency detuning, interaction rate, and the TLS lifetime will be randomly distributed. Therefore, the total decay rate depends on the specific TLS realization that the mechanical oscillator interacts with and is expected to be a random quantity itself. However, it is possible to follow a simplified model to get crude estimates for the mechanical decay rate.

In this model, all of the TLS defects are assumed to be interacting with the mechanical resonator at the same coupling rate $\bar{g}_{\mathrm{TLS}}$ and the frequency separation between the neighboring defects is assumed to be a fixed value of $\delta/2\pi = \rho^{-1}$. The TLS is also assumed to be decay limited with a fixed decay rate of $\bar{\Gamma}_{1,\mathrm{TLS}}$. The power broadening is also neglected since we have conducted measurements at the single

phonon regime. Further noting that $\tanh(\hbar\omega_{\mathrm{TLS}}/2k_BT) \approx 1$ in our temperature range ($\hbar\omega_{\mathrm{TLS}} \gg k_BT$), the expression for the oscillator decay rate can be written as [186]

$$\Gamma_{1,\mathrm{m}} = \sum_{k=-\infty}^{\infty} \frac{\bar{g}_{\mathrm{TLS}}^2 \bar{\Gamma}_{1,\mathrm{TLS}}}{(k\delta + \delta_0)^2 + (\bar{\Gamma}_{1,\mathrm{TLS}}/2)^2}. \tag{6.8}$$

Here $\delta_0 \in \{0, \delta/2\}$ is the frequency separation between the oscillator and the nearest TLS. We note that there exists an analytical expression for this infinite sum [186]

$$\Gamma_{1,\mathrm{m}} = \pi a b \frac{\sinh(2\pi b)}{\cosh(2\pi b) - \cos(2\pi bc)}, \tag{6.9}$$

where $a = 4\bar{g}_{\mathrm{TLS}}^2/\bar{\Gamma}_{1,\mathrm{TLS}}$, $b = \bar{\Gamma}_{1,\mathrm{TLS}}/2\delta$ and $c = 2\delta_0/\bar{\Gamma}_{1,\mathrm{TLS}}$.

We then move on to our estimates for the resonant absorption limited lifetime for the simplified model presented in Eq. (6.8). We use an average interaction rate of $\bar{g}_{\mathrm{TLS}}/2\pi = 1$ MHz (where the average tunneling energy ratio is $\Delta_0/E \approx 1$ [114]). For a best case TLS distribution where the closest TLS is away by $\delta_0 = \delta/2$, we can calculate the mechanical lifetime limit due to the resonant absorption for a given set of TLS densities and TLS lifetimes (see Fig. 6.1b). For our device, we expect $\delta/2\pi = \rho^{-1} = 70$ MHz which is set by the TLS density estimate of 14 GHz^{-1}. TLS lifetimes have been measured to be $1/\bar{\Gamma}_{1,\mathrm{TLS}} = T_{1,\mathrm{TLS}} \approx 0.1 - 1\,\mu$s on silicon substrates [187, 188]. Using these numbers, we would expect to have a mechanical lifetime of $1/\Gamma_{1,\mathrm{m}} = T_{1,\mathrm{m}} \approx 50 - 500\,\mu$s, 2 orders of magnitude smaller than the observed lifetime of 25 ms (see Section 5.3).

However, this apparent contradiction can be resolved by noting that TLS lifetime can be modified through phononic engineering. Specifically, since the TLS relaxation occurs mainly through interaction with phonons, the TLS decay rate is related to the phononic density of states (DOS), which is a function of the device geometry [139]. Comparable devices that utilize phononic shields have shown enhanced TLS lifetimes (median lifetime of $\approx 400\,\mu$s) through suppression of the phononic DOS inside the phononic bandgap [168].

The combination of the previously measured TLS lifetimes and our simulations indicating a 2 GHz wide phononic bandgap (see Section 3.2) can be used to estimate the acoustic loss due to TLS inside the bandgap to be $\Gamma_{1,\mathrm{m}} \approx 2\pi \times 0.8$ Hz. Notably, this number is smaller than the observed decay rate of $\Gamma_{1,\mathrm{m}} \approx 2\pi \times 6$ Hz. Importantly, resonant loss from these TLS is expected to be saturable [139]. The absence of saturable loss in our measurements (see Fig. 5.4) further corroborates that the resonant loss due to TLS inside the bandgap is minimal.

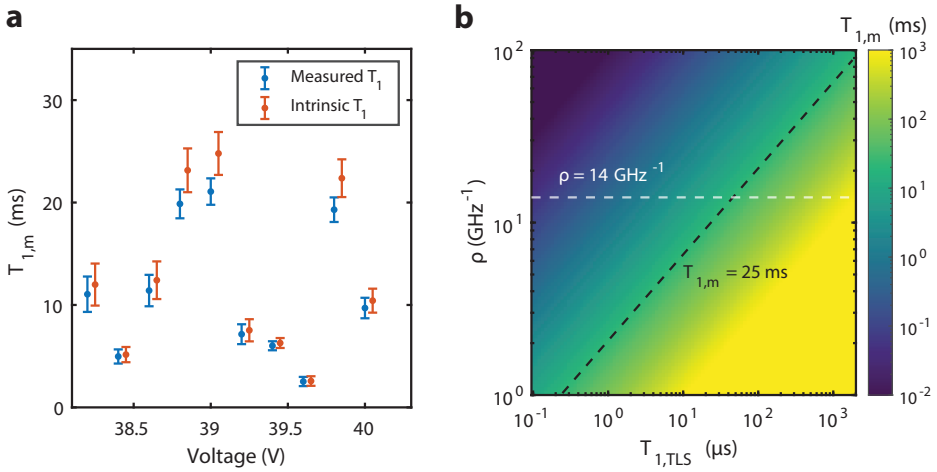


Figure 6.1: **Acoustic loss. a,** Measurement of mechanical lifetime as the voltage is varied in fixed steps. Blue data points represent the measured lifetime of mechanics A (introduced in Chapter 5) for various voltages. Red data points show the intrinsic lifetime obtained by subtracting the inverse Purcell decay from the measured decay rate. The error bars represent 2σ confidence interval for the lifetime obtained through theory fits. **b,** Mechanical lifetime limit ($T_{1,\mathrm{m}} = 1/\Gamma_{1,\mathrm{m}}$) for resonant absorption as the TLS lifetime and the TLS density are varied. The data is calculated for the best case scenario of $\delta_0 = \delta/2$. The white dashed horizontal line represents the estimated TLS density of 14 GHz^{-1}. The black dashed line indicates the TLS lifetime and density combinations that lead to a mechanical lifetime limit of 25 ms, the longest lifetime we have measured.

The TLS outside the bandgap, on the other hand, is expected to have shorter lifetimes and have been measured to possess a median lifetime of $\approx 4\,\mu$s on comparable geometries [168]. Similarly, using this TLS lifetime, the loss due TLS outside the bandgap can be estimated to be $\Gamma_{1,\mathrm{m}} \approx 2\pi \times 1$ Hz, a number comparable to the TLS loss inside bandgap.

Relaxation damping

We next explore the loss due to the longitudinal interaction between mechanical oscillator and TLS. The longitudinal interaction in Eq. (6.4), manifests itself as a modulation of the TLS energy due to the acoustic displacement. Specifically, for a system with a non-zero temperature, this modulation moves the TLS out of thermal equilibrium. The TLS then absorbs energy from phonons and relaxes towards thermal equilibrium, giving rise to acoustic loss at nonzero temperatures. The acoustic loss due to this process is called *relaxation damping*, whose magnitude

can be expressed as [139]

$$\Gamma_{1,\mathrm{m}} = \sum_{\mathrm{TLS}} \frac{2g_{\mathrm{TLS},\ell}^2}{\omega_{\mathrm{m}}} \frac{\hbar\Gamma_{1,\mathrm{TLS}}}{k_B T} \mathrm{sech}^2(\hbar\omega_{\mathrm{TLS}}/2k_B T). \tag{6.10}$$

Due to the $\mathrm{sech}^2(\hbar\omega_{\mathrm{TLS}}/2k_B T)$ term, the loss is mainly dominated by thermally active TLS, having energies of $\hbar\omega_{\mathrm{TLS}} \lesssim k_B T$. This in turn leads to a dissipation rate that increases with temperature as more of the TLS become thermally active at elevated temperatures. Specifically, for a system with dimensionality of D (where the dimensionality D quantifies the phononic density of states), the relaxation damping rate scales with temperature as $\Gamma_{1,\mathrm{m}} \propto T^D$ [139]. The temperature scaling and the absence of saturation can enable one to distinguish relaxation damping from resonant absorption.

For our estimates, we utilize our experimentally measured bath temperature of $T \sim 70$ mK, which corresponds to thermally active TLS with frequencies $\omega_{\mathrm{TLS}}/2\pi \lesssim 1.4$ GHz. Similar to the procedure we have followed for resonant loss, we also assume that that the TLS have a uniform frequency separation of $\delta/2\pi = 70$ MHz. We note that due to the non-resonant nature of this interaction (there is no detuning term in Eq. (6.10)), the dissipation rate is insensitive to the specific distribution of TLS frequencies. We furthermore assume that all the TLS interact with the oscillator with the average longitudinal coupling rate $\bar{g}_{\mathrm{TLS},\ell}/2\pi \approx 0.6$ MHz (where the average asymmetry energy ratio is $\epsilon/E \approx 0.6$ [114]). The remaining parameter needed for calculation is the TLS decay rate.

The decay rates for TLS depends on the phononic DOS at the TLS frequency as discussed above. Specifically, at the frequencies of the thermally active TLS, we expect our phononic DOS to deviate from the 3D case, as the dimensions of our beam ($\sim 0.2\,\mu$m thickness and $\sim 0.5\,\mu$m width) are much smaller than the acoustic wavelength of $\gtrsim 5\,\mu$m. Hence, the decay rates of the TLS can be attributed to a phononic system with dimensionality between 1D and 2D [42], which lends itself to analytical formulas for idealized systems [139]. Using these decay rates, we can calculate the relaxation damping rate to be $\Gamma_{1,\mathrm{m}} \approx 2\pi \times 0.7$ Hz. This decay rate is comparable to the estimates for resonant loss.

In the preceding analysis, we have used identical densities for high-frequency TLS that cause near-resonant loss and low-frequency thermally active TLS that lead to relaxation damping. However, it should be noted that there have been observations of thermally active TLS densities being larger due to an abundance of surface spins [189].

Temperature dependence of acoustic loss

In the previous discussion, we have estimated the contribution of the TLS-induced acoustic loss mechanisms to the total dissipation experienced by our mechanical oscillator at $T = 70$ mK. The total sum of the estimated decay rates from TLS loss mechanisms amounts to $\Gamma_{1,\mathrm{m}} \approx 2\pi \times 2.5$ Hz. Although this number is subject to a large uncertainty (because of the order-of-magnitude nature of the estimates), it is in reasonable agreement with the observed loss $2\pi \times 6$ Hz.

However, we are unable to precisely disentangle the contribution from each loss mechanism through the measurement of the acoustic loss at a single temperature. This can be achieved by investigating the temperature dependence of the acoustic dissipation rate [42, 45].

The aluminum Josephson junction our qubit experiences quasiparticle poisoning at relatively low temperatures ($T \gtrsim 200$ mK) [190], precluding an extensive investigation of the acoustic loss at the single phonon regime with our devices. As an alternative, we employ mechanical oscillators that are directly coupled to microwave waveguides (see Appendix B.5), where the waveguide loss remains negligible even at elevated temperatures. However, these devices feature relatively small external coupling rates to the waveguide, making it necessary to study decoherence phenomena at large phonon occupation numbers due to SNR constraints.

Due to the sparse nature of the TLS bath and the non-trivial phononic DOS in our device, we expect a complex temperature dependence of both the resonant absorption and relaxation damping. However, to capture qualitative features, we can approximate their temperature dependence as [45]

$$\Gamma_{1,\mathrm{m}} = \Gamma_{\mathrm{res}} \tanh\left(\hbar\omega_{\mathrm{m}}/2k_B T\right) + \Gamma_{\mathrm{relax}}(T_0)(T/T_0)^D + \Gamma_0, \tag{6.11}$$

where Γ_{res} (Γ_{relax}) is the magnitude of resonant absorption (relaxation damping) at temperature $T = 0$ ($T = T_0$, which can be arbitrarily chosen), D is the dimensionality of the system, and Γ_0 is the decay rate from mechanisms that have no temperature dependence.

Based on prior systematic characterization of similar devices, we expect TLS to be the only temperature-dependent loss mechanism with a significant contribution to decoherence within our temperature range [42]. Other non-TLS mechanisms, such as acoustic radiation and electromechanical readout, are expected to exhibit no temperature dependence and only weak voltage dependence in the latter case.

Therefore, investigating loss mechanisms that do not exhibit strong voltage dependence allows us to characterize the temperature-independent contributions to the total decay.

Specifically, for the device whose temperature dependence is to be characterized, we first measure the decay rate as a function of the bias voltage at the base temperature of our fridge. The best lifetimes obtained are $T_1 \gtrsim 50$ ms, which sets an upper bound on the temperature-independent decay mechanisms ($\Gamma_0 \leq 2\pi \times 3$ Hz). We then move to a bias point where the lifetime is shorter, selecting a voltage such that $\Gamma_{1,\mathrm{m}}/2\pi = 10$ Hz at the lowest temperature. This pronounced voltage dependence indicates the presence of significant TLS-induced loss for this device at the chosen operating point, which is therefore used for the subsequent characterization.

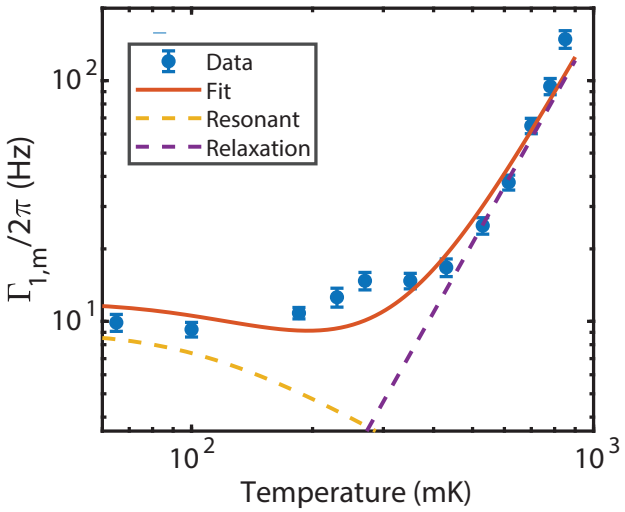


Figure 6.2: **Oscillator decay rate vs temperature.** Measurement of the oscillator decay rate obtain through ringdown measurements. The data points are obtained from exponential fits to these curves, with the error bars representing the 2σ confidence interval. The solid red line shows the fit to the decay rate using Eq. (6.11). The yellow (purple) dashed line indicates the contribution to the decay rate from resonant absorption (relaxation damping). For the temperature, we have used the reading from our temperature sensor, except the lowest temperature point where we use the previously measured bath temperature of 70 mK instead of the sensor reading of 10 mK.

We measure the lifetime by conducting ringdown measurements as the temperature of the mixing stage of our dilution refrigerator is varied. As shown in Fig. 6.2, the simplified model for the temperature dependence of the TLS-induced decay (Eq. (6.11)) exhibits reasonable agreement with the experimental data. From the fit, we extract the parameters as $\Gamma_{\mathrm{res}}/2\pi = 9 \pm 3$ Hz, $\Gamma_{\mathrm{relax}}(T_0 = 300\ \mathrm{mK})/2\pi =$

5 ± 2 Hz, $\Gamma_0/2\pi = 3$ Hz (reached upper bound set by measurements) and $D = 3.0 \pm 0.7$. We choose $T_0 = 300$ mK for the fitting reference since this temperature approximately corresponds to the onset of significant relaxation damping. At lower temperatures, the effective dimensionality of the system is expected to decrease, making extrapolation of the relaxation contribution less reliable in that regime.

The above measurements further corroborate the significant role played by TLS in contributing to acoustic loss. Furthermore, they indicate that at the base temperature, the decay rate is predominantly limited by resonant absorption. At the phonon populations used in these experiments, TLS within the phononic bandgap are expected to be strongly saturated. Nevertheless, the observed magnitude of the decay suggests that TLS located outside the bandgap make a substantial contribution to resonant absorption. The discrepancy of this contribution relative to our estimates may arise from TLS lifetimes being shorter than the values assumed in our calculations.

6.3 TLS-induced Frequency Noise

Alongside acoustic loss, interactions with TLS can also lead to frequency noise for mechanical oscillators. Below, we will provide a description of the physics that lead to this frequency noise. First, we describe how the TLS shifts the oscillator frequency, with fluctuations in TLS parameters later manifesting as frequency noise.

Frequency shift

The frequency shift of the oscillator occurs mainly due to the transverse interaction with the TLS. Specifically, the coupling to the TLS modifies the real part of the acoustic susceptibility, which manfifests as a frequency shift whose value can be expressed as [129]

$$\delta\omega_\mathrm{m} = -\sum_\mathrm{TLS} \frac{g_\mathrm{TLS}(\omega_\mathrm{m} - \omega_\mathrm{TLS})\langle\hat{\sigma}_\mathrm{z,TLS}\rangle}{(\omega_\mathrm{m} - \omega_\mathrm{TLS})^2 + \Gamma_\mathrm{2,TLS}^2 + \Omega_\mathrm{TLS}^2\Gamma_\mathrm{2,TLS}\Gamma_\mathrm{1,TLS}^{-1}}. \tag{6.12}$$

We note that the frequency shift is proportional to $1/(\omega_\mathrm{m} - \omega_\mathrm{TLS})$, hence the far detuned TLS have significant contributions to this effect. This manifests itself as a weak dependence of these frequency shifts on cavity population and TLS decoherence rates.

When the TLS is in thermal equilibrium with a bath of temperature T, the expectation value of its sigma-z operator is $\langle\hat{\sigma}_\mathrm{z,TLS}\rangle = -\tanh(\hbar\omega_\mathrm{TLS}/2k_bT)$. Substituting this into the above equation, we obtain

$$\delta\omega_{\mathrm{m}} = \sum_{\mathrm{TLS}} \frac{g_{\mathrm{TLS}}(\omega_{\mathrm{m}} - \omega_{\mathrm{TLS}}) \tanh\left(\hbar\omega_{\mathrm{TLS}}/2k_bT\right)}{(\omega_{\mathrm{m}} - \omega_{\mathrm{TLS}})^2 + \Gamma_{2,\mathrm{TLS}}^2 + 4g_{\mathrm{TLS}}^2\bar{n}\Gamma_{2,\mathrm{TLS}}\Gamma_{1,\mathrm{TLS}}^{-1}}. \tag{6.13}$$

The temperature dependence of this TLS-induced frequency shift underlies the anomalous low-temperature behavior of the oscillator frequency: as the device is cooled below 1 K, the frequency decreases, a trend that sharply contrasts with the expected increase in frequency due to conventional material stiffening upon cooling [45, 191].

Experimentally, we observe similar temperature dependence of the oscillator frequency as shown in Fig. 6.3. We compare this experimental data to a numerical solution of Eq. (6.13), using the parameters estimated in the previous sections and assuming a TLS distribution with uniform frequency spacing. By applying a simple scaling factor of 0.7 to the numerical result, we obtain good agreement with the measured data (see Fig. 6.3). This relative consistency highlights the effectiveness of the TLS model and our estimated parameters in capturing the essential physics governing the frequency shift of our mechanical oscillators.

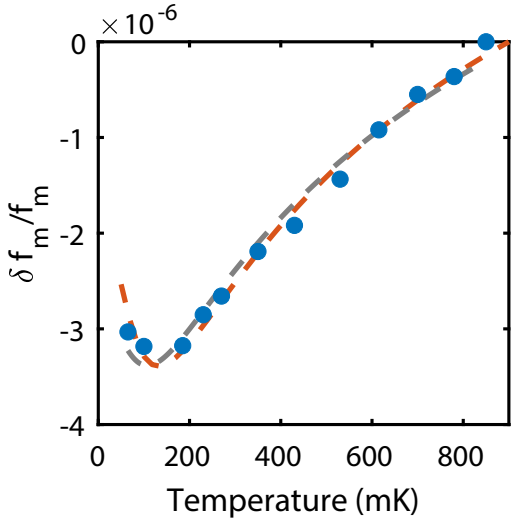


Figure 6.3: **Anomalous oscillator frequency shift.** The blue points represent measurements of the fractional oscillator frequency as the temperature is varied. The red dashed line is a numerical solution of Eq. (6.13) for our system with our average TLS parameters and $\bar{n} \approx 10^3$. The numerical calculations are scaled by a factor of 0.72 to fit the experimental data. The grey line represents a fit to the continuum model (Eq. (6.14)) with $F \tan\delta_{\mathrm{TLS}} = 7.4 \times 10^{-6}$.

We note that in the continuum limit of a TLS bath, there exists an analytical solution

for the temperature dependence of mechanical frequency given as [45]

$$\frac{\delta\omega_{\mathrm{m}}}{\omega_{\mathrm{m}}} = \frac{F\tan\delta_{\mathrm{TLS}}}{\pi}\left[\mathrm{Re}\left\{\Psi\left(\frac{1}{2}+\frac{\hbar\omega_{\mathrm{m}}}{2\pi i k_b T}\right)\right\} - \ln\frac{\hbar\omega_{\mathrm{m}}}{2\pi k_b T}\right], \tag{6.14}$$

where F is the TLS energy participation ratio, $\tan\delta_{\mathrm{TLS}}$ is the TLS loss tangent and Ψ is the complex digamma function. Our data can be fit to this equation, as shown in Fig. 6.3. However, due to the sparse nature of our TLS bath, which does not satisfy the assumptions of the continuum model, the total loss obtained from the fit, $F\tan\delta_{\mathrm{TLS}} = 7.4\times10^{-6}$, is significantly larger than that obtained from measurements of mechanical decay (1.2×10^{-9}). While the continuum model captures the overall temperature dependence, it is not suitable for extracting the TLS density in our devices, since the TLS are discrete in this regime. Our more detailed modeling, as presented above, provides a more accurate estimate of the TLS contribution to the behavior our mechanical oscillators.

Frequency noise

Frequency noise in a system manifests itself as a time varying resonance frequency. Specifically, for our mechanical oscillator the resonance frequency becomes a function of time (i.e. $\omega_{\mathrm{m}}(t)$). Due to the stochastic nature of this noise, it is most often characterized through its noise power spectral density (PSD)

$$S_{\delta\omega}(\omega) = \lim_{\tau\to\infty}\frac{1}{\tau}\int_0^\tau\int_0^\tau \langle\omega_{\mathrm{m}}(t_1)\omega_{\mathrm{m}}(t_2)\rangle e^{i\omega(t_1-t_2)}dt_1dt_2. \tag{6.15}$$

For the following analysis, we will utilize results from the literature that focuses on the noise power spectral density for TLS-induced frequency noise. Other measurements that can be used to characterize frequency noise such as Ramsey interferometry and dynamical decoupling will de discussed later on. Due to the complex nature of the analysis, we will not reproduce the full derivation but instead refer to the important results.

A natural avenue for frequency noise to originate from mechanics-TLS interactions is fluctuations in the parameters that determine TLS-induced frequency shifts. Examining Eq. (6.12), one parameter expected to vary over time is the expectation value of the TLS sigma-z operator ($\langle\hat{\sigma}_{\mathrm{z,TLS}}\rangle$). Specifically, thermal energy in the system causes the TLS to stochastically fluctuate between its ground and excited states, leading to time-dependent variations in ($\langle\hat{\sigma}_{\mathrm{z,TLS}}\rangle$) and consequently, in the mechanical resonance frequency.

The fluctuations from the mean value can be described with the following statistics [129]

$$\langle(\hat{\sigma}_{z,\mathrm{TLS}}(t) - \tanh(\hbar\omega_{\mathrm{TLS}}/2k_bT))^2\rangle = 1 - \tanh^2(\hbar\omega_{\mathrm{TLS}}/2k_bT) \\ = \cosh^{-2}(\hbar\omega_{\mathrm{TLS}}/2k_bT). \quad (6.16)$$

By integrating over the TLS bath, these fluctuations can be shown to cause frequency noise that has a power spectral density of the form [129]

$$S_{\delta\omega}(\omega) \propto \frac{T^2}{\omega}. \quad (6.17)$$

This noise has two important properties: (i) it has $1/f$ type spectrum and (ii) the noise is expected to reduce significantly as the lower temperatures are reached.

We observe a $1/f$ type spectrum for our devices that is in agreement with the above expression (see Fig. 6.5c, the details of this measurement will be discussed in detail later). In order to investigate the temperature dependence of frequency noise, we extract the pure dephasing rate of our devices by measuring their linewidth and subtracting the decay contribution. Interestingly, the experimental behavior deviates significantly from the predicted behavior in Eq. (6.16)): the frequency noise worsens as the temperature is reduced (see Fig. 6.4).

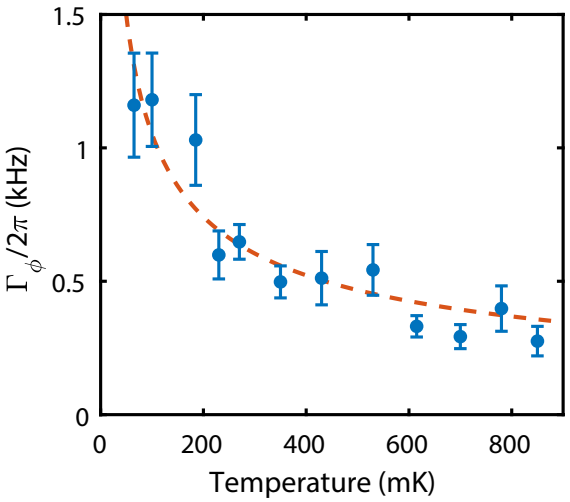


Figure 6.4: **Acoustic dephasing vs temperature.** The blue points represent measurements of the mechanical oscillator dephasing rate as the temperature is varied. The measurements are conducted at $\bar{n} \approx 10^3$. The red dashed line is a fit to the data of the form $\Gamma_\phi \propto T^d$ where $d = -0.5 \pm 0.1$.

However, this observation doesn't indicate that our dephasing is due to a non-TLS mechanism. In fact, this anomalous temperature dependence of frequency noise has been previously observed in microwave cavities [189, 192] and mechanical oscillators [193]. This discrepancy with standard TLS theory can be resolved through introducing the notion of TLS-TLS interactions [129, 194].

Specifically, the TLS-TLS interactions are hypothesized to be mediated by phonons and are described through the Hamiltonian [195]

$$H_{\text{TLS-TLS}} = \sum_{i>j} \frac{U_{ij}}{4} \frac{\epsilon_i}{E_i} \frac{\epsilon_j}{E_j} \hat{\sigma}_{\text{z,TLS},i} \hat{\sigma}_{\text{z,TLS},j}, \tag{6.18}$$

where $U_{ij} = U_0/R_{ij}^3$, with $U_0 \approx 10^{-48}$ J.m^3 being the TLS-TLS interaction constant [196] and R_{ij} the distance between the two TLS. Direct experimental signatures of these TLS-TLS interactions have been observed in the last 10 years, providing providing strong support for this hypothesis [197, 198].

To quantify the strength of TLS-TLS interactions, one can define the dimensionless parameter $\chi = U_0 P_D \approx 10^{-3}$, which compares the energy separation between TLS (average distance $R^3 \sim P_D$) to their interaction rate. As $\chi \ll 1$, TLS-TLS interactions do not play a dominant role in TLS physics. However, they contribute significantly to frequency fluctuations of TLS.

Specifically, the frequency of a given TLS (say TLS i) depends on the sigma-z operator values of the surrounding TLS bath

$$\omega'_{\text{TLS},i} = \omega_{\text{TLS},i} + \frac{\epsilon_i}{E_i} \sum_{i>j} \frac{U_{ij}}{2\hbar} \frac{\epsilon_j}{E_j} \hat{\sigma}_{\text{z,TLS},j}. \tag{6.19}$$

As the surrounding TLS bath undergo thermal flips, $\hat{\sigma}_{\text{z,TLS},j}$ fluctuates with time, leading to fluctuations of the TLS frequency (i.e. $\omega'_{\text{TLS},i}(t)$). These fluctuations are more pronounced for thermally active TLS with $\hbar\omega_{\text{TLS},j} \lesssim k_b T$ (see Eq. (6.16)). These thermally active TLS will be referred to as thermal fluctuators.

These frequency fluctuations can be evaluated under the Gaussian assumption to obtain a TLS decoherence rate of [129]

$$\Gamma_{2,\text{TLS}} \propto \chi T^{1+\mu}, \tag{6.20}$$

where $\mu \approx 0.3$ is a hypothesized modification of the TLS DOS due to TLS-TLS interactions. Therefore, the TLS decoherence rate is expected to increase with temperature, as verified experimentally [199].

Alongside this Gaussian component, there exists non-Gaussian noise due to strongly coupled thermal fluctuators (i.e. $U_{ij} > \Gamma_{1,\mathrm{TLS},j}$). The impact of these fluctuators can be examined by treating them as classical fluctuators undergoing a classical switching process. Here the TLS frequency can be expressed as

$$\omega_{\mathrm{TLS},i}(t) = \omega_{\mathrm{TLS},i} + \sum_{i \neq j} \frac{U_{ij}}{2} n_j(t). \tag{6.21}$$

Here $n_j(t) = \pm 1$ represents a random telegrapher noise process with switching rate γ_j.

Introducing fluctuations of TLS frequency into Eq. (6.12) and integrating over the TLS distribution leads to the expression for the frequency noise of the form [129]

$$S_{\delta\omega}(\omega) \propto \frac{T^{-(1+\mu)}}{\omega}. \tag{6.22}$$

This model frequency noise also exhibits a power dependence approximately given by $\propto (1 + \bar{n}/n_c)^{-1/2}$, where n_c is the critical phonon number which is mainly set by the coupling strength to the TLS bath.

This model captures several features that are consistent with our experimental observations: (i) $1/f$ type frequency noise (see Fig. 6.5c), (ii) increase in frequency noise at lower temperatures (see Fig. 6.4) and (iii) reduction in the frequency noise with power (see Fig. 4.12c). These observations suggest that the interplay between TLS–TLS and TLS–mechanics interactions is most likely responsible for the frequency noise observed in our mechanical oscillators.

Noise PSD measurements

We have previously described how TLS theory can accurately describe the frequency shifts and frequency noise experienced by our mechanical oscillator. Here, we will expand on our measurements of acoustic frequency noise PSD and demonstrate how they provide further evidence for the significant impact of TLS on frequency noise.

The frequency noise can be characterized through repeated measurements of the oscillation frequency, where the noise manifests itself as frequency fluctuations. A method to measure the frequency of the mechanical oscillator is to rely on Ramsey measurements. Specifically, the fringe frequency is set by the detuning between the drive tone and the mechanical frequency, providing a way to infer the mechanical frequency for a known drive frequency. Utilizing this method, we investigate the frequency noise through extensive measurements.

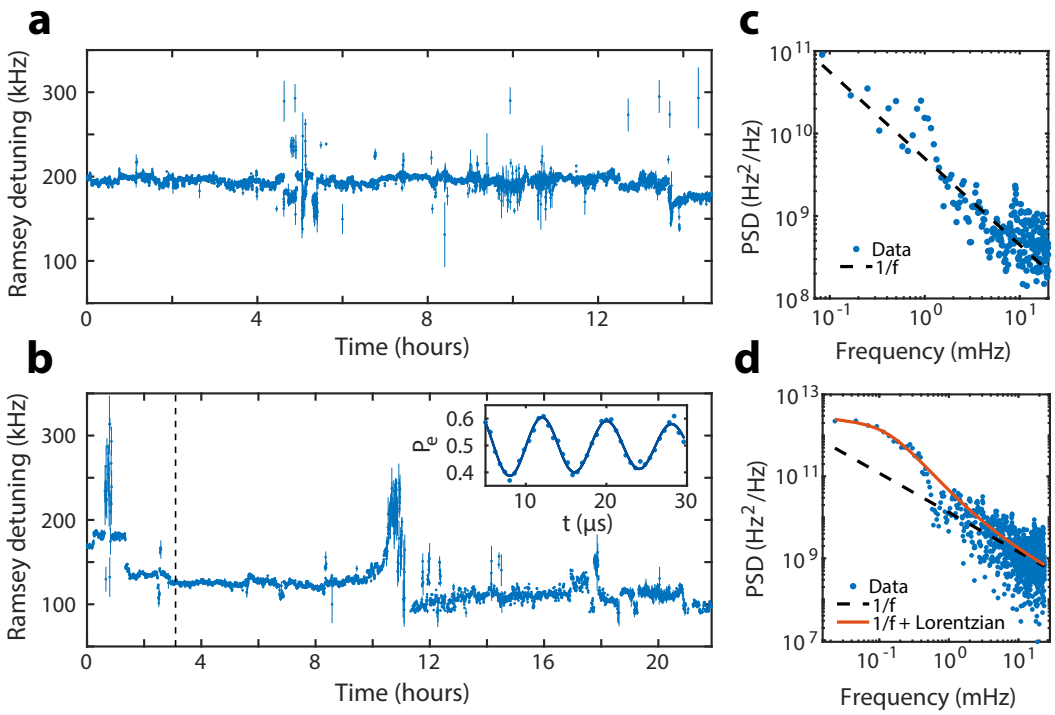


Figure 6.5: **Mechanical frequency fluctuations. a,** (**b,**) Ramsey frequency detuning of mechanical oscillator with voltage bias of 50 (40) V. As shown with an example in the inset of **b**, the Ramsey frequency is calculated using fits to the Ramsey interferometry of the oscillator conducted via the qubit. The error bars represent the 2σ confidence interval for the Ramsey frequency obtained through the fits. The 40 V operation point is chosen to bring TLS close to the mechanical oscillator. **c,** The frequency noise PSD of data in panel a, revealing $1/f^{\alpha}$ type noise with $\alpha = 1.0 \pm 0.1$. **d,** PSD of the data in panel b, demonstrating $1/f^{\alpha}$ type noise (with $\alpha = 0.96 \pm 0.08$) at large frequencies and added Lorentzian noise at low frequencies attributed to telegrapher noise from a dominant TLS.

Time-dependent dynamics of oscillation frequency is presented in Fig. 6.5a. By taking the Fourier transform of the time traces, the power spectral density of the frequency noise can be obtained (we use Welch's method for this process). The measurements are conducted approximately every 20 seconds, which sets an upper bound on the frequency of the PSD that can be captured without aliasing, known as Nyquist frequency. The PSD, as presented in Fig. 6.5c, reveals a $1/f^{\alpha}$ type spectrum, a characteristic feature of a variety of solid-state systems [200]. This type of frequency noise is quite often attributed to a bath of TLS defects. In our case, this $1/f$ spectrum agrees with frequency noise due to TLS-TLS interactions (see Eq. (6.22)).

In order to further investigate how this frequency noise is related to TLS, we change

the bias voltage in our system. Specifically, we adjust the voltage to tune a TLS to the spectral vicinity of our mechanical oscillator. When we look at the time series of frequency fluctuations, we see clear signatures of an increase in the frequency noise (see Fig. 6.5b). This voltage dependence of the frequency noise provides further evidence to the role played by TLS.

Looking at the noise PSD at this operation point, we interestingly see a deviation from the $1/f$ spectrum (see Fig. 6.5d). Instead, our PSD is better described by a Lorentzian added to the $1/f^{\alpha}$ noise floor. The Lorentzian corresponds to a telegrapher noise process, whose PSD is given by

$$S_{\delta\omega}(\omega) = \frac{\nu_1^2}{\pi} \frac{\gamma_1}{\gamma_1^2 + \omega^2}, \tag{6.23}$$

where γ_1 is the switching rate and ν_1 is the switching amplitude. From the fit, we extract $\gamma_1/2\pi = 0.1$ mHz and $\nu_1/2\pi = 40$ kHz for this telegrapher noise process.

Importantly, individual TLS are known to cause telegrapher-type frequency noise, where the switching rate of the process corresponds to the relaxation rate of the TLS [129]. Normally, the $1/f$ noise is obtained from the superposition of numerous Lorentzian processes. However, there can be instances where a single strongly coupled TLS dominates the noise [201], leading to a pronounced Lorentzian feature. The observed PSD can be attributed to a similar process.

Ramsey and Echo measurements

In the previous section, we established that the theory of TLS-induced frequency noise is consistent with our experimental observations of the power dependence, temperature dependence, and power spectral density (PSD) of the frequency noise. In this section, we turn to measurements of mechanical coherence, obtained from free induction (Ramsey) and Hahn echo experiments (see Section 5.3). Our goal is to relate these coherence measurements to the theoretical framework of TLS-induced dephasing.

As a starting point, we introduce the standard Gaussian theory of dephasing, following Ithier et al. [153]. This framework is of particular importance because, under the assumption of Gaussian frequency noise, the noise PSD fully determines the expected outcomes of both free induction and echo measurements.

First we start with describing the free induction measurement. The free induction signal ($f_{z,R}$) is related to the frequency noise $\delta\omega(t) = \omega_{\mathrm{m}}(t) - \bar{\omega}_{\mathrm{m}}$ (where $\bar{\omega}_{\mathrm{m}}$ is the

mean mechanical frequency) through the random accumulated phase

$$\Delta\phi = \int_0^t dt' \delta\omega(t'), \tag{6.24}$$

where $f_{z,R} = \langle \exp(i\Delta\phi) \rangle$. For a Ramsey free induction measurement, the signal $f_{z,R}$ corresponds to the envelope of the oscillations. Similarly, the echo signal $f_{z,E}$ is related to the frequency noise by an echo phase, that includes the refocusing effect of the echo experiment

$$\Delta\phi_E = \int_0^{t/2} dt' \delta\omega(t') - \int_{t/2}^t dt' \delta\omega(t'), \tag{6.25}$$

where $f_{z,E} = \langle \exp(i\Delta\phi_E) \rangle$.

In the presence of Gaussian frequency noise with power spectral density $S_{\delta\omega}(\omega)$, the free induction ($f_{z,R}$) and echo ($f_{z,E}$) signals can be expressed as

$$\ln\left(f_{z,R}(t)\right) = x_R(t) = -\frac{t^2}{2} \int d\omega S_{\delta\omega}(\omega) \mathrm{sinc}^2 \frac{\omega t}{2}, \tag{6.26}$$

$$\ln\left(f_{z,E}(t)\right) = x_E(t) = -\frac{t^2}{2} \int d\omega S_{\delta\omega}(\omega) \sin^2 \frac{\omega t}{4} \mathrm{sinc}^2 \frac{\omega t}{2}. \tag{6.27}$$

For white Gaussian noise, these results lead to an exponential decay with $x_R \approx x_E \approx t S_{\delta\omega}(0)/2$. Therefore, the echo process is expected to be inefficient in the case of white noise. Instead, noise that is concentrated at low frequencies is needed for the efficiency of the echo procedure. For example, Gaussian $1/f$ noise with $S_{\delta\omega}(\omega) = A/|\omega|$ gives rise to free induction and echo signals of the form

$$x_R(t) \approx -t^2 A \ln\left(\frac{1}{\omega_{\mathrm{ir}} t}\right), \tag{6.28}$$

$$x_E(t) = -t^2 A \ln 2, \tag{6.29}$$

where ω_{ir} is the infrared cutoff frequency, generally identified with the reciprocal of the averaging time. Therefore, for Gaussian $1/f$ noise, both Ramsey and echo signals have Gaussian functional (for Ramsey $\ln(1/\omega_{\mathrm{ir}} t)$ is approximately constant as a function of time throughout the measurement duration). The echo lifetime exceeds the Ramsey lifetime by a factor of

$$\frac{T_2^E}{T_2^*} \approx \sqrt{\frac{\ln\left(\frac{1}{\omega_{\mathrm{ir}} T_2^*}\right)}{\ln 2}}. \tag{6.30}$$

Despite observing $1/f$ type frequency noise (see Section 6.3) and seeing strong improvements with the echo procedure, the functional forms of our measured Ramsey

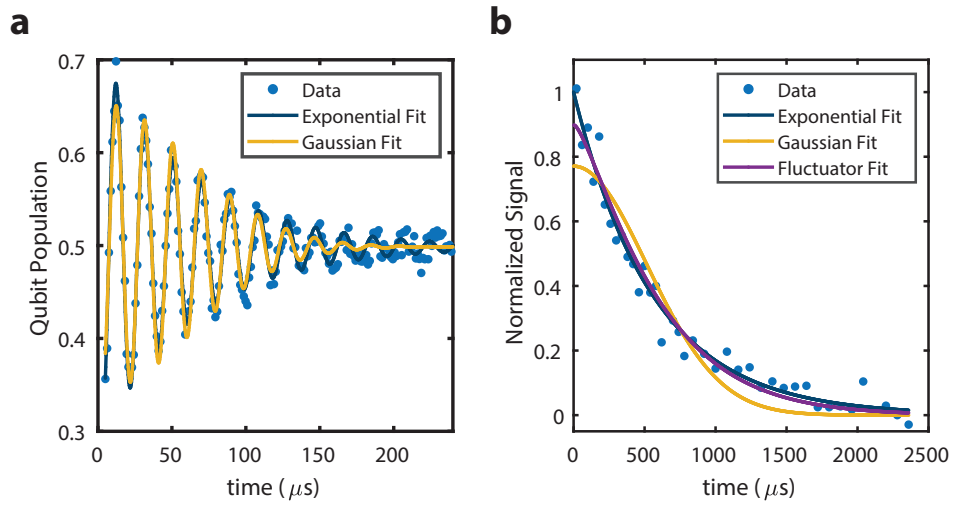


Figure 6.6: **Ramsey and echo fits. a,** Exponential and Gaussian fits to the Ramsey signal showing that the exponential fit better captures the coherence at long times. **b,** Different theory fits to the Hahn echo signal, with the exponential fit from the main text displayed with a Gaussian fit and a fluctuator model fit with $\gamma_{\max} = 10^5$ s^{-1}.

and echo signals are better described by exponential functions and are not Gaussian (see Fig. 6.6a and b), inconsistent with the predictions for Gaussian $1/f$ noise.

These observations are not too surprising, as the frequency noise originating from TLS-TLS interactions which was described in the previous section is non-Gaussian in general [129, 187]. This can be most easily seen by considering a single "telegrapher" noise process, where the frequency switches between two stable states $\pm\nu$ with a switching rate γ. This process is Gaussian only under the specific limit of $\nu \ll \gamma$ [202]. As thermal fluctuators possess a wide range of switching rates and amplitudes, only certain ones satisfy this Gaussian condition. In fact, in our measurements of noise PSD, we have observed signatures of a non-Gaussian noise process with $\nu \gg \gamma$ (see Fig. 6.5d).

In principle, the framework developed by Faoro and Ioffe [129] could be extended to derive functional forms for the free induction and echo signals. However, such an analysis is technically involved and lies beyond the scope of this thesis. Instead, we adopt the model proposed by Galperin et al. [203], which is rooted in TLS physics and, as will be shown below, reproduces the key qualitative features observed in our experiments.

Here, the frequency noise is modeled as an ensemble of telegrapher noise processes caused by thermal fluctuators, with amplitudes (ν) and switching rates (γ) having a

distribution of [203]

$$P(\nu, \gamma) = \frac{\xi}{\gamma \nu^2}. \tag{6.31}$$

The distribution is defined in the domain $[\nu_{\min}, \infty] \times [\gamma_{\min}, \gamma_{\max}]$ and ξ is a normalization parameter. The switching rates of thermal fluctuators (i.e. thermally active TLS) is given by their decay rates, which is set mainly by interactions with phonons [129]. $\gamma_{\min}$ is defined as the largest of two values: switching rate of the slowest fluctuator in the ensemble (observed to be $\lesssim$ 1 mHz [129]) and the reciprocal of the observation duration. This value turns out to be around $10^3 \mathrm{s}^{-1}$ in our case. $\gamma_{\max}$ is the switching rate of the fastest fluctuator in the ensemble. At our bath temperature of $\sim$ 70 mK the fastest fluctuators (with $\hbar\omega_{\mathrm{TLS}} \approx k_B T$) are expected to switch at a rate of $\gamma_{\max} \sim 10^5\ \mathrm{s}^{-1}$ based on previous observations [188]). First principle estimates for the TLS decay rate in the presence of 1D or 2D acoustic baths agrees with this number [139].

This distribution gives rise to noise with a $1/f$ power spectral density. The corresponding Ramsey and echo signals are given as

$$x_R(t) \approx -t\xi \ln\left(\gamma_{\max}/\gamma_{\min}\right), \tag{6.32}$$

$$x_E(t) \approx -t\xi \ln(\gamma_{\max} t). \tag{6.33}$$

The Ramsey signal has the exponential form noted in our experiments. The echo expression is valid when $t > \gamma_{\max}^{-1}$. We expect our experiments to satisfy this condition, as the dynamics of the most rapid fluctuator in the system should be faster than the echo timescale (i.e. $t \sim T_2^E \approx 500$ us $> \gamma_{\max}^{-1} \approx 10$ us). We observe that a fit to our data using the echo function in Eq. (6.33) with $\gamma_{\max} = 10^5$ shows good agreement, as seen in Fig. 6.6b.

It is important to note that the echo and Ramsey signals depend on the specific set of fluctuators that a device interacts with. This is in line with our observations of Ramsey and echo times showing variance with device and voltage (see Fig. 6.7). The voltage dependence can be potentially attributed to the TLS frequencies getting Stark shifted due to the electrostatic bias field, altering the fluctuator ensemble that the device interacts with.

The echo efficiency predicted by this model can be expressed as

$$\frac{T_2^E}{T_2^*} \approx \frac{\ln\left(\gamma_{\max}/\gamma_{\min}\right)}{\ln(\gamma_{\max} T_2^E)}. \tag{6.34}$$

The thermal fluctuators can exhibit a wide range of switching rates, as discussed above, leading to $\ln(\gamma_{\max}/\gamma_{\min}) \approx 20$. This results in an estimated echo efficiency of ≈ 5 for our devices. The estimate is in line with our average improvement of ≈ 6 (see Fig. 6.7).

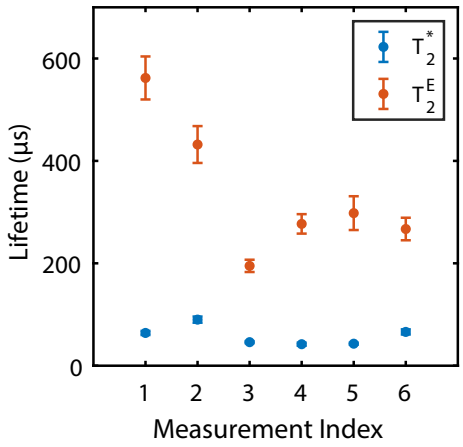


Figure 6.7: **Ramsey and Hahn echo coherence times.** Measurements of Ramsey and Hahn echo coherence times for mechanical oscillators A and B at different voltage operation points (labeled with a measurement index between 1-6), demonstrating the consistent efficiency of the echo procedure in removing frequency noise. The data points represent the coherence times extracted via theory fits; the error bars indicate the 2σ confidence intervals of the fits.

Therefore, we see that the model we have followed, can explain the observed power spectral density, functional forms of the Ramsey and echo signals, the improved lifetimes in the presence of dynamical decoupling, and voltage dependence of the lifetimes. We once more note that the probability distribution of the telegrapher noise processes, despite being physically motivated, is phenomenological and a more systematic analysis would have to depart from TLS-TLS interactions as a starting point [129].

Chapter 7

ROLE OF METALS IN ACOUSTIC DECOHERENCE

In the previous chapters (3-6), we have explored the mechanisms that lead to decoherence of our mechanical oscillators. In general, our results revealed that (i) two-level system defects play a significant role in acoustic decoherence, and (ii) devices with metalized moving parts tend to experience greater decoherence compared to their non-metalized counterparts.

In this chapter, we present measurements designed to investigate the impact of metals on acoustic coherence. These measurements are aimed at obtaining a better understanding of physical mechanisms underlying acoustic decoherence due to metals. Gaining such understanding is valuable for the development of future devices, as it could enable the realization of metalized moving capacitors that combine strong electromechanical coupling with minimal acoustic decoherence.

7.1 Experiment

We have observed that metal free mechanical oscillators (see Section 5.3) possess a lifetime of $\sim$ 25 ms, significantly larger than the $\sim$ 250 μs lifetime of metalized devices (see Section 4.4). A similar trend, though with a smaller relative difference, is seen in the coherence times: the metal free devices exhibit coherence times around 60 μs, whereas this value is only around 10 μs for the metalized devices. However, a one-to-one comparison between these devices is challenging, since they feature different acoustic shields, and beam geometries while being fabricated through different processes.

In order to better isolate contributions to acoustic decoherence from metals, we devise an experiment where the only variable is the presence or absence of metal on the central beam of our moving capacitor. We use identical beam geometries and phononic shields, as can be seen in Fig. 7.1a,b. For the metalized devices, we deposit 15 nm of aluminum on the central beam using electron beam evaporation, with the film thickness verified by atomic force microscopy. Electron microscopy revealed that a portion of the sidewalls were coated with aluminum as well. This is potentially due to the finite angular spread of the material flux and sticking during evaporation. All of the devices are fabricated on the same chip to exclude chip to

chip variations.

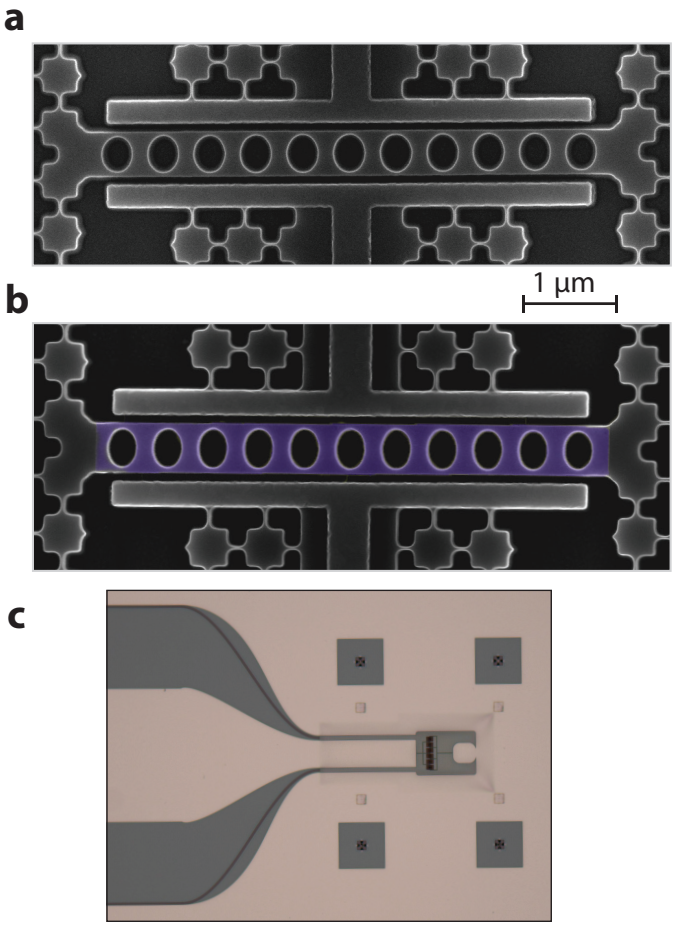


Figure 7.1: **Chip Image. a,b,** False colored electron microscope image showing the top view of moving capacitors with metal free (**a,**) and metalized (**b,**) central beam. The metal on the outer electrodes is not colored. The purple shading indicates the aluminum on the beam for the metalized device. **c,** Optical microscope image of the coplanar waveguide and moving capacitor. The rectangular features around the waveguide are alignment markers.

The moving capacitors are connected to a coplanar waveguide (see Fig. 7.1c), which serves both to provide the voltage bias necessary for the electromechanical interaction and to drive and read out the mechanical motion.

We first characterize the temperature dependence of the frequency of our mechanical oscillators. As can be seen in Fig. 7.2, the TLS model (Eq. (6.13)) can accurately model the experimental behavior for both devices. This suggests that for the metalized devices, TLS play a major role in the modifying the oscillator frequency.

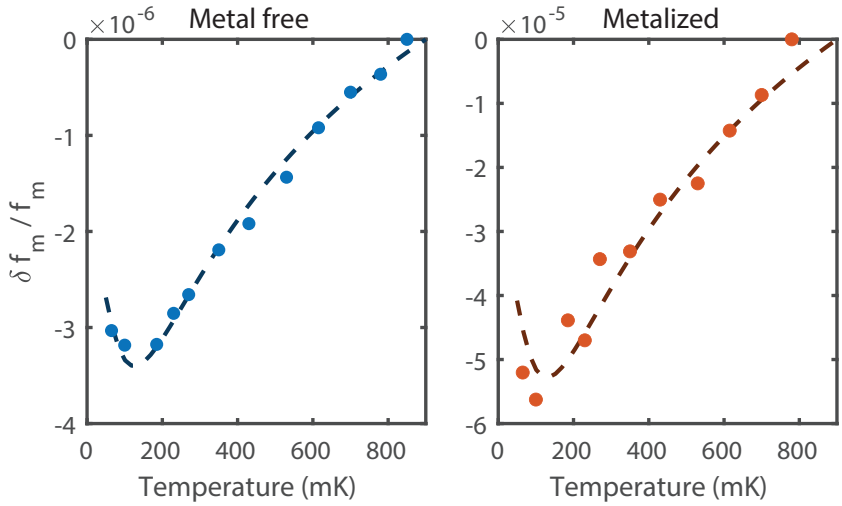


Figure 7.2: **Mechanical frequency shift with temperature.** The measured change in the mechanical frequency as a function of the cryostat temperature is indicated by the blue (red) markers for the metal free (metalized) device (the metal free device data was previously presented in Fig. 6.3). The blue (red) dashed line is a fit to Eq. (6.13). For the fit to the metal free device, we keep the parameters that we used for modeling TLS in metal free devices and only use a scaling factor of 0.72 to match the experimental data (for details see the discussion in Section 6.3). While fitting the metalized device data, we keep the scaling factor and the interaction rate identical to the metal free device, while setting the TLS density as the only variable. This fit gives us $\delta/2\pi = 4.5$ MHz, corresponding to a TLS density for the metalized devices ($\rho = 220\ \mathrm{GHz}^{-1}$) that is a factor of 15 larger than the metal free devices.

Based on the model, we can compare the TLS density of the metalized devices with the metal free ones. For this purpose, we assume that the average TLS-mechanics interaction rate isn't modified through the introduction of the metal and only the TLS density changes. Allowing the TLS density of the metalized device to vary as a free parameter in the fit, we obtain a density of $\rho = 220\ \mathrm{GHz}^{-1}$, which is a factor of 15 larger than the metal free devices. This suggests that one way metals could contribute to excess decoherence is by increasing the TLS density. We discuss potential mechanisms underlying the increase in TLS density later in this chapter.

Since TLS lead to frequency noise alongside frequency shifts (for details of the underlying physics see Chapter 6), we would expect the metalized device to experience more severe frequency noise than the metal free device, as it has a larger TLS density. To investigate this, we can measure the linewidth of the mechanical oscillators ($\Gamma_m = \Gamma_{1,m} + 2\Gamma_\phi$). This is achieved by probing the oscillators in reflection with a VNA, where the measurements are then fit to theory. We obtain a mechanical

linewidth of $\Gamma_m/2\pi = 6.0$ kHz (40.6 kHz) for the metal free (metalized) devices, as shown in Fig. 7.3. As will be discussed later, these linewidths are not decay-limited, with most of the contribution arising from frequency noise (i.e. $\Gamma_m \approx 2\Gamma_\phi$). These results indicate that the higher TLS density in the metalized device directly correlates with increased frequency noise.

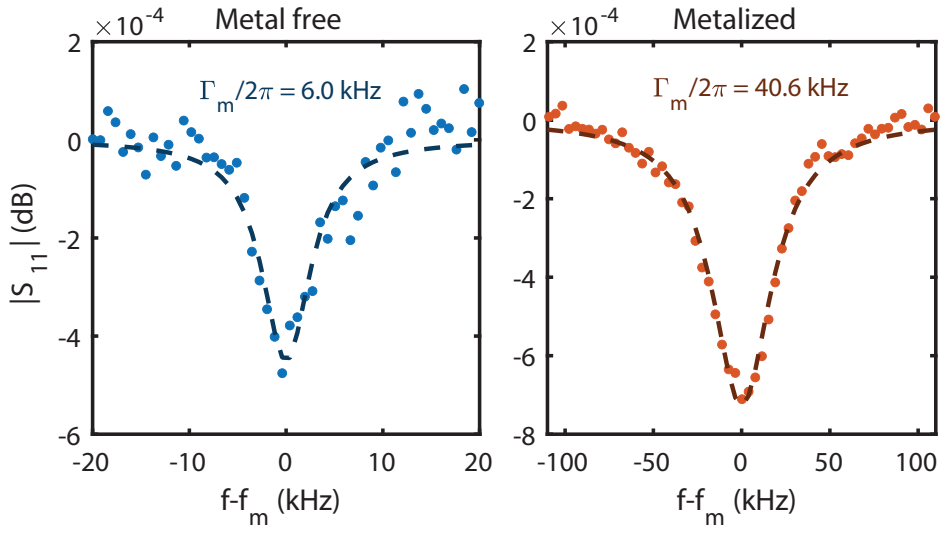


Figure 7.3: **Mechanical linewidth.** Blue (red) data points show the magnitude of the normalized reflection ($|S_{11}|$) of the metal free (metalized) mechanical oscillators. The dashed lines are theory fits to the response of a one-sided cavity, which is used to extract the mechanical linewidth. The linewidth is noted above the data for each plot. From the fit, we can also extract the decay rate into the waveguide to be $2\pi \times 0.2$ Hz ($2\pi \times 3$ Hz) for the metal free (metalized) device. This rate will be utilized later on in our analysis of driven response.

We then move on the measurements of the mechanical lifetime for these devices. For the metal free device, we are able to conduct a ringdown measurement, where we measure its lifetime to be $T_{1,m} \approx 15$ ms. However, for the metalized device, we find that sufficiently populating the device and reading out the mechanical motion is challenging due to its larger linewidth. Instead, we rely on the steady-state driven response of these mechanical oscillators to characterize their lifetime, as this method doesn't require temporally resolving the free decay, allowing measurements at lower SNR levels.

The detailed theory of this measurement can be found in Appendix A.4. Here, we briefly summarize its basics. When an oscillator with frequency noise is driven, there exists both elastic and inelastic scattering processes. The elastic response corresponds to emission of phonons that maintain a fixed phase relation to the

drive (set by the delay between the absorption and emission events). In contrast, the inelastic response corresponds to the emission of phonons without any phase relation to the drive, due to frequency noise in the oscillator. We quantify the relative strengths of these two processes by the number of elastically (n_{coh}) and inelastically (n_{inc}) scattered phonons, which are directly related to the decoherence rates of the mechanical oscillator as

$$\frac{n_{\mathrm{inc}}}{n_{\mathrm{coh}}} = \frac{\Gamma_{\mathrm{m}}}{\Gamma_{1,\mathrm{m}}} - 1. \tag{7.1}$$

Therefore, by measuring the phonon populations corresponding to each process, we can calculate our lifetime $1/\Gamma_{1,\mathrm{m}}$.

First, we utilize this method to characterize the metal free device (see Fig. 7.4), where we calculate a lifetime of 19 ms, in relatively good agreement with the ringdown measurement (15 ms). Next, we investigate the driven response of our metalized device, from which we calculate a lifetime of 67 μs ($\Gamma_{1,\mathrm{m}}/2\pi = 2.4$ kHz). These measurements demonstrate that the metalized device experiences significantly more acoustic loss compared to metal free devices.

We note that we have characterized one more metalized mechanical oscillator, which exhibited a total linewidth of $\Gamma_{\mathrm{m}}/2\pi = 53$ kHz and a lifetime of $1/\Gamma_{1,\mathrm{m}} = 25$ μs, providing further evidence to the excess decoherence experienced by the metalized devices.

7.2 Discussion

We have obtained systematic results that allows us to correlate excess acoustic decoherence with the presence of metal on the moving parts of our electrostatic transducers. In the following, we discuss in greater detail the specific mechanisms by which aluminum can contribute to acoustic decoherence.

The TLS density extracted from the frequency shifts is expected to accurately capture the difference in TLS density between the two devices. This is because, unlike decoherence rates, the frequency shift is largely insensitive to the individual TLS configuration and decoherence rates. We note that the weak temperature dependence of the frequency shift in TLS theory ($\delta\omega_{\mathrm{m}} \propto \ln T$ when $\hbar\omega_{\mathrm{m}} \ll k_b T$) is quite distinct from frequency shifts due to quasiparticles, which is expected to scale exponentially with temperature below the superconducting transition temperature [105].

Therefore, we have unambiguous evidence of the excess TLS due metalization of our devices. The extra TLS observed in the metalized devices can potentially arise

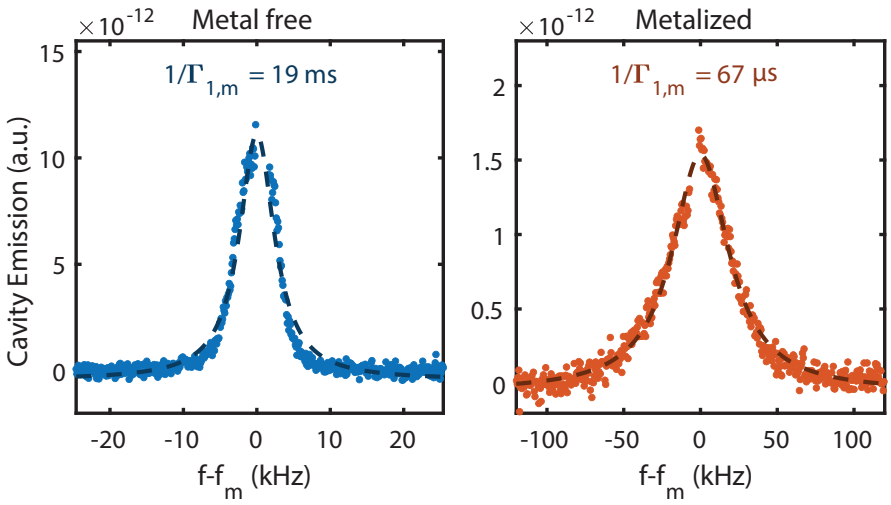


Figure 7.4: **Driven response of mechanical oscillator.** Blue (red) data points indicate the inelastic scattering of phonons from the metal free (metalized) mechanical oscillators, as measured by a spectrum analyzer. The background corresponding to amplifier noise has been subtracted from these measurements alongside the drive tone. The dashed lines are theory fits that are used to extract the mechanical linewidth and calculate the total inelastic scattering. The linewidth obtained from the fit is $\Gamma_m/2\pi = 5.8$ kHz (45 kHz) for the metal free (metalized) devices, in reasonable agreement with the VNA measurements shown in Fig. 7.3. By analyzing the data, we obtain $n_{\mathrm{coh}} = 5.7 \times 10^2$ (5×10^2) and $n_{\mathrm{inc}} = 3.1 \times 10^4$ (4.9×10^2) for the metal free (metalized) devices, from which we calculate the lifetimes indicated on the plots. As our ringdown measurements are phase-insensitive, they measure the mean number of phonons (i.e. $n_{\mathrm{inc}} + n_{\mathrm{coh}}$), which is much smaller for the metalized device, underlying the challenge of conducting ringdown measurements with it.

from two contributions: surface and bulk. It is well known that the surface oxide of aluminum (alumina) and the aluminum-silicon interface are amorphous regions and can therefore host TLS [113].

Beyond these surface contributions, polycrystalline aluminum films have been observed to exhibit excess dissipation compared to single-crystal aluminum [204, 205]. This loss has been identified as originating within the bulk of the material, and its magnitude has been measured to be consistent with that of glassy materials [205, 206]. Recent measurements have further shown that TLS density increases proportionally with aluminum film thickness [149]. Taken together, these observations strongly suggest that TLS may reside not only at the surfaces but also within the bulk of polycrystalline aluminum films, such as those we evaporated.

For our devices, we are unable to disentangle the contributions of surface and bulk

TLS in aluminum, since we have only measured devices with a single film thickness. In the future, systematic studies in which the aluminum thickness is varied could allow these two potential sources of TLS to be separated.

Now that we have established that the metalized devices possess a larger TLS density, we discuss whether the increased TLS density can explain the larger decoherence rates.

As discussed previously (see Section 4.9), TLS is expected to be the only mechanism that causes significant frequency noise in our devices. Consistent with this expectation, the higher TLS density in the metalized devices manifests as increased frequency noise. Consequently, the excess frequency noise can most likely be attributed to the larger TLS density in these devices. Though the the ratio of the two linewidths (6) do not precisely match the ratio of the extracted TLS densities (15), this can be due to the dependence of the frequency noise on other factors such as TLS decoherence rates.

The situation pertaining to acoustic loss is more complex, as the presence of the metal on our device introduces extra loss channels. One of these is electron-phonon scattering, where electrons in aluminum behave like a viscous gas and cause acoustic damping [207]. We model this contribution to acoustic loss in our devices (see Appendix C.1 for details), where we estimate that this mechanism would limit the quality factor to approximately 10^{10}, much larger than the measurement result ($Q = 2\times10^{6}$). A second mechanism is Ohmic loss: deformation of the piezoelectric resonator generates spatially varying electrostatic potentials, which in turn drive electrical currents and produce Joule heating. This process is proportional to the real part of the film's surface impedance [45]. Because the inversion layer on silicon (see Section 2.4) is expected to have a substantially larger surface resistance than superconducting aluminum, we expect Ohmic losses to be more pronounced in the inversion layer than in the metal electrodes. Consequently, the Ohmic contribution should not increase for the metalized devices.

Taken together, these considerations suggest that direct interactions with quasiparticles is unlikely to play a significant role in limiting the acoustic quality factor. This suggests that TLS may still be a dominant mechanism for acoustic loss, consistent with our previous evaluation of loss mechanisms in metalized devices (see Chapter 4).

For TLS-induced acoustic loss mechanisms, relaxation damping is expected to

scale linearly with the TLS density, while resonant absorption is expected to scale quadratically with the TLS density (see Section 6.2). Therefore, resonant absorption is expected to dominate in the metal-covered devices. Indeed, we find that the ratio of the mechanical lifetimes of the two devices (280) is comparable to the square of the TLS density ratio (225), supporting this hypothesis. We note that non-equilibrium quasiparticles can also alter the TLS loss by providing electrical relaxation channels to TLS. Although this electrical decay of TLS is typically small [208], it may become significant when compared to the enhanced TLS lifetimes within the acoustic bandgap, as recently observed experimentally [168].

Collectively, all of our observations suggest that increased TLS density due to metals plays a major role in the increased decoherence of metalized oscillators. Nevertheless, more systematic studies that probe the temperature and quasiparticle density dependence of acoustic decoherence are required to rigorously disentangle the various decoherence mechanisms and quantitatively establish their relative contributions. The temperature dependent studies can be conducted in a way similar to the data presented in Chapter 6. The quasiparticle dependence can be explored by using large magnetic fields to cause transition into a normal state for aluminum [209].

A better understanding of the acoustic decoherence from metals can provide avenues for their mitigation. For example, metals with lower surface TLS densities or epitaxially grown single-crystal metals could be employed to reduce the TLS densities [210, 211]. Alongside practical benefits, more extensive characterization of devices can help answer still open questions about TLS in polycrystalline metals (discussed in Chapter 8) [204, 205].

Chapter 8

OUTLOOK

In this chapter, we outline potential directions for future research that build upon the results presented in this thesis. We will explore two main directions: (i) utilizing the mechanical oscillators for quantum information processing and (ii) further exploring the physics of microscopic defects.

8.1 Quantum Information Processing with Mechanical Oscillators

Within the field of circuit quantum electrodynamics, bosonic elements in the form of microwave resonators are ubiquitous. By combining the relatively high coherence of microwave resonators ($T_1 \gtrsim 1$ ms for 3D cavities and $T_1 \gtrsim 50\ \mu$s for planar devices) with large coupling strengths to nonlinear superconducting circuits ($g/2\pi \gtrsim 10$ MHz), universal quantum control of bosonic modes has been achieved [170, 212, 213]. The high degree of controllability afforded by these systems, together with the ability to engineer strong nonlinear interactions, has established microwave resonators as valuable resources for both computation and storage. On the computational side, they have been used to engineer error-protected states [214, 215] and implement quantum error-correction protocols [216–218]. On the storage side, they have been explored as quantum memories [219–221].

Mechanical oscillators can be potentially utilized for these tasks, where they possess advantageous properties (as demonstrated in Chapter 5): (i) their footprints are more than three orders of magnitude smaller than those of planar microwave resonators and (ii) their intrinsic lifetimes can exceed those of the best planar microwave resonators by over an order of magnitude. Therefore, mechanical oscillators are situated in an attractive position for potentially construction scalable architectures that store and process quantum information [11, 12, 120].

However, these advantages do not simply imply that mechanical oscillators are superior to microwave resonators. Realistic architectures must consider factors such as error rates, which are often dominated or strongly influenced by ancillary superconducting elements. Identifying the specific architectures and parameter spaces in which mechanical oscillators provide a genuine functional advantage over microwave resonators is therefore a nontrivial challenge.

Mechanical Memory

Here, we examine the use of mechanical oscillators as memory elements. In analogy with classical computing architectures, a memory element in a superconducting quantum processor could serve as a long-lived storage unit, while faster processing units interact with it by reading and writing information at slower rates [222]. Beyond computation, quantum memories can be utilized in quantum networking with superconducting qubits. For instance, many remote entanglement generation protocols require the storage of quantum information for at least the duration of the photon transmission ($\approx 5\mu$s per km of fiber) [223, 224]. The need for highly coherent quantum memories become even more prominent when entanglement distillation is required to boost Bell state fidelities [225].

Because mechanical oscillators can exhibit exceptionally long lifetimes, it is natural to consider them as a candidate platform for constructing quantum memories: during idle periods they could accumulate significantly fewer errors than their electrical counterparts. However, their electromechanical interaction rate is also much smaller than the strong electrical coupling that can be engineered between qubits and microwave resonators, so the fidelity of control operations on mechanical modes is expected to be lower. Therefore, the utility of these mechanical oscillators as memories would be dependent on the achievable control fidelities alongside the required idle times.

We look at storing arbitrary quantum states within the single excitation manifold of the bosonic elements (i.e. any properly normalized wavefunction of the form $|\psi\rangle = \alpha\,|0\rangle + \beta\,|1\rangle$). We explore a scenario where the state will be initially present in a qubit without any errors, swapped to the oscillator with fidelity $\mathcal{F}_s$, stored in the oscillator for an idle duration t_i with fidelity $\mathcal{F}_i$ and be swapped back to the ancilla qubit (similar to the state preparation and storage protocol explored in Chapter 5).

Here, ancilla qubit has decay (pure dephasing) rate of γ (γ_ϕ) and the oscillator has a decay (pure dephasing) rate of κ (κ_ϕ). We assume that the decoherence rate of the ancilla qubit is much larger than that of the oscillator (i.e., $\gamma + \gamma_\phi \gg \kappa + \kappa_\phi$). We furthermore assume that the dressed decoherence of the oscillator due to the qubit can be made negligible during the idling, potentially by frequency shifting the qubit or utilizing a parametric interaction.

The average fidelity (defined as an average over the Bloch sphere) of the swap and

idling operations are [40]

$$\mathcal{F}_s = 1 - \left(\frac{\gamma}{6} + \frac{\gamma_\phi}{8}\right) t_{\text{swap}}, \tag{8.1}$$

$$\mathcal{F}_i = 1 - \left(\frac{\kappa}{3} + \frac{\kappa_\phi}{6}\right) t_{\text{i}}, \tag{8.2}$$

where t_{swap} is the swap duration.

We note that the swap operation can be achieved either resonantly or via sideband interactions [40]. We focus on the resonant case, which we had experimentally explored (see Chapter 5). Here, the swap duration is given as $t_{\text{swap}} = \pi/2g$, where g is the interaction rate between the oscillator and the ancilla qubit.

As the protocol involves two swaps with idling in between, the fidelity of the full protocol can be expressed as

$$\mathcal{F} \approx \mathcal{F}_s^2 \mathcal{F}_i. \tag{8.3}$$

One can also envision a protocol that incorporates dynamical decoupling in the form of an echo pulse applied midway through the idling period. The echo can be implemented by swapping the excitation to the qubit, doing a pi-pulse, and swapping it back to the oscillator (for an example see Fig. 5.5). The resulting fidelity of the echoed sequence is

$$\mathcal{F}_{\text{e}} \approx \mathcal{F}_s^4 \mathcal{F}_i, \tag{8.4}$$

where we assume that the pi-pulse on the qubit can be performed with unity fidelity. For the echo procedure, the dephasing rate in calculations of the idling fidelity would be an echoed dephasing rate, $\kappa_{\phi\text{e}}$.

Armed with these expressions, we can compare the fidelities for a microwave memory and a mechanical memory. We assume that both bosonic elements are controlled with an ancilla qubit with $1/\gamma = 10$ μs and no pure dephasing ($\gamma_\phi = 0$).

For the microwave oscillator, we assume it experiences no pure dephasing (i.e. $\kappa_{\phi,\text{r}} = 0$) and has a lifetime of $1/\kappa_{\text{r}} = 100$ μs. Furthermore, we assume it is coupled to the qubit with a rate of $g_{\text{r}}/2\pi = 50$ MHz.

For the decoherence rates of the mechanical oscillator, we rely on the measurements presented in Chapter 5. Therefore, we set $1/\kappa_{\text{m}} = 25$ ms, $1/\kappa_{\phi,\text{m}} = 60$ μs and $1/\kappa_{\phi\text{e,m}} = 550$ μs. Utilizing these decoherence rates, we can calculate the memory infidelity ($1 - \mathcal{F}$) for the mechanical oscillator for two electromechanical interaction rates: (i) $g_{\text{em}}/2\pi = 0.25$ MHz which is the value of the devices we have characterized

and (ii) $g_{\mathrm{em}}/2\pi = 2$ MHz corresponding to a potential future scenario where the interaction rate can be significantly extended.

The calculations are presented in Fig. 8.1. Owing to the relatively weak electromechanical coupling, swap errors constitute the dominant contribution to the mechanical memory infidelity at short idle times. At longer idle times, the echo protocol yields a clear advantage over the case without dynamical decoupling for the mechanical oscillator, despite the additional swap overhead. Finally, we observe that the performance of the echoed mechanical memory can surpass the microwave resonator at sufficiently long idle times (around $t_{\mathrm{i}} = 2\ \mu$s and 20 μs for larger and smaller interaction rates respectively).

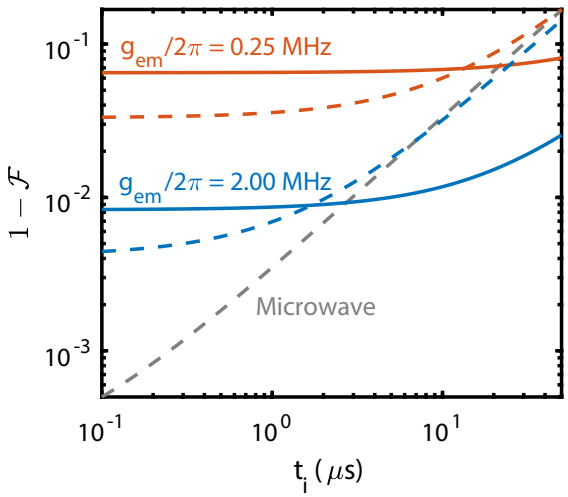


Figure 8.1: **Memory infidelity.** The infidelity $(1 - \mathcal{F})$ of the microwave memory as a function of the idle time is shown with the grey dashed lines. The red solid (dashed) lines demonstrate the infidelity in the presence (absence) of dynamical decoupling, for an electromechanical interaction rate of $g_{\mathrm{em}}/2\pi = 0.25$ MHz, which is the measured value of our devices. The blue lines repeat the same calculations assuming an interaction rate of $g_{\mathrm{em}}/2\pi = 2$ MHz.

These results demonstrate that the high coherence of the mechanical oscillators can enable their employment as quantum memories in regimes where longer storage times (exceeding microseconds) are required. Moreover, the most direct route toward further reducing the infidelity for these timescales is to increase the electromechanical interaction rate and improve the ancilla qubit coherence, suppressing the swap errors.

Hardware-Efficient Computation

Having focused previously on the use of our mechanical oscillators as quantum memories, here we focus on their potential future use in hardware efficient quantum computation.

As we have demonstrated in our experiments (see Fig. 4.1), multiple mechanical oscillators can be connected to a single superconducting qubit owing to their compact footprint. In such a configuration, the qubit can be used to engineer universal gates between arbitrary pairs of mechanical oscillators, which would behave as qubits in the single excitation manifold (i.e. superpositions of zero phonon and single phonon Fock states) [12, 120]. This architecture is appealing due to two key reasons.

First, the ability to implement gates between any selected oscillators leads to substantially improved connectivity compared to conventional superconducting qubit architectures, where interactions are typically limited to nearest neighbors. Achieving such improved connectivity could significantly benefit quantum computation. For instance, it could enable the implementation of quantum low-density parity-check (qLDPC) error-correction protocols, which can exhibit more favorable scaling of rate and distance than the surface code [226], thereby reducing the overall hardware overhead.

Second, because multiple mechanical oscillators can share a single superconducting qubit for control, the architecture effectively realizes a multi-qubit register within the footprint of a single superconducting qubit. Together, these features suggest a promising route toward hardware-efficient quantum computation based on mechanical oscillators.

Universal quantum computation in this architecture can be achieved by engineering beamsplitter interactions between pairs of bosonic modes, together with controlled-phase (CZ) gates (though the precise requirements depend on the chosen logical encoding) [12]. Below, we discuss how these gates can be realized.

Multiple protocols exist for controlling bosonic modes using superconducting qubits. One approach implements gates directly through qubit–oscillator interactions, where real qubit excitations participate in the dynamics [120, 220]. Alternatively, one can implement virtual gates between oscillator modes by exploiting the qubit's nonlinearity, such that the qubit participates only virtually in the interaction [12]. In practice, experiments typically employ a combination of these strategies: beamsplitter interactions utilize the four-wave-mixing capability of the qubit, while CZ

gates rely on the qubit as a logical element that control the interaction [227, 228].

Here, following Hann et al. [12], we focus on the special case where the beamsplitter and controlled-phase operations are all implemented virtually. The main strength of this approach is that in principle all of the operations are parallelizable, something that is not possible when the qubit must directly take part in the gates. The two and three mode interactions between bosonic modes, which implement the beamsplitter and CZ operations respectively, can be described by the following Hamiltonians

$$\hat{H}_{\text{int},2}/\hbar = g_2(\hat{b}_A\hat{b}_B^\dagger + \hat{b}_A^\dagger\hat{b}_B) \tag{8.5}$$

$$\hat{H}_{\text{int},3}/\hbar = g_3(\hat{b}_A\hat{b}_B\hat{b}_C^\dagger + \hat{b}_A^\dagger\hat{b}_B^\dagger\hat{b}_C), \tag{8.6}$$

where $\hat{b}_i$ are the annihilation operators for the bosonic modes labeled by the index $i = A, B, C$. g_2 (g_3) is the interaction rate given by

$$g_2 = -2\alpha\frac{g_{\text{em}}^2}{\Delta_A\Delta_B}\frac{\Omega_1\Omega_2}{\delta_1\delta_2}, \tag{8.7}$$

$$g_3 = -2\alpha\frac{g_{\text{em}}^3}{\Delta_A\Delta_B\Delta_C}\frac{\Omega_1}{\delta_1}, \tag{8.8}$$

where g_{em} is the interaction rate between mechanical oscillators and qubit, which are detuned by $\Delta_A = \omega_A - \omega_q$. There exist drives on the qubit of strength Ω and detuning δ, whose their frequencies satisfy the four-wave mixing condition. The frequency matching condition for the two-mode (three-mode) interaction is $\omega_2 - \omega_1 = \omega_B - \omega_A$ ($\omega_1 = \omega_A - \omega_B - \omega_C$). We furthermore note that the above expressions are valid in the limit $\Delta \gg \alpha, g_{\text{em}}$.

We next focus on the infidelity for the SWAP and CZ gates, which is given as

$$1 - \mathcal{F}_{\text{SWAP}} \approx \frac{\kappa\pi}{2g_2} + \left(\frac{g_2}{\Delta\nu}\right)^2, \tag{8.9}$$

$$1 - \mathcal{F}_{\text{CZ}} \approx \frac{\kappa\pi}{g_3} + \left(\frac{g_3}{\Delta\nu}\right)^2. \tag{8.10}$$

Here $\Delta\nu$ is a parameter that quantifies the frequency non-uniformity of the mechanical oscillators. This non-uniformity is important since the selectivity of the gates is dependent on satisfying precise frequency matching conditions. For instance, if the mechanical oscillators were to possess a uniform free-spectral range, the two qubit gates would be applied to all neighboring mechanical oscillators.

In systems with uniform free-spectral range such as bulk acoustic modes, this non-uniformity is challenging to satisfy. However, for our phononic crystal oscillators,

the mechanical frequencies can be targeted. For arbitrary two node connectivity, the optimal frequency non-uniformity can be expressed as $\Delta\nu = 2D/(N(N-1)-2)$, where D (N) is the frequency span (number) of the oscillators [229].

We then proceed to explore the infidelity of the operations for an optimistic future scenario where the electromechanical interaction rate has been significantly boosted to $g_{\mathrm{em}}/2\pi = 10$ MHz. The decoherence rates of the mechanical oscillator (qubit) is assumed to be $1/\kappa_{\mathrm{m}} = 500\ \mu$s ($1/\gamma_{\mathrm{q}} = 10\ \mu$s).

We analyze how the infidelity scales with the number of oscillators, as shown in Fig. 8.2. Our calculations indicate that as the number of mechanical oscillators increases, the infidelity grows rapidly due to the scaling $\Delta\nu \propto N^{-2}$. Nevertheless, arbitrary connectivity among approximately 20 mechanical oscillators can still be achieved with infidelities at the few-percent level. These calculations suggest that significant hardware efficiency and enhanced connectivity could potentially be achieved in the future by using multiple mechanical oscillators controlled by a single transmon qubit.

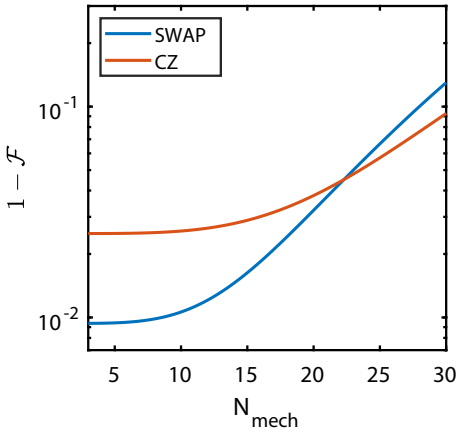


Figure 8.2: **Virtual gate infidelity.** The infidelity $(1-\mathcal{F})$ of SWAP and CZ operations between mechanical memory as a function of the number of oscillators, based on Eq. (8.10). For the calculations, we have assumed $g_{\mathrm{em}}/\Delta = 1/10$, $\alpha/2\pi = 100$ MHz, $D/2\pi = 100$ MHz, $\Omega/\delta = 0.2(0.3)$ for SWAP (CZ) gates.

Technical Improvements

The preceding discussion highlights the importance of enhancing both the coherence of the ancilla qubit and the electromechanical interaction rate to improve the performance of our hybrid quantum system. In the following, we outline potential strategies for achieving these improvements.

Qubit coherence In our experiments where we have used the transmon as an ancilla qubit to control mechanical motion (see Chapter 5), we have observed a qubit lifetime ($T_1 \approx 1.6\ \mu$s) and coherence time ($T_2^* \approx 1.2\ \mu$s), values that fall well below those of state-of-the-art transmon qubits. Below, we discuss possible approaches to improving both quantities.

First we focus on the qubit lifetime. A significant source of loss for the qubit arose from the imperfect operation of the filter in our experiments, as discussed in Section 5.5. The filter suppressed the decay rate to the waveguide only to $2\pi\times40$ kHz level, imposing a radiative lifetime limit of $\approx 4\ \mu$s. Full-chip simulations indicate that this limitation originates from unintended capacitive coupling between the filter and the transmon. To mitigate this effect, we redesigned the filter geometry by shifting the charge antinode farther from the qubit, thereby reducing this coupling. Simulations of the revised design predict a radiative lifetime limit exceeding 50 μs.

Even after accounting for radiative loss, the intrinsic qubit lifetime still remains relatively short ($\approx 3\,\mu$s). As we have just characterized a single geometry, we cannot unambiguously identify prominent loss mechanisms for the qubit. Conducting a systematic study, for example by examining how the loss scales with the participation ratios of different interfaces, can help identify the dominant contributions to loss [230]. Such insights may then enable mitigation strategies, for example through redesigning the device geometry or through improved surface treatments [135].

Alternatively, a flip-chip approach can be employed. In this scheme, only the mechanical device would be fabricated on a SOI substrate, while the qubit chip can utilize a different substrate, such as high-resistivity silicon or sapphire [159, 160]. These substrates are advantageous for microwave coherence because they lack the sacrificial oxide layer of SOI and possess very low loss tangents [135, 182, 231]. In our laboratory, qubits fabricated on silicon have exceeded lifetimes of 20 μs. Integrating such qubits with mechanical oscillators via a flip-chip process therefore offers a realistic route to significantly extending the qubit lifetime.

Alongside the lifetime, the qubit coherence time has to be improved as well. In our experiments, we saw that a significant contribution to qubit dephasing came from flux noise in our frequency tunable transmon qubits (see Section 5.5). We characterized the flux noise amplitude to be substantially larger than values reported for state-of-the-art SQUID loops. Improvements in the the SQUID loop design and fabrication processes can potentially reduce this noise and the associated dephasing [166].

As an alternative approach, one could employ fixed-frequency qubits, which are intrinsically insensitive to flux noise. Due to the small electromechanical interaction rate, this approach requires precise frequency targeting, which could be achieved through post-fabrication tuning techniques for the qubit [232, 233]. Once the qubit frequency is close enough to that of the mechanical oscillator, AC Stark shift can be used to achieve the desired detuning [234].

Electromechanical interaction rate

We have taken great care to maximize the electromechanical interaction rate for our devices by optimizing the phononic crystal design (see Section 3.3). However, despite the improvements obtained via this approach, further enhancements to the electromechanical interaction rate are still needed. This can be achieved via two main methods: (i) reducing the vacuum gap dimensions and (ii) employing superconducting qubits with large phase fluctuations. We expand on these below.

The electromechanical interaction rate depends strongly on the vacuum gap dimension (d) for our geometry, scaling as $g_0 \propto d^{-1.3}$ (see Fig. 3.7). In our experiments, the vacuum gap dimensions were around 70 nm (see Fig. 4.1d and Fig. 5.1b), limited by challenges in achieving very small critical dimensions with positive electron beam resist used in our lithography steps. Features with smaller critical dimensions can be fabricated by utilizing alternative techniques such as hard masks [65, 156] and focused ion beam litography [235]. An alternative approach that enables the formation of narrow vacuum gaps without requiring the fabrication of smaller critical dimensions is self-assembly [236].

In our experiments, we have employed a transmon qubit due to its relatively high coherence, ease of fabrication and control. However, transmon qubits inherently exhibit small phase fluctuations, since they are instead designed to possess large charge fluctuations in order to suppress charge noise [55]. This design choice limits the achievable electromechanical interaction rate. As an alternative to the transmon, one can utilize superconducting qubits with large phase fluctuations such as a fluxonium. We can estimate how much the electromechanical interaction strength would be enhanced by moving to a fluxonium qubit by comparing the phase transition matrix elements (φ_{ge}, which sets interaction rate as seen in Eq. (2.50)). For our transmon with $E_J/E_C = 70$, this transition matrix element is $\varphi_{ge} \approx (2E_C/E_J)^{1/4} = 0.4$. By contrast, heavy fluxonium devices can reach much larger φ_{ge} values, as high as π [157]. Therefore, transitioning from a transmon to a fluxonium can, in principle, enhance the electromechanical interaction rate by roughly a factor of 8. We note that

moving to a fluxonium would also likely require using lower frequency mechanical oscillators in order to place them in spectral proximity to a fluxonium qubit [237].

Through the aforementioned improvements, we believe electromechanical interaction rates at the MHz level (i.e. $g_{\mathrm{em}}/2\pi \gtrsim 1$ MHz) will be realistically within reach.

8.2 Experiments with Microscopic Quantum Defects

In the previous chapters, we have been mainly interested in TLS a source of acoustic decoherence. We have obtained clear signatures of mechanics-TLS interactions and explored in depth how TLS causes acoustic decoherence. Here, we will discuss how our platform can be further utilized to explore the rich physics of microscopic quantum defects in our devices.

Defects in polycrystalline metals

As discussed in Section 7.2, there exist experimental indications of TLS-like behavior originating within the bulk of polycrystalline metals. However, the experimental results haven't been fully consistent with standard TLS theory. For instance, in cases where dissipation consistent with TLS theory has been observed, the accompanying frequency shifts have not fully matched theoretical expectations [204, 205]. Alternatively, in instances where excess frequency shifts have been correlated with bulk metal, corresponding excess decay couldn't be identified [149]. Therefore, open questions remain regarding TLS-like behavior in polycrystalline metals, which can be investigated with our platform.

With our mechanical oscillators, we are able to clearly observe individual TLS interacting with our mechanical oscillators (see Section 5.5). This is achieved by electrically tuning the defects. If defects exist deep within the metal, we expect them not to be electrically tunable because the metal surface screens static electric fields. However, such defects would still be tunable by strain fields. By incorporating strain tuning into our setup, we could identify individual TLS located within the metal, where they could be distinguished from other TLS based on their lack of electrical tuning [238]. This capability would give us a definitive way to test whether TLS are present in the bulk metal. If such defects are observed, we could then extract their density and deformation potential, potentially obtaining insights into their microscopic origins.

Quantum nonlinearity from defects

TLS defects are highly nonlinear entities due to their excitation spectrum only

harboring two states. When these defects are coupled to a mechanical oscillator, the system's dynamics are governed by a Hamiltonian identical to the coupled qubit-oscillator system explored in Chapter 5. Specifically, both are described by the Jaynes-Cummings Hamiltonian (see Section 5.5) [239]. Therefore, a TLS can be employed in a manner similar to superconducting qubits to explore mechanical motion in the quantum regime [114]. For instance, the nonlinearity of the Jaynes-Cummings ladder can be utilized to achieve phonon blockade, where a non-classical oscillator field forms when the system is probed with a weak external drive [41, 114]. Alternatively, if the TLS frequency can be rapidly controlled, by electrical tuning [240] or via the AC Stark shift, arbitrary non-classical states of motion can be generated by the Law-Eberly protocol [58].

What makes TLS particularly interesting as a source of nonlinearity is the relative ease with which large TLS-mechanics interaction rates ($g_{\mathrm{TLS}}/2\pi \gtrsim 1$ MHz) can be engineered in nanoscale mechanical oscillators (see Section 5.5). Furthermore, since these defects are intrinsically present within the oscillators themselves, they can mitigate certain hybrid integration challenges.

However, working with TLS introduce significant complications as well. Though TLS can be engineered to exhibit long lifetimes when surrounded by phononic shields [168], they are subjected to significant frequency noise due to TLS-TLS interactions. This noise severely limits their coherence times ($T_2^* \lesssim 1\ \mu$s) [180, 187, 188, 199], which are significantly less than state-of-the-art superconducting qubits. To counteract this reduced coherence, the attainment of large TLS-mechanics interaction rates is necessitated, as this minimizes the dressed decoherence of the mechanical oscillator. These large interaction rates could be obtained by exploring oscillator geometries that have large zero-point fluctuations of strain.

A further challenge lies in readout of the oscillator state. In our experiments, we characterized the mechanical oscillator state based on the combination of the qubit-oscillator coupling and the ability to rapidly read out the state of a superconducting qubit. Unlike a superconducting qubit, achieving dispersive readout of a TLS is challenging. This is because the electrical coupling strength between TLS that reside our mechanical oscillator and a microwave resonator would be rather small ($\lesssim 2\pi \times 50$ kHz), hindering dispersive state readout. An alternative method to characterize the oscillator state could performing state tomography based on the electrical emission from the mechanical oscillator [241].

Despite the challenges, we believe that there exists a realistic pathway for using

these defects to generate non-classical states of motion. For instance, an experiment where one could probe the coupled TLS-oscillator system to observe a non-classical emission with $g^2(0) < 1$ is likely within reach with our current experimental parameters [114].

BIBLIOGRAPHY

[1] S. D. Senturia, *Microsystem Design* (Springer US, Boston, MA, 2001), 10.1007/b117574.

[2] J. W. Judy, "Microelectromechanical systems (MEMS): fabrication, design and applications", Smart Materials and Structures **10**, 1115 (2001) 10.1088/0964-1726/10/6/301.

[3] C. K. O'Sullivan and G. G. Guilbault, "Commercial quartz crystal microbalances – theory and applications", Biosensors and Bioelectronics **14**, 663–670 (1999) 10.1016/S0956-5663(99)00040-8.

[4] N. Yazdi, F. Ayazi, and K. Najafi, "Micromachined inertial sensors", Proceedings of the IEEE **86**, 1640–1659 (1998) 10.1109/5.704269.

[5] W. P. Eaton and J. H. Smith, "Micromachined pressure sensors: review and recent developments", Smart Materials and Structures **6**, 530 (1997) 10.1088/0964-1726/6/5/004.

[6] C. C. W. Ruppel, "Acoustic Wave Filter Technology–A Review", IEEE Transactions on Ultrasonics, Ferroelectrics, and Frequency Control **64**, 1390–1400 (2017) 10.1109/TUFFC.2017.2690905.

[7] C. M. Caves, K. S. Thorne, R. W. P. Drever, V. D. Sandberg, and M. Zimmermann, "On the measurement of a weak classical force coupled to a quantum-mechanical oscillator. I. Issues of principle", Reviews of Modern Physics **52**, 341–392 (1980) 10.1103/RevModPhys.52.341.

[8] D. Mason, J. Chen, M. Rossi, Y. Tsaturyan, and A. Schliesser, "Continuous force and displacement measurement below the standard quantum limit", Nature Physics **15**, 745–749 (2019) 10.1038/s41567-019-0533-5.

[9] Q. R. Rahman, I. Kladarić, M.-E. Kern, L. Lachman, Y. Chu, R. Filip, and M. Fadel, "Genuine Quantum Non-Gaussianity and Metrological Sensitivity of Fock States Prepared in a Mechanical Resonator", Physical Review Letters **134**, 180801 (2025) 10.1103/PhysRevLett.134.180801.

[10] K. C. McCormick, J. Keller, S. C. Burd, D. J. Wineland, A. C. Wilson, and D. Leibfried, "Quantum-enhanced sensing of a single-ion mechanical oscillator", Nature **572**, 86–90 (2019) 10.1038/s41586-019-1421-y.

[11] C. Chamberland, K. Noh, P. Arrangoiz-Arriola, E. T. Campbell, C. T. Hann, J. Iverson, H. Putterman, T. C. Bohdanowicz, S. T. Flammia, A. Keller, G. Refael, J. Preskill, L. Jiang, A. H. Safavi-Naeini, O. Painter, and F. G. Brandão, "Building a Fault-Tolerant Quantum Computer Using Concatenated Cat Codes", PRX Quantum **3**, 010329 (2022) 10.1103/PRXQuantum.3.010329.

[12] C. T. Hann, C.-L. Zou, Y. Zhang, Y. Chu, R. J. Schoelkopf, S. M. Girvin, and L. Jiang, "Hardware-Efficient Quantum Random Access Memory with Hybrid Quantum Acoustic Systems", Physical Review Letters **123**, 250501 (2019) 10.1103/PhysRevLett.123.250501.

[13] G. Kurizki, P. Bertet, Y. Kubo, K. Mølmer, D. Petrosyan, P. Rabl, and J. Schmiedmayer, "Quantum technologies with hybrid systems", Proceedings of the National Academy of Sciences **112**, 3866–3873 (2015) 10.1073/pnas.1419326112.

[14] X. Han, W. Fu, C.-L. Zou, L. Jiang, and H. X. Tang, "Microwave-optical quantum frequency conversion", Optica **8**, 1050–1064 (2021) 10.1364/OPTICA.425414.

[15] M. Aspelmeyer, T. J. Kippenberg, and F. Marquardt, "Cavity optomechanics", Reviews of Modern Physics **86**, 1391–1452 (2014) 10.1103/RevModPhys.86.1391.

[16] A. D. O'Connell, M. Hofheinz, M. Ansmann, R. C. Bialczak, M. Lenander, E. Lucero, M. Neeley, D. Sank, H. Wang, M. Weides, J. Wenner, J. M. Martinis, and A. N. Cleland, "Quantum ground state and single-phonon control of a mechanical resonator", Nature **464**, 697–703 (2010) 10.1038/nature08967.

[17] J. Chan, T. P. M. Alegre, A. H. Safavi-Naeini, J. T. Hill, A. Krause, S. Gröblacher, M. Aspelmeyer, and O. Painter, "Laser cooling of a nanomechanical oscillator into its quantum ground state", Nature **478**, 89–92 (2011) 10.1038/nature10461.

[18] J. D. Teufel, T. Donner, D. Li, J. W. Harlow, M. S. Allman, K. Cicak, A. J. Sirois, J. D. Whittaker, K. W. Lehnert, and R. W. Simmonds, "Sideband cooling of micromechanical motion to the quantum ground state", Nature **475**, 359–363 (2011) 10.1038/nature10261.

[19] M. Rossi, D. Mason, J. Chen, Y. Tsaturyan, and A. Schliesser, "Measurement-based quantum control of mechanical motion", Nature **563**, 53–58 (2018) 10.1038/s41586-018-0643-8.

[20] M. O. Scully and M. S. Zubairy, *Quantum Optics* (Cambridge University Press, Cambridge, 1997), 10.1017/CBO9780511813993.

[21] S. Lloyd and S. L. Braunstein, "Quantum Computation over Continuous Variables", Physical Review Letters **82**, 1784–1787 (1999) 10.1103/PhysRevLett.82.1784.

[22] C. Samanta, S. L. De Bonis, C. B. Møller, R. Tormo-Queralt, W. Yang, C. Urgell, B. Stamenic, B. Thibeault, Y. Jin, D. A. Czaplewski, F. Pistolesi, and A. Bachtold, "Nonlinear nanomechanical resonators approaching the quantum ground state", Nature Physics **19**, 1340–1344 (2023) 10.1038/s41567-023-02065-9.

[23] Y. Chu and S. Gröblacher, "A perspective on hybrid quantum opto- and electromechanical systems", Applied Physics Letters **117**, 150503 (2020) 10.1063/5.0021088.

[24] S. Hong, R. Riedinger, I. Marinković, A. Wallucks, S. G. Hofer, R. A. Norte, M. Aspelmeyer, and S. Gröblacher, "Hanbury Brown and Twiss interferometry of single phonons from an optomechanical resonator", Science **358**, 203–206 (2017) 10.1126/science.aan7939.

[25] A. D. Armour, M. P. Blencowe, and K. C. Schwab, "Entanglement and Decoherence of a Micromechanical Resonator via Coupling to a Cooper-Pair Box", Physical Review Letters **88**, 148301 (2002) 10.1103/PhysRevLett.88.148301.

[26] E. K. Twyeffort Irish and K. Schwab, "Quantum measurement of a coupled nanomechanical resonator–Cooper-pair box system", Physical Review B **68**, 155311 (2003) 10.1103/PhysRevB.68.155311.

[27] M. D. LaHaye, J. Suh, P. M. Echternach, K. C. Schwab, and M. L. Roukes, "Nanomechanical measurements of a superconducting qubit", Nature **459**, 960–964 (2009) 10.1038/nature08093.

[28] J.-M. Pirkkalainen, S. U. Cho, J. Li, G. S. Paraoanu, P. J. Hakonen, and M. A. Sillanpää, "Hybrid circuit cavity quantum electrodynamics with a micromechanical resonator", Nature **494**, 211–215 (2013) 10.1038/nature11821.

[29] F. Rouxinol, Y. Hao, F. Brito, A. O. Caldeira, E. K. Irish, and M. D. LaHaye, "Measurements of nanoresonator-qubit interactions in a hybrid quantum electromechanical system", Nanotechnology **27**, 364003 (2016) 10.1088/0957-4484/27/36/364003.

[30] J. J. Viennot, X. Ma, and K. W. Lehnert, "Phonon-Number-Sensitive Electromechanics", Physical Review Letters **121**, 183601 (2018) 10.1103/PhysRevLett.121.183601.

[31] X. Ma, J. J. Viennot, S. Kotler, J. D. Teufel, and K. W. Lehnert, "Non-classical energy squeezing of a macroscopic mechanical oscillator", Nature Physics **17**, 322–326 (2021) 10.1038/s41567-020-01102-1.

[32] K. Gerashchenko, R. Rousseau, L. Balembois, H. Patange, P. Manset, W. C. Smith, Z. Leghtas, E. Flurin, T. Jacqmin, and S. Deléglise, *Probing the quantum motion of a macroscopic mechanical oscillator with a radio-frequency superconducting qubit*, May 2025, 10.48550/arXiv.2505.21481.

[33] Y. Chu, P. Kharel, W. H. Renninger, L. D. Burkhart, L. Frunzio, P. T. Rakich, and R. J. Schoelkopf, "Quantum acoustics with superconducting qubits", Science **358**, 199–202 (2017) 10.1126/science.aao1511.

[34] K. J. Satzinger, Y. P. Zhong, H.-S. Chang, G. A. Peairs, A. Bienfait, M.-H. Chou, A. Y. Cleland, C. R. Conner, É. Dumur, J. Grebel, I. Gutierrez, B. H. November, R. G. Povey, S. J. Whiteley, D. D. Awschalom, D. I. Schuster, and A. N. Cleland, "Quantum control of surface acoustic-wave phonons", Nature **563**, 661–665 (2018) 10.1038/s41586-018-0719-5.

[35] U. von Lüpke, Y. Yang, M. Bild, L. Michaud, M. Fadel, and Y. Chu, "Parity measurement in the strong dispersive regime of circuit quantum acoustodynamics", Nature Physics **18**, 794–799 (2022) 10.1038/s41567-022-01591-2.

[36] E. A. Wollack, A. Y. Cleland, R. G. Gruenke, Z. Wang, P. Arrangoiz-Arriola, and A. H. Safavi-Naeini, "Quantum state preparation and tomography of entangled mechanical resonators", Nature **604**, 463–467 (2022) 10.1038/s41586-022-04500-y.

[37] M. Bild, M. Fadel, Y. Yang, U. von Lüpke, P. Martin, A. Bruno, and Y. Chu, "Schrödinger cat states of a 16-microgram mechanical oscillator", Science **380**, 274–278 (2023) 10.1126/science.adf7553.

[38] H. Qiao, É. Dumur, G. Andersson, H. Yan, M.-H. Chou, J. Grebel, C. R. Conner, Y. J. Joshi, J. M. Miller, R. G. Povey, X. Wu, and A. N. Cleland, "Splitting phonons: Building a platform for linear mechanical quantum computing", Science **380**, 1030–1033 (2023) 10.1126/science.adg8715.

[39] W. Cai, Y. Ma, W. Wang, C.-L. Zou, and L. Sun, "Bosonic quantum error correction codes in superconducting quantum circuits", Fundamental Research **1**, 50–67 (2021) 10.1016/j.fmre.2020.12.006.

[40] I. Pietikäinen, O. Černotík, A. Eickbusch, A. Maiti, J. W. Garmon, R. Filip, and S. M. Girvin, "Strategies and Trade-Offs for Controllability and Memory Time of Ultra-High-Quality Microwave Cavities in Circuit Quantum Electrodynamics", PRX Quantum **5**, 040307 (2024) 10.1103/PRXQuantum.5.040307.

[41] Y. Yang, I. Kladarić, M. Drimmer, U. von Lüpke, D. Lenterman, J. Bus, S. Marti, M. Fadel, and Y. Chu, "A mechanical qubit", Science **386**, 783–788 (2024) 10.1126/science.adr2464.

[42] G. S. MacCabe, H. Ren, J. Luo, J. D. Cohen, H. Zhou, A. Sipahigil, M. Mirhosseini, and O. Painter, "Nano-acoustic resonator with ultralong phonon lifetime", Science **370**, 840–843 (2020) 10.1126/science.abc7312.

[43] S. Galliou, M. Goryachev, R. Bourquin, P. Abbé, J. P. Aubry, and M. E. Tobar, "Extremely Low Loss Phonon-Trapping Cryogenic Acoustic Cavities for Future Physical Experiments", Scientific Reports **3**, 2132 (2013) 10.1038/srep02132.

[44] N. J. Engelsen, A. Beccari, and T. J. Kippenberg, "Ultrahigh-quality-factor micro- and nanomechanical resonators using dissipation dilution", Nature Nanotechnology **19**, 725–737 (2024) 10.1038/s41565-023-01597-8.

[45] E. A. Wollack, A. Y. Cleland, P. Arrangoiz-Arriola, T. P. McKenna, R. G. Gruenke, R. N. Patel, W. Jiang, C. J. Sarabalis, and A. H. Safavi-Naeini, "Loss channels affecting lithium niobate phononic crystal resonators at cryogenic temperature", Applied Physics Letters **118**, 123501 (2021) 10.1063/5.0034909.

[46] R. G. Gruenke-Freudenstein, E. Szakiel, G. P. Multani, T. Makihara, A. G. Hayden, A. Khalatpour, E. A. Wollack, A. Akoto-Yeboah, S. Salmani-Rezaie, and A. H. Safavi-Naeini, "Surface and bulk two-level-system losses in lithium niobate acoustic resonators", Physical Review Applied **23**, 064055 (2025) 10.1103/tgs3-kkw8.

[47] M. Scigliuzzo, L. E. Bruhat, A. Bengtsson, J. J. Burnett, A. F. Roudsari, and P. Delsing, "Phononic loss in superconducting resonators on piezoelectric substrates", New Journal of Physics **22**, 053027 (2020) 10.1088/1367-2630/ab8044.

[48] D. F. McGuigan, C. C. Lam, R. Q. Gram, A. W. Hoffman, D. H. Douglass, and H. W. Gutche, "Measurements of the mechanical Q of single-crystal silicon at low temperatures", Journal of Low Temperature Physics **30**, 621–629 (1978) 10.1007/BF00116202.

[49] A. S. Algamili, M. H. M. Khir, J. O. Dennis, A. Y. Ahmed, S. S. Alabsi, S. S. Ba Hashwan, and M. M. Junaid, "A Review of Actuation and Sensing Mechanisms in MEMS-Based Sensor Devices", Nanoscale Research Letters **16**, 16 (2021) 10.1186/s11671-021-03481-7.

[50] H. Zhao, A. Bozkurt, and M. Mirhosseini, "Electro-optic transduction in silicon via gigahertz-frequency nanomechanics", Optica **10**, 790–796 (2023) 10.1364/OPTICA.479162,

[51] S. M. Girvin, "Circuit QED: superconducting qubits coupled to microwave photons", in *Quantum Machines: Measurement and Control of Engineered Quantum Systems*, edited by M. Devoret, B. Huard, R. Schoelkopf, and L. F. Cugliandolo, 1st ed. (Oxford University PressOxford, June 2014), pp. 113–256, 10.1093/acprof:oso/9780199681181.003.0003.

[52] R. Lifshitz and M. C. Cross, "Nonlinear Dynamics of Nanomechanical and Micromechanical Resonators", in *Reviews of Nonlinear Dynamics and Complexity*, edited by H. G. Schuster (Wiley-VCH Verlag GmbH & Co. KGaA, Weinheim, Germany, Apr. 2008), pp. 1–52, 10.1002/9783527626359.ch1.

[53] M. Agarwal, S. A. Chandorkar, H. Mehta, R. N. Candler, B. Kim, M. A. Hopcroft, R. Melamud, C. M. Jha, G. Bahl, G. Yama, T. W. Kenny, and B. Murmann, "A study of electrostatic force nonlinearities in resonant microstructures", Applied Physics Letters **92**, 104106 (2008) 10.1063/1.2834707.

[54] T. A. Palomaki, J. W. Harlow, J. D. Teufel, R. W. Simmonds, and K. W. Lehnert, "Coherent state transfer between itinerant microwave fields and a mechanical oscillator", Nature **495**, 210–214 (2013) 10.1038/nature11915.

[55] J. Koch, T. M. Yu, J. Gambetta, A. A. Houck, D. I. Schuster, J. Majer, A. Blais, M. H. Devoret, S. M. Girvin, and R. J. Schoelkopf, "Charge-insensitive qubit design derived from the Cooper pair box", Physical Review A **76**, 042319 (2007) 10.1103/PhysRevA.76.042319.

[56] P. Krantz, M. Kjaergaard, F. Yan, T. P. Orlando, S. Gustavsson, and W. D. Oliver, "A quantum engineer's guide to superconducting qubits", Applied Physics Reviews **6**, 021318 (2019) 10.1063/1.5089550.

[57] E. Jaynes and F. Cummings, "Comparison of quantum and semiclassical radiation theories with application to the beam maser", Proceedings of the IEEE **51**, 89–109 (1963) 10.1109/PROC.1963.1664.

[58] C. K. Law and J. H. Eberly, "Arbitrary Control of a Quantum Electromagnetic Field", Physical Review Letters **76**, 1055–1058 (1996) 10.1103/PhysRevLett.76.1055.

[59] P. Arrangoiz-Arriola and A. H. Safavi-Naeini, "Engineering interactions between superconducting qubits and phononic nanostructures", Physical Review A **94**, 063864 (2016) 10.1103/PhysRevA.94.063864.

[60] S. E. Nigg, H. Paik, B. Vlastakis, G. Kirchmair, S. Shankar, L. Frunzio, M. H. Devoret, R. J. Schoelkopf, and S. M. Girvin, "Black-Box Superconducting Circuit Quantization", Physical Review Letters **108**, 240502 (2012) 10.1103/PhysRevLett.108.240502.

[61] P. Groszkowski and J. Koch, "Scqubits: a Python package for superconducting qubits", Quantum **5**, 583 (2021) 10.22331/q-2021-11-17-583.

[62] M. F. Gely and G. A. Steele, "QuCAT: quantum circuit analyzer tool in Python", New Journal of Physics **22**, 013025 (2020) 10.1088/1367-2630/ab60f6.

[63] P. Forn-Díaz, L. Lamata, E. Rico, J. Kono, and E. Solano, "Ultrastrong coupling regimes of light-matter interaction", Reviews of Modern Physics **91**, 025005 (2019) 10.1103/RevModPhys.91.025005.

[64] A. H. Safavi-Naeini and O. Painter, "Optomechanical Crystal Devices", in *Cavity Optomechanics: Nano- and Micromechanical Resonators Interacting with Light*, edited by M. Aspelmeyer, T. J. Kippenberg, and F. Marquardt (Springer, Berlin, Heidelberg, 2014), pp. 195–231, 10.1007/978-3-642-55312-7_10.

[65] A. Pitanti, J. M. Fink, A. H. Safavi-Naeini, J. T. Hill, C. U. Lei, A. Tredicucci, and O. Painter, "Strong opto-electro-mechanical coupling in a silicon photonic crystal cavity", Optics Express **23**, 3196–3208 (2015) 10.1364/OE.23.003196.

[66] S. G. Johnson, M. Ibanescu, M. A. Skorobogatiy, O. Weisberg, J. D. Joannopoulos, and Y. Fink, "Perturbation theory for Maxwell's equations with shifting material boundaries", Physical Review E **65**, 066611 (2002) 10.1103/PhysRevE.65.066611.

[67] A. Beckers, F. Jazaeri, A. Grill, S. Narasimhamoorthy, B. Parvais, and C. Enz, "Physical Model of Low-Temperature to Cryogenic Threshold Voltage in MOSFETs", IEEE Journal of the Electron Devices Society **8**, 780–788 (2020) 10.1109/JEDS.2020.2989629.

[68] R. Van Laer, R. N. Patel, T. P. McKenna, J. D. Witmer, and A. H. Safavi-Naeini, "Electrical driving of X-band mechanical waves in a silicon photonic circuit", APL Photonics **3**, 086102 (2018) 10.1063/1.5042428.

[69] A. Bozkurt, H. Zhao, C. Joshi, H. G. LeDuc, P. K. Day, and M. Mirhosseini, "A quantum electromechanical interface for long-lived phonons", Nature Physics **19**, 1326–1332 (2023) 10.1038/s41567-023-02080-w,

[70] M. S. Kushwaha, P. Halevi, L. Dobrzynski, and B. Djafari-Rouhani, "Acoustic band structure of periodic elastic composites", Physical Review Letters **71**, 2022–2025 (1993) 10.1103/PhysRevLett.71.2022.

[71] P. A. Deymier, ed., *Acoustic Metamaterials and Phononic Crystals*, Vol. 173, Springer Series in Solid-State Sciences (Springer, Berlin, Heidelberg, 2013), 10.1007/978-3-642-31232-8.

[72] J. D. Joannopoulos, J. N. Winn, and S. G. Johnson, *Photonic Crystals: Molding the Flow of Light - Second Edition* (Princeton University Press, Princeton, NJ, 2011), 10.1515/9781400828241.

[73] H. Tong, S. Liu, M. Zhao, and K. Fang, "Observation of phonon trapping in the continuum with topological charges", Nature Communications **11**, 5216 (2020) 10.1038/s41467-020-19091-3.

[74] A. H. Safavi-Naeini and O. Painter, "Design of optomechanical cavities and waveguides on a simultaneous bandgap phononic-photonic crystal slab", Optics Express **18**, 14926–14943 (2010) 10.1364/OE.18.014926.

[75] J. Chan, A. H. Safavi-Naeini, J. T. Hill, S. Meenehan, and O. Painter, "Optimized optomechanical crystal cavity with acoustic radiation shield", Applied Physics Letters **101**, 081115 (2012) 10.1063/1.4747726.

[76] P.-L. Yu, K. Cicak, N. S. Kampel, Y. Tsaturyan, T. P. Purdy, R. W. Simmonds, and C. A. Regal, "A phononic bandgap shield for high-Q membrane microresonators", Applied Physics Letters **104**, 023510 (2014) 10.1063/1.4862031.

[77] O. Florez, G. Arregui, M. Albrechtsen, R. C. Ng, J. Gomis-Bresco, S. Stobbe, C. M. Sotomayor-Torres, and P. D. García, "Engineering nanoscale hypersonic phonon transport", Nature Nanotechnology **17**, 947–951 (2022) 10.1038/s41565-022-01178-1.

[78] H. Ren, M. H. Matheny, G. S. MacCabe, J. Luo, H. Pfeifer, M. Mirhosseini, and O. Painter, "Two-dimensional optomechanical crystal cavity with high quantum cooperativity", Nature Communications **11**, 3373 (2020) 10.1038/s41467-020-17182-9.

[79] M. Kalaee, M. Mirhosseini, P. B. Dieterle, M. Peruzzo, J. M. Fink, and O. Painter, "Quantum electromechanics of a hypersonic crystal", Nature Nanotechnology **14**, 334–339 (2019) 10.1038/s41565-019-0377-2.

[80] R. N. Kleiman, G. Agnolet, and D. J. Bishop, "Two-level systems observed in the mechanical properties of single-crystal silicon at low temperatures", Physical Review Letters **59**, 2079–2082 (1987) 10.1103/PhysRevLett.59.2079.

[81] M. Eichenfield, J. Chan, R. M. Camacho, K. J. Vahala, and O. Painter, "Optomechanical crystals", Nature **462**, 78–82 (2009) 10.1038/nature08524.

[82] A. J. Keller, P. B. Dieterle, M. Fang, B. Berger, J. M. Fink, and O. Painter, "Al transmon qubits on silicon-on-insulator for quantum device integration", Applied Physics Letters **111**, 042603 (2017) 10.1063/1.4994661.

[83] F. Moraes, G. H. M. De Aguiar, E. G. De Melo, G. S. Wiederhecker, and T. P. M. Alegre, "Optimization of diamond optomechanical crystal cavities", Journal of the Optical Society of America B **39**, 2735 (2022) 10.1364/JOSAB.469497.

[84] D. M. Olsson and L. S. Nelson, "The Nelder-Mead Simplex Procedure for Function Minimization", Technometrics **17**, 45–51 (1975) 10.1080/00401706.1975.10489269.

[85] N. Le Thomas, Z. Diao, H. Zhang, and R. Houdré, "Statistical analysis of subnanometer residual disorder in photonic crystal waveguides: Correlation between slow light properties and structural properties", Journal of Vacuum Science & Technology B **29**, 051601 (2011) 10.1116/1.3622289.

[86] M. Patterson, S. Hughes, S. Combrié, N.-V.-Q. Tran, A. De Rossi, R. Gabet, and Y. Jaouën, "Disorder-Induced Coherent Scattering in Slow-Light Photonic Crystal Waveguides", Physical Review Letters **102**, 253903 (2009) 10.1103/PhysRevLett.102.253903.

[87] Y. Taguchi, Y. Takahashi, Y. Sato, T. Asano, and S. Noda, "Statistical studies of photonic heterostructure nanocavities with an average Q factor of three million", Optics Express **19**, 11916–11921 (2011) 10.1364/OE.19.011916.

[88] H. Hagino, Y. Takahashi, Y. Tanaka, T. Asano, and S. Noda, "Effects of fluctuation in air hole radii and positions on optical characteristics in photonic crystal heterostructure nanocavities", Physical Review B **79**, 085112 (2009) 10.1103/PhysRevB.79.085112.

[89] M. Minkov, U. P. Dharanipathy, R. Houdré, and V. Savona, "Statistics of the disorder-induced losses of high-Q photonic crystal cavities", Optics Express **21**, 28233–28245 (2013) 10.1364/OE.21.028233.

[90] G. S. MacCabe, "Phonon Dynamics and Damping in Three-Dimensional Acoustic Bandgap Cavity-Optomechanical Resonators", PhD thesis (California Institute of Technology, 2019), 10.7907/7R9W-EV53.

[91] W. H. Renninger, P. Kharel, R. O. Behunin, and P. T. Rakich, "Bulk crystalline optomechanics", Nature Physics **14**, 601–607 (2018) 10.1038/s41567-018-0090-3.

[92] A. Beccari, D. A. Visani, S. A. Fedorov, M. J. Bereyhi, V. Boureau, N. J. Engelsen, and T. J. Kippenberg, "Strained crystalline nanomechanical resonators with quality factors above 10 billion", Nature Physics **18**, 436–441 (2022) 10.1038/s41567-021-01498-4.

[93] A. A. Clerk, K. W. Lehnert, P. Bertet, J. R. Petta, and Y. Nakamura, "Hybrid quantum systems with circuit quantum electrodynamics", Nature Physics **16**, 257–267 (2020) 10.1038/s41567-020-0797-9.

[94] A. H. Safavi-Naeini, D. Van Thourhout, R. Baets, and R. Van Laer, "Controlling phonons and photons at the wavelength scale: integrated photonics meets integrated phononics", Optica **6**, 213 (2019) 10.1364/OPTICA.6.000213.

[95] M. Xu, X. Han, W. Fu, C.-L. Zou, and H. X. Tang, "Frequency-tunable high- Q superconducting resonators via wireless control of nonlinear kinetic inductance", Applied Physics Letters **114**, 192601 (2019) 10.1063/1.5098466.

[96] A. Wallucks, I. Marinković, B. Hensen, R. Stockill, and S. Gröblacher, "A quantum memory at telecom wavelengths", Nature Physics **16**, 772–777 (2020) 10.1038/s41567-020-0891-z.

[97] M. Mirhosseini, A. Sipahigil, M. Kalaee, and O. Painter, "Superconducting qubit to optical photon transduction", Nature **588**, 599–603 (2020) 10.1038/s41586-020-3038-6.

[98] G. A. Peterson, S. Kotler, F. Lecocq, K. Cicak, X. Y. Jin, R. W. Simmonds, J. Aumentado, and J. D. Teufel, "Ultrastrong Parametric Coupling between a Superconducting Cavity and a Mechanical Resonator", Physical Review Letters **123**, 247701 (2019) 10.1103/PhysRevLett.123.247701.

[99] J. D. Teufel, D. Li, M. S. Allman, K. Cicak, A. J. Sirois, J. D. Whittaker, and R. W. Simmonds, "Circuit cavity electromechanics in the strong-coupling regime", Nature **471**, 204–208 (2011) 10.1038/nature09898.

[100] W. P. Mason and H. J. McSkimin, "Attenuation and Scattering of High Frequency Sound Waves in Metals and Glasses", The Journal of the Acoustical Society of America **19**, 464–473 (1947) 10.1121/1.1916504.

[101] F. Zeng, S. R. Agnew, B. Raeisinia, and G. R. Myneni, "Ultrasonic Attenuation Due to Grain Boundary Scattering in Pure Niobium", Journal of Nondestructive Evaluation **29**, 93–103 (2010) 10.1007/s10921-010-0068-2.

[102] A. Shearrow, G. Koolstra, S. J. Whiteley, N. Earnest, P. S. Barry, F. J. Heremans, D. D. Awschalom, E. Shirokoff, and D. I. Schuster, "Atomic layer deposition of titanium nitride for quantum circuits", Applied Physics Letters **113**, 212601 (2018) 10.1063/1.5053461.

[103] T. M. Hazard, A. Gyenis, A. Di Paolo, A. T. Asfaw, S. A. Lyon, A. Blais, and A. A. Houck, "Nanowire Superinductance Fluxonium Qubit", Physical Review Letters **122**, 010504 (2019) 10.1103/PhysRevLett.122.010504.

[104] I. V. Pechenezhskiy, R. A. Mencia, L. B. Nguyen, Y.-H. Lin, and V. E. Manucharyan, "The superconducting quasicharge qubit", Nature **585**, 368–371 (2020) 10.1038/s41586-020-2687-9.

[105] J. Zmuidzinas, "Superconducting Microresonators: Physics and Applications", Annual Review of Condensed Matter Physics **3**, 169–214 (2012) 10.1146/annurev-conmatphys-020911-125022.

[106] S. A. Vitale, J. Kedzierski, P. Healey, P. W. Wyatt, and C. L. Keast, "Work-Function-Tuned TiN Metal Gate FDSOI Transistors for Subthreshold Operation", IEEE Transactions on Electron Devices **58**, 419–426 (2011) 10.1109/TED.2010.2092779.

[107] D. M. Fleetwood, P. S. Winokur, R. A. Reber, T. L. Meisenheimer, J. R. Schwank, M. R. Shaneyfelt, and L. C. Riewe, "Effects of oxide traps, interface traps, and "border traps" on metal-oxide-semiconductor devices", Journal of Applied Physics **73**, 5058–5074 (1993) 10.1063/1.353777.

[108] E. Gutiérrez-D., J. Deen, and C. Claeys, *Low Temperature Electronics*, edited by E. A. Gutiérrez-D., M. J. Deen, and C. Claeys (Academic Press, San Diego, Jan. 2001), 10.1016/B978-012310675-9/50000-1.

[109] Y. Zhang, J. Moser, J. Güttinger, A. Bachtold, and M. I. Dykman, "Interplay of Driving and Frequency Noise in the Spectra of Vibrational Systems", Physical Review Letters **113**, 255502 (2014) 10.1103/PhysRevLett.113.255502.

[110] L. Grünhaupt, N. Maleeva, S. T. Skacel, M. Calvo, F. Levy-Bertrand, A. V. Ustinov, H. Rotzinger, A. Monfardini, G. Catelani, and I. M. Pop, "Loss Mechanisms and Quasiparticle Dynamics in Superconducting Microwave Resonators Made of Thin-Film Granular Aluminum", Physical Review Letters **121**, 117001 (2018) 10.1103/PhysRevLett.121.117001.

[111] K. Serniak, M. Hays, G. de Lange, S. Diamond, S. Shankar, L. D. Burkhart, L. Frunzio, M. Houzet, and M. H. Devoret, "Hot Nonequilibrium Quasiparticles in Transmon Qubits", Physical Review Letters **121**, 157701 (2018) 10.1103/PhysRevLett.121.157701.

[112] W. A. Phillips, "Two-level states in glasses", Reports on Progress in Physics **50**, 1657 (1987) 10.1088/0034-4885/50/12/003.

[113] C. Müller, J. H. Cole, and J. Lisenfeld, "Towards understanding two-level-systems in amorphous solids: insights from quantum circuits", Reports on Progress in Physics **82**, 124501 (2019) 10.1088/1361-6633/ab3a7e.

[114] T. Ramos, V. Sudhir, K. Stannigel, P. Zoller, and T. J. Kippenberg, "Nonlinear Quantum Optomechanics via Individual Intrinsic Two-Level Defects", Physical Review Letters **110**, 193602 (2013) 10.1103/PhysRevLett.110.193602.

[115] R. Manenti, M. J. Peterer, A. Nersisyan, E. B. Magnusson, A. Patterson, and P. J. Leek, "Surface acoustic wave resonators in the quantum regime", Physical Review B **93**, 041411 (2016) 10.1103/PhysRevB.93.041411.

[116] G. Andersson, A. L. O. Bilobran, M. Scigliuzzo, M. M. de Lima, J. H. Cole, and P. Delsing, "Acoustic spectral hole-burning in a two-level system ensemble", npj Quantum Information **7**, 1–5 (2021) 10.1038/s41534-020-00348-0.

[117] J. Lisenfeld, A. Bilmes, A. Megrant, R. Barends, J. Kelly, P. Klimov, G. Weiss, J. M. Martinis, and A. V. Ustinov, "Electric field spectroscopy of material defects in transmon qubits", npj Quantum Information **5**, 105 (2019) 10.1038/s41534-019-0224-1.

[118] B. Machielse, S. Bogdanovic, S. Meesala, S. Gauthier, M. J. Burek, G. Joe, M. Chalupnik, Y. I. Sohn, J. Holzgrafe, R. E. Evans, C. Chia, H. Atikian, M. K. Bhaskar, D. D. Sukachev, L. Shao, S. Maity, M. D. Lukin, and M. Lončar, "Quantum Interference of Electromechanically Stabilized Emitters in Nanophotonic Devices", Physical Review X **9**, 031022 (2019) 10.1103/PhysRevX.9.031022.

[119] M. Peruzzo, A. Trioni, F. Hassani, M. Zemlicka, and J. M. Fink, "Surpassing the resistance quantum with a geometric superinductor", Physical Review Applied **14**, 044055 (2020) 10.1103/PhysRevApplied.14.044055.

[120] M. Pechal, P. Arrangoiz-Arriola, and A. H. Safavi-Naeini, "Superconducting circuit quantum computing with nanomechanical resonators as storage", Quantum Science and Technology **4**, 015006 (2018) 10.1088/2058-9565/aadc6c.

[121] H. G. Leduc, B. Bumble, P. K. Day, B. H. Eom, J. Gao, S. Golwala, B. A. Mazin, S. McHugh, A. Merrill, D. C. Moore, O. Noroozian, A. D. Turner, and J. Zmuidzinas, "Titanium nitride films for ultrasensitive microresonator detectors", Applied Physics Letters **97**, 102509 (2010) 10.1063/1.3480420.

[122] R. W. Johnstone and M. Parameswaran, *An Introduction to Surface Micromachining*, edited by R. W. Johnstone and M. Parameswaran (Springer US, Boston, MA, 2004), 10.1007/978-1-4020-8021-0_1.

[123] Y. He, J. Marchetti, C. Gallegos, and F. Maseeh, "Accurate fully-coupled natural frequency shift of MEMS actuators due to voltage bias and other external forces", in Technical Digest. IEEE International MEMS 99 Conference. Twelfth IEEE International Conference on Micro Electro Mechanical Systems (Cat. No.99CH36291) (Jan. 1999), pp. 321–325, 10.1109/MEMSYS.1999.746846.

[124] M. Sandberg, M. R. Vissers, J. S. Kline, M. Weides, J. Gao, D. S. Wisbey, and D. P. Pappas, "Etch induced microwave losses in titanium nitride superconducting resonators", Applied Physics Letters **100**, 262605 (2012) 10.1063/1.4729623.

[125] J. M. Sage, V. Bolkhovsky, W. D. Oliver, B. Turek, and P. B. Welander, "Study of loss in superconducting coplanar waveguide resonators", Journal of Applied Physics **109**, 063915 (2011) 10.1063/1.3552890.

[126] H. Wang, M. Hofheinz, J. Wenner, M. Ansmann, R. C. Bialczak, M. Lenander, E. Lucero, M. Neeley, A. D. O'Connell, D. Sank, M. Weides, A. N. Cleland, and J. M. Martinis, "Improving the coherence time of superconducting coplanar resonators", Applied Physics Letters **95**, 233508 (2009) 10.1063/1.3273372.

[127] M. R. Vissers, J. Gao, D. S. Wisbey, D. A. Hite, C. C. Tsuei, A. D. Corcoles, M. Steffen, and D. P. Pappas, "Low loss superconducting titanium nitride coplanar waveguide resonators", Applied Physics Letters **97**, 232509 (2010) 10.1063/1.3517252.

[128] T. Faust, J. Rieger, M. J. Seitner, J. P. Kotthaus, and E. M. Weig, "Signatures of two-level defects in the temperature-dependent damping of nanomechanical silicon nitride resonators", Physical Review B **89**, 100102 (2014) 10.1103/PhysRevB.89.100102.

[129] L. Faoro and L. B. Ioffe, "Interacting tunneling model for two-level systems in amorphous materials and its predictions for their dephasing and noise in superconducting microresonators", Physical Review B **91**, 014201 (2015) 10.1103/PhysRevB.91.014201.

[130] P. Mohanty, D. A. Harrington, K. L. Ekinci, Y. T. Yang, M. J. Murphy, and M. L. Roukes, "Intrinsic dissipation in high-frequency micromechanical resonators", Physical Review B **66**, 085416 (2002) 10.1103/PhysRevB.66.085416.

[131] M. Wallquist, K. Hammerer, P. Rabl, M. Lukin, and P. Zoller, "Hybrid quantum devices and quantum engineering", Physica Scripta **2009**, 014001 (2009) 10.1088/0031-8949/2009/T137/014001.

[132] M. Kjaergaard, M. E. Schwartz, J. Braumüller, P. Krantz, J. I.-J. Wang, S. Gustavsson, and W. D. Oliver, "Superconducting Qubits: Current State of Play", Annual Review of Condensed Matter Physics **11**, 369–395 (2020) 10.1146/annurev-conmatphys-031119-050605.

[133] N. P. de Leon, K. M. Itoh, D. Kim, K. K. Mehta, T. E. Northup, H. Paik, B. S. Palmer, N. Samarth, S. Sangtawesin, and D. W. Steuerman, "Materials challenges and opportunities for quantum computing hardware", Science **372**, eabb2823 (2021) 10.1126/science.abb2823.

[134] S. Ganjam, Y. Wang, Y. Lu, A. Banerjee, C. U. Lei, L. Krayzman, K. Kisslinger, C. Zhou, R. Li, Y. Jia, M. Liu, L. Frunzio, and R. J. Schoelkopf, "Surpassing millisecond coherence in on chip superconducting quantum memories by optimizing materials and circuit design", Nature Communications **15**, 3687 (2024) 10.1038/s41467-024-47857-6.

[135] K. D. Crowley, R. A. McLellan, A. Dutta, N. Shumiya, A. P. M. Place, X. H. Le, Y. Gang, T. Madhavan, M. P. Bland, R. Chang, N. Khedkar, Y. C. Feng, E. A. Umbarkar, X. Gui, L. V. H. Rodgers, Y. Jia, M. M. Feldman, S. A. Lyon, M. Liu, R. J. Cava, A. A. Houck, and N. P. de Leon, "Disentangling Losses in Tantalum Superconducting Circuits", Physical Review X **13**, 041005 (2023) 10.1103/PhysRevX.13.041005.

[136] M. Tuokkola, Y. Sunada, H. Kivijärvi, J. Albanese, L. Grönberg, J.-P. Kaikkonen, V. Vesterinen, J. Govenius, and M. Möttönen, "Methods to achieve near-millisecond energy relaxation and dephasing times for a superconducting transmon qubit", Nature Communications **16**, 5421 (2025) 10.1038/s41467-025-61126-0.

[137] Y. Tao, J. M. Boss, B. A. Moores, and C. L. Degen, "Single-crystal diamond nanomechanical resonators with quality factors exceeding one million", Nature Communications **5**, 3638 (2014) 10.1038/ncomms4638.

[138] Y. Liu, H. Sun, Q. Liu, H. Wu, M. A. Sillanpää, and T. Li, "Degeneracy-breaking and long-lived multimode microwave electromechanical systems enabled by cubic silicon-carbide membrane crystals", Nature Communications **16**, 1207 (2025) 10.1038/s41467-025-56497-3.

[139] R. O. Behunin, F. Intravaia, and P. T. Rakich, "Dimensional transformation of defect-induced noise, dissipation, and nonlinearity", Physical Review B **93**, 224110 (2016) 10.1103/PhysRevB.93.224110.

[140] S. Barzanjeh, A. Xuereb, S. Gröblacher, M. Paternostro, C. A. Regal, and E. M. Weig, "Optomechanics for quantum technologies", Nature Physics **18**, 15–24 (2022) 10.1038/s41567-021-01402-0.

[141] G. Catto, W. Liu, S. Kundu, V. Lahtinen, V. Vesterinen, and M. Möttönen, "Microwave response of a metallic superconductor subject to a high-voltage gate electrode", Scientific Reports **12**, 6822 (2022) 10.1038/s41598-022-10833-5.

[142] K. Geerlings, Z. Leghtas, I. M. Pop, S. Shankar, L. Frunzio, R. J. Schoelkopf, M. Mirrahimi, and M. H. Devoret, "Demonstrating a Driven Reset Protocol for a Superconducting Qubit", Physical Review Letters **110**, 120501 (2013) 10.1103/PhysRevLett.110.120501.

[143] Y. Chu, P. Kharel, T. Yoon, L. Frunzio, P. T. Rakich, and R. J. Schoelkopf, "Creation and control of multi-phonon Fock states in a bulk acoustic-wave resonator", Nature **563**, 666–670 (2018) 10.1038/s41586-018-0717-7.

[144] E. Jeffrey, D. Sank, J. Y. Mutus, T. C. White, J. Kelly, R. Barends, Y. Chen, Z. Chen, B. Chiaro, A. Dunsworth, A. Megrant, P. J. J. O'Malley, C. Neill, P. Roushan, A. Vainsencher, J. Wenner, A. N. Cleland, and J. M. Martinis, "Fast Accurate State Measurement with Superconducting Qubits", Physical Review Letters **112**, 190504 (2014) 10.1103/PhysRevLett.112.190504.

[145] D. Sank, A. Opremcak, A. Bengtsson, M. Khezri, J. Chen, O. Naaman, and A. Korotkov, "System characterization of dispersive readout in superconducting qubits", Physical Review Applied **23**, 024055 (2025) 10.1103/PhysRevApplied.23.024055.

[146] Y. Zhang, B. J. Lester, Y. Y. Gao, L. Jiang, R. J. Schoelkopf, and S. M. Girvin, "Engineering bilinear mode coupling in circuit QED: Theory and experiment", Physical Review A **99**, 012314 (2019) 10.1103/PhysRevA.99.012314.

[147] A. Bienfait, K. J. Satzinger, Y. P. Zhong, H.-S. Chang, M.-H. Chou, C. R. Conner, É. Dumur, J. Grebel, G. A. Peairs, R. G. Povey, and A. N. Cleland, "Phonon-mediated quantum state transfer and remote qubit entanglement", Science **364**, 368–371 (2019) 10.1126/science.aaw8415.

[148] A. Y. Cleland, E. A. Wollack, and A. H. Safavi-Naeini, "Studying phonon coherence with a quantum sensor", Nature Communications **15**, 4979 (2024) 10.1038/s41467-024-48306-0.

[149] A. L. Emser, C. Metzger, B. C. Rose, and K. W. Lehnert, *Thin-film quartz for high-coherence piezoelectric phononic crystal resonators*, June 2024, 10.48550/arXiv.2406.14660.

[150] B. Sarabi, A. N. Ramanayaka, A. L. Burin, F. C. Wellstood, and K. D. Osborn, "Projected Dipole Moments of Individual Two-Level Defects Extracted Using Circuit Quantum Electrodynamics", Physical Review Letters **116**, 167002 (2016) 10.1103/PhysRevLett.116.167002.

[151] H. Y. Carr and E. M. Purcell, "Effects of Diffusion on Free Precession in Nuclear Magnetic Resonance Experiments", Physical Review **94**, 630–638 (1954) 10.1103/PhysRev.94.630.

[152] C. Arenz, D. Burgarth, and R. Hillier, "Dynamical decoupling and homogenization of continuous variable systems", Journal of Physics A: Mathematical and Theoretical **50**, 135303 (2017) 10.1088/1751-8121/aa6017.

[153] G. Ithier, E. Collin, P. Joyez, P. J. Meeson, D. Vion, D. Esteve, F. Chiarello, A. Shnirman, Y. Makhlin, J. Schriefl, and G. Schön, "Decoherence in a superconducting quantum bit circuit", Physical Review B **72**, 134519 (2005) 10.1103/PhysRevB.72.134519.

[154] J. Bylander, S. Gustavsson, F. Yan, F. Yoshihara, K. Harrabi, G. Fitch, D. G. Cory, Y. Nakamura, J.-S. Tsai, and W. D. Oliver, "Noise spectroscopy through dynamical decoupling with a superconducting flux qubit", Nature Physics **7**, 565–570 (2011) 10.1038/nphys1994.

[155] S. Chakram, K. He, A. V. Dixit, A. E. Oriani, R. K. Naik, N. Leung, H. Kwon, W.-L. Ma, L. Jiang, and D. I. Schuster, "Multimode photon blockade", Nature Physics **18**, 879–884 (2022) 10.1038/s41567-022-01630-y.

[156] W. M. Jones, D. Lukin, and A. Scherer, "Practical nanoscale field emission devices for integrated circuits", Applied Physics Letters **110**, 263101 (2017) 10.1063/1.4989677.

[157] B.-L. Najera-Santos, R. Rousseau, K. Gerashchenko, H. Patange, A. Riva, M. Villiers, T. Briant, P.-F. Cohadon, A. Heidmann, J. Palomo, M. Rosticher, H. le Sueur, A. Sarlette, W. C. Smith, Z. Leghtas, E. Flurin, T. Jacqmin, and S. Deléglise, "High-Sensitivity ac-Charge Detection with a MHz-Frequency Fluxonium Qubit", Physical Review X **14**, 011007 (2024) 10.1103/PhysRevX.14.011007.

[158] N. R. Lee, Y. Guo, A. Y. Cleland, E. A. Wollack, R. G. Gruenke, T. Makihara, Z. Wang, T. Rajabzadeh, W. Jiang, F. M. Mayor, P. Arrangoiz-Arriola, C. J. Sarabalis, and A. H. Safavi-Naeini, "Strong Dispersive Coupling Between a Mechanical Resonator and a Fluxonium Superconducting Qubit", PRX Quantum **4**, 040342 (2023) 10.1103/PRXQuantum.4.040342.

[159] D. Rosenberg, D. Kim, R. Das, D. Yost, S. Gustavsson, D. Hover, P. Krantz, A. Melville, L. Racz, G. O. Samach, S. J. Weber, F. Yan, J. L. Yoder, A. J. Kerman, and W. D. Oliver, "3D integrated superconducting qubits", npj Quantum Information **3**, 1–5 (2017) 10.1038/s41534-017-0044-0.

[160] C. R. Conner, A. Bienfait, H.-S. Chang, M.-H. Chou, É. Dumur, J. Grebel, G. A. Peairs, R. G. Povey, H. Yan, Y. P. Zhong, and A. N. Cleland, "Superconducting qubits in a flip-chip architecture", Applied Physics Letters **118**, 232602 (2021) 10.1063/5.0050173.

[161] J. Guillaud and M. Mirrahimi, "Repetition Cat Qubits for Fault-Tolerant Quantum Computation", Physical Review X **9**, 041053 (2019) 10.1103/PhysRevX.9.041053.

[162] D. K. Tuckett, S. D. Bartlett, and S. T. Flammia, "Ultrahigh Error Threshold for Surface Codes with Biased Noise", Physical Review Letters **120**, 050505 (2018) 10.1103/PhysRevLett.120.050505.

[163] H. Card, "Aluminum—Silicon Schottky barriers and ohmic contacts in integrated circuits", IEEE Transactions on Electron Devices **23**, 538–544 (1976) 10.1109/T-ED.1976.18449.

[164] A. A. Houck, J. Koch, M. H. Devoret, S. M. Girvin, and R. J. Schoelkopf, "Life after charge noise: recent results with transmon qubits", Quantum Information Processing **8**, 105–115 (2009) 10.1007/s11128-009-0100-6.

[165] M. D. Hutchings, J. B. Hertzberg, Y. Liu, N. T. Bronn, G. A. Keefe, M. Brink, J. M. Chow, and B. L. T. Plourde, "Tunable Superconducting Qubits with Flux-Independent Coherence", Physical Review Applied **8**, 044003 (2017) 10.1103/PhysRevApplied.8.044003.

[166] J. Braumüller, L. Ding, A. P. Vepsäläinen, Y. Sung, M. Kjaergaard, T. Menke, R. Winik, D. Kim, B. M. Niedzielski, A. Melville, J. L. Yoder, C. F. Hirjibehedin, T. P. Orlando, S. Gustavsson, and W. D. Oliver, "Characterizing and Optimizing Qubit Coherence Based on SQUID Geometry", Physical Review Applied **13**, 054079 (2020) 10.1103/PhysRevApplied.13.054079.

[167] M. D. Reed, B. R. Johnson, A. A. Houck, L. DiCarlo, J. M. Chow, D. I. Schuster, L. Frunzio, and R. J. Schoelkopf, "Fast reset and suppressing spontaneous emission of a superconducting qubit", Applied Physics Letters **96**, 203110 (2010) 10.1063/1.3435463.

[168] M. Chen, J. C. Owens, H. Putterman, M. Schäfer, and O. Painter, "Phonon engineering of atomic-scale defects in superconducting quantum circuits", Science Advances **10**, eado6240 (2024) 10.1126/sciadv.ado6240.

[169] M. Zemlicka, E. Redchenko, M. Peruzzo, F. Hassani, A. Trioni, S. Barzanjeh, and J. Fink, "Compact vacuum-gap transmon qubits: Selective and sensitive probes for superconductor surface losses", Physical Review Applied **20**, 044054 (2023) 10.1103/PhysRevApplied.20.044054.

[170] M. Hofheinz, H. Wang, M. Ansmann, R. C. Bialczak, E. Lucero, M. Neeley, A. D. O'Connell, D. Sank, J. Wenner, J. M. Martinis, and A. N. Cleland, "Synthesizing arbitrary quantum states in a superconducting resonator", Nature **459**, 546–549 (2009) 10.1038/nature08005.

[171] A. I. Lvovsky, H. Hansen, T. Aichele, O. Benson, J. Mlynek, and S. Schiller, "Quantum State Reconstruction of the Single-Photon Fock State", Physical Review Letters **87**, 050402 (2001) 10.1103/PhysRevLett.87.050402.

[172] M. C. Grant and S. P. Boyd, "Graph Implementations for Nonsmooth Convex Programs", in Recent Advances in Learning and Control, edited by V. D. Blondel, S. P. Boyd, and H. Kimura (2008), pp. 95–110, 10.1007/978-1-84800-155-8_7.

[173] E. A. Sete, J. M. Gambetta, and A. N. Korotkov, "Purcell effect with microwave drive: Suppression of qubit relaxation rate", Physical Review B **89**, 104516 (2014) 10.1103/PhysRevB.89.104516.

[174] M. Carroll, S. Rosenblatt, P. Jurcevic, I. Lauer, and A. Kandala, "Dynamics of superconducting qubit relaxation times", npj Quantum Information **8**, 1–7 (2022) 10.1038/s41534-022-00643-y.

[175] G. J. Grabovskij, T. Peichl, J. Lisenfeld, G. Weiss, and A. V. Ustinov, "Strain Tuning of Individual Atomic Tunneling Systems Detected by a Superconducting Qubit", Science **338**, 232–234 (2012) 10.1126/science.1226487.

[176] R. C. Zeller and R. O. Pohl, "Thermal Conductivity and Specific Heat of Noncrystalline Solids", Physical Review B **4**, 2029–2041 (1971) 10.1103/PhysRevB.4.2029.

[177] J. M. Martinis, K. B. Cooper, R. McDermott, M. Steffen, M. Ansmann, K. D. Osborn, K. Cicak, S. Oh, D. P. Pappas, R. W. Simmonds, and C. C. Yu, "Decoherence in Josephson Qubits from Dielectric Loss", Physical Review Letters **95**, 210503 (2005) 10.1103/PhysRevLett.95.210503.

[178] A. D. O'Connell, M. Ansmann, R. C. Bialczak, M. Hofheinz, N. Katz, E. Lucero, C. McKenney, M. Neeley, H. Wang, E. M. Weig, A. N. Cleland, and J. M. Martinis, "Microwave dielectric loss at single photon energies and millikelvin temperatures", Applied Physics Letters **92**, 112903 (2008) 10.1063/1.2898887.

[179] B. D. Hauer, P. H. Kim, C. Doolin, F. Souris, and J. P. Davis, "Two-level system damping in a quasi-one-dimensional optomechanical resonator", Physical Review B **98**, 214303 (2018) 10.1103/PhysRevB.98.214303.

[180] M. Neeley, M. Ansmann, R. C. Bialczak, M. Hofheinz, N. Katz, E. Lucero, A. O'Connell, H. Wang, A. N. Cleland, and J. M. Martinis, "Process tomography of quantum memory in a Josephson-phase qubit coupled to a two-level state", Nature Physics **4**, 523–526 (2008) 10.1038/nphys972.

[181] M. J. A. Stoutimore, M. S. Khalil, C. J. Lobb, and K. D. Osborn, "A Josephson junction defect spectrometer for measuring two-level systems", Applied Physics Letters **101**, 062602 (2012) 10.1063/1.4744901.

[182] W. Woods, G. Calusine, A. Melville, A. Sevi, E. Golden, D. Kim, D. Rosenberg, J. Yoder, and W. Oliver, "Determining Interface Dielectric Losses in Superconducting Coplanar-Waveguide Resonators", Physical Review Applied **12**, 014012 (2019) 10.1103/PhysRevApplied.12.014012.

[183] M. V. P. Altoé, A. Banerjee, C. Berk, A. Hajr, A. Schwartzberg, C. Song, M. Alghadeer, S. Aloni, M. J. Elowson, J. M. Kreikebaum, E. K. Wong, S. M. Griffin, S. Rao, A. Weber-Bargioni, A. M. Minor, D. I. Santiago, S. Cabrini, I. Siddiqi, and D. F. Ogletree, "Localization and Mitigation of Loss in Niobium Superconducting Circuits", PRX Quantum **3**, 020312 (2022) 10.1103/PRXQuantum.3.020312.

[184] C. T. Earnest, J. H. Béjanin, T. G. McConkey, E. A. Peters, A. Korinek, H. Yuan, and M. Mariantoni, "Substrate surface engineering for high-quality silicon/aluminum superconducting resonators", Superconductor Science and Technology **31**, 125013 (2018) 10.1088/1361-6668/aae548.

[185] L. Faoro and L. B. Ioffe, "Internal Loss of Superconducting Resonators Induced by Interacting Two-Level Systems", Physical Review Letters **109**, 157005 (2012) 10.1103/PhysRevLett.109.157005.

[186] M. Odeh, K. Godeneli, E. Li, R. Tangirala, H. Zhou, X. Zhang, Z.-H. Zhang, and A. Sipahigil, *Non-Markovian dynamics of a superconducting qubit in a phononic bandgap*, Dec. 2023.

[187] J. Lisenfeld, A. Bilmes, S. Matityahu, S. Zanker, M. Marthaler, M. Schechter, G. Schön, A. Shnirman, G. Weiss, and A. V. Ustinov, "Decoherence spectroscopy with individual two-level tunneling defects", Scientific Reports **6**, 23786 (2016) 10.1038/srep23786.

[188] Y. Shalibo, Y. Rofe, D. Shwa, F. Zeides, M. Neeley, J. M. Martinis, and N. Katz, "Lifetime and Coherence of Two-Level Defects in a Josephson Junction", Physical Review Letters **105**, 177001 (2010) 10.1103/PhysRevLett.105.177001.

[189] S. E. de Graaf, L. Faoro, J. Burnett, A. A. Adamyan, A. Y. Tzalenchuk, S. E. Kubatkin, T. Lindström, and A. V. Danilov, "Suppression of low-frequency charge noise in superconducting resonators by surface spin desorption", Nature Communications **9**, 1143 (2018) 10.1038/s41467-018-03577-2.

[190] A. Anferov, S. P. Harvey, F. Wan, J. Simon, and D. I. Schuster, "Superconducting Qubits above 20 GHz Operating over 200 mK", PRX Quantum **5**, 030347 (2024) 10.1103/PRXQuantum.5.030347.

[191] H. J. McSkimin, "Measurement of Elastic Constants at Low Temperatures by Means of Ultrasonic Waves–Data for Silicon and Germanium Single Crystals, and for Fused Silica", Journal of Applied Physics **24**, 988–997 (1953) 10.1063/1.1721449.

[192] J. Burnett, L. Faoro, I. Wisby, V. L. Gurtovoi, A. V. Chernykh, G. M. Mikhailov, V. A. Tulin, R. Shaikhaidarov, V. Antonov, P. J. Meeson, A. Y. Tzalenchuk, and T. Lindström, "Evidence for interacting two-level systems from the 1/f noise of a superconducting resonator", Nature Communications **5**, 4119 (2014) 10.1038/ncomms5119.

[193] M. P. Maksymowych, M. Yuksel, O. A. Hitchcock, N. R. Lee, F. M. Mayor, W. Jiang, M. L. Roukes, and A. H. Safavi-Naeini, *Frequency Fluctuations in Nanomechanical Resonators due to Quantum Defects*, Jan. 2025, 10.48550/arXiv.2501.08289.

[194] A. L. Burin, S. Matityahu, and M. Schechter, "Low-temperature 1 / f noise in microwave dielectric constant of amorphous dielectrics in Josephson qubits", Physical Review B **92**, 174201 (2015) 10.1103/PhysRevB.92.174201.

[195] J. Joffrin and A. Levelut, "Virtual phonon exchange in glasses", Journal de Physique **36**, 811 (1975) 10.1051/jphys:01975003609081100.

[196] J. L. Black and B. I. Halperin, "Spectral diffusion, phonon echoes, and saturation recovery in glasses at low temperatures", Physical Review B **16**, 2879–2895 (1977) 10.1103/PhysRevB.16.2879.

[197] J. Lisenfeld, G. J. Grabovskij, C. Müller, J. H. Cole, G. Weiss, and A. V. Ustinov, "Observation of directly interacting coherent two-level systems in an amorphous material", Nature Communications **6**, 6182 (2015) 10.1038/ncomms7182.

[198] S. M. Meißner, A. Seiler, J. Lisenfeld, A. V. Ustinov, and G. Weiss, "Probing individual tunneling fluctuators with coherently controlled tunneling systems", Physical Review B **97**, 180505 (2018) 10.1103/PhysRevB.97.180505.

[199] J. Lisenfeld, C. Müller, J. H. Cole, P. Bushev, A. Lukashenko, A. Shnirman, and A. V. Ustinov, "Measuring the Temperature Dependence of Individual Two-Level Systems by Direct Coherent Control", Physical Review Letters **105**, 230504 (2010) 10.1103/PhysRevLett.105.230504.

[200] E. Paladino, Y. M. Galperin, G. Falci, and B. L. Altshuler, "$\Mathbsf{1}/\mathbsfit{f}$ noise: Implications for solid-state quantum information", Reviews of Modern Physics **86**, 361–418 (2014) 10.1103/RevModPhys.86.361.

[201] S. Schlör, J. Lisenfeld, C. Müller, A. Bilmes, A. Schneider, D. P. Pappas, A. V. Ustinov, and M. Weides, "Correlating Decoherence in Transmon Qubits: Low Frequency Noise by Single Fluctuators", Physical Review Letters **123**, 190502 (2019) 10.1103/PhysRevLett.123.190502.

[202] J. Bergli, Y. M. Galperin, and B. L. Altshuler, "Decoherence in qubits due to low-frequency noise", New Journal of Physics **11**, 025002 (2009) 10.1088/1367-2630/11/2/025002.

[203] Y. M. Galperin, B. L. Altshuler, and D. V. Shantsev, "Low-Frequency Noise as a Source of Dephasing of a Qubit", in *Fundamental Problems of Mesoscopic Physics: Interactions and Decoherence*, edited by I. V. Lerner, B. L. Altshuler, and Y. Gefen (Springer Netherlands, Dordrecht, 2004), pp. 141–165, 10.1007/1-4020-2193-3_9.

[204] X. Liu, E. Thompson, B. E. White, and R. O. Pohl, "Low-temperature internal friction in metal films and in plastically deformed bulk aluminum", Physical Review B **59**, 11767–11776 (1999) 10.1103/PhysRevB.59.11767.

[205] A. D. Fefferman, R. O. Pohl, and J. M. Parpia, "Elastic properties of polycrystalline Al and Ag films down to 6 mK", Physical Review B **82**, 064302 (2010) 10.1103/PhysRevB.82.064302.

[206] R. O. Pohl, X. Liu, and E. Thompson, "Low-temperature thermal conductivity and acoustic attenuation in amorphous solids", Reviews of Modern Physics **74**, 991–1013 (2002) 10.1103/RevModPhys.74.991.

[207] W. P. Mason and A. Rosenberg, "Phonon and Electron Drag Coefficients in Single-Crystal Aluminum", Physical Review **151**, 434–441 (1966) 10.1103/PhysRev.151.434.

[208] A. Bilmes, S. Zanker, A. Heimes, M. Marthaler, G. Schön, G. Weiss, A. V. Ustinov, and J. Lisenfeld, "Electronic decoherence of two-level systems in a Josephson junction", Physical Review B **96**, 064504 (2017) 10.1103/PhysRevB.96.064504.

[209] O. Maillet, D. Cattiaux, X. Zhou, R. R. Gazizulin, O. Bourgeois, A. D. Fefferman, and E. Collin, "Nanomechanical damping via electron-assisted relaxation of two-level systems", Physical Review B **107**, 064104 (2023) 10.1103/PhysRevB.107.064104.

[210] J. Narayan, P. Tiwari, X. Chen, J. Singh, R. Chowdhury, and T. Zheleva, "Epitaxial growth of TiN films on (100) silicon substrates by laser physical vapor deposition", Applied Physics Letters **61**, 1290–1292 (1992) 10.1063/1.107568.

[211] F. Cheng, P.-H. Su, J. Choi, S. Gwo, X. Li, and C.-K. Shih, "Epitaxial Growth of Atomically Smooth Aluminum on Silicon and Its Intrinsic Optical Properties", ACS Nano **10**, 9852–9860 (2016) 10.1021/acsnano.6b05556.

[212] R. W. Heeres, B. Vlastakis, E. Holland, S. Krastanov, V. V. Albert, L. Frunzio, L. Jiang, and R. J. Schoelkopf, "Cavity State Manipulation Using Photon-Number Selective Phase Gates", Physical Review Letters **115**, 137002 (2015) 10.1103/PhysRevLett.115.137002.

[213] A. Eickbusch, V. Sivak, A. Z. Ding, S. S. Elder, S. R. Jha, J. Venkatraman, B. Royer, S. M. Girvin, R. J. Schoelkopf, and M. H. Devoret, "Fast universal control of an oscillator with weak dispersive coupling to a qubit", Nature Physics **18**, 1464–1469 (2022) 10.1038/s41567-022-01776-9.

[214] A. Grimm, N. E. Frattini, S. Puri, S. O. Mundhada, S. Touzard, M. Mirrahimi, S. M. Girvin, S. Shankar, and M. H. Devoret, "Stabilization and operation of a Kerr-cat qubit", Nature **584**, 205–209 (2020) 10.1038/s41586-020-2587-z.

[215] R. Lescanne, M. Villiers, T. Peronnin, A. Sarlette, M. Delbecq, B. Huard, T. Kontos, M. Mirrahimi, and Z. Leghtas, "Exponential suppression of bit-flips in a qubit encoded in an oscillator", Nature Physics **16**, 509–513 (2020) 10.1038/s41567-020-0824-x.

[216] N. Ofek, A. Petrenko, R. Heeres, P. Reinhold, Z. Leghtas, B. Vlastakis, Y. Liu, L. Frunzio, S. M. Girvin, L. Jiang, M. Mirrahimi, M. H. Devoret, and R. J. Schoelkopf, "Extending the lifetime of a quantum bit with error correction in superconducting circuits", Nature **536**, 441–445 (2016) 10.1038/nature18949.

[217] P. Campagne-Ibarcq, A. Eickbusch, S. Touzard, E. Zalys-Geller, N. E. Frattini, V. V. Sivak, P. Reinhold, S. Puri, S. Shankar, R. J. Schoelkopf, L. Frunzio, M. Mirrahimi, and M. H. Devoret, "Quantum error correction of a qubit encoded in grid states of an oscillator", Nature **584**, 368–372 (2020) 10.1038/s41586-020-2603-3.

[218] H. Putterman, K. Noh, C. T. Hann, G. S. MacCabe, S. Aghaeimeibodi, R. N. Patel, M. Lee, W. M. Jones, H. Moradinejad, R. Rodriguez, N. Mahuli, J. Rose, J. C. Owens, H. Levine, E. Rosenfeld, P. Reinhold, L. Moncelsi, J. A. Alcid, N. Alidoust, P. Arrangoiz-Arriola, J. Barnett, P. Bienias, H. A. Carson, C. Chen, L. Chen, H. Chinkezian, E. M. Chisholm, M.-H. Chou, A. Clerk, A. Clifford, R. Cosmic, A. V. Curiel, E. Davis, L. DeLorenzo, J. M. D'Ewart, A. Diky, N. D'Souza, P. T. Dumitrescu, S. Eisenmann, E. Elkhouly, G. Evenbly, M. T. Fang, Y. Fang, M. J. Fling, W. Fon, G. Garcia, A. V. Gorshkov, J. A. Grant, M. J. Gray, S. Grimberg, A. L. Grimsmo, A. Haim, J. Hand, Y. He, M. Hernandez, D. Hover, J. S. C. Hung, M. Hunt, J. Iverson, I. Jarrige, J.-C. Jaskula, L. Jiang, M. Kalaee, R. Karabalin, P. J. Karalekas, A. J. Keller, A. Khalajhedayati, A. Kubica, H. Lee, C. Leroux, S. Lieu, V. Ly, K. V. Madrigal, G. Marcaud, G. McCabe, C. Miles, A. Milsted, J. Minguzzi, A. Mishra, B. Mukherjee, M. Naghiloo, E. Oblepias, G. Ortuno, J. Pagdilao, N. Pancotti, A. Panduro, J. P. Paquette, M. Park, G. A. Peairs, D. Perello, E. C. Peterson, S. Ponte, J. Preskill, J. Qiao, G. Refael, R. Resnick, A. Retzker, O. A. Reyna, M. Runyan, C. A. Ryan, A. Sahmoud, E. Sanchez, R. Sanil, K. Sankar, Y. Sato, T. Scaffidi, S. Siavoshi, P. Sivarajah, T. Skogland, C.-J. Su, L. J. Swenson, S. M. Teo, A. Tomada, G. Torlai, E. A. Wollack, Y. Ye, J. A. Zerrudo, K. Zhang, F. G. S. L. Brandão, M. H. Matheny, and O. Painter, "Hardware-efficient quantum error correction via concatenated bosonic qubits", Nature **638**, 927–934 (2025) 10.1038/s41586-025-08642-7.

[219] M. Reagor, W. Pfaff, C. Axline, R. W. Heeres, N. Ofek, K. Sliwa, E. Holland, C. Wang, J. Blumoff, K. Chou, M. J. Hatridge, L. Frunzio, M. H. Devoret, L. Jiang, and R. J. Schoelkopf, "Quantum memory with millisecond coherence in circuit QED", Physical Review B **94**, 014506 (2016) 10.1103/PhysRevB.94.014506.

[220] R. K. Naik, N. Leung, S. Chakram, P. Groszkowski, Y. Lu, N. Earnest, D. C. McKay, J. Koch, and D. I. Schuster, "Random access quantum information processors using multimode circuit quantum electrodynamics", Nature Communications **8**, 1904 (2017) 10.1038/s41467-017-02046-6.

[221] O. Milul, B. Guttel, U. Goldblatt, S. Hazanov, L. M. Joshi, D. Chausovsky, N. Kahn, E. Çiftyürek, F. Lafont, and S. Rosenblum, "Superconducting Cavity Qubit with Tens of Milliseconds Single-Photon Coherence Time", PRX Quantum **4**, 030336 (2023) 10.1103/PRXQuantum.4.030336.

[222] C. Liu, M. Wang, S. A. Stein, Y. Ding, and A. Li, *Quantum Memory: A Missing Piece in Quantum Computing Units*, Nov. 2023, 10.48550/arXiv.2309.14432.

[223] H. J. Kimble, "The quantum internet", Nature **453**, 1023–1030 (2008) 10.1038/nature07127.

[224] S. Wehner, D. Elkouss, and R. Hanson, "Quantum internet: A vision for the road ahead", Science **362**, eaam9288 (2018) 10.1126/science.aam9288.

[225] N. Dirnegger, M. Malekakhlagh, V. Siddhu, A. Rao, C. Xiong, M. Kumph, J. Orcutt, and A. Falk, *Monte Carlo model of distilled remote entanglement between superconducting qubits across optical channels*, Mar. 2025, 10.48550/arXiv.2503.10842.

[226] N. P. Breuckmann and J. N. Eberhardt, "Quantum Low-Density Parity-Check Codes", PRX Quantum **2**, 040101 (2021) 10.1103/PRXQuantum.2.040101.

[227] Y. Y. Gao, B. J. Lester, K. S. Chou, L. Frunzio, M. H. Devoret, L. Jiang, S. M. Girvin, and R. J. Schoelkopf, "Entanglement of bosonic modes through an engineered exchange interaction", Nature **566**, 509–512 (2019) 10.1038/s41586-019-0970-4.

[228] B. J. Chapman, S. J. de Graaf, S. H. Xue, Y. Zhang, J. Teoh, J. C. Curtis, T. Tsunoda, A. Eickbusch, A. P. Read, A. Koottandavida, S. O. Mundhada, L. Frunzio, M. Devoret, S. Girvin, and R. Schoelkopf, "High-On-Off-Ratio Beam-Splitter Interaction for Gates on Bosonically Encoded Qubits", PRX Quantum **4**, 020355 (2023) 10.1103/PRXQuantum.4.020355.

[229] M. Atkinson, N. Santoro, and J. Urrutia, "Integer Sets with Distinct Sums and Differences and Carrier Frequency Assignments for Nonlinear Repeaters", IEEE Transactions on Communications **34**, 614–617 (1986) 10.1109/TCOM.1986.1096587.

[230] C. Wang, C. Axline, Y. Y. Gao, T. Brecht, Y. Chu, L. Frunzio, M. H. Devoret, and R. J. Schoelkopf, "Surface participation and dielectric loss in superconducting qubits", Applied Physics Letters **107**, 162601 (2015) 10.1063/1.4934486.

[231] A. P. Read, B. J. Chapman, C. U. Lei, J. C. Curtis, S. Ganjam, L. Krayzman, L. Frunzio, and R. J. Schoelkopf, "Precision Measurement of the Microwave Dielectric Loss of Sapphire in the Quantum Regime with Parts-per-Billion Sensitivity", Physical Review Applied **19**, 034064 (2023) 10.1103/PhysRevApplied.19.034064.

[232] H. Kim, C. Jünger, A. Morvan, E. S. Barnard, W. P. Livingston, M. V. P. Altoé, Y. Kim, C. Song, L. Chen, J. M. Kreikebaum, D. F. Ogletree, D. I. Santiago, and I. Siddiqi, "Effects of laser-annealing on fixed-frequency superconducting qubits", Applied Physics Letters **121**, 142601 (2022) 10.1063/5.0102092.

[233] D. P. Pappas, M. Field, C. J. Kopas, J. A. Howard, X. Wang, E. Lachman, J. Oh, L. Zhou, A. Gold, G. M. Stiehl, K. Yadavalli, E. A. Sete, A. Bestwick, M. J. Kramer, and J. Y. Mutus, "Alternating-bias assisted annealing of amorphous oxide tunnel junctions", Communications Materials **5**, 150 (2024) 10.1038/s43246-024-00596-z.

[234] D. I. Schuster, A. Wallraff, A. Blais, L. Frunzio, R.-S. Huang, J. Majer, S. M. Girvin, and R. J. Schoelkopf, "Ac Stark Shift and Dephasing of a Superconducting Qubit Strongly Coupled to a Cavity Field", Physical Review Letters **94**, 123602 (2005) 10.1103/PhysRevLett.94.123602.

[235] S. M. Lewis, M. S. Hunt, G. A. DeRose, H. R. Alty, J. Li, A. Wertheim, L. De Rose, G. A. Timco, A. Scherer, S. G. Yeates, and R. E. P. Winpenny, "Plasma-Etched Pattern Transfer of Sub-10 nm Structures Using a Metal–Organic Resist and Helium Ion Beam Lithography", Nano Letters **19**, 6043–6048 (2019) 10.1021/acs.nanolett.9b01911.

[236] A. N. Babar, T. A. S. Weis, K. Tsoukalas, S. Kadkhodazadeh, G. Arregui, B. Vosoughi Lahijani, and S. Stobbe, "Self-assembled photonic cavities with atomic-scale confinement", Nature **624**, 57–63 (2023) 10.1038/s41586-023-06736-8.

[237] L. B. Nguyen, Y.-H. Lin, A. Somoroff, R. Mencia, N. Grabon, and V. E. Manucharyan, "High-Coherence Fluxonium Qubit", Physical Review X **9**, 041041 (2019) 10.1103/PhysRevX.9.041041.

[238] A. Bilmes, S. Volosheniuk, A. V. Ustinov, and J. Lisenfeld, "Probing defect densities at the edges and inside Josephson junctions of superconducting qubits", npj Quantum Information **8**, 1–6 (2022) 10.1038/s41534-022-00532-4.

[239] M. Yuksel, M. P. Maksymowych, O. A. Hitchcock, F. M. Mayor, N. R. Lee, M. I. Dykman, A. H. Safavi-Naeini, and M. L. Roukes, *Intrinsic Phononic Dressed States in a Nanomechanical System*, Apr. 2025, 10.48550/arXiv.2502.18587.

[240] M. S. Khalil, S. Gladchenko, M. J. A. Stoutimore, F. C. Wellstood, A. L. Burin, and K. D. Osborn, "Landau-Zener population control and dipole measurement of a two-level-system bath", Physical Review B **90**, 100201 (2014) 10.1103/PhysRevB.90.100201.

[241] M. P. da Silva, D. Bozyigit, A. Wallraff, and A. Blais, "Schemes for the observation of photon correlation functions in circuit QED with linear detectors", Physical Review A **82**, 043804 (2010) 10.1103/PhysRevA.82.043804.

[242] J. M. Fink, M. Kalaee, A. Pitanti, R. Norte, L. Heinzle, M. Davanço, K. Srinivasan, and O. Painter, "Quantum electromechanics on silicon nitride nanomembranes", Nature Communications **7**, 12396 (2016) 10.1038/ncomms12396.

[243] A. H. Safavi-Naeini, J. Chan, J. T. Hill, S. Gröblacher, H. Miao, Y. Chen, M. Aspelmeyer, and O. Painter, "Laser noise in cavity-optomechanical cooling and thermometry", New Journal of Physics **15**, 035007 (2013) 10.1088/1367-2630/15/3/035007.

[244] K. Koshino, "Theory of resonance fluorescence from a solid-state cavity QED system: Effects of pure dephasing", Physical Review A **84**, 033824 (2011) 10.1103/PhysRevA.84.033824.

[245] H. Nyquist, "Thermal Agitation of Electric Charge in Conductors", Physical Review **32**, 110–113 (1928) 10.1103/PhysRev.32.110.

[246] M. D. LaHaye, F. Rouxinol, Y. Hao, S.-B. Shim, and E. K. Irish, "Superconducting circuitry for quantum electromechanical systems", in Quantum Information and Computation XIII, Vol. 9500 (May 2015), pp. 276–295, 10.1117/12.2182719.

[247] C. Wang, Y. Y. Gao, I. M. Pop, U. Vool, C. Axline, T. Brecht, R. W. Heeres, L. Frunzio, M. H. Devoret, G. Catelani, L. I. Glazman, and R. J. Schoelkopf, "Measurement and control of quasiparticle dynamics in a superconducting qubit", Nature Communications **5**, 5836 (2014) 10.1038/ncomms6836.

[248] G. Catelani, R. J. Schoelkopf, M. H. Devoret, and L. I. Glazman, "Relaxation and frequency shifts induced by quasiparticles in superconducting qubits", Physical Review B **84**, 064517 (2011) 10.1103/PhysRevB.84.064517.

[249] X. Y. Jin, A. Kamal, A. P. Sears, T. Gudmundsen, D. Hover, J. Miloshi, R. Slattery, F. Yan, J. Yoder, T. P. Orlando, S. Gustavsson, and W. D. Oliver, "Thermal and Residual Excited-State Population in a 3D Transmon Qubit", Physical Review Letters **114**, 240501 (2015) 10.1103/PhysRevLett.114.240501.

[250] M. F. Ritter, A. Fuhrer, D. Z. Haxell, S. Hart, P. Gumann, H. Riel, and F. Nichele, "A superconducting switch actuated by injection of high-energy electrons", Nature Communications **12**, 1266 (2021) 10.1038/s41467-021-21231-2.

[251] J. R. Johansson, P. D. Nation, and F. Nori, "QuTiP: An open-source Python framework for the dynamics of open quantum systems", Computer Physics Communications **183**, 1760–1772 (2012) 10.1016/j.cpc.2012.02.021.

[252] J. R. Johansson, P. D. Nation, and F. Nori, "QuTiP 2: A Python framework for the dynamics of open quantum systems", Computer Physics Communications **184**, 1234–1240 (2013) 10.1016/j.cpc.2012.11.019.

[253] A. Blais, A. L. Grimsmo, S. M. Girvin, and A. Wallraff, "Circuit Quantum Electrodynamics", Reviews of Modern Physics **93**, 025005 (2021) 10.1103/RevModPhys.93.025005.

[254] M. Kristen, A. Schneider, A. Stehli, T. Wolz, S. Danilin, H. S. Ku, J. Long, X. Wu, R. Lake, D. P. Pappas, A. V. Ustinov, and M. Weides, "Amplitude and frequency sensing of microwave fields with a superconducting transmon qudit", npj Quantum Information **6**, 57 (2020) 10.1038/s41534-020-00287-w.

[255] W. P. Mason, "Ultrasonic Attenuation Due to Lattice-Electron Interaction in Normal Conducting Metals", Physical Review **97**, 557–558 (1955) 10.1103/PhysRev.97.557.

[256] Mason Warren P., *Electromechanical Transducers And Wave Filters* (1942).

[257] W. P. Mason and H. E. Bömmel, "Ultrasonic Attenuation at Low Temperatures for Metals in the Normal and Superconducting States", The Journal of the Acoustical Society of America **28**, 930–943 (1956) 10.1121/1.1908524.

[258] D. H. Filson, "Low-Temperature Ultrasonic Attenuation in Tin and Aluminum", Physical Review **115**, 1516–1519 (1959) 10.1103/PhysRev.115.1516.

[259] E. Lax, "Acoustic Attenuation in Aluminum due to Electron-Lattice Interaction", Physical Review **115**, 1591–1594 (1959) 10.1103/PhysRev.115.1591.

Appendix A

SUPPLEMENTARY INFORMATION FOR CHAPTER 4

A.1 Electrostatic Interaction

Coherent Response

The full Hamiltonian our system is (see Section 2.2 for derivation and details)

$$H/\hbar = \omega_r \hat{a}^\dagger \hat{a} + \omega_m \hat{b}^\dagger \hat{b} + i g_{\mathrm{em}} (\hat{a}\hat{b}^\dagger - \hat{a}^\dagger \hat{b}). \tag{A.1}$$

In probing our cavity-mechanics system, we use a microwave tone. We can write the Langevin equations for Eq. (A.1) as

$$\dot{\hat{a}} = -(i\omega_r + \kappa/2)\,\hat{a} - g_{\mathrm{em}}\hat{b} - \sqrt{\kappa_e}\hat{a}_{\mathrm{in}} \tag{A.2}$$

$$\dot{\hat{b}} = -(i\omega_m + \gamma/2)\,\hat{b} + g_{\mathrm{em}}\hat{a}, \tag{A.3}$$

where we have neglected the thermal fluctuations entering the microwave and mechanics, as we are focused on the coherent response of our system.

Taking the Fourier transform of the Langevin equations, we obtain

$$(i\Delta + \kappa/2)\,\hat{a}(\omega) = -g_{\mathrm{em}}\hat{b}(\omega) - \sqrt{\kappa_e}\,\hat{a}_{\mathrm{in}}(\omega) \tag{A.4}$$

$$(i\delta + \gamma/2)\,\hat{b}(\omega) = g_{\mathrm{em}}\hat{a}(\omega), \tag{A.5}$$

where $\Delta = \omega_r - \omega$ and $\delta = \omega_m - \omega$. Substituting Eq. (A.5) into Eq. (A.4), we can express the microwave cavity operator as

$$\hat{a}(\omega) = -\frac{\sqrt{\kappa_e}\,\hat{a}_{\mathrm{in}}(\omega)}{i\Delta + \kappa/2 + \frac{g_{\mathrm{em}}^2}{i\delta+\gamma/2}}. \tag{A.6}$$

Using input-output theory, we can define the output operator as $\hat{a}_{\mathrm{out}}(\omega) = \hat{a}_{\mathrm{in}}(\omega) + \sqrt{\kappa_e}\hat{a}(\omega)$. Using Eq. (A.6), we obtain an expression similar to the familiar electromechanically induced transparency (EIT) expression

$$\frac{\hat{a}_{\mathrm{out}}(\omega)}{\hat{a}_{\mathrm{in}}(\omega)} = 1 - \frac{\kappa_e}{i\Delta + \kappa/2 + \frac{g_{\mathrm{em}}^2}{i\delta+\gamma/2}}. \tag{A.7}$$

We utilize this expression to fit the reflection traces we obtain of the cavity-mechanics system.

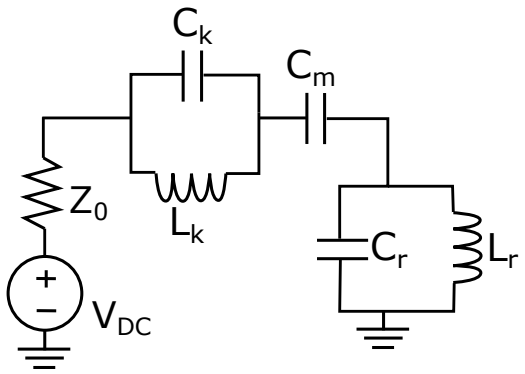


Figure A.1: **Equivalent circuit.** Equivalent electrical circuit of our system.

Equivalent Circuit Model

The calculation of the electromechanical coupling strength via finite element method simulations is sufficient to completely describe the behavior of our system which consists of two coupled resonators. However, obtaining an electrical equivalent circuit for the mechanical resonator is crucial for making the analysis of complex electromechanical circuits more tractable. For this purpose, we model our mechanical resonator by a parallel LC resonator (C_k,L_k) in series with a capacitor C_m. This model can be seen in Fig. A.1, where the coupling to the lumped element microwave resonator (C_r,L_r) is capacitive via C_m.

The equivalent mechanical capacitance can be expressed as (for details and derivation see Section 2.3)

$$C_\mathrm{k} = \frac{\hbar C_\mathrm{m}^2 \omega_m}{2\left(\partial_x C_\mathrm{m}\, x_\mathrm{zpf}\, V_\mathrm{DC}\right)^2} - C_\mathrm{m}. \tag{A.8}$$

The equivalent mechanical inductance can be obtained following the calculation of C_k by noting that $\omega_m = [L_\mathrm{k}(C_\mathrm{k} + C_\mathrm{m})]^{-1/2}$. This circuit model gives us the correct expression for the electromechanical coupling strength, which is attained by capacitive coupling between the two circuit modes where

$$g_\mathrm{em} = \frac{C_\mathrm{m}}{2\sqrt{(C_\mathrm{k} + C_\mathrm{m})(C_\mathrm{r} + C_\mathrm{m})}}\sqrt{\omega_r \omega_m}. \tag{A.9}$$

In this capacitive coupling picture, the value of C_r primarily sets the zero point fluctuations of voltage for the microwave resonator since we have a small electromechanical participation ratio ($\eta = C_\mathrm{m}/(C_\mathrm{m} + C_\mathrm{r}) \ll 1$). The small participation ratio of our capacitor is caused by the small physical dimensions of our electromechanical capacitor which is commensurate with 1 μm transverse acoustic wavelength at 5

GHz. This leads to the electrical energy on top of the electromechanical capacitor being substantially diluted compared to the total electrical energy stored on the microwave resonator.

We express the circuit parameters for device B in Table A.1. We note that the equivalent circuit model parameters for the mechanical resonator are dependent on the external voltage bias V_{DC}. This scaling is noted in the table, where L_{k} and C_{k} are provided for 1 V.

Table A.1: **Equivalent circuit parameters for device B.** The mechanical parameters C_{k} and L_{k} are dependent on the applied external voltage. The given values are for 1 V and the dependence on V_{DC} is specified.

Parameter	Value
C_{m}	0.2 fF
C_{r}	12.1 fF
L_{r}	75.8 nH
η	1.5 %
L_{k}	43.5 fH $(1\mathrm{V}/V_{\mathrm{DC}})^2$
C_{k}	21.1 nF $(V_{\mathrm{DC}}/1\mathrm{V})^2$
$f_{r,m}$	5.26 GHz
$g_0/2\pi$	45.4 kHz/V

In the circuit model, one can see that the mechanical resonator is capacitively coupled to the CPW which has an impedance $Z_0 = 50\ \Omega$. This leads to some direct external decay to the CPW. However, even at the maximum voltage we can apply of 25 V, due to our massive equivalent capacitance this readout is at the level of 5 Hz, which is negligible and further emphasizes the need for a microwave cavity to enhance electromechanical readout of mechanics.

A.2 Measurement Setup

The chip is wirebonded to a PCB, which is placed into a copper box and then mounted to the mixing stage of the dilution refrigerator at $\sim$ 15 mK. The box has a coil on top for magnetic field tuning of the microwave resonators. The coil is obtained by hand winding a superconducting wire around a cylindrical extrusion.

The device is measured in reflection with the aid of a cryogenic circulator. A bias tee (QMC-CRYODPLX-0218) is placed between the chip and the circulator to enable DC biasing of the transducer and readout of the microwave cavity via the same CPW.

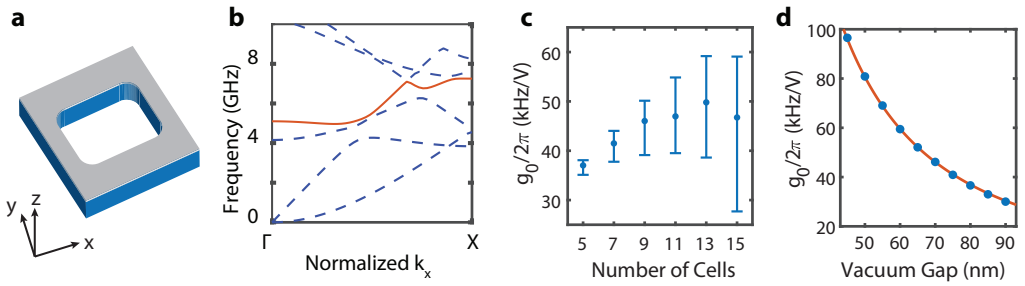


Figure A.2: **Moving capacitor design.** (a) Unit cell of the inner electrode of the electrostatic transducer. The beam is oriented along the x-direction. (b) Unit cell acoustic band diagram. (c) Disorder simulations of coupling strength vs number of unit cells of the inner electrode for $\sigma = 2$ nm disorder and 55 realizations for each data point. The simulations are for a 70-nm vacuum gap. The data is presented as the mean with 2 standard deviation errobars. (d) Average coupling strength vs vacuum gap size for 9 unit cells. The simulated average values are in the presence of fabrication disorder. The fit is $\propto \text{gap}^{-1.66}$.

The twisted wire pair DC input line has no attenuation and is directly attached to the bias tee (low frequency transmission band up to 500 MHz). The DC bias is provided by a Yokogawa GS2000 supply. The RF input line consists of multiple cascaded attenuators with a total attenuation of 74 dB. A tunable attenuator is further added to the input line to control the input power in a programmable manner. At the output, we have an amplifier chain that consists of a HEMT amplifier thermalized to the 4 K stage and a room temperature amplifier, with a total gain of $\sim$ 65 dB.

The current for the tuning coil is applied via a multi-channel programmable low-noise DC source. Since a significant amount of current is required to tune the microwave resonators, the normal metal section used for soldering the coil wiring leads to spurious heating of the mixing stage. We find the resistance of this normal metal section as 22 mΩ. The coherent response of the mechanics-cavity system is probed via a vector network analyzer (VNA) in reflection. For thermometry and investigations of the full-driven response of the system, microwave emission is detected by a spectrum analyzer. For time-resolved measurements, we use Quantum Machines OPX+ module. This tool enables the generation of pulses with an arbitrary waveform generator (AWG), heterodyne detection, demodulation of signals via a digitizer, and the processing of detected signals with an FPGA.

A.3 Mechanics Design

The mechanical behavior of our structures is investigated via FEM simulations on COMSOL. The inner electrode of the electrostatic transducer is patterned to form a phononic crystal cavity consisting of multiple identical unit cells, with the unit cell depicted in Fig. A.2a. These unit cells are completely metallized with a 15-nm layer of TiN on top of a 220-nm Si membrane (the anisotropic elasticity tensor is used for silicon in simulations following [75]). We are primarily interested in the Γ point of the breathing mode shown by the red band on the unit cell band diagram on Fig. A.2b. The breathing mode is chosen because it has a displacement profile that significantly modulates the electromechanical capacitance. The Γ mode is further necessary to ensure phase matching of the electromechanical interaction. Once multiple unit cells are attached to form a 1-D chain and are clamped by phononic shields that have a full bandgap, they hybridize to form a supermode that spans all the unit cells, which is our mechanical mode of interest.

Ideally, we would like to have as many unit cells as possible in forming our central electrode since the electromechanical interaction strength scales as $\propto \sqrt{N_{\text{cells}}}$. In practice, however, fabrication disorder leads to mode break-up, limiting the number of cells that can be utilized. We investigate this phenomenon via disorder simulations, which constitute a crucial tool in investigating the disorder-limited properties of periodically patterned acoustic and optical structures [85, 89, 90]. The disorder can be modeled as random changes in the center positions and the width of the negative patterns, which are etched to form the actual structure (for a detailed discussion see Section 3.3). These random changes are represented as realizations of independent Gaussian random variables with zero mean and standard deviation σ. The precise algorithm is as follows: (i) the center of the etched filleted rectangles are varied by σ in each direction (ii) the height and width of the rectangles are varied by 2σ. Since each simulation represents a given disorder realization, to accurately extract the statistics we simulate multiple instances for a given number of unit cells. We investigate the impact of the disorder on the coupling strength as shown in Fig. A.2c. In this situation, the changes in the mode profile and potential disorder-induced mode breakup are captured in variations in the coupling strength, which is the experimentally relevant parameter to us. We can see that up until 9 unit cells, g_0 grows with the number of cells. However, beyond this number, the growth rate diminishes and the disorder-induced variations increase substantially. At 9 unit cells and a 70-nm gap, we have a coupling strength of 46^{+4}_{-7} kHz/V which is in excellent agreement with our experimental results. The device parameters for

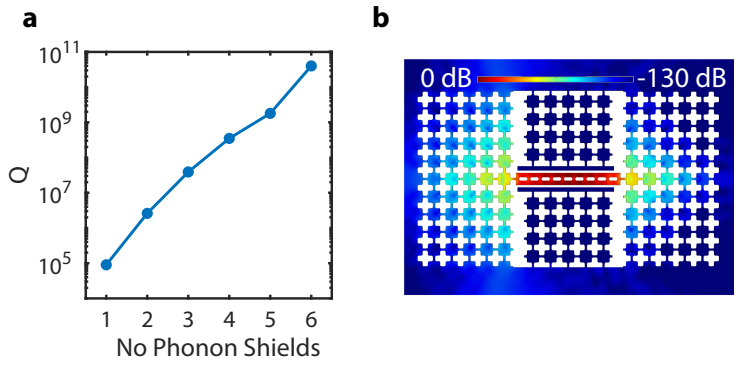


Figure A.3: **Mechanical quality factor.** (a) Radiation limited acoustic quality factor vs the number of phonon shield periods in the absence of disorder. (b) Logarithmic plot of mechanical energy density for 5 shield periods.

the moving capacitor based on this result is tabulated in Table A.2. Finally, we investigate the dependence of the coupling strength on the vacuum gap as shown in Fig. A.2d. The fit indicates that the coupling strength is a very strong function of the gap and the scaling is more rapid than that of a parallel plate capacitor.

Since acoustic waves cannot propagate in vacuum, the only radiative leakage pathway is through the silicon substrate. We minimize this loss by clamping our acoustic resonator with a phononic shield that has a complete bandgap. We investigate the effectiveness of the phononic shields in suppressing radiation loss via finite-element simulations, where the continuum of modes in the substrate is modeled by a perfectly matched layer. The simulations provide us with the radiation limited mechanical Q in the absence of fabrication disorder. As depicted in Fig. A.3a the mechanical quality factor scales nearly exponentially with the number of phononic shields. We have used 5 shield periods in our final design, for which we plot the acoustic energy distribution in Fig. A.3b.

Table A.2: Parameters of the moving capacitor.

Parameter	Value
m_{eff}	76 fg
x_{zpf}	4.7 fm
k_{eff}	7.5×10^{7} N/m
$\partial C/\partial x$	5.76×10^{-10} F/m

A.4 Thermometry

Theory

We perform thermometry by measuring the emission from the microwave and mechanical resonators with a spectrum analyzer. Our Hamiltonian is identical to that of a red-detuned optomechanical system with a large sideband resolution ($\omega_m/\kappa \gg 1$). Hence, in order to extract the thermal occupancy values for the microwave and mechanical thermal baths, we use the expression for the noise power spectral density following previous electromechanics work [18, 242]. The power spectral density at the output of the amplifier chain is

$$S(\omega) = \hbar\omega 10^{\mathcal{G}/10}\left(n_{\text{add}} + \frac{1}{2} + n_{\text{wg}}\left|\left(1 - \frac{\kappa_e\chi_r}{1 + g_{\text{em}}^2\chi_m\chi_r}\right)\right|^2 + n_{\text{b,r}}\frac{\kappa_e\kappa_i|\chi_r|^2}{|1 + g_{\text{em}}^2\chi_m\chi_r|^2} + n_{\text{b,m}}\frac{\kappa_e\gamma_i g_{\text{em}}^2|\chi_r|^2|\chi_m|^2}{|1 + g_{\text{em}}^2\chi_m\chi_r|^2}\right). \quad \text{(A.10)}$$

Here, $\mathcal{G}$ is the amplifier gain in dB, and n_{add} is the noise added by our amplifiers, which is dominated by the HEMT in our case. In this picture, the microwave resonator interacts with an intrinsic bath of occupancy $n_{\text{b,r}}$ with the rate κ_i and the waveguide having occupancy of n_{wg} with the rate κ_e. Similarly, the mechanical resonator is coupled to an intrinsic bath having occupancy of $n_{\text{b,m}}$ with the rate γ_i. The electromechanical interaction with strength g_{em} will further lead to Purcell decay into the microwave for the mechanics, giving rise to electromechanical cooling. The PSD expression also includes the bare electrical and mechanical susceptibilities which are given as

$$\chi_r^{-1}(\omega) = \kappa/2 - i(\omega - \omega_r) \quad \text{(A.11)}$$

$$\chi_m^{-1}(\omega) = \gamma_i/2 - i(\omega - \omega_m), \quad \text{(A.12)}$$

where ω_r (ω_m) is the microwave (mechanics) resonance frequency. In the weak coupling regime, we can express the mechanics and microwave resonator thermal occupancies as

$$n_r = \frac{\kappa_i n_{\text{b,r}} + \kappa_e n_{\text{wg}}}{\kappa_e + \kappa_i}, \quad \text{(A.13)}$$

$$n_m = \frac{n_{\text{b,m}} + C n_r}{1 + C}. \quad \text{(A.14)}$$

Here, $C = \frac{g_{\text{em}}^2\kappa\gamma_i^{-1}}{\Delta^2 + (\kappa/2)^2}$ is the effective cooperativity when the mechanical and microwave resonators are detuned by Δ. In the absence of any detuning and at large bias

voltages, the cooperativity becomes large, leading to substantial electromechanical cooling, which makes it challenging to unambiguously find the mechanical intrinsic bath occupancy ($n_{\mathrm{b,m}}$). Therefore, we operate in a low-cooperativity regime (large Δ), which permits precise extraction of thermal bath occupancies. Extraction of the mechanical intrinsic bath occupancy is particularly important for quantum memory applications of our mechanical resonators, as there won't be permanent electromechanical cooling in this scenario and the thermal decoherence rate depends on this intrinsic bath occupancy.

To facilitate the analysis, we simplify the emission due to the mechanics' intrinsic bath in Eq. (A.10) as

$$S_m(\delta) \sim 4\tilde{n}_{\mathrm{m}} \frac{\kappa_e}{\kappa} \frac{\Gamma_{\mathrm{em}}}{\gamma} \frac{(\gamma/2)^2}{\delta^2 + (\gamma/2)^2}. \tag{A.15}$$

Here, $\delta = \omega - \tilde{\omega}_m$ is the detuning between the emission frequency and mechanical resonance frequency, with $\tilde{\omega}_m$ being the mechanical frequency shifted by the electrical spring effect. $\gamma = \gamma_i + \Gamma_{\mathrm{em}}$ is the total mechanical linewidth and $\tilde{n}_{\mathrm{m}} = n_{\mathrm{b,m}}\gamma_i/\gamma$ is the thermal occupancy of the mechanical resonator due to fluctuations of the intrinsic mechanical bath.

To accurately utilize the expressions for the noise power spectral density, it is crucial to take into account the distinction between broadening due to frequency jitter and radiative coupling to an intrinsic bath for the mechanical resonator. To this end, we note that the area underneath $S_m(\delta)$ is proportional to the total Purcell enhanced emission from mechanics, which is given as $\Gamma_{\mathrm{em}}\tilde{n}_{\mathrm{m}}$. Hence, we can see that Eq. (A.15) represents the emission for a mechanical resonator that has a total linewidth γ with arbitrary frequency jitter. To take the distinction between jitter and decay into account, once we have extracted $\tilde{n}_{\mathrm{m}}$, we should use only the mechanical intrinsic decay rate Γ_i to calculate the bath thermal occupancy as

$$n_{\mathrm{b,m}} = \tilde{n}_{\mathrm{m}} \frac{\Gamma_{\mathrm{em}} + \Gamma_i}{\Gamma_i}. \tag{A.16}$$

We note that due to the small non-zero microwave bath occupancy, we have some emissions from the mechanical resonator due to microwave thermal fluctuations entering the mechanics by electromechanical energy exchange. This emission interferes with that of the microwave resonator and leads to noise squashing, as can be seen in the term in Eq. (A.10) proportional to $n_{\mathrm{b,r}}$ [243]. This noise squashing is also taken into account in our analysis to calculate our mechanical bath occupancy correctly.

Following this approach, we can investigate the intrinsic microwave ($n_{b,r}$) and mechanical ($n_{b,m}$) bath occupancies as a function of the cryostat temperature. As seen in Fig. A.4, as the temperature of the cryostat is increased, both bath temperatures follow the cryostat temperature, indicating the validity of our measurement approach.

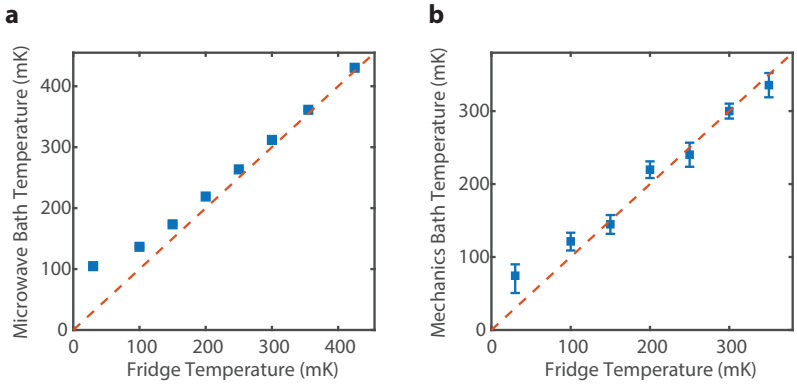


Figure A.4: **Resonator bath thermalization.** The effective temperature for the intrinsic (a) microwave ($n_{b,r}$) and (b) mechanical ($n_{b,m}$) as the cryostat temperature is increased. The dashed line represents perfect thermalization. The presented data is from theory fits with the errorbars indicating $\pm 3\sigma$ confidence interval.

Driven Response

We generally do not see significant emission from the mechanical resonator during thermometry, due to the mechanics being deep in its motional ground state. Due to the noise introduced by our HEMT, the spectrum analyzer traces are noisy to an extent that precludes numerically fitting the mechanical emission. Thus, in order to accurately analyze this noisy data and extract the mechanical thermal occupancy, it is crucial to find the mechanical frequency, linewidth, and decay rate at a given voltage.

We achieve this by investigating the driven response of our resonators. Following the application of a coherent tone in resonance with our mechanics, the drive tone is elastically scattered, leading to a delta-like emission from the mechanics and the generation of a coherent phonon population defined as $n_{coh} = |\langle \hat{a} \rangle|^2$. These coherent population dynamics is the origin of the microwave spectrum which can be detected by a VNA. However, the frequency jitter of our system also leads to inelastic scattering of the drive tone. For frequency noise which has a correlation time smaller than the decay rate, we get an emission with the cavity lineshape

as the absorbed incoherent phonons lose memory of the drive frequency due to frequency jitter [109]. This inelastic scattering is due to the generation of a number of incoherent phonons in the cavity, whose population is $n_{\mathrm{inc}} = \langle \hat{a}^\dagger \hat{a} \rangle - |\langle \hat{a} \rangle|^2$. The incoherent emission enables us to extract the cavity linewidth and frequency via fitting the Lorentzian response. This routine for parameter extraction is repeated prior to mechanics thermometry for each voltage to facilitate accurate calculations with Eq. (A.15) and center the spectrum analyzer detection window.

Apart from extracting the lineshape of the mechanics, we can also use the driven response to measure the intrinsic decay rate Γ_i. The total coherent and incoherent phonon populations are related to the total decay rate $\Gamma_{\mathrm{d}} = \Gamma_i + \Gamma_{\mathrm{em}}$ and the total linewidth γ as follows [244]:

$$\frac{n_{\mathrm{inc}}}{n_{\mathrm{coh}}} = \frac{\gamma}{\Gamma_{\mathrm{d}}} - 1. \tag{A.17}$$

These phonon populations can be further related to the areas detected via the spectrum analyzer, where S_δ is the area underneath the coherent emission, S_{bb} (S_{nb}) is the area underneath the incoherent emission due to broadband (narrow-band) frequency noise. Therefore, the relation between the decay rates can be expressed as

$$\frac{\gamma}{\Gamma_{\mathrm{d}}} = 1 + \frac{S_{\mathrm{bb}}}{S_\delta}\left(1 - \frac{S_{\mathrm{nb}}}{S_\delta}\right), \tag{A.18}$$

where the broadband frequency noise can be arbitrarily strong, and the narrow-band noise is weak [109]. Subtracting the electromechanical readoıut rate from the total decay rate, we can calculate Γ_i. The Γ_i obtained in this manner is used to extract the mechanical bath occupancy via Eq. (A.16).

Line Calibration

We calibrate the total gain of the output line using thermometry of a 50 Ω cryogenic terminator that is thermalized to the mixing (MXC) stage of the cryostat. The output line consists of a HEMT amplifier (LNF-LNC48C) thermalized to the 4 K stages and a room-temperature amplifier. The MXC stage temperature is raised by reducing cooling power by turning off the turbo to reduce ^{3}He/^{4}He mixture flow and applying heat using the MXC stage heater. With no external input power, we measure the output power from the amplifier chain with a spectrum analyzer at different mixing stage temperatures T_{MXC}. The measured output power has contributions from the thermal noise of the resistor thermalized to the MXC stage, and the HEMT noise is characterized by a fixed noise temperature T_{HEMT}. The total power measured in an IF bandwidth $\Delta\nu_{\mathrm{IF}}$ on the spectrum analyzer is equal to the sum of the Johnson-Nyquist

noise from the two sources and is given by

$$P_{\mathrm{OUT}} = \Delta\nu_{\mathrm{IF}} k_{\mathrm{B}} G_{\mathrm{A}} \left(T_{\mathrm{MXC}} + T_{\mathrm{HEMT}}\right) \tag{A.19}$$

Here, G_A is the absolute (net) gain factor of the output line, and is a combination of the total gain due to the amplifier chain and losses due to coaxial cables. At $T_{\mathrm{MXC}} = 10$ mK, the measured output power is dominated by HEMT noise. The output gain G_A can be calculated by subtracting the contribution of the HEMT noise from the total output power measured at various T_{MXC}. We perform this measurement at multiple different MXC temperatures between 730 mK and 1.05 K. These measurements' mean and standard deviation are used to obtain G_A. We use a factor $\eta = (\hbar\omega/k_B T)/(\exp(\hbar\omega/k_B T) - 1)$ to account for corrections to Eq. (A.19) due to the Bose-Einstein distribution in the regime $\hbar\omega \sim k_B T$ [245]. Using this calibration method, we obtain a net gain of 65.6 ± 0.4 dB for the output line.

Appendix B

SUPPLEMENTARY INFORMATION FOR CHAPTER 5

B.1 Measurement setup

The fabricated chip hosting the device is wire-bonded to a printed circuit board (PCB) and placed in a copper box with a superconducting coil attached to the lid of the box. This coil is used for flux tuning the qubit, where a low-noise DC source (QDevil QDAC) provides the bias current. To further reduce the current noise on the coil, a low-pass electrical filter with a 1 kHz cutoff frequency (Thorlabs EF110) is employed along with an Aivon Therma-uD25-GL cryogenic RC lowpass filter that has a 30 kHz cutoff frequency. The box, including the chip, is mounted to the mixing stage of a He-3/He-4 dilution fridge and is covered by magnetic shields. The mixing stage of the dilution fridge is cooled down to a base temperature of around 10 mK. The wire delivering the input RF signal to the device is attenuated at each stage of the fridge, as shown in Fig. B.1, to reduce the thermal noise. Additionally, Eccosorb filters are used to suppress IR radiation, and K&L microwave filters (Tubular .250 Inch Lowpass Filters) with a cutoff frequency of 12 GHz are employed to suppress millimeter-wave radiation. The reflected signal from the device is sent to an output line, where it is amplified using a High-Electron Mobility Transistor amplifier (LNF - LNC0.3-14B HEMT at the 4K stage) and a pair of room-temperature amplifiers. The chip is isolated from the amplifier noise in this path by using an array of three cascaded isolators.

Signal generation and measurements are performed with a multichannel arbitrary waveform generator (AWG) and digitizer (Quantum Machines OPX+). The up- and down-conversion of the signals between the radio frequency and the intermediate frequency band are performed with local oscillators and IQ mixers. For tuning the qubit via the ac Stark shift, we use the up-converted signal from an AWG channel amplified by a room-temperature amplifier. When applying this strong tone, we use a tunable notch filter (Micro Lambda Wireless, MLBFR-0212) in the detection path to avoid saturation at the digitizer.

The setup details related to the voltage biasing of the mechanical oscillators are provided in Appendix B.3.

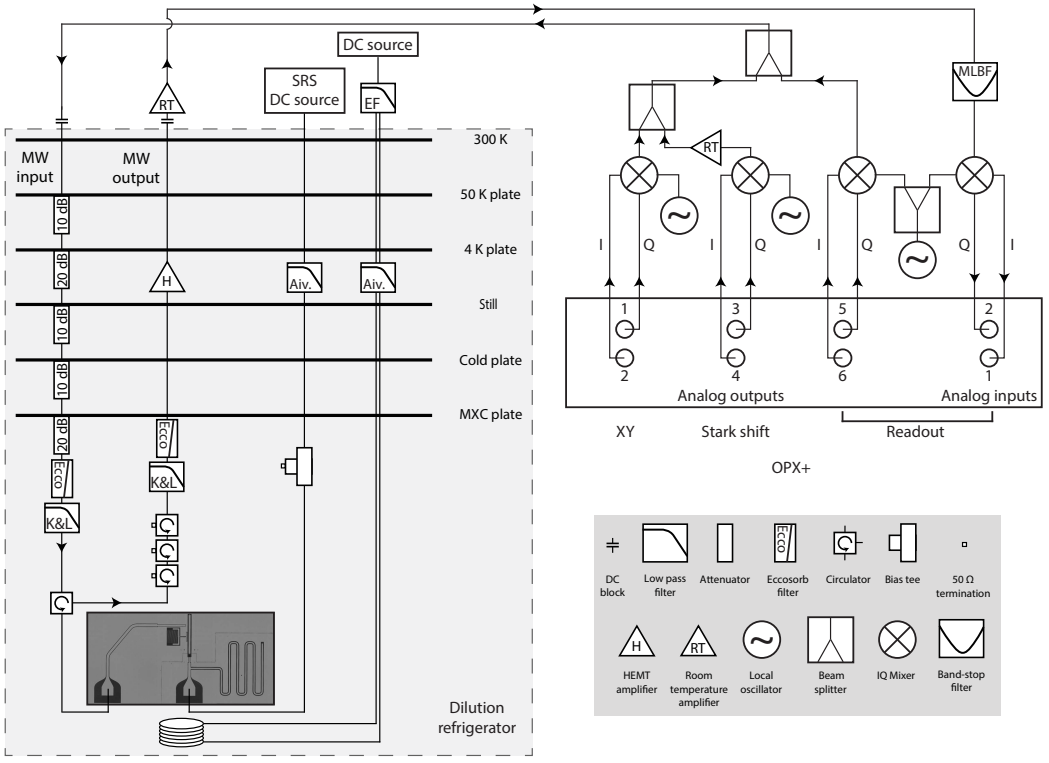


Figure B.1: **The measurement setup.** The schematic of the dilution fridge, cryogenic wiring, and room temperature electronics.

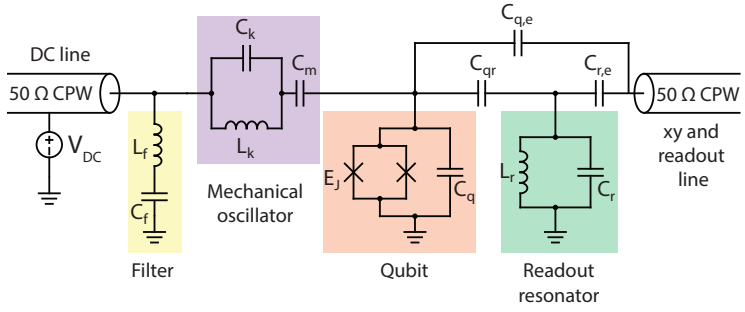


Figure B.2: **Electrical circuit diagram.** The electrical circuit diagram of our full system. The equivalent electrical circuit of the mechanical oscillator is indicated by purple shading.

B.2 Electrical Circuit

The system system Hamiltonian of our system, alongside its derivation can be found in Section 2.2. This Hamiltonian, which includes the interaction term can be utilized to accurately describe the dynamics of qubit-mechanics interaction. Nonetheless, the analysis of more sophisticated electrical circuits incorporating our mechanical oscillators can benefit significantly from an equivalent electrical circuit for our

mechanical oscillator, shown in Fig. B.2. In this equivalent circuit model, C_m corresponds to the moving capacitor and C_k is an equivalent capacitance that is given as (for details see Section 2.3)

$$C_\mathrm{k} = \frac{\hbar C_\mathrm{m}^2 \omega_m}{2\left(\partial_x C_\mathrm{m}\, x_\mathrm{zpf}\, V_\mathrm{dc}\right)^2} - C_\mathrm{m}. \tag{B.1}$$

The inductance value can be obtained by satisfying the mechanical resonance frequency condition

$$L_\mathrm{k} = \frac{1}{\omega_\mathrm{m}^2 (C_\mathrm{k} + C_\mathrm{m})}. \tag{B.2}$$

As can be seen from Fig. B.2, the interaction with the qubit in this model is due to capacitive coupling, through C_m, which can be expressed as [51]

$$\hbar g_\mathrm{em} = \beta \frac{2en_\mathrm{eg}}{C_\mathrm{m} + C_\mathrm{k}} Q_\mathrm{zpf,m}, \tag{B.3}$$

where $\beta = C_\mathrm{m}/C_\Sigma$ and $Q_\mathrm{zpf,m} = \sqrt{\hbar\omega_\mathrm{m}(C_\mathrm{m} + C_\mathrm{k})/2}$ is the zero-point-fluctuations of charge of the electrical equivalent circuit for the mechanical oscillator.

The value of the moving capacitor can be calculated to be $C_\mathrm{m} \approx 0.15$ fF, based on finite-element method simulations. At a voltage bias of 50 V, the equivalent electrical circuit parameters are $C_\mathrm{k} \approx 40$ pF (29 pF) and $L_\mathrm{k} \approx 26$ pH (38 pH) for mechanical oscillator A (B) based on the measured electromechanical coupling rate. For different voltages, the equivalent parameters can be calculated by the following scaling relations: $C_\mathrm{k} \propto V_\mathrm{dc}^{-2}$, $L_\mathrm{k} \propto V_\mathrm{dc}^2$, which are valid when $C_\mathrm{k} \gg C_\mathrm{m}$.

B.3 Voltage biasing

DC voltage setup

The DC voltage for electrostatic biasing of the mechanical oscillators is applied with a Stanford Research Systems DC205 voltage source, whose power supply is filtered with an Onfilter CleanSweep AC EMI filter. The twisted pair lines that carry the DC voltage to the device are further filtered at the 4 K stage breakout with an Aivon Therma-uD25-GL cryogenic RC lowpass filter that has a 30 kHz cutoff frequency. Finally, at the mixing stage, the Quantum Microwave QMC-CRYOTEE-0.218 bias-T acts as a lowpass filter with a 600 kHz cutoff frequency for the DC bias. A 50 Ω termination is attached to the RF port of the bias-T.

Impact of voltage bias on qubit

Since a large DC voltage is applied to the mechanical oscillator, which is in turn attached to the qubit, it is crucial to investigate potential parasitic effects on the qubit

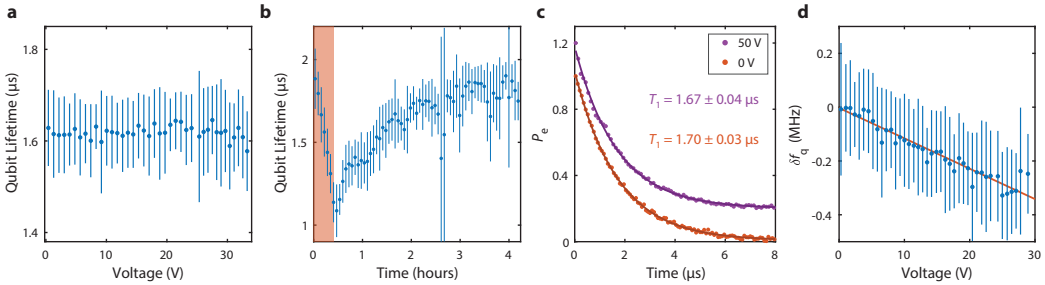


Figure B.3: **DC voltage effects on qubit. a,** Qubit lifetime (T_1) as the voltage is ramped continuously from 0 V to 25 V with a rate of 2 mV/s and from 25 V to 35 V with a rate of 1 mV/s. **b,** Qubit lifetime (T_1) degrading due to ramping of the voltage and subsequently recovering with time. The red shaded region indicates the duration where the voltage was increased from 37 V to 40 V with a rate of 2 mV/s. For the rest of the plot, the voltage is kept fixed at 40 V. **c,** Qubit decay measurements without any voltage applied and at 50 V following recovery of the qubit. The solid lines are exponential fits. The data is offset vertically for clarity. **d,** Changes in qubit frequency (δf_q) vs voltage obtained by Ramsey measurements. The red solid line is a linear fit with slope -11 kHz/V. The lifetime measurements presented in **a** is interleaved with Ramsey measurements utilized to extract qubit frequency in **d**. Each data point in **a,b,d** represents the average of 30 consecutive measurements with error bars indicating 2σ standard deviation, which is mainly set by time dependent fluctuations.

that may degrade its performance. To this end, we monitor our qubit by conducting decay and Ramsey measurements as the voltage is varied. We observe that the qubit lifetime does not exhibit any systematic degradation as the voltage is slowly ramped to around 35 V (see Fig. B.3a), with a rate of $\sim$ 1 mV/s, similar to [246]. However, at higher voltages we start to see a transient degradation of the qubit lifetime as the voltage is increased, followed by a slow recovery on the timescale of hours as seen in Fig. B.3b. The excess transient decay could be due to a currently unknown mechanism that generates quasiparticles during the charging of our capacitor, however, the long recovery timescale is not consistent with the quasiparticle recombination timescale on aluminum ($\sim$ 10 ms) [247]. We qualitatively observe that reducing the ramp rate helps reduce the transient degradation of the qubit and the degradation strongly depends on the voltage at which the ramp occurs, becoming worse at higher voltages where the recovery takes longer as well. Further studies will be needed to better understand the underlying physical mechanisms. Nonetheless, we observe that the qubit completely recovers following a ramp, a behavior repeatedly verified up to our maximum voltage of 50 V (limited by the bias-T) as seen in Fig. B.3c. The coherence time (T_2^*) obtained by Ramsey measurements is identical for 0 V and 50

V as well, testifying to the absence of excess dephasing due to the voltage bias.

Apart from enabling us to explore the voltage dependence of decoherence, Ramsey measurements also provide information about the qubit frequency, based on the frequency of the Ramsey fringes. Interestingly, we observe that the qubit frequency reduces with voltage, as shown in Fig. B.3d. Since quasiparticles are known to reduce qubit frequencies, whether the observed reduction is consistent with quasiparticle physics need to be explored. Relying on analytical expressions for the quasiparticle induced frequency shift [248], we calculate that for $\approx$ 500 kHz frequency shift, the required normalized quasiparticle density is $x_{qp} \approx 10^{-4}$. This relatively large quasiparticle density would limit the qubit lifetime to $T_{1,q} < 300$ ns and increase the qubit excited state population to $P_e > 0.1$ [249], inconsistent with the absence of noticeable lifetime degradation and heating we have measured. Therefore, the frequency shift is unlikely to be caused by quasiparticles and can instead be attributed to either the vacuum gaps or the membrane height of the device shrinking due to electrostatic forces, which in turn increase the total capacitance of the transmon.

In combination with the thermometry results that show identical qubit thermal occupation at 0 V and at 50 V, our measurements indicate the absence of any noticeable steady-state degradation of our qubit due to the applied voltage.

Leakage current measurements

We have discussed in detail the effects of the voltage bias on the qubit, through time domain characterization and thermometry measurements. In our experiments, the maximum voltage we could reach of 50 V was set by the bias-T. However, for future experiments, understanding the maximum voltage that the devices can endure is important, since it provides information about the ultimate limits of coupling enhancement. To explore this question, we have fabricated devices that have a structure comparable to our quantum acoustic system. Importantly, when a voltage is applied to a device, the current supplied by the voltage source (referred to as leakage current) provides information about the onset of breakdown or pull-in events [69, 250]. Since this is an exclusively DC measurement, we can apply a voltage without needing a bias-T and utilize a picoammeter (Keithley 6485) to measure the leakage current. As shown in Fig. B.4, we observe a small current that increases linearly with voltage (attributed to cable resistance) until 64 V, where it abruptly increases, consistent with the onset of pull-in instability [69]. These results indicate that with an improved setup, there may be room to further enhance the electromechanical

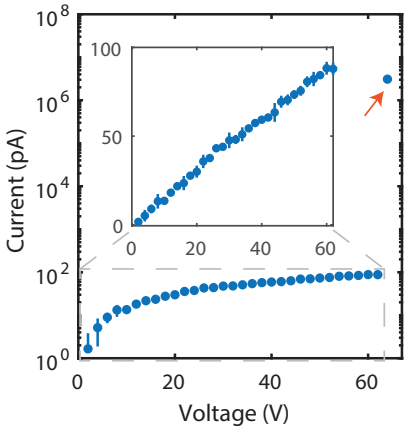


Figure B.4: **Leakage current measurements.** Leakage current measured by the picoammeter for waveguide device I, as the voltage is varied. The data points represent the mean of 8 measurements for each voltage, with error bars indicating 2σ standard error of the mean. The inset shows the region from 0 V to 62 V where the current increases linearly. The baseline resistance is set by the cable resistance, which was verified by detaching the device through a switch and observing an unchanged slope for the current.

interaction rate via higher bias voltages.

B.4 Thermometry

To do measure the qubit's effective temperature, we use the Rabi Population Measurement (RPM) method, introduced by Geerlings *et al.* [142]. For this purpose, we first conduct two-tone spectroscopy to find the frequency of the qubit's e-f transition. We then measure the baseline or reference population by applying an e-g π-pulse, followed by an X rotation on the first and second excited states, and do qubit population measurement. The π-pulse swaps the ground and first excited state populations, and the X rotation puts the population in the first excited state to a superposition of the first and second excited states. By varying the angle of the X rotation, we get Rabi oscillations where the amplitude of the measured signal is proportional to the initial ground state population P_g. To measure the population of the first excited state we repeat the same procedure without the initial π-pulse, which results in the measured amplitude being proportional to the first excited state population P_e. By assuming that the thermal populations in higher excited states are negligible, which is justified based on the resulting low residual thermal population, and normalizing the measured populations to their sum, we get the residual thermal population of the qubit. The amplitude of the oscillations in Fig. 3a are normalized to this sum,

such that the amplitude of the oscillations in the right panel is proportional to the thermal populations.

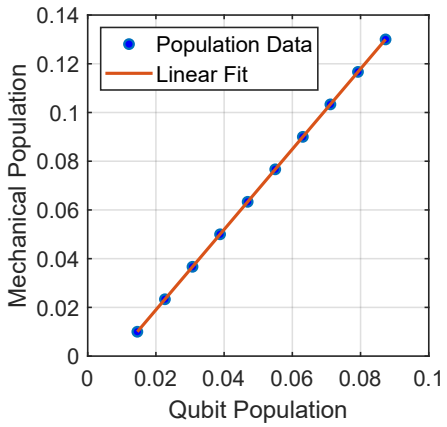


Figure B.5: **Qubit vs mechanics population.** Simulated corresponding mechanics population of mechanics B for a given measured qubit population in the thermometry setup. For the simulation, we start with a qubit thermal population of 4%, caused by the ac Stark shift, and vary the thermal population of the mechanical oscillator. Then we let the qubit and oscillator interact on resonance for half a Rabi cycle, swapping excitations, and measure the resulting qubit population. Notably, during the qubit-mechanics interaction we use a bath population of 2% for the qubit dissipator since the Stark drive is turned off for this step.

To use the same technique for mechanics thermometry we do a swap operation between the mechanics and qubit before the experiment described above. To ensure the oscillator is in equilibrium with its thermal bath, we wait around 60 ms (which is much longer than the mechanical lifetime) before each measurement. We use numerical modeling to back out the mechanical temperature from the results of this experiment to properly account for the infidelity of the swap operation, the potentially different temperatures of the qubit's and oscillator's baths, and excess population of the qubit caused by the ac Stark shift tone, which is needed to adjust the qubit-mechanics detuning. We measure this ac Stark shift drive-induced population of the qubit to be 0.039 ± 0.003 using the qubit thermometry while this drive tone is on and use it in a use Master equation analysis with the QuTiP package [251, 252] to find the corresponding mechanical population (see Fig. B.5).

B.5 Mechanical lifetime measurements

Intermediate-phonon-number measurement

To measure mechanical lifetime at intermediate phonon numbers, we apply a 1 ms-long tone, resonant with the mechanical oscillator, through the qubit to excite the oscillator. Subsequently, we wait for a varying time interval t, followed by a measurement of the qubit frequency. The excitation of the mechanical oscillator induces an ac Stark shift to the qubit transition frequency, described by [35, 253]

$$\delta\omega_{\mathrm{q}} = -\frac{2g_{\mathrm{em}}^2\alpha}{\Delta(\Delta-\alpha)}\bar{n}_{\mathrm{phonon}} \approx \frac{2g_{\mathrm{em}}^2}{\Delta}\bar{n}_{\mathrm{phonon}}. \tag{B.4}$$

Here, $\bar{n}_{\mathrm{phonon}}$ is the average phonon number in the oscillator, α is the qubit anharmonicity, g_{em} is the electromechanical coupling rate, and $\Delta = \omega_{\mathrm{q}} - \omega_{\mathrm{m}}$ represents the detuning between the oscillator and qubit bare frequencies. The approximation holds under the condition $\alpha \gg \Delta$. Consequently, the phonon number in the oscillator can be inferred from measurements of qubit frequency. To extract qubit frequencies, we perform Ramsey measurement, and fit the resulting data to determine the shift in the qubit transition frequency [201, 254]. The fitted frequencies of the Ramsey fringes relate to the qubit frequency by $\omega_{\mathrm{q}} = \omega_{\mathrm{drive}} - \omega_{\mathrm{Fit}}$, such that $\delta\omega_{\mathrm{q}} = -\delta\omega_{\mathrm{Fit}}$. To remove the offset of the drive frequency, we subtract the frequency of the last data point from each data point. An example of this measurement is illustrated in Fig. B.6, which shows the Ramsey measurement results, theoretical fits, and corresponding fitted frequencies for two representative data points.

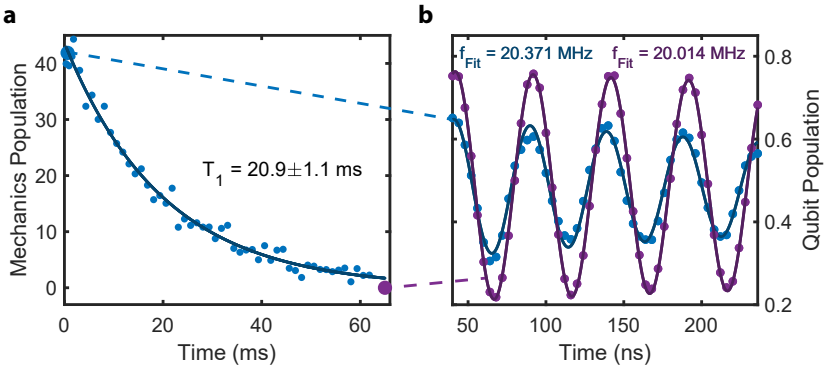


Figure B.6: **Intermediate-phonon-number measurement.** **a**, Intermediate-phonon-number decay measurement for mechanics A performed at around 40 V applied DC voltage. **b**, Ramsey fringes for two representative points from the early (blue) and late (purple) stages of the measurement, with fitted Ramsey frequencies of 20.371 and 20.014 MHz, respectively. The solid lines indicate the theory fits used to extract the qubit frequency.

High-phonon-number measurement

To assess the lifetime of mechanical oscillators at higher phonon numbers, we fabricated an array of similar devices coupled directly to a waveguide rather than to the qubit, as with mechanics A and B. The fabrication of these extra devices was necessary as the notch filters preclude electrical addressing of the mechanical oscillators coupled to the qubit. Decay measurements conducted on these oscillators, which include mechanics C presented in Fig. 4, reveal lifetimes of approximately 20 ms for multiple devices at high phonon numbers. These measurements exhibit small device-to-device variations, underscoring the reliability of achieving long lifetimes in mechanical oscillators. The results of these measurements are summarized in Table B.1.

To determine the phonon number in these oscillators, we have measured the emitted power from a mechanical oscillator into the waveguide. The relation is given by the expression [69]:

$$P_{\text{out}} = n_{\text{ph}} \frac{\hbar \omega_{\text{m}} \kappa_{\text{e,m}}}{2}, \tag{B.5}$$

where P_{out} is the output power, n_{ph} is the phonon number in the oscillator, ω_{m} is the frequency of the mechanical oscillator, and $\kappa_{\text{e,m}}$ is the external coupling rate of the oscillator to the waveguide. The detected signal consists of two contributions: the desired emission from the mechanical oscillator and the noise from the amplifier. The amplifier noise is characterized and subtracted, allowing the phonon number to be accurately determined.

Table B.1: **Lifetime of waveguide coupled oscillators.** Lifetime of all mechanical oscillators coupled to the waveguide and measured using the high-phonon-number measurement method.

mechanics	T_1 (ms)
C	21 ± 1
D	34 ± 1
E	20.1 ± 0.9
F	19.7 ± 0.6
G	22 ± 1
H	16.1 ± 0.8

Appendix C

SUPPLEMENTARY INFORMATION FOR CHAPTER 7

C.1 Acoustic Loss due to Electron-Phonon Scattering

Here, we will provide a brief description of the physics underlying acoustic loss due to electron-phonon scattering in metals. This mechanism has been experimentally observed to be quite pronounced in normal metals at cryogenic temperatures [255]. This behavior arises naturally from the temperature dependence of the process: as the temperature decreases, the electrical conductivity of a metal increases sharply, enhancing electron-phonon scattering, as will be explained below.

Since the experiments presented in Chapter 7 is conducted at cryogenic temperatures using a metal with large conductivity (aluminum), potential loss from electron-phonon scattering has to be taken into account. In order to estimate its value, we first provide a description of electron-phonon scattering in normal metals, which is then modified to take into account the impact of superconductivity.

The acoustic loss from electron-phonon scattering can be analyzed by treating the electron gas as a viscous medium with viscosity η. Within a viscous medium, there exists a damping force experienced by planes that move with different velocities. Specifically, for the exemplary case of two planes separated in y direction with a distance dy and moving in the x-direction with a velocity $\dot{u}$, there exists a viscous damping force of the form $-\eta\, d\dot{u}/dy$ [256].

The viscosity of a gas of free electrons can be expressed as [257]

$$\eta = N m_e \bar{l} v_F / 3, \tag{C.1}$$

where N is the electron density (1.8×10^{29} m^{-3} for Al), m_e is the electron mass (free electron mass in this model), $\bar{l}$ is the mean free path and v_F is the Fermi velocity (2×10^6 m/s for Al).

The mean free path is given as

$$\bar{l} = \frac{\sigma m_e v_F}{N e^2}, \tag{C.2}$$

where σ is the electrical conductivity, which we have measured to be 3×10^8 S/m for our thin aluminum films at temperatures just above the superconducting transition. From our conductivity, we can calculate the mean free path to be $\bar{l}$ = 130 nm.

Though the modeling is quite simple, these equations have been very successful in describing the acoustic loss in aluminum [207, 258, 259].

We note that the above equations rely on two assumptions:

- The timescale of mechanical motion, should be much slower than the relaxation time of electrons. Based on our conductivity, we can calculate the electronic relaxation time to be $\tau_e = \sigma m_e / N e^2 \approx 60$ fs, which satisfies the assumption of $\omega_{\mathrm{m}} \tau_e \ll 1$.
- The acoustic wavevector ($k = 2\pi/\nu$) is assumed to be much larger than mean free path, i.e. $k\bar{l} \ll 1$. Though, we expect to be in the regime $k\bar{l} \approx 1$, the correction factor for the loss is expected to be on the order of unity for our devices [257].

As these assumptions are satisfied, we can use the viscous damping model to estimate the loss for our devices.

When the aluminum films become superconducting, the impact of the this transition on the viscosity can be expressed based on the two-fluid model of superconductivity. Specifically, the total number of normal electrons (quasiparticles) is defined as $N x_{\mathrm{qp}}$, where x_{qp} is the normalized quasiparticle density. Based on our measurement of qubit excited state population (around 2%, see Fig. 5.3), we can bound our normalized quasiparticle density to be $x_{\mathrm{qp}} \approx 5 \times 10^{-6}$ [249].

Based on the above numbers, we can calculate the viscosity in the superconducting state for our aluminum films to be $\eta \approx 5 \times 10^{-8}$ Pa $\cdot$ s. By introducing this viscous damping to our finite element method simulations with COMSOL, we can estimate the mechanical Q as limited by electron phonon scattering to be $Q \approx 8 \times 10^{9}$.